UNIVERSIDAD DE MÁLAGA

bionand Centro Andaluz de Nanomedicina & Biotecnología

Tesis doctoral

Synthesis and characterization of new chromophores with two-photon absorption properties and study of their application in bioimaging

Carlos Benítez Martín

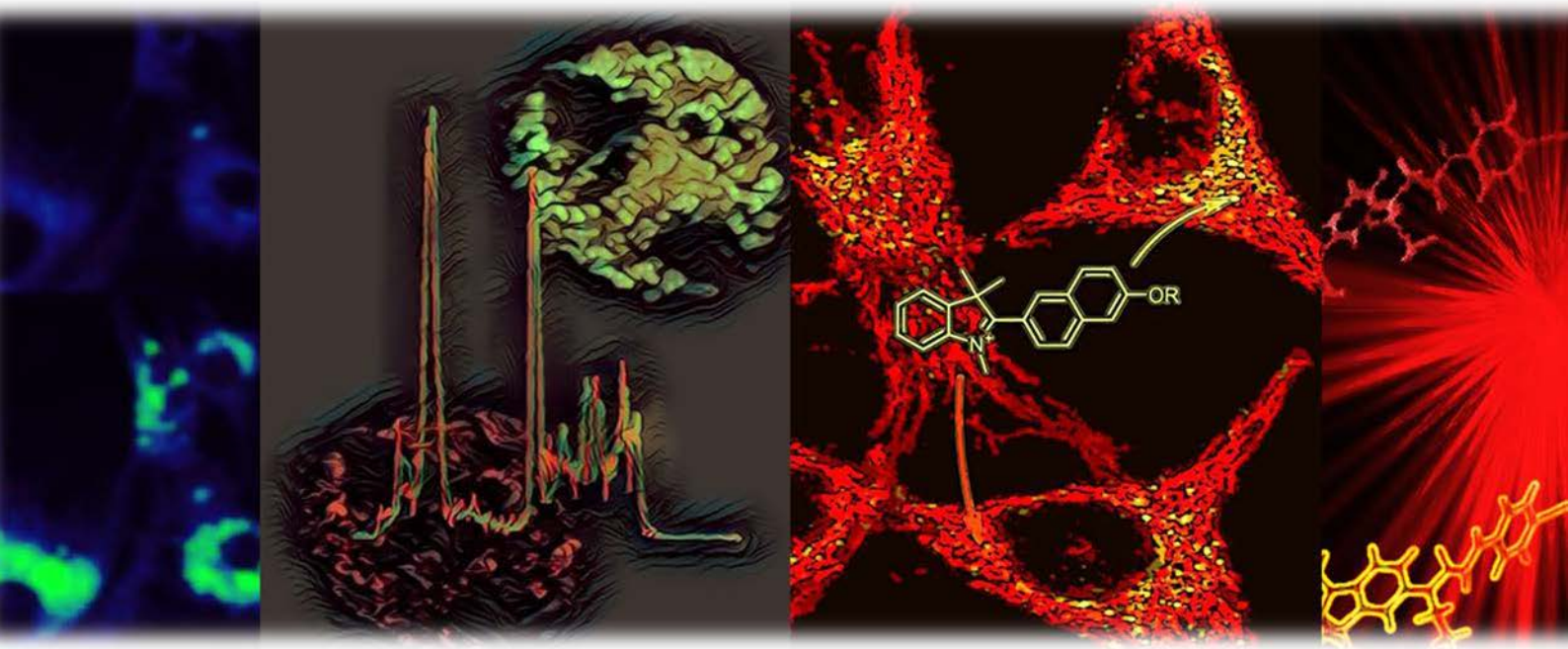

Programa de Doctorado: Química y Tecnologías Químicas. Materiales y Nanotecnología

Directores:

Dr. Ezequiel Perez-Inestrosa y Dr. Francisco Nájera

Facultad de Ciencias

Universidad de Málaga, octubre de 2021

AUTOR: Carlos Benítez Martín

https://orcid.org/0000-0003-1821-9388

EDITA: Publicaciones y Divulgación Científica. Universidad de Málaga

UNIVERSIDAD DE MÁLAGA

FACULTAD DE CIENCIAS

DEPARTAMENTO DE QUÍMICA ORGÁNICA

TESIS DOCTORAL

Synthesis and characterization of new chromophores with two-photon absorption properties and study of their application in bioimaging

Memoria para optar al grado de

Doctor en Química
(Mención Internacional)

por la Universidad de Málaga

Presenta:

Carlos Benítez Martín

Málaga, octubre de 2021

UNIVERSITY OF MALAGA

FACULTY OF SCIENCES

ORGANIC CHEMISTRY DEPARTMENT

DOCTORAL THESIS

Synthesis and characterization of new chromophores with two-photon absorption properties and study of their application in bioimaging

Dissertation to apply for the degree of

PhD on Chemistry
(International Mention)

from the University of Malaga

Submitted by:

Carlos Benitez-Martin

Malaga, October 2021

D. Ezequiel Pérez de Inestrosa de Villatoro, Catedrático de Química Orgánica y **D. Francisco Nájera Albendín**, Profesor Titular de Química Orgánica de la Facultad de Ciencias de la Universidad de Málaga,

CERTIFICAN:

Que la memoria adjunta, titulada **SYNTHESIS AND CHARACTERIZATION OF NEW CHROMOPHORES WITH TWO-PHOTON ABSORPTION PROPERTIES AND STUDY OF THEIR APPLICATION IN BIOIMAGING**, que para optar al grado de Doctor con Mención Internacional presenta **Carlos Benítez Martín**, ha sido realizada bajo nuestra dirección en los laboratorios del Departamento de Química Orgánica y del Centro Andaluz de Nanomedicina y Biotecnología (BIONAND).

Considerando que constituye un trabajo de Tesis Doctoral, autorizamos su presentación en la Facultad de Ciencias de la Universidad de Málaga.

Y para que así conste, firmamos el presente certificado en Málaga a septiembre de 2021.

Fdo. Dr. Ezequiel Pérez de Inestrosa Villatoro

Fdo. Dr. Francisco Nájera Albendín

DECLARACIÓN DE AUTORÍA Y ORIGINALIDAD DE LA TESIS PRESENTADA PARA OBTENER EL TÍTULO DE DOCTOR

D./Dña CARLOS BENÍTEZ MARTÍN
Estudiante del programa de doctorado QUIMICA Y TECNOLOGÍAS QUÍMICAS. MATERIALES Y NANOTECNOLOGÍA de la Universidad de Málaga, autor/a de la tesis, presentada para la obtención del título de doctor por la Universidad de Málaga, titulada: SYNTHESIS AND CHARACTERIZATION OF NEW CHROMOPHORES WITH TWO-PHOTON ABSORPTION PROPERTIES AND STUDY OF THEIR APPLICATION IN BIOIMAGING

Realizada bajo la tutorización de D. FRANCISCO NÁJERA ALBENDÍN y dirección de D. EZEQUIEL PEREZ DE INESTROSA VILLATORO Y D. FRANCISCO NÁJERA ALBENDÍN

DECLARO QUE:

La tesis presentada es una obra original que no infringe los derechos de propiedad intelectual ni los derechos de propiedad industrial u otros, conforme al ordenamiento jurídico vigente (Real Decreto Legislativo 1/1996, de 12 de abril, por el que se aprueba el texto refundido de la Ley de Propiedad Intelectual, regularizando, aclarando y armonizando las disposiciones legales vigentes sobre la materia), modificado por la Ley 2/2019, de 1 de marzo.

Igualmente asumo, ante a la Universidad de Málaga y ante cualquier otra instancia, la responsabilidad que pudiera derivarse en caso de plagio de contenidos en la tesis presentada, conforme al ordenamiento jurídico vigente.

En Málaga, a 16 de SEPTIEMBRE de 2021

Edificio Pabellón de Gobierno. Campus El Ejido. 29071
Tel.: 952 13 10 28 / 952 13 14 61 / 952 13 71 10
E-mail: doctorado@uma.es

AGRADECIMIENTOS

Se acerca el final de una de una etapa sin duda muy bonita a la vez que sacrificada, y no hay mejor momento que este para echar la vista atrás y recordar a todas esas personas que me han acompañado y ayudado durante estos cuatro años dedicados a la investigación.

En primer lugar, me gustaría dar las gracias a mis queridos directores, el Dr. Ezequiel Pérez de Inestrosa y el Dr. Francisco Nájera. Gracias por todo lo que me habéis enseñado durante este tiempo, por la confianza depositada en mí y por la ayuda que me habéis prestado siempre para cualquier cosa que he necesitado. Sin duda alguna, sé que no podría haber estado en mejores manos que en las vuestras y aunque ambos sois igualmente importantes para mí, me gustaría agradecerte especialmente a ti, Paco, las mil horas que habremos echado al teléfono, los cientos de cafés que te debo y tu paciencia infinita para aguantarme. Eres y serás siempre la calma en mitad de la tormenta, el ejemplo perfecto de como templar los nervios y actuar de la manera más lógica y razonable.

Dar las gracias a otros profesores del Departamento de Química Orgánica, y más concretamente a la Dra. Yolanda Vida y al Dr. Daniel Collado, por vuestra disposición y cercanía, y por ayudarme siempre que lo he necesitado.

A todos los compañeros de laboratorio en Bionand con los que he tenido el placer de compartir experiencias durante más o menos tiempo en estos cuatro años: Anjara, Antonio, Noemí, Irene, José Juan, Vladimir, Esther, Elsa, Violeta,… sois muchos con los que he coincidido y aunque alguno se me habrá quedado en el tintero, deciros a todos que ha sido un verdadero gusto trabajar con profesionales tan buenos como vosotros, incluso aunque hayamos tenidos nuestros más y nuestros menos. Os deseo todo lo mejor, y espero que el tiempo vuelva a cruzar nuestros caminos.

No olvidar a otros compañeros de Bionand, como Carlos, Maribel, Patri, John,…. Gracias en especial a ti John, por tantísimas horas que me has aguantado y sufrido, por tu ayuda con experimentos cada vez más complicados, por los ratos de risa que hemos echado

mientras veíamos en la pantalla como todo iba de la peor forma posible, o por como gracias a tu experiencia y a la insistencia todo alcanzaba buen puerto.

Por supuesto, gracias también al Dr. Jose María Perez-Pomares y al Dr. Juan Antonio Guadix por su colaboración con los ensayos celulares. Especialmente a Juan Antonio, ya que no solo has puesto tus células y tus manos a nuestra disposición y no te has rendido hasta que todo ha salido “de libro”, sino también por las charlas y consejos.

Mencionar además a los técnicos del SCAI Jose María, Zafra y Cristina, quienes siempre han estado dispuestos a ayudar en lo que fuera necesario. También a Sergio, Irene y Abel del Departamento de Química Física, con los cuales no solo he compartido silla durante unos cuantos años durante el Grado y el Máster, sino que cada vez que he pasado por la Facultad han hecho siempre un huequecillo para mí.

I would like to thank Dr. Joakim Andréasson for giving me the opportunity of joining his research group, as well as for his help, teaching and kindness during my stay at Chalmers. I am also grateful with Dr. Uwe Pischel, whose knowledge was essential in the project developed during the above-cited stay.

Agradecer el contrato predoctoral FPU recibido por parte del Ministerio de Educación (FPU16/02516) para la realización de esta tesis, así como la ayuda de IBIMA para la estancia en Gotemburgo y los diversos proyectos de distintos organismos estatales que han permitido financiar la investigación realizada (PID2019-104293GB-I00, MEC CTQ2016-75870-P y UMA18-FEDERJA-007).

Por último, y precisamente no menos importante, agradecer a quiénes han estado siempre ahí para todo, a quienes más me han apoyado durante este camino. Gracias a mis padres, a mi hermana y a Tere… a mi familia, por darme las fuerzas que me han permitido llegar hasta aquí. Os quiero.

A mis padres,

Francisco y Ana

TABLE OF CONTENTS

Summary / Resumen

English

As consequence of the non-invasive nature of the light, fluorescence-based methods have become essential to understand biological processes, these ranging from the monitoring of cellular events to the identification of subcellular organelles. Recently, two-photon microscopy has aroused much interest in this field, mainly due to the use of lower energy excitation wavelengths or the possibility of focus in depth. Thus, the design and the development of new probes for two-photon (2P) microscopy bioimaging is an interesting research challenge nowadays.

Firstly, in this thesis, I introduce new indolenines and indoliniums derivatives conceived to be applied in 2P microscopy. These molecular architectures are characterized for their synthetic flexibility as well as for demonstrating adequate photophysical properties for 2P microscopy bioimaging. Their versatility allows ready implementation of these dyes in diverse applications *via* straightforward and efficient structural modifications. Thereby, a new "off/on" indolinium-based system for detecting lysosomal hydroxyl radical in 2P microscopy is devised in **Chapter 3**. The reduction of compound **1** leads to a non-fluorescent form **2,** which selectively accumulates in lysosomes due to the presence of a tertiary amine in its structure. The later action of hydroxyl radical together with the acid environment in these organelles are responsible of the oxidation of **2** to generate the fluorescent form **1**. Besides, this process is enhanced when inducing oxidative stress. That is, by using this system is possible to measure the endogenous production of lysosomal hydroxyl radical as well as the stimulated generation of this species by other agents affecting cellular oxidative stress. On the other hand, indolenine **4**, obtained in the synthetic route towards **1** and **2**, displays an interesting optical response to *pH* changes. This "off/on" response to acid environments under 2P excitation conditions can be harnessed for developing new *pH* sensors with application in subcellular contexts. Thus, methoxy group in model **4** is replaced in **Chapter 4** and two different groups with different subcellular targets are incorporated: a carbitol group with non-specific target in **5**, and a *N*-

alkylmorpholine moiety in **6** which is intended to act as lysosomotropic agent. These compounds are also studied into cell environments, where **5** is capable of measuring changes in the intracellular *pH*, and **6** demonstrates an exceptional performance as lysosensor. In addition, the substitution of methoxy group in **1** by the two above-mentioned alkoxy groups gives rise to indolinium-based **11** and **12**. The fluorescence of these analogues is not dependent on secondary processes such as oxidation or protonation, and in **Chapter 6** it is shown how the combination of two different target vectors (the indolinium ring as a mitochondrial vector, and the different alkoxy groups as previously detailed) together with the occurrence of *J*-aggregation phenomena, results in an interesting ability of these compounds to label mitochondria and lysosomes simultaneously. Moreover, the assemblies of these dyes are only present in mitochondria and the monomer form is detected in lysosomes, which leads to organelle-specific photophysical properties that can be tracked by combination of confocal and 2P microscopy. Although more experiments are required, the preliminary studies with compound **12** suggest that these compounds could be exploited to monitor mitophagy. Finally, the results obtained in a short stay at Chalmers University with of Prof. Dr. Joakim Andréasson (September-December 2019) are presented in **Chapter 7**. The project performed during this time consisted of devising a new strategy that allows to overcome one of the drawbacks of 2P microscopy: the 3D-resolution. Taking into account that the 3D-resolution is better as long as more photons are concurrently involved in the excitation process, a new dyad system consisting of the combination of a fluorenyl derivative and a diarylethene photoswitch, is described and characterized. This system is operated by two 2P-mediated processes: 2PA and FRET sensitized by 2P-excited fluorescence. The performance of this system under ideal conditions would lead to a quartic dependence of the light intensity on the excitation energy, typically observed in 4-absorbers. All in all, this system based on conventional two-photon absorber dyes would proportionate an improved three-dimensional resolution when applied into two-photon microscopy. This system exhibits a good performance in agreement to the theoretical-experimental models, and the proof-of-principle is demonstrated. This strategy, that can be extrapolated to any pair of two-photon absorber dye and a FRET-efficient photochromic system, could open new avenues for the application of 2P absorption process.

Español

A consencuencia de la naturaleza no invasiva de la luz, los métodos basados en fluorescencia han adquirido un rol fundamental para la compresión de los procesos biológicos, comprendiendo desde el estudio de procesos celulares hasta la identificación de estructuras subcelulares. Recientemente, la microscopía de absorción de dos fotones ha experimentado un gran desarrollo en este campo, principalmente debido al uso de longitudes de onda de excitación de menor energía y a un mayor poder de penetración en tejidos. Debido a todo esto, el diseño y desarrollo de nuevos compuestos con aplicación para bioimagen con microscopía de absorción de 2P constituye un desafío para la investigación en la actualidad.

En esta tesis, en primer lugar se presentan nuevos derivados de indoleninas e indoleninios concebidos para su uso en microscopía de absorción de 2P. Estos diseños moleculares se caracterizan por su flexibilidad sintética y por demostrar propiedades fotofísicas adecuadas para su aplicación en biomagen con microscopía de absorción de 2P. La versatilidad de su diseño permite una adaptación buena para diversos fines a través de modificaciones estructurales sencillas y eficientes. De este modo, en el **Capítulo 3** se ha desarrollado un nuevo sistema "*off/on*" para la detección de radical hidroxilo en lisosomas. La reducción del compuesto **1** da lugar a la forma no fluorescente **2**, la cual se acumula selectivamente en lisosomas debido a la presencia de una amina terciaria en su estructura. La posterior acción del radical hidroxilo junto con la presencia de medio ácido en estos orgánulos son responsables de la oxidación de **2** que resulta en la forma fluorescente **1**. Este proceso además se ve favorecido cuando se induce estrés oxidativo. Por tanto, este sistema permite el estudio tanto de la producción endógena de radical hidroxilo como monitorizar la producción de esta especie cuando se induce estrés óxidativo. Por otra parte, la indolenina **4**, obtenida en la ruta sintética para **1** y **2**, muestra una interesante respuesta óptica a los cambios de pH. Esta respuesta "*off/on*" a los ambientes ácidos bajo condiciones de excitación de 2P es aprovechada para el desarrollo de nuevos sensores de *pH* con aplicación en contextos subcelulares. De esta forma, el grupo metoxilo en **4** se reemplaza en el **Capítulo 4** por dos sustituyentes con diferente diana subcelular: una

cadena de carbitol, sin objetivo específico, en el compuesto **5**; y, una cadena de N-alquilmorfolina en **6** con la cual se pretende alcanzar selectivamente lisosomas. Estos compuestos se estudian además en ambientes celulares, donde el compuesto **5** es capaz de monitorizar cambios de *pH* intracelular y el compuesto **6** demuestra una habilidad excepcional como "lisosensor". Siguiendo una estrategia similar, la sustitución del grupo metoxilo de **1** por los sustituyentes antes mencionados da lugar a los compuestos **11** y **12** respectivamente en el **Capítulo 6.** Sin embargo, la fluorescencia de estos derivados no depende de procesos secundarios como la oxidación o la protonación. En este Capítulo, se muestra como la combinación del anillo de indoleninio con los sustituyentes antes mencionados, junto con la presencia de fenómenos de J-agregación, confiere a estos compuestos una interesante habilidad para marcar mitocondrias y lisosomas de manera simultánea. Mientras que los agregados se forman exclusivamente en las mitocondrias, el monómero se observa en lisosomas. Las distintas propieades fotofísicas de estas especies permiten el estudio de las poblaciones de orgánulos de manera diferenciada y simultánea mediante la combinación de microscopía confocal y de absorción de 2P. Aunque se requieren más estudios, las investigaciones preliminares realizadas con el compuesto **12** apuntan a este como un buen candidato para la monitorización de mitofagia. Finalmente, los resultados obtenidos durante una estancia breve en la Universidad de Chalmers (Septiembre-Diciembre 2019) con el Prof. Dr. Joakim Andréasson se recogen en el **Capítulo 7**. El proyecto desarrollado durante este tiemo tuvo como objetivo el alcanzar una estrategia que permitiera superar una de las desventajas de la microscopía de 2P: la resolución tridimensional. Teniendo en cuenta que la resolución tridimensional se mejora a medida que más fotones están involucrados de manera simultánea en una transicion, se desarrolló una nueva diada que combina un fluoreno y un fotocromo basado en diarileteno. El funcionamiento de este sistema se basa en enlazar dos procesos mediados por absorción de 2P: la propia absorción de 2P y la FRET sensibilizada por la emisión inducida por absorción de 2P. En condiciones ideales, este sistema daría lugar a una dependencia cuártica de la luz con la instensidad de la fuente de excitación, típica de compuestos con capacidad para absorción de cuatro fotones. Por tanto, el empleo de este sistema en microscopía de 2P proporcionaría una mejora de la resolución tridimensional. Este sistema demuestra un comportamiento que se ajusta a los modelos teórico-experimentales,

probándose así la hipótesis inicial. Esta estrategia además puede ser implementada en otras combinaciones de cromóforos con propiedades de absorción de dos fotones con un diarileteno con buena respuesta FRET, lo cual puede suponer nuevas oportunidades para la aplicación del proceso de absorción de 2P.

List of abbreviations

#	
1P	one photon
1PA	one-photon absorption
2P	two photons
2PA	two-photon absorption
2PEF	two-photon excited fluorescence
2PEP	two-photon excited phosphorescence
2PM	two-photon microscopy
3D	three-dimensional
3P	three photons
3PA	three-photon absorption
4P	four photons
5P	five photons
A	
Å	angstrom
A	aceptor
Abs	absorbance
ACN	acetonitrile
AcOH	acetic acid
AIE	aggregation-induced emission
aq	aqueous
a.u.	arbitrary units
C	
c	closed
COSY	^{1}H-^{1}H homonuclear correlation spectroscopy
D	
δ	NMR chemical shift in parts per million
$\Delta\lambda$	difference between the absorption and emission maxima
$\Delta\upsilon$	Stokes shift, expressed as cm^{-1}
d	doublet

dd	double-doublet
D	donor
DCM	dichloromethane
DFT	density functional theory
DMF	*N*,*N*-dimethylformamide
DMSO	dimethylsulphoxide
DMSO-d_6	deuterated dimethylsulphoxide
DNA	desoxirribonucleic acid
DTE	diarylethene

E

ε	molar absorption coefficient
e^-	electron
E	energy
ESA	excited-state absorption
ESI	electrospray ionization

F

$\phi_{c\rightarrow o}$	isomerization quantum yield for the ring-opening reaction
ϕ_{Δ}	singlet oxygen formation quantum yield
ϕ_f	fluorescence quantum yield
ϕ_{FRET}	Förster's Resonance Energy Transfer efficiency
$\phi_{o\rightarrow c}$	isomerization quantum yield for the ring-closing reaction
$f_{k\rightarrow l}$	oscilator strenght for the transition from *k* to *l* states
FRET	Förster's Resonance Energy Transfer

G

g	*gerade*

H

HeLa	immortal cell line derived from cervical cancer cells taken from Henrietta Lacks
hept	heptuplet
HMBC	^{1}H-^{13}C heteronuclear multiple bond correlation
HOMO	highest occupied molecular orbital
HPLC	high-perfomance liquid cromatography

HRMS	high-resolution mass spectrometry
HSQC	^{1}H-^{13}C heteronuclear single quantum correlation
Hz	hertzs

I

I_f	fluorescence intensity
ICT	intramolecular charge transfer
IR	infrared

J

J	coupling constant in Hz
J (λ)	overlap integral

K

κ^2	orientation factor

L

λ	wavelength
λ_{abs}	absorption wavelength
λ_{em}	emission or fluorescence wavelength
$\lambda_{exc,1P}$	excitation wavelength under one-photon conditions
$\lambda_{exc,2P}$	excitation wavelength under two-photon conditions
LTDR	lysotracker deep red
LUMO	lowest unocuppied molecular orbital

M

m	multiplet
M	molar
m.p.	melting point
MDV	mitochondria derived vesicles
MEF	mouse embryonic fibroblast
MTG	mitotracker green FM
MTR	mitotracker red CMXRos

N

n_D	refractive index
NADPH	nicotinamide adenine dinucleotide phosphate
NLO	non-linear optics
NLT	non-linear transmitance
NMR	nuclear magnetic resonance
NTO	natural transition orbital
N_e	number of π electrons
NIR	near infrared

O

o	open

P

PCC	Pearson's correlation coefficient
PCM	polarizable continuum model
pHi	intracellular pH
ppm	parts per million
PSS	photostationary state

Q

quint	quintuplet

R

R_0	Förster's critical radius
RNS	reactive nitrogen species
ROI	region of interest
ROS	reactive oxygen species
r.t.	room temperature

S

σ_p^+	Hammet-Browm constant
σ_{2PA}	two-photon absorption coefficient
s	singlet
S_0	ground state
S_1	first excited state

S_n	n-excited state
SEFT	spin-echo Fourier transform

T

τ_f	fluorescence lifetime
t	triplet
td	triple-doublet
TD-DFT	time-dependent density functional theory
TBHP	*tert*-butyl hydroperoxide
TFA	trifluoroacetic acid
THF	tetrahydrofuran
Tol	toluene

U

u	ungerade
UV	ultraviolet

V

V	volts
vis	visible

W

W	watts
WLC	white-continuum light technique

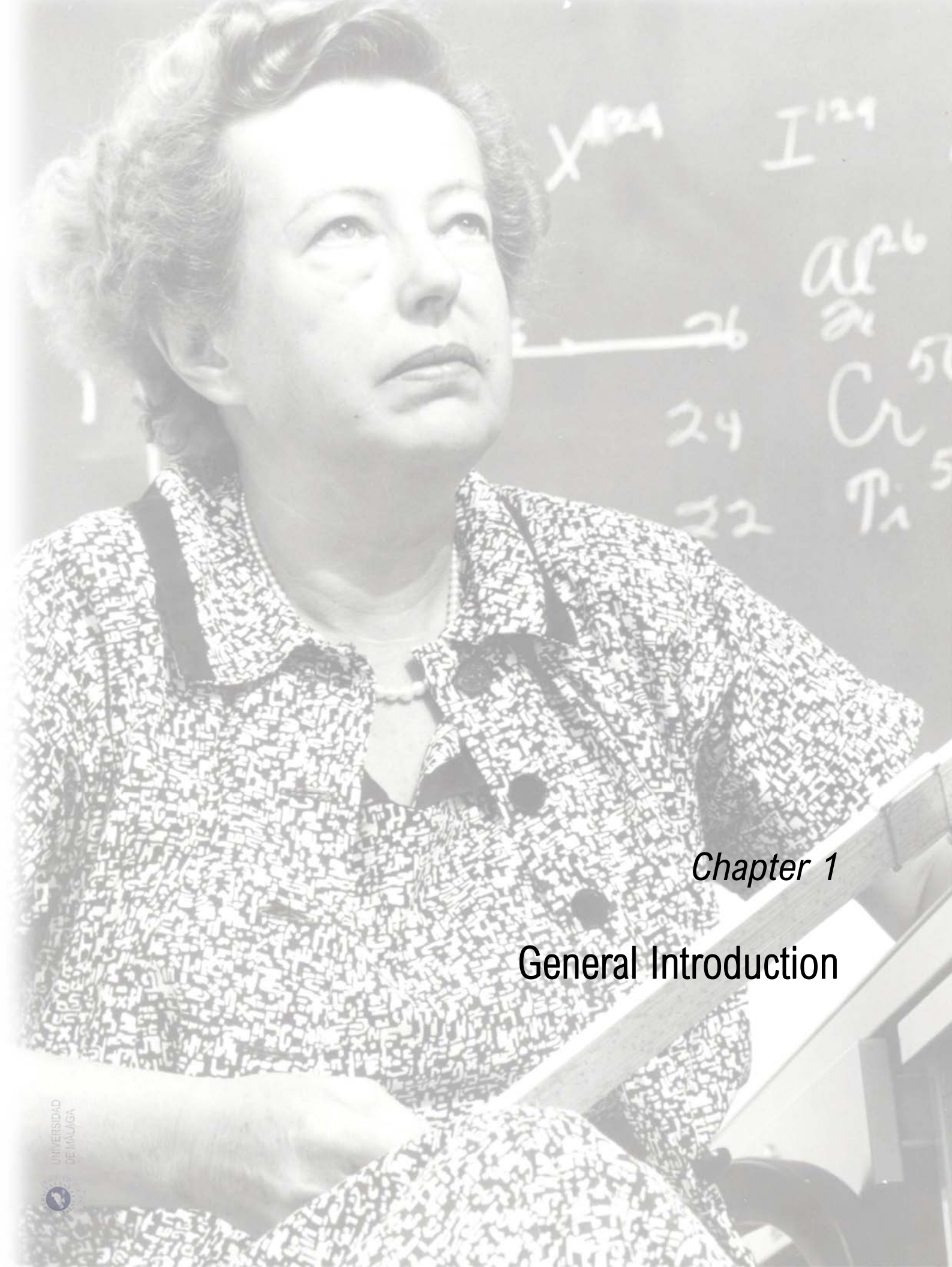

Chapter 1

General Introduction

1.1 THE TWO-PHOTON ABSORPTION PROCESS

The absorption of a single photon by a material generally triggers an electronic transition to a certain excited state. However, this process can also be accomplished by the joint action of various lower energy photons as long as the sum of their energies equals to that of the transition. These alternative mechanisms, known as multiphoton processes, include thus all the excitation regimes in which more than a single photon operate.

Fig. 1. Maria Göppert-Mayer (1906, Kattowitz – 1972, San Diego). Another portrait occupies the Chapter's cover.

In particular, the two-photon absorption (2PA) process was theoretically envisioned by Maria Göppert-Mayer (**Fig. 1**) back in the 1930s.[1] This theory, in which she centered her PhD thesis, was not her unique contribution to the sciences field along her outstanding career. She was also implicated in the development of the nuclear shell model of the atomic nucleus.[2] After Marie Curie, she was the second woman awarded with the Nobel Prize (1963) in the history.[3] In her honor, the employed unit for measuring the ability of a compound or a material to absorb two photons (2P) receives her name: the Göppert-Mayer unit, abbreviated as GM. The 2PA first experimental demonstration had to wait however *ca.* 30 years from the theoretical prediction. Kaiser and Garrett demonstrated this phenomenon in $CaF_2:Eu^{2+}$ crystals in 1961,[4] thanks to the advent of the first laser a few

years before.[5] The investigation of 2PA became easier in the 1990s, when ultrashort-pulsed lasers became more accessible.

Since its first evidence, 2PA has aroused a fundamental interest among spectroscopists for the study of basic properties of materials as well as the matter-light interaction. Different selection rules apply in one-photon absorption (1PA) and 2PA, that is, complementary data from a same object of study are thus accessible. In addition, 2PA is susceptible to be combined with other processes that take place immediately after the biphotonic excitation, *e.g.*, fluorescence emission, photochemical reactions, or energy transfer processes. These applications are mainly built on exploiting the square dependence of the process on the excitation light intensity, which interestingly enable the excitation of a material to be three-dimensional spatially controlled. Nowadays, 2PA process lays on the foundation of numerous state-of-the-art techniques that find extensive application in multitude of diverse fields, as it will be discussed in detail later in this Chapter.

Higher-order absorption processes have also been described, although their occurrence is substantially limited by technological issues: an increasingly high laser intensity is required as more photons concurrently participate in the electronic transition. Moreover, the excitation wavelengths in these phenomena are extremely red shifted: excitation at 1200 nm will be required in a three-photon absorption (3PA) process if starting from a 1PA at around 400 nm, for example. This also constitutes a major challenge in terms of devising new materials that fulfills adequate features. Even so, elementary studies and/or applications about these multiphotonic processes can be found in the literature, in which three photons (3P),[6–14] four photons (4P),[11,13,15,16] or even more rarely five-photons (5P)[13,17,18] are concerned.

1.1.1 Fundamental principles

Focusing on the 2PA process, this implies *per se* the absorption of two photons of energies E_1 and E_2. To that end, it is demanded that the sum of the energies, $E_1 + E_2$, is in resonance with one of the electronic states of the system. If this is the case, the molecule reaches an excited state $|f\rangle$, this being located at $E_1 + E_2$ above the ground state $|g\rangle$. Subsequent

relaxation of the system to the original situation takes place, which deactivates first by non-radiative pathways (mainly internal conversion and vibrational relaxation) until the lowest vibronic level of the lowest-energy excited state |r⟩ (Kasha's rule).[19] From this state, the final return towards the ground state can be mediated by both radiative and non-radiative processes (**Fig. 2**).

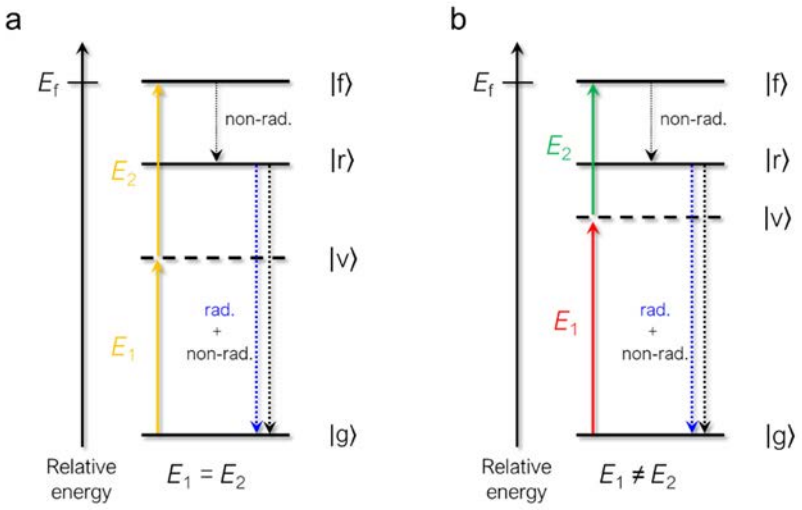

Fig. 2. Schematic energy level diagram of the 2P excitation process. Two situations are conceivable for the biphotonic excitation: (a) the involved photons have the same energy (degenerate approach), or (b) these have different energies (non-degenerate approach). In any case, $E_f = E_1 + E_2$ needs to be accomplished. The blue arrow symbolizes the possibility of the fluorescence emission from the state |r⟩ within the deactivation events, at difference of the black one that represents only the non-radiative processes.

Regarding to how the two photons are absorbed, one of the most accepted mechanism builds on the existence of a temporary virtual state of energy |v⟩, which is reminiscent of the fundamentals of Rayleigh scattering and non-resonant Raman scattering.[20,21] The initial interaction of a photon of energy E_1 conducts to this non real state, that solely exists for a short time interval. For photons in the visible and near infrared (NIR) spectral region, this time is typically in the scale of 10^{-15}-10^{-16} s.[20,22] As long as the virtual state is still present, the final state will be attained after a second photon of energy E_2 interacts with the molecule.

This interpretation of the 2PA process, known as the two-state model, proposes thus that a) the sequential interaction of the two photons with the molecule is practically simultaneous and b) non-real states participate as intermediate in the process.

In the manner of what is established for 1PA process, the existence of an electronic state of the adequate energy (E_1 + E_2) is not sufficient to achieve the electronic transition. Indeed, it is just the first of the conditions that needs to be satisfied. The symmetry of the species and the polarization of the excitation beam (or beams) will also determine if the system has the ability to absorb two photons according to the two-photon tensor model.[23–26] This tensorial description accounts thus from the intrinsic characteristics of the system to the given experimental conditions, being its interpretation far too complicated. Nevertheless, the following facts are frequently present in the great majority of experimental approaches:

→ The two photons involved in the transition dispose of the same energy, *i.e.*, $E_1 = E_2$ (**Fig. 2a**). This situation is usually known as the "degenerate" case. Although its use is far less common, "non-degenerate" ($E_1 \neq E_2$, **Fig. 2b**) pathway has also been reported and is indeed the basis of applications such as 3D optical data storage.[27,28]

→ The two photons belong to the same excitation beam and are generated by a coherent source, commonly a laser. Although the 2PA can arise when incoherent light is used (*e.g.*, when using a lamp), the probability in these cases is almost negligible and appreciable signals are not detected unless large excitation intensities are employed.

These conditions, which in the first instance seem to be restrictive, are certainly the ones that conduct to an easier implementation of the 2PA process in experimental applications.

Additionally, these conditions allow a simplified description of the 2PA occurrence: the dipolar approach, this consisting of the application of the Lambert-Beer law to this type of processes.

According to this approach, the 2PA cross-section molecular coefficient, σ_{2PA} , is determined by **Eq. (1)**:

$$\sigma_{2PA,max} \propto \frac{S_{fg}}{\Gamma} \qquad \textbf{Eq. (1)}$$

where Γ is the half-width at half maximum of the 2PA band in energy units, and S_{fg} is a summation[29–31] that after some considerations and rearrangements,[32] is defined by **Eq. (2)**:

$$S_{fg} = \frac{1}{5}\left[\left(\frac{\Delta\mu_{gf}\,\mu_{gf}}{h\upsilon}\right)^2 + \sum_{i \neq f,g}\left(\frac{\mu_{gi}^2\,\mu_{if}^2}{(E_{gi} - h\upsilon)^2}\right)\right]^2 \qquad \textbf{Eq. (2)}$$

D term T term

In this expression, E_{gl} is the energy gap between the ground state and an intermediate electronic *i* nearby to the virtual state; $h\upsilon$ is the photon energy; μ refers to the amplitude of the transition dipole moment induced by the electric field of a light wave, whose frequency must be coincident with the energy difference between two electronic states; and $\Delta\mu_{gf}$ represents the change in the static dipolar moment. Here, two terms are distinguished: the "dipolar" D term and the "two-photon" T term. The selection rules for 2PA processes can be deduced from the previous equations.

Centrosymmetric molecules

The dipolar approach finds its simplest application in centrosymmetric chromophores. Given that the static dipole moments are zero in these molecular architectures, the D term is cancelled, and **Eq. (2)** is reduced to the T term. When considering this fact in **Eq. (1)**, the next expression arises:

$$\sigma_{2PA,max} \propto \frac{\mu_{gi}^2\,\mu_{if}^2}{\left[(E_{gi}/h\upsilon) - 1\right]^2\,\Gamma}\,C \qquad \textbf{Eq. (3)}$$

where *C* is a constant.

The 2PA cross-section is therefore operated by the interaction of the ground state with two excited states (**Fig. 3**). These states have alternating symmetry: |g⟩ and |f⟩ are "*gerade*", *i.e.*, symmetric with respect to the center of inversion. On the contrary, the intermediate state |i⟩ is antisymmetric or "*ungerade*".

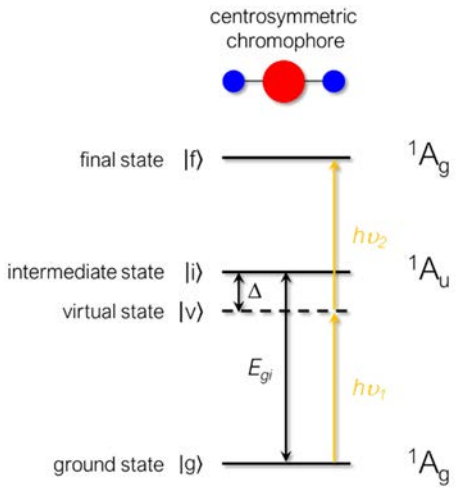

Fig. 3. Energy level diagram for the essential states in a centrosymmetric scaffold. The states are labeled for C_i symmetry. The diagram is applicable to the lowest 2PA transition in all the molecules whose point groups contain a center of inversion among their symmetry operations.

According to the two-states model, the 2PA process is divided in two 1PA processes. Thus, 1PA selection rules apply, and all the electronic transitions that imply a change in the symmetry are enabled, and transitions $g \leftrightarrow i$ and $i \leftrightarrow f$ are one-photon (1P) electric-dipole-allowed (**Fig. 3**). Considering the overall effect of the 2PA process (*i.e.*, the *g* to *f* transition), it is concluded that the selection rule for a 2PA process referred to the symmetry is reversal to that proposed for 1PA: 2P-active transitions are those that connect electronic states with the same symmetry.[20,21,33]

On the other hand, the magnitudes of μ_{gi}^2 and μ_{if}^2 are proportional to the 1P oscillator strengths, so their values are experimentally available from the linear absorption spectrum. Conversely, μ_{if} is not often estimated from the experimental data. This can be determined by computational calculations,[34–40] which are an essential and useful tool in 2PA

chromophores designing. The theoretical methods serve as a key guidance for molecular devising and allow avoiding from by *trial and error* method, that is, these save from unnecessary chemical efforts and its subsequent environmental impact.

Concerning to μ_{gf}^2, this term can be enhanced by installing electron donors (D) and acceptors (A) at the extremes of a π-conjugated chromophore. The enhanced displacement of charge from a donor-centered HOMO (Highest Occupied Molecular Orbital) to an acceptor-centered LUMO (Lowest Unoccupied Molecular Orbital) translates into a higher dipolar transition moment. Consequently, centrosymmetric D-π-A-π-D or A-π-D-π-A schemes are the basis of a wide number of centrosymmetric 2P-absorbers, these achieving considerable 2PA cross-sections.[41,42] However, the excited states and their occupancies cannot accurately be described through elementary molecular orbitals. Fortunately, a faithful description is accessible by means of the natural transition orbitals (NTOs),[43] that account and combinate proportionally the different elementary orbitals involved in a same transition. This results in single configurations for the corresponding electronic transition. Thereby, the Hole NTO represents the ground state, and the Electron NTO is associated with the excited ones.

An experimental example of all these statements for centrosymmetric scaffolds is illustrated in **Fig. 4**.[44] The bis(dioxaborine) represented in this figure corresponds to a quadrupolar A-π-D-π-A structure with C_i symmetry, this being the simplest point group that contains a center of inversion between its symmetry operations. For this molecule, two bands were experimentally determined in the 2PA spectrum: one centered at 890 nm (σ_{2PA} = 337 GM), and other one at 730 nm (σ_{2PA} = 2800 GM). About the 1PA spectrum, only one band is appreciated with maximum at 440 nm.[44] The use of Time-Dependent Density Functional Theory (TD-DFT) together with the use of the NTOs allows to delve in this behavior. Looking at the transition to the first excited state, this corresponds to the $^1A_g \rightarrow {}^1A_u$ transition at 2.80 eV and with an oscillator strength (noted as $f_{0\rightarrow n}$, where 0 and n refer to the ground and the n-excited states involved in the transition) of $f_{0\rightarrow 1}$ = 1.807. The second electronic transition is associated with the $^1A_g \rightarrow {}^1A_g$ transition and is located at 3.24 eV. Given that the symmetry is maintained, this last one is not 1P-active, and a considerable

reduced oscillator strength is calculated ($f_{0\rightarrow2}$ = 0.000). The situation in 2P-excitation conditions is totally reversed, where this transition is indeed the truly active one. Both transitions share a common electronic configuration in the Hole NTO, which is mainly centered at the donor moiety of the molecule and corresponds with a ^1A_g symmetry. Nevertheless, the Electron NTO is substantially different in these transitions. Whereas the electron density of the first excited state is spread along the length of the chromophore (^1A_u symmetry), the polarization in the second one is dramatically increased. In this case, the Electron NTO is located at the extremes of the molecule, specifically over the acceptor moieties. In addition, its symmetry is ^1A_g, which is coincident with the one of the ground state. The increased quadrupolar polarization in the second excited state is the reason for a higher 2PA cross-section value in this last electronic transition.

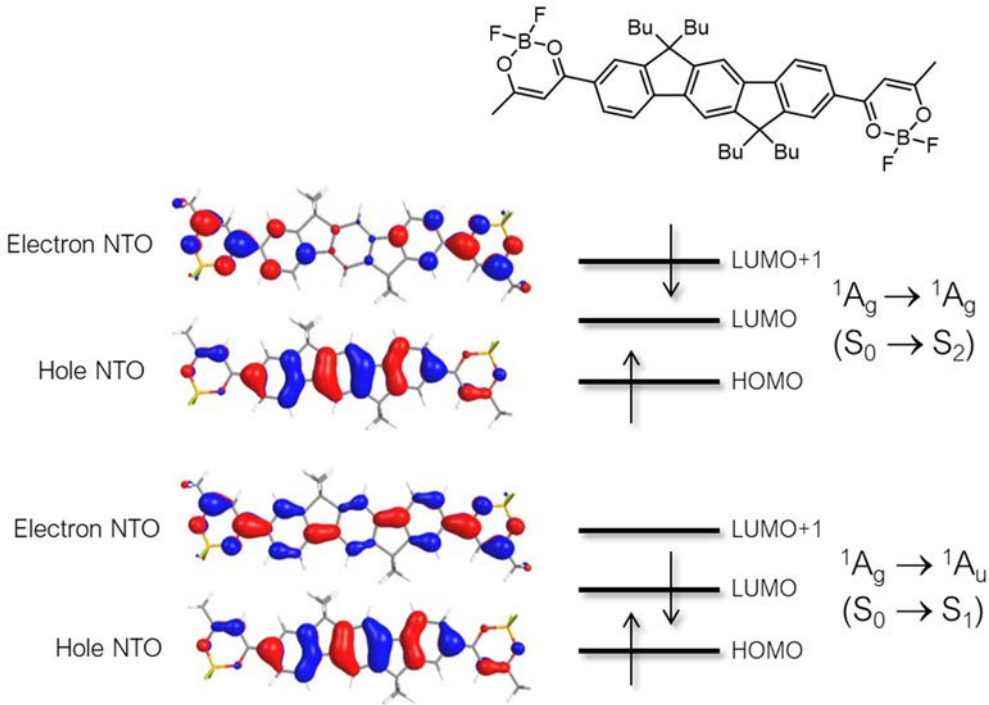

Fig. 4. Electronic structures obtained for the electronic states involved in the two first electronic transitions for a representative bis(dioxaborine). These were obtained by TD-DFTs and the NTOs are represented at the left. The occupancies of the HOMO, LUMO and LUMO+1 energy levels are detailed at the right. Assuming that alkyl chains have not influence on the electronic properties of the system, the butyl chains were shortened to methyl groups.

Non-centrosymmetric molecules

In contrast with those of the centrosymmetric scaffolds, the static dipoles moments are non-zero in non-centrosymmetric dipolar chromophores. This entails that both D and T terms operate in **Eq. (2)**, and consequently in **Eq. (1)**. Regarding the electronic states, |f⟩ plays now the role of |i⟩, which implies that the transition $g \leftrightarrow f$ is active under both 1P- and 2P-excitation conditions (**Fig. 5**). When analyzing the contribution of the D and T terms, firstly it is found that the contribution of the T term to $\sigma_{2PA,max}$ is smaller than in centrosymmetric molecules. This is due to the relationship of the T term with transitions to higher excited states and, in this case, the transition involves the first excited state instead of the second one. On the other hand, the D term for dipolar chromophores (assuming that $\Delta\mu_{gf} \approx \mu_{gf}$) is intrinsically lower than the T term for centrosymmetric architectures. All in all, these arguments partially explain why quadrupolar molecules have a higher 2PA cross-section *vs.* similar dipolar analogues. Regarding μ_{gf}^2, the construction of a dipolar D-π-A system is essential for providing adequate 2PA cross-sections. Thus, studies of structure-properties relationship become fundamental to design this type of 2P-chromophores.

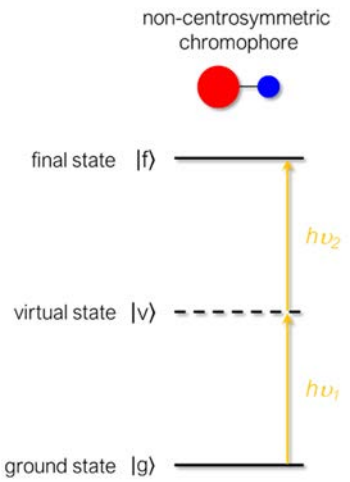

Fig. 5. Energy level diagram for the essential states in a non-centrosymmetric dipolar chromophore.

1.1.2 Experimental methods for quantifying the 2PA cross-section

Several experimental methods have been developed into 2PA spectroscopy for measuring the 2PA cross-section. According to how the 2PA process is examined, two categories are distinguished:

→ Direct methods: based on measuring the beam attenuation after this one goes through a medium where a 2PA chromophore is present.
→ Indirect methods: the quantity to be measured is one of the effects produced by the generation of population in an excited state reached after the 2PA.

Additionally, a third category of methods can be found in the literature: the wave-mixing methods. These techniques imply the use of more than one beam, that usually incises in the sample from different directions.[45] One example of these methods is White-Light Continuum (WLC) technique, which allows to obtain non-degenerate 2PA spectra.[46–48] Nevertheless, both direct and indirect methods are the most used, so we will focus on them in this Section.

Direct methods

These methods can be conceived as an extension of the techniques used to characterize 1PA by measuring the transmittance or the absorbance of a sample. Here, the 2PA process is directly observed, generally as a decrease in the intensity of an incident beam. The study of how the transmittance varies with the incident intensity leads to determine the 2PA cross-section. **Non-linear transmission (NLT)** and **Z-scan** methods are the main ones.[45]

In **NLT**, the sample is positioned in the path of the excitation beam and the pulse energy is measured before and after the sample. Then, the pulse energy is varied, and the transmittance is measured for each of the conditions. The transmittance depends on the incident energy, given that the absorption process is supposed to be non-linear. Accounting this together with the pulse features and the optical configuration, the 2PA cross-section can be determined.[45,49,50] However, the use of high laser intensities with (or without) long pulse rates, can derive in a non-desired process: the excited state absorption

(ESA). The build-up of excited-state populations can lead to this event, which results in apparently larger 2PA cross-section values. This effect can be reduced by using wavelengths out of the 1PA spectrum, very short laser pulses (<1 ps) and low repetition rates.

On the other hand, **Z-scan** technique is the most selected alternative, among direct methods. Here, the sample is also placed in the path of the light. Unlike the previous one, the pulse energy is kept constant, and the sample is displaced along the propagation direction. This direction, referred to as z-axis, is from which the technique receives its name. The movement of the sample around the focal point entails changes in the transmittance, so this parameter is measured at each position of the sample in this path. Considering that 2PA requires of a high density of photons at the excitation point, the probability of the process decreases as a function of $1/r^4$, where r is the distance from the focal point of the laser. Therefore, the transmittance is 1 when the sample is far from the focus of the beam, and it decreases as the sample is moved closer to this point. At this location, the measured transmittance reaches its minimum. As long as the sample is displaced in the opposite direction, the transmittance displays the inverted trend.[45,51,52]

There are two possible experimental setups for Z-scan, which are represented in **Fig. 6**. In case that the detector has a narrow aperture (**Fig. 6 a**), the collected signal is sensitive to the intensity-dependent changes in the refractive index, this resulting from third-order non-linear polarizability or the thermal effects. These effects, usually given when the aperture of the detector is too narrow or too far from the sample, can lead to focusing or defocusing of the beam. These issues translate into the "adulteration" of the 2PA cross-section measurements. Alternatively, the absence of an aperture makes that all the intensity is collected (**Fig. 6 b**). Even if this option is apparently more faithful in terms of 2PA quantification, ESA effects can arise in both experimental configurations for Z-scan measurements.

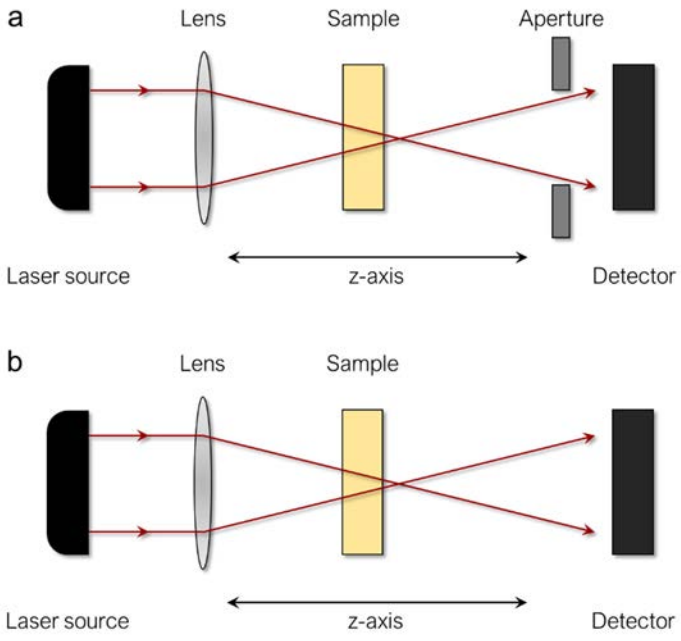

Fig. 6. Schematic representation of the Z-scan experimental setups: (a) "closed-aperture" mode and (b) "open-aperture" mode.

By and large, direct methods suffer from two major downsides: ESA and self-defocusing of the laser beam (particularly more relevant in Z-scan technique).[51,53] These effects result in overestimated 2PA cross-section values. Additionally, and as shown on the 1,3,4-oxadiazole derivative represented in **Fig. 7**, the measurements by these techniques are extremely dependent on the laser pulse rate.[54] It is therefore convenient to indicate which pulse rate is used for the determination of the 2PA cross-section values with these techniques. The comparatives with the results obtained by other methods, such as the indirect ones, is feasible if the laser pulse rate is in the same scale of time. Considerable amounts of the material are also necessary, since the measurements are typically performed with solutions of concentrations no lower than 10^{-3} M. Even so, these techniques allow an accurate 2PA cross-section determination provided that the spatial and the temporal profiles of the beam are known. Despite these drawbacks, the relative simplicity of the optical setup and their non-dependence on a secondary process after 2PA takes place, are their major advantages.

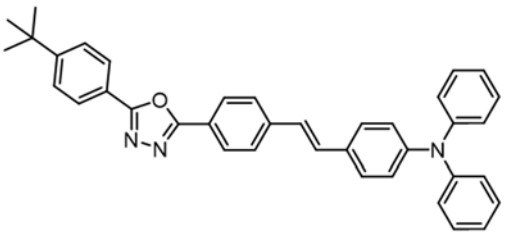

σ_{2PA} [NLT, ns, $\lambda_{exc,2P}$ = 810 nm, tetrachloroethylene] = 14880 GM
σ_{2PA} [NLT, fs, $\lambda_{exc,2P}$ = 796 nm, tetrachloroethylene] = 88 GM

Fig. 7. Example of 2P cross-sections values determined for a 1,3,4-oxadiazole derivative by NLT using two lasers with different pulse rates as indicated.[54] The wavelength of study and the solvent used are also detailed in the square brackets.

Indirect methods

After being raised to the corresponding excited state by 2PA, the molecules return to the ground state and the acquired energy is released to the environment. Several deactivation outcomes are possible depending on the features of the chromophore. Indirect methods focus on measuring one of these relaxation pathways, thus opening to two possibilities: 1) indirect techniques that measure non-radiative processes and 2) the ones which track radiative events.

About the first category, **thermal lensing** (or **thermal blooming**) is the main technique for monitoring non-radiative pathways. To that end, the optical effects provoked by the energy liberated as heat to the host medium are evaluated. In addition to the expected augment of the local temperature, the refractive index changes as well. Both temperature and variations in the refractive index depend at first instances on the 2PA properties of the chromophore, although they are also related to the characteristics of the beam and the thermal properties of the medium. An appropriate treatment of the data, considering these previous issues, allows the quantification of the 2PA process.[55–59] Moreover, the local heating can implicate other effects, such as changes in the pressure of the system or the generation of acoustic waves. These phenomena can also be employed for the determination of the 2PA cross-section.[60–62]

Alternatively, the most commonly used are the techniques based on radiative deactivation mechanisms: fluorescence and phosphorescence essentially. Indeed, the **two-photon excited fluorescence (2PEF)** is considered the indirect technique par excellence. Regardless of the excited state reached by 2PA, the molecule rapidly relaxes (typically in *ca.*1 ps)[19] by internal conversion to the lowest vibronic level of the first excited state (Kasha's rule). At this stage, both radiative and non-radiative processes can befall, and their proportion is driven by the intrinsic characteristics of the fluorophore and the surrounding environment. In case that fluorescence outcomes, the 2PEF spectra can be recorded and measured. The comparative essence of this technique substantially eases the obtaining of 2PA spectra from monitoring the fluorescence intensity, being this due to the experimental parameters are considered by the method itself (*e.g.*, the calibration of the system or the characteristics of the excitation beam).[22,33,45] Diverse variations of this approach have been developed since reported by Xu and Webb,[63] being the technique greatly optimized by Rebane *et al.*[64] The recent reports of accurate references 2PA spectra for a wide number of commercially available dyes,[65,66] makes this technique particularly attractive.

If working in a regime where the fluorescence signal depends on the laser intensity in a quadratic manner, it can be assumed that the emission contribution from 1PA is negligible. The application of this method resembles the one established by the IUPAC for the determination of the fluorescence quantum yield by comparative procedure.[67] Dilute solutions are employed, usually at concentrations below 10^{-4} M. As well, the equation applied to estimate the 2PA cross-sections [**Eq. (4)**][68] is in part comparable to that used for the fluorescence quantum yield determination.

$$\sigma_{2PA,s} = \sigma_{2PA,r} \frac{C_r\, n_{D,r}\, \phi_{f,r}\, F_s}{C_s\, n_{D,s}\, \phi_{f,s}\, F_r} \qquad \textbf{Eq. (4)}$$

In this expression, *s* refers to the sample and *r* to the reference compound, σ_{2PA} is the 2PA cross-section, *C* is the concentration of the specie, ϕ_f is the fluorescence quantum yield, n_D is the refractive index of the used solvent and *F* is the area under the emission spectrum. In this manner, the 2PA cross-section is determined for each excitation wavelength as long

as the sample and the reference are excited under identical conditions, that is, same laser intensity and geometry of the system. Although the use of a pulsed laser about 100 fs is desirable, the precision of the obtained values is not extremely compromised to this experimental condition as it occurs with the other procedures.[42] The dynamic range of this method can be large, and background noise due to scattering is considerably reduced in case that the signal is spectrally resolved. All in all, the typical errors in the obtained 2PA cross-sections values with this method, even under the best experimental conditions, are about 10%. Furthermore, this method finds two limitations. On the one hand, it can only be applied in spectral regions where the 1PA is totally negligible (this being extensible to all the techniques summarized in this Section). On the other hand, this method is restricted to photoluminescent species.

However, the de-excitation of the molecule can be followed in other ways. For example, if the system presents large intersystem crossing rates that leads to a lower energy triplet excited state, phosphorescence process is possible and then **two-photon excited phosphorescence** (**2PEP**) can be employed. This technique follows similar principles to those established for 2PEF.[69,70] Other alternative is the quantification by means of a secondary photochemical process, such as the luminescence from singlet oxygen by energy transfer from a 2PA-mediated triplet excited state of the chromophore.[71]

In summary, the main limitation of the indirect methods is that they build on secondary processes. Consequently, these cannot be applied for all the 2PA chromophores, owing that not all of them present the necessary properties and/or behaviors. Besides, 2PEF and 2PEP are difficult to be employed in compounds that display wavelength-dependent emission (in either band shape or efficiency) or dual emission. Thermal or photoacoustic methods require of certain knowledge of the material and the environment, but fortunately most of the necessary information is available in the literature. Although it is mandatory to demonstrate that 1PA does not take place in the study conditions, the 2PA observation is better when separated from the experimental conditions in these methods. An added surplus of the indirect methods is their superb accuracy, reliability, and reproducibility, which makes them the most attractive option. As mentioned before, the dependence on the pulse rate is not as crucial as in direct methods. More importantly, 2PEF method is the

most widely used as consequence of the massive application of 2P spectroscopy in the bioimaging field.[72] This makes accessible a wide variety of commercial microscopes with adequate laser sources. Certainly, this is the technique that will be employed for the study of the 2PA properties in this thesis.

1.1.3 Two-photon active molecules: structure-activity relationships

2PA in organic dyes was first experimentally proved by Peticolas *et al.* in 1963.[73] However, the first descriptions about structure-properties relationships were reported in the 90s.[74,75] Nowadays, this subject is still emergent and a comprehensive account of multiphoton dyes can be found in recent literature.[68,76–78] These works not only focus on analyzing the structure-properties relationships in a wide variety of described compounds, but also pretend to serve as guidelines for the development of efficient two-photon chromophores. Unfortunately, it is not always simple to disentangle the different but interdependent factors that influence the 2PA properties.

Noteworthy, some of the key ingredients described in these reviews are deduced from the theory described in Section 1.1. The following statements for maximizing the 2PA cross-sections can be summarized:

→ Peripheral donor and acceptor groups lead to high values of μ_{gi}, μ_{if}, μ_{gf}, and/or $\Delta\mu_{gf}$ [see **Eq. (2)**].[41,79,80]

→ π-conjugated chains with high coplanarity ensure large conjugation and contribute to a higher σ_{2PA}.[41,81–83]

→ Centrosymmetric designs improve on 2PA cross-sections, since these usually provide of a strong 1PA transition nearby to the 2PA laser wavelength (small Δ in **Fig. 3**, which eases the reaching of a virtual state).

From an electronic and structural point of view, there is thus a strong correlation between intramolecular charge transfer (ICT)[19] and 2PA properties.[84–86] This is especially noted in dipolar D-A systems, where the presence of an electron-withdrawing component, an electron-rich one, or both elements is rather obvious. The symmetrization of these

scaffolds (even at the expense of the ICT character in some occasion)[87] is also a formidable strategy to provide high 2PA cross-section values. Indeed, quadrupolar and octopolar architectures have been proven to be extremely efficient to enhance the ability for 2PA, leading to dyes with schemes such as D-π-D, A-π-A, D-A-D, D-π-A-π-D, A-π-D-π-A, or branched combinations of the previous. The research groups of Marder,[41,88–90] Prasad,[54,75,91] and Blanchard-Desce[92–96] have been pioneers in the development of these types of structures.

However, not only the innate properties of the compounds are important, but also the environment in which the dye is immersed.[97] This can severely influence on the effective 2PA cross-section. Thereby, solvent polarity can adversely affect to the 2PA properties, as well as hydrogen bonding and solvent-mediated aggregation phenomena should be considered.[98] This has aroused a great interest in the last years, with many contributions that show how Aggregation-Induced Emission (AIE)[99] can be an extremely useful allied for 2PA in bioimaging-related applications.[100–105] Furthermore, a large number of chromophores display a somewhat reduced ability for absorbing 2P in aqueous or high polar media, whereas this process is considerably favored in a non-polar environment, such as an organic solvent (*e.g.*, toluene) or a micellar location.[106]

Thereupon, the structural motifs that compose 2P-chromophores and their relevance on the 2PA properties are exemplified, mainly focusing on dipolar structures. The selected cases aim to show the general trends when changing the cited moieties within the scaffolds, even if some of these cases are illustrated with symmetrical structures (the same principles apply for dipolar designs) or if different techniques have been performed for the quantification of the 2PA properties.

Donor groups

Traditionally, amines assume the role of electron-rich group, although oxygen-based donors are also employed. The ready availability of these groups from a synthetic point of view makes them the most recurred options for constructing 2PA chromophores. Since these groups do not display the same electron-donor behavior, their incorporation in the

molecular architectures will provide different capacities for 2PA, as illustrated in **Fig. 8** for two fluorene derivatives with different electron donor groups.[95] To explain the different attained properties, it is very instructive to compare the Hammet-Brown constants (noted as σ_p^+)[107,108] of the different electron-donor groups incorporated: for a dialkyl amino group this coefficient is of σ_p^+ = -1.7, while the one for alkoxy substituent is σ_p^+ = -0.78.

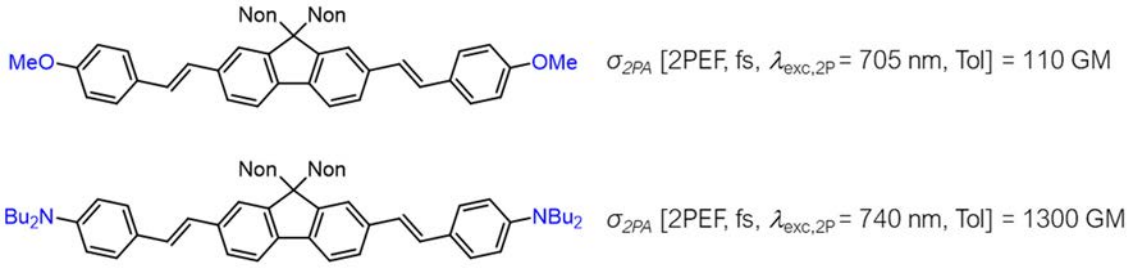

Fig. 8. Structures of fluorene derivatives bearing different electron-donor groups.[95] Further details about the quantification of the 2PA cross-section are indicated in the square brackets.

Aryl amino groups are even most recurred than alkyl ones. Despite of a lower donor-character (σ_p^+ = -1.4), the aryl amino moieties seem to provide better 2PA cross-section. This fact, *a priori* contradictory, can be ascribed to the greater number of π-electrons that these groups add to the whole system. Amino derivatives, both alkyl and aryl ones, are however prone to undergo photoinduced electron transfer especially in polar solvents, being this process translated into fluorescence quenching.[109–111] In addition, alkoxy groups can be synthetically derivated in alcoxides, which display an even better electron-donor capacity (σ_p^+ = -4.7).

Alternatively, π-excessive heterocycles such as thiophene have been proposed as donor groups (see **Fig. 9**). Nevertheless, these are not as efficient as triarylamino groups. The difference in normalized per π-electrons 2PA cross-section (σ_{2PA}/N_e, where N_e is the number of π-conjugated electrons) supports this observation: 26 π-electrons, 2.5 GM/e$^-$ in the benzothiazole-thiophene derivative *vs.* 40 π-electrons, 4.4 GM/e$^-$ in the benzothiazole-triphenylamino one.[112]

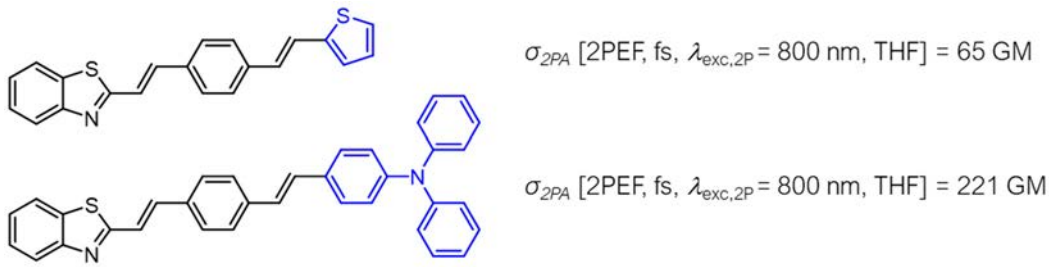

Fig. 9. Structures of some benzothiazoles with different donor groups.[112] Further details about the quantification of the 2PA cross-section are indicated in the square brackets.

Moreover, the electron-donor behavior of some groups can be enhanced by extra decoration with other attached moieties. Thereby, the methoxy-assisted diphenylamino leads to an improved 2PA cross-section (see **Fig. 10**).[75]

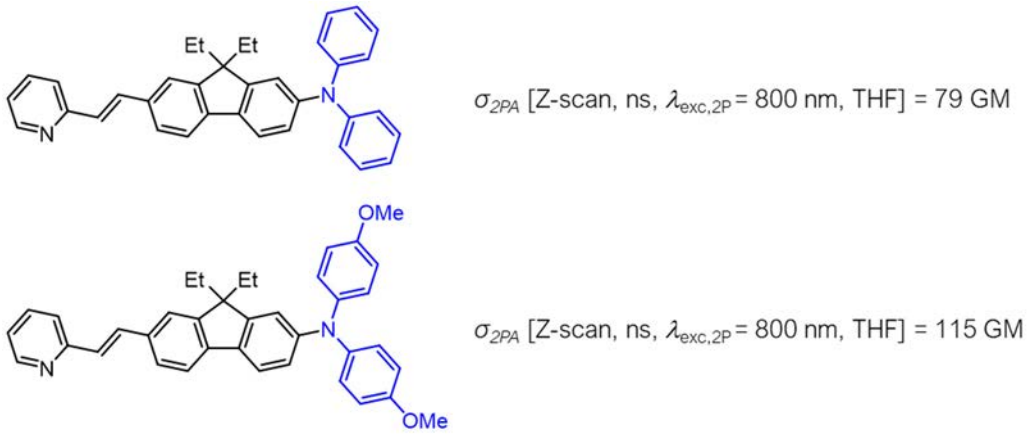

Fig. 10. Structures of fluorene dyes incorporating diphenylamino and methoxy-assisted diphenylamino moieties as electron-donor groups.[75] Further details about the quantification of the 2PA cross-section are indicated in the square brackets.

Acceptor groups

The variability in donor groups is relatively limited, since the design criteria for most of the cases described in the literature lay on the examples shown above. On the contrary, there is a large number of groups that have been studied as acceptor motifs.

Among them, classical functional groups such as nitro,[113–116] cyano/malononitrile,[41] sulfonyl,[93,94,114,115,117–119] triflyl,[93,94] and carbonyl [120–126] groups are highlighted and have been widely utilized. π-deficient heterocycles also constitutes a suitable choice.[127] In this regard, we can find plentitude of examples in the literature referring to 4-pyridyl, 2-benzoxazole, 2-benzimidazole, 2-benzothiazole,[112,121,122,128–130] quinoxazole, quinoline, or oxadiazole,[131] as electron withdrawing components. The positive charged alternatives are even more attractive, such as those that contain *N*-methylpyridium,[132–134] *N*-methylbenzothiazolium,[135] or 1,3,3-trimethylindolium[135–140] groups. Last but not least, there is an ongoing interest in the use of organoboron groups to play the electron-acceptor role.[44,87,141] These groups, when properly adapted, not only lead to excellent 2PA properties but also to superb photophysical features.

Taking into account the massive number of possibilities and for a better understanding, the examples in this case have been reduced to those depicted in **Fig. 11**. In these dyes series, it is nicely observed how the 2PA cross-section increases according to the electron-acceptor character of the used moiety. Hence, compound bearing the nitro group yields the highest value in this collection as consequence of the improved ICT character.[116]

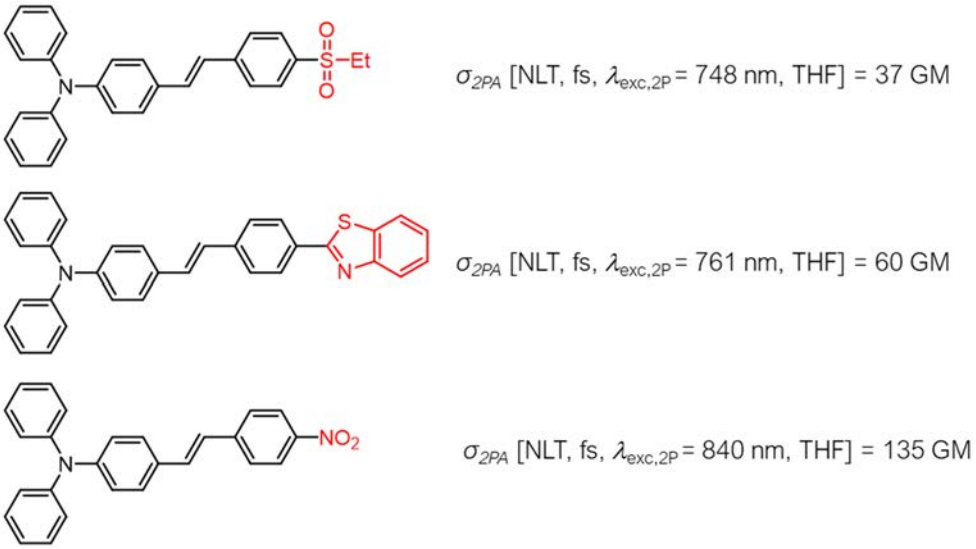

Fig. 11. Structures of stilbene-based dyes with different acceptor groups.[116] Further details about the quantification of the 2PA cross-section are indicated in the square brackets.

π-conjugated system

The aim of this structural element is to facilitate the displacement of the electronic density, being its role to function the system even more crucial than the presence of exceptional donor and/or acceptor groups.

There are two main parameters that must be considered when analyzing this architectonic motif:

→ Size, translated into the number of π-electrons which are incorporated through the diverse elements that compose the structure.
→ Conformation, that is, if it is rigid or flexible.

Starting at the central core, a few very common examples are illustrated in **Fig. 12**. When comparing the naphthalene-based dye (so-called Prodan[120]) with the fluorene analogue, it is observed the 2PA properties are enhanced in this last one.

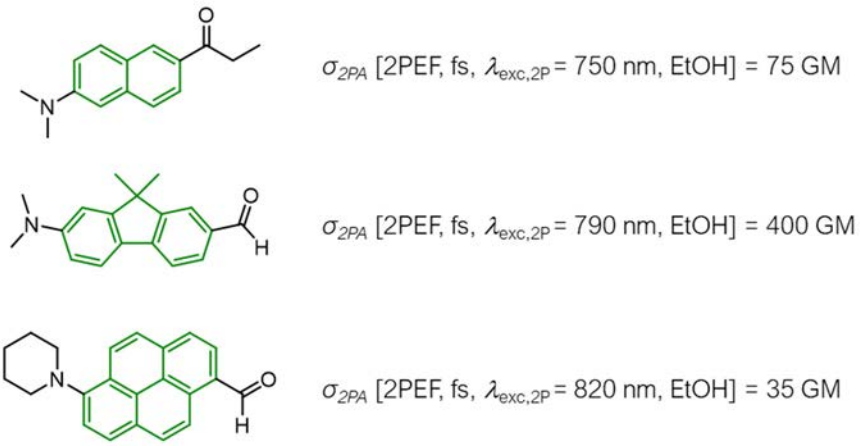

Fig. 12. Structures of Prodan[120] (top compound) and diverse analogues with different central cores.[142,143] Further details about the quantification of the 2PA cross-section are indicated in the square brackets.

Although both compounds have the same number of π-electrons, the effective π-conjugation is superior in fluorene derivative.[120,142] That is, in naphthalene the electrons do not move in a linear direction, whereas in the 2,7-fluorenyl core they do. Both naphthalene and 2,7-fluorenyl are widely exploited in a large collection of 2PA chromophores. On the

other hand, more electrons are implicated in the pyrene derivative,[143] but the electronic movement is substantially hindered in this core for a similar reason to that figured out for the naphthalene *vs.* fluorenyl comparison. Interestingly, the analogue bearing the pyrene core offers the maximum of the 2PA band in a longest wavelength.

Other popular and simple approaches are those based on phenylene/vinylene or phenylethynyl/ethynyl moieties. More carbocycles have been explored, including dihydrophenanthrene[92,144] or anthracene[145] among others. Combinations of carbocycles and heterocycles are also feasible, such as phenantroline,[122] bezonfurane or indole[146] based-nucleus. In recent years, benzothiadiazole[147–152] and benzotriazole[151] cores have been paid significant attention owing their suitable properties and high synthetical versatility.

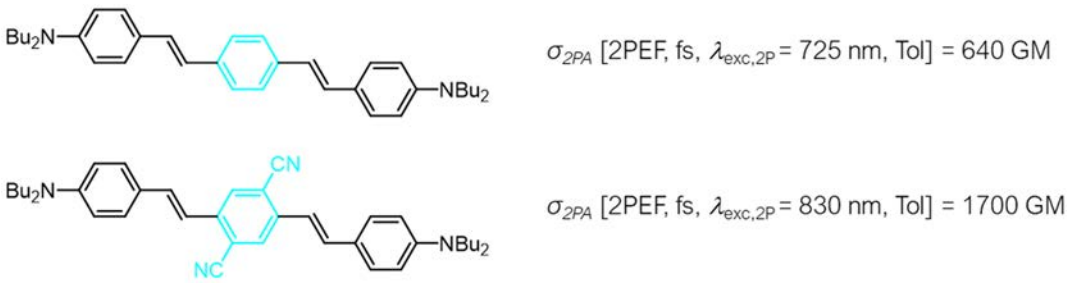

Fig. 13. Structures of phenylene/vinylene dyes with different extended π-conjugated systems.[41,88] Further details about the quantification of the 2PA cross-section are indicated in the square brackets.

Additionally, the central core often assumes the role of acceptor or donor group. Consequently, there are cases in which extra donor or acceptor moieties are attached to the central core with the aim of improving the electronic movements. Thus, the electron acceptor or donor character of the central core is also a factor to be considered. This is illustrated in **Fig. 13**, where the cyano-decorated phenylene/vinylene attains a 2PA cross section almost three times higher.[41,88]

The length of the π-system, measured by the number of π-electrons that are involved, also has a considerable effect on the 2PA properties. As it can be appreciated in **Fig. 14**, the inclusion of an additional phenylethynyl motif in the scaffold improves the 2PA properties.

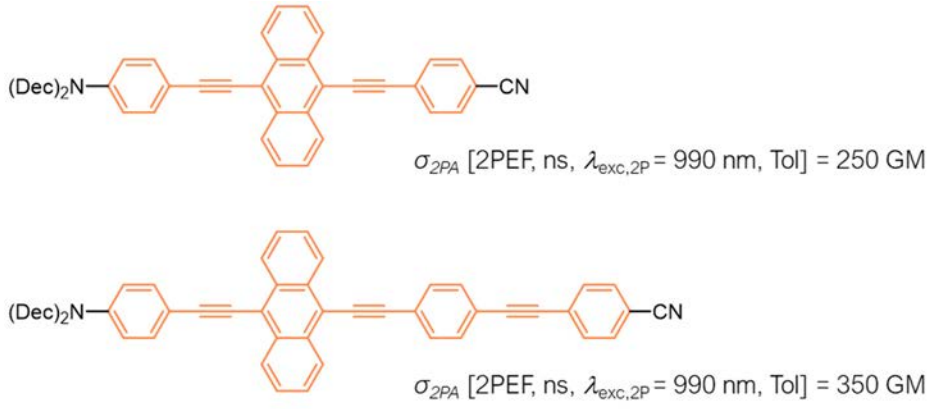

Fig. 14. Structures of anthracene-based dyes with different extended π-conjugated systems.[153] Further details about the quantification of the 2PA cross-section are indicated in the square brackets.

However, the inclusion of a double bond in the structure is more effective than a phenylethynyl moiety (**Fig. 15**).[75] This structural modification attains a larger improvement of the 2PA properties, and it can be drawn that double bond facilitates the π-conjugation in a greater extent that triple one.

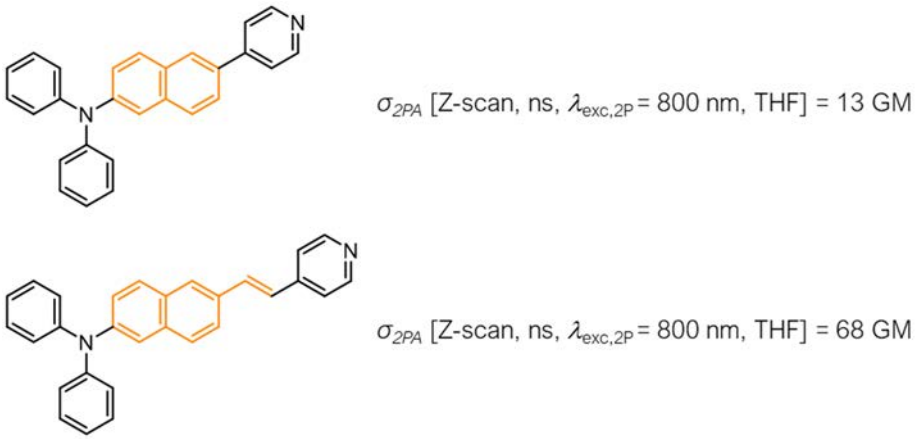

Fig. 15. Structures of naphthalene-based dyes with different extended π-conjugated systems.[75] Further details about the quantification of the 2PA cross-section are indicated in the square brackets.

It is important to note that 2PA cross-sections are molecular quantities. Combining together two chromophores in a manner that does not involve electronic delocalization will simply double this magnitude. Nevertheless, if the π-systems are strongly coupled, the increment is not directly proportional to the number of electrons introduced in the system and is

usually larger than the expected. A beautiful illustration of this can be found in the series **Fig. 16**, where the progressive inclusion of phenyl rings in the central core provides a massive augment in the 2PA cross-section.[44]

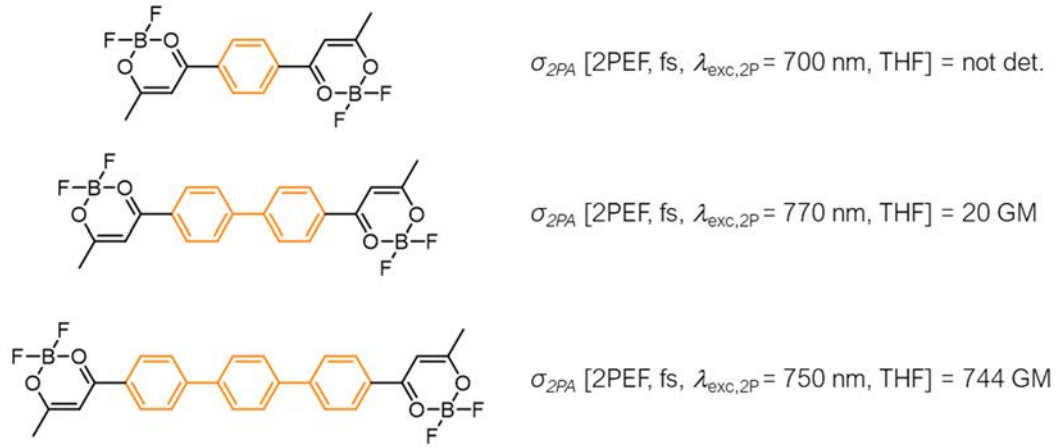

Fig. 16. Structures of compounds bis(dioxaborine) dyes with different central cores.[44] Further details about the quantification of the 2PA cross-section are indicated in the square brackets.

Certainly, and in line with how the units are connected, it is necessary to emphasize the importance of the used bridge in comparable conjugated systems. Focusing on multiple bonds and as mentioned above, vinylene-linked systems (sp^2) reach a better electronic communication than or ethynylene-linked ones (sp). This behavior ascribes to molecular orbital energies that are non-coincident at C(sp) – C(sp^2) connections and because of the different bond lengths.[154] This can be appreciated in **Fig. 17**.[95] The change in the 2PA cross-section even gentle, is noted when using a vinylene motif.

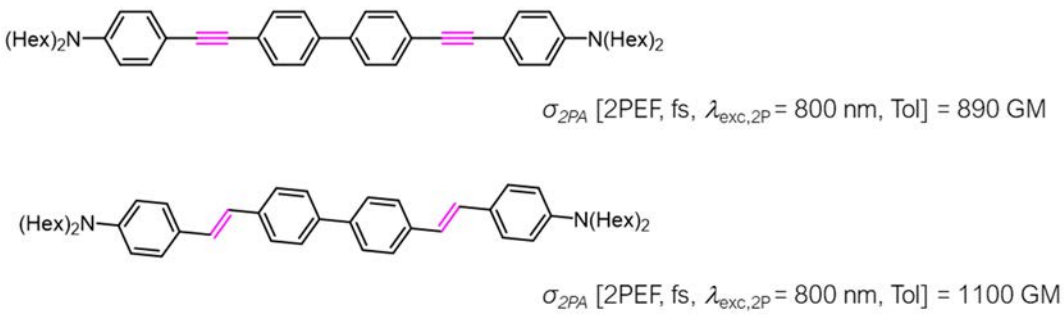

Fig. 17. Structures of different-linked biphenyl-based dyes.[95] Further details about the quantification of the 2PA cross-section are indicated in the square brackets.

The opposite trend is however plausible, and it is shown in **Fig. 18**.[151] Although the π-conjugated system has apparently improved when using a double bond instead of a triple one, steric hindrance and conformation can play a fundamental role in the properties of the dyes and specially when voluminous groups are implicated.[151,155,156] In all cases, the electronic coupling is optimized when a π-system adopts a planar geometry as consequence of maximizing the π-orbital overlap, and in this case, this is attained in the system that incorporates the triple bonds.

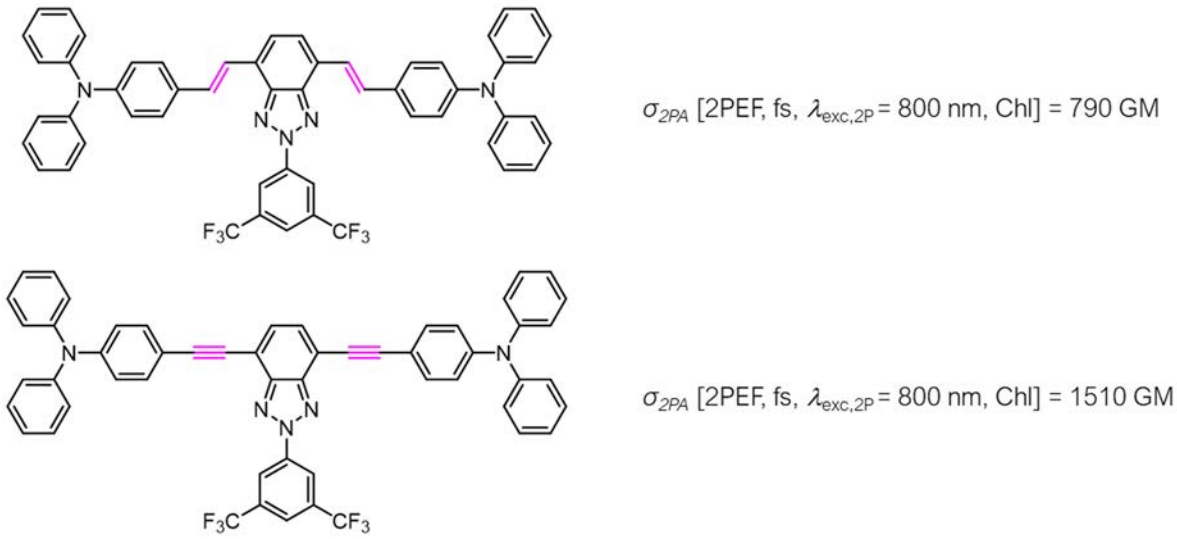

Fig. 18. Structures of different-linked benzotriazole dyes.[151] Further details about the quantification of the 2PA cross-section are indicated in the square brackets.

By and large, there are many parameters that can be considered when designing a 2PA chromophore. As illustrated, not all the relationships can be tightly correlated, and, on some occasions, it is impossible to rigorously predict the exact features of the system. Although barely mentioned, the σ_{2P}/N_e parameter is a very instructive figure of merit to analyze the efficiency of the elements incorporated within a molecular design to modulate the 2PA, allowing thus the comparison between different structural models.

Out of the context of dipolar structures, some asymmetrical non-dipolar structures have been described. Nevertheless, these have been developed to gain insight into higher-order architectures in which they are installed. For example, the analysis of asymmetrical

compounds on the top of **Fig. 19** allows to partially explain the features of the branched dendrimers at the bottom of this one. In general, and when deepening in this type of scaffolds, it can be deduced that cooperative effect results in the measured cross section value being higher than the sum of the discrete units that constitute the whole molecular system.[157]

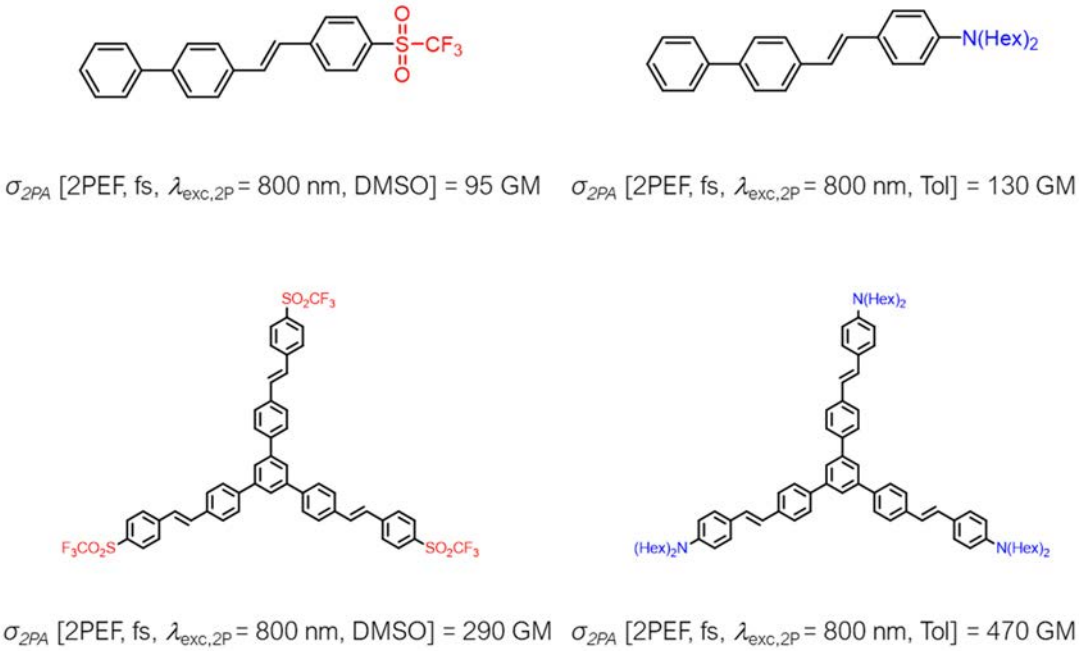

Fig. 19. Non-dipolar chromophores for composing branched dendrimers with 2PA properties.[157] Further details about the quantification of the 2PA cross-section are indicated in the square brackets.

1.2 APPLICATIONS OF TWO-PHOTON EXCITATION

As previously mentioned, 2P-excitation occurs efficiently when a high number of photons are focused on a discrete volume. That is, the probability of the process sharply falls when moving out of this volume, as function of $1/r^4$, where r is the distance from the focal point of the laser. This behavior can be observed in **Fig. 20**, which illustrates how the fluorescence emission from a fluorescein solution exactly reveals where the excitation is happening in both 1P and 2P-mediated conditions. More importantly, this performance is

a consequence of the square dependence of the process on the excitation energy, and it allows the excitation volume to be three-dimensionally controlled.

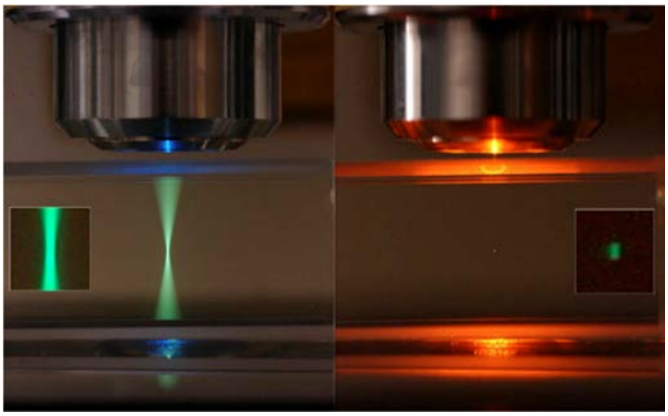

Fig. 20. *Left*: 1P excitation by focused light in a fluorescein solution ($\lambda_{exc,1P}$ = 488 nm). *Right*: 2P excitation at the same solution. In this case, fluorescence only outcomes from the focal point. Please note that no more data about the excitation conditions (*i.e.*, employed laser or wavelength) or the concentration of the fluorescein sample are available for 2P regime. Image reproduced from http://microscopy.berkeley.edu/.

Hence, parasitic photoinduced processes in areas nearby to the focal point are nicely avoided. This is precisely the key factor that most of the application of 2PA process exploit, whether if the interest is on the photophysical properties of the reached excited states or if this is on the processes that can take place after the 2PA. Noteworthy, most organic chromophores obey Kasha's rule, that is, the lowest vibrational level of the first singlet excited state is attained with independence of the accessed excited state. Subsequent photophysical or photochemical processes arise from this point, as well as from the lowest triplet state in case that intersystem crossing is feasible. In addition to the excitation volume control, 2P process supposes a considerable reduction of the scattering losses. Given that Rayleigh scattering is inversely proportional to the fourth power of the used wavelength ($1/\lambda^4$), the use of excitation wavelengths in the NIR spectral region severely prevents this phenomenon. Moreover, the samples, regardless of their nature, tends to absorb more at shorter wavelengths, being this event also precluded.[158,159]

These advantages have aroused interest for applications in two main areas, as hereinafter described: a) materials science and b) biological and biomedical fields. Whereas the

interest in the first one has decreased over the last years, the application of the 2PA process in biology-related applications (specially 2P-bioimaging) is continuously growing nowadays.

1.2.1 Uses in materials sciences

Microfabrication

Fabrication in the micro scale (or even in the nano one) of three-dimensional (3D) objects is substantially facilitated by radical polymerization. In this concern, 2P-induced radical chemistry is extremely useful, and it can be performed through a) direct formation of reactive intermediates from the photoexcited species, or b) subsequent electron or energy transfer from the 2P-excited moieties to another species that can commence the radical reactions. 2P-initiated polymerization is doable in resins such as those containing acrylate monomers and/or oligomers, and was first demonstrated in the early 90s by Webb and coworkers.[160,161] In these first studies, negative-tone resists (materials that become less soluble to irradiation) were used, and polymerization was achieved with the aid of conventional photoinitiators, that is, compounds devised to 1PA based applications. Although non-optimized to work under 2P conditions,[162] this classical photoinitiators were used until new 2P-chromophores were specially developed (**Fig. 21**).[163,164]

The classical initiators are known to undergo photocleavage upon irradiation, giving rise to PhCO• and R• radical species, that in turn initiate the acrylate polymerization. When containing more than one polymerizable acrylate group, this process leads to crosslinking of the polymer chains, which in turn yields insoluble material around the focus of the laser beam. The later develop of the film is performed by using an adequate solvent that removes the excess resin material from the unexposed areas. A similar process can be drawn for the improved 2P-photoinitiators, although the radical formation is mainly operated by energy transfer processes. These compounds allow substantial improvements in the process: lower concentrations of initiator were necessary, faster fabrication speed was increased and the laser intensity was lowered.

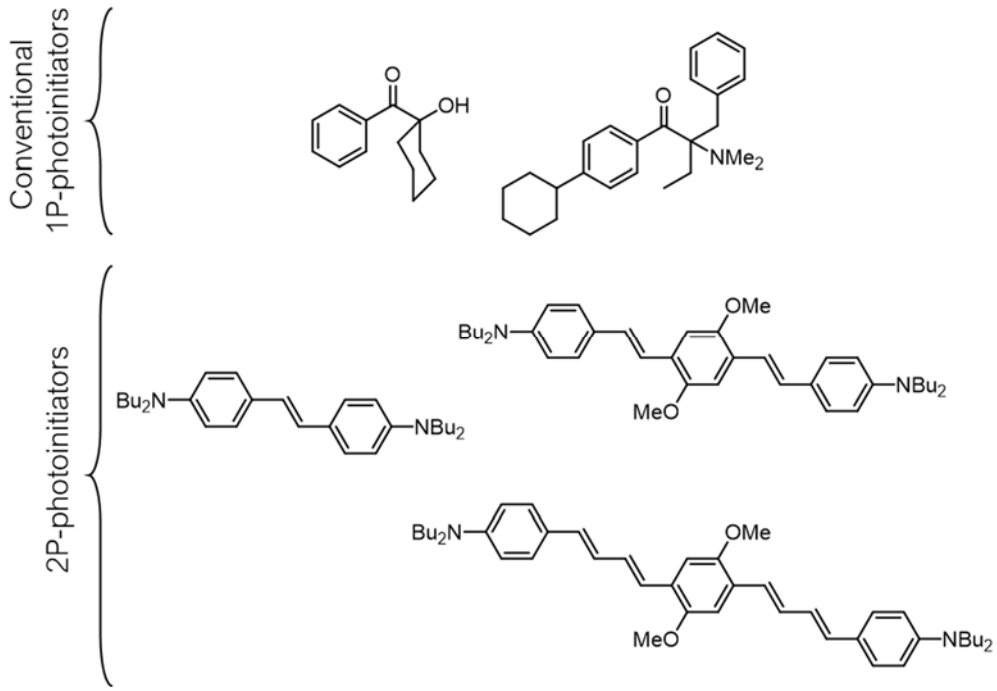

Fig. 21. Structures of conventional 1P-photinitiators and specially devised 2P-photoinitiators.

Using this strategy, structures as these shown in **Fig. 22 a, b** and **c** were achieved. [164–166] Other examples can be found in the literature following similar procedures.[167–171] Cationic polymerization has also been demonstrated, although its use is more related to the optical data storage. However, this procedure was employed to obtain the micro-propeller of **Fig. 22 d**.[172]

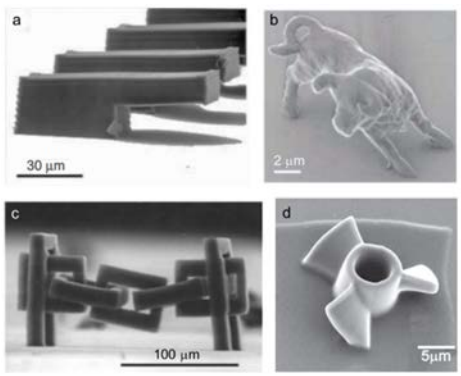

Fig. 22. Microstructures fabricated through 2P-induced radical polymerization: (a) cantilever,[164] (b) bull,[165] (c) chain with interlocking rings[166] and (d) propeller.[172] The images are reproduced with permission from the corresponding references.

3D optical data storage

The highly localized 2PA excitation volume and the high discrimination against the surrounding background led to the generation of high-density 3D optical memories, which offer considerable increases in the data density in relation to traditional 2D magnetic or optical media.[27,173] Although 2P-mediated radical processes have been utilized in the construction of optical memories, cationic polymerization has been further exploited in this concern. This process builds on the generation of a cationic specie after the 2PA process, being this moiety responsible for originating the polymerization process. Despite the great similarity of the radical polymerization, this type of process entails some added advantages such as the possibility of using positive-tone resists, *i.e.*, materials whose solubility increases on irradiation. The latter develop of the soluble obtained polymer provides a high fidelity writing from monomers such as epoxides.[174] As it occurred for microfabrication, the first studies about optical memories were accomplished using a well-established 1P-initiator under 2P-excitation conditions.[162] Subsequently, 2P-optimized initiator were *ad hoc* devised, improving thus the process.[175,176] An outstanding example of optical memory constructed by 2P-excitation was described by Walker and Rentzepis in 2008 (see **Fig. 23**).[177] In this work, these researchers demonstrated the potential application of the biphotonic process by making a DVD-size disk of up to 10 TB of capacity. Although this dispositive had a huge storage capacity, it took about 4 days to write because of the writing speed (3 MB/s).

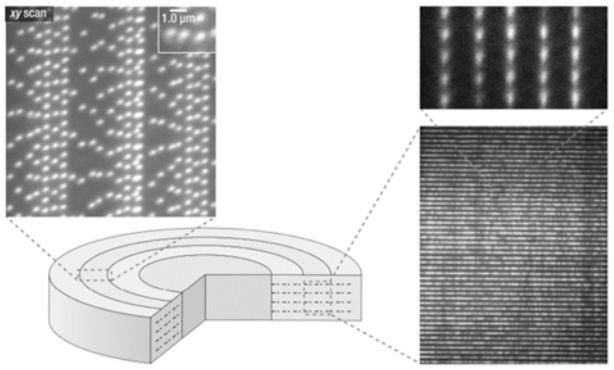

Fig. 23. 3D data storage disk written by 2P excitation. The image is reproduced with permission from the reference [177].

Up-converted lasing

Dye solutions and dye-doped solid materials are excellent candidates for lasing materials, because of the low pump threshold requirement, lasing wavelength tunability, high lasing efficiency, low cost, and so on. Immediately after the advent of lasers, 2PA and 3PA-induced frequency-up-converted fluorescence was informed in organic dye materials upon pulsed laser excitation.[73,178–180] These phenomena aroused increasingly interest specially between the 70s and the 90s, when the 2P-excited up-converted emission from a wide variety of commercial organic dyes was investigated in pumped-light systems.[181–188] Recently, 3P and 4P-pumped lasing in dyes solutions have been reported. [10,16,189,190] It is worth noting that whereas for most of the applications a large cross-section is highly desirable, the requirements for multiphoton-pumped lasing dyes are different. In these dyes, the easiness for establishing population inversion and a higher lasing efficiency are the most important design criteria. Because of these reasons, only a small number of the reported multiphoton active chromophores are suitable for multiphoton pumped lasing. These dyes are essentially salt-type dipolar compounds, most of them containing positive charged groups as strong electron-withdrawing moieties (*e.g.*, compound represented in **Fig. 24**).[189,191,192] The performance of a solution containing this dye is exhibited for 4P-pumped lasing in the figure below.[189,193]

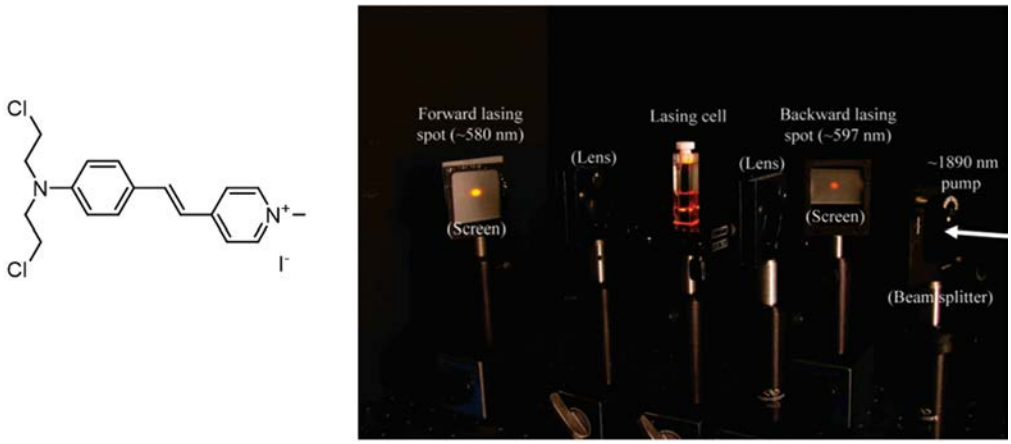

Fig. 24. 4P-pumped lasing in a solution of the compound[189] illustrated at the left. In the screens, it is observed the change in the color of the forward and backward lasing output beams. Image reproduced with permission from reference [193].

Optical limiting

An optical power limiter can be defined as a material that exhibits intensity-dependent absorption, *i.e.*, the transmissivity through it decreases as long as the input signal intensity increases.[194] This behavior is represented in **Fig. 25**,[74] where is shown the performance of the same dye solution upon being excited with different input energy conditions. At low input energies, practically all the light is transmitted and the dye solution behaves as transparent. The opposite featuring is appreciated when exposing to high input energies (even greater than 150 μJ), where most of the light is absorbed and the output energy is below 20 μJ. That is, the solution acts in these high energy situations as an opaque medium, impeding thus the transmission of the light. The design and performance of optical limiters lays on diverse nonlinear optical effects.[50,194–196]

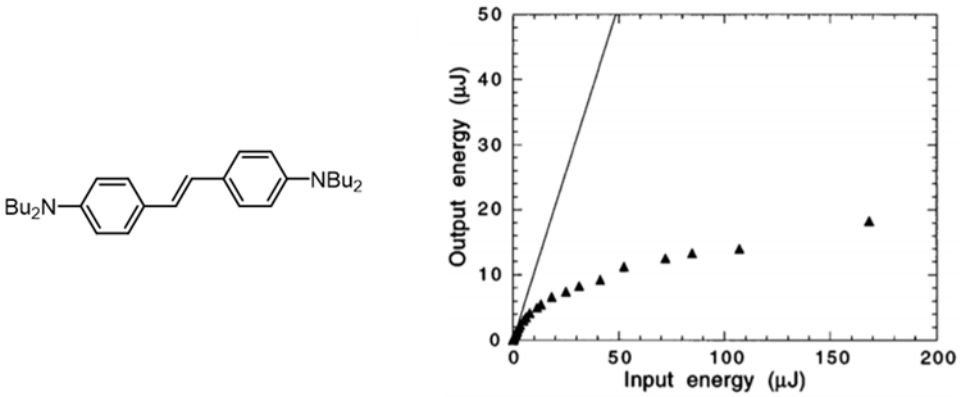

Fig. 25. Optical limiting response of the stilbene-based dye represented at the left in acetone solution upon being excited with 5 ns laser pulses at 600 nm and at different input energies (concentration: 0.14 M). The solid line corresponds to the linear transmission of the solution (95%). The graph is reproduced with permission from reference [74].

1.2.2 Uses in biological and biomedical fields

The invention of two-photon fluorescence microscopy (2PM) by Webb and coworkers in 1990 meant to be a turning point in the bioimaging field.[72] Between the above-mentioned advantages of 2PA processes, one of them must be specially considered here: the opportunity of exciting at wavelengths within the biological windows (see **Fig. 26**).[197–200]

Accordingly, the relative transparency of the tissues at these wavelengths ensures a penetration in depth in 2P microscopy typically between 500 and 1000 μm,[201–204] which is considerable greater than the attained in confocal microscopy (roughly less than 100 μm).[205,206] Whether if the purpose is to gain insight in biological structures and/or processes or if the intention is to study photoinduced processes in a determined environment, 2PM is definitely settled as an extremely useful tool. In the next pages, some of the main applications of 2PA process in these contexts are described.

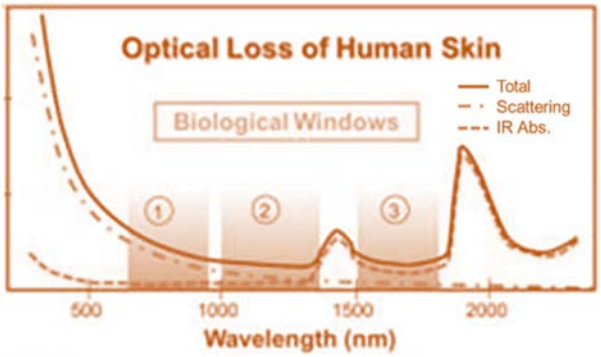

Fig. 26. Absorption spectrum of human skin showing the first (NIR-I, from 700 to 950 nm), second (NIR-II, from 1000 to 1350 nm) and third (NIR-III, from 1550 to 1870 nm) biological windows. Image modified from reference [207].

Tracers and probes: 2P-bioimaging

The use of NIR excitation wavelengths not only enables imaging in deep, but in turn facilitates *in vivo* monitoring because of the low phototoxicity of the employed light. Because of the reasons above, it is relatively easy to justify the growing importance of 2PM in bioimaging tasks. Particularly interesting is the ability to obtain three-dimensional images along the z direction in a thick sample, being this application proved with non-optimized fluorophores a few years after the 2PM was introduced.[208] New fluorophores specially devised for 2P-bioimaging emerged which can be classified in two categories: 1) 2P-fluorophores envisioned for staining subcellular compartments and 2) 2P-fluorophores Intended to monitor subcellular processes or chemical species within cells.

Regardless of the latter use, 2P dyes for bioimaging should display an adequate solubility in water in addition to suitable photophysical properties. The water solubility is indeed much more crucial for the staining than the optical features, since these last ones could be close conditioned by the external surrounding as mentioned above.[97] Considering the solubility, if too high the compound will not stain the cells because is more stable in aqueous solution than in subcellular environments. On the other hand, a low solubility may involve mistargeting problems.[209]

Following the design criteria described in Section 1.1.3, the enhancement of the 2PA cross-sections is usually achieved through increasing molecular size (often achieved by greater π-conjugated systems). However, large molecules entail generally more cytotoxicity and a lower solubility in water. Therefore, small molecules are the most appropriate candidates for 2P bioimaging, which needs to be accurately designed for obtaining the better properties and performance in the smaller size. One of the most recurred strategies to that end is enclosing the conjugation-bridge within a heterocycle, which leads to an additional increment in photostability in most of the cases.

Once the appropriated dye has been selected, additional groups are usually incorporated to the scaffold for a fine-tuned targeting.[210] The most useful moieties for staining different organelles are listed below:

- → Cationic groups, such as triphenylphosphonium, are extremely useful for labelling mitochondria.[211–215] This is reasoned on the membrane inner potential of these organelles.
- → The reversible protonation at a physiological pH of *N*-alkylmorpholine facilitates the selective accumulation within lysosomes of dyes bearing this group.[212,215–217]
- → Propyl chloride[212,218] and pentafluorophenyl[214,215,219] groups have demonstrated a good targeting-ability for this endoplasmic reticulum.
- → Non-polar groups, *e.g.* cyclohexyl moieties, promotes the immersion of the dyes in lipid droplets.[220]
- → Groups containing hydrocarbon chains with zwitterionic polar heads ease the accumulation and retention of dyes within the cell membrane.[221]

→ Myristic acid has been pointed as a promising targeting group for Golgi apparatus.[222]

Although less controlled and more difficult to predict, the intrinsic properties of the dyes can make them excellent probes for certain subcellular environments. This is for example the case of Laurdan (**Fig. 27 a, top compound**), which has demonstrated an excellent polarity probe for the model membrane composed of 1,2-dipalmitoyl-*sn-glycero*-3-phosphocholine. This behavior is related to the interaction of the dye with the linear hydrophobic domains of the cellular membrane, especially with those rich in saturated hydrocarbon chains, cholesterol, and hydrophobic proteins. Nevertheless, the interaction with unsaturated molecules is not as a favorable, and new derivatives containing new functionalities were devised to improve this performance (**Fig. 27 a**). As illustrated in **Fig. 27 b**, these derivatives exhibited an enhanced ability to stain the plasma membrane. Specially interesting is the case of the last compound represented in **Fig. 27 a**, whose internalization within the cell is minimum (**Fig. 27 b**, bottom). [123,125,126,223–225]

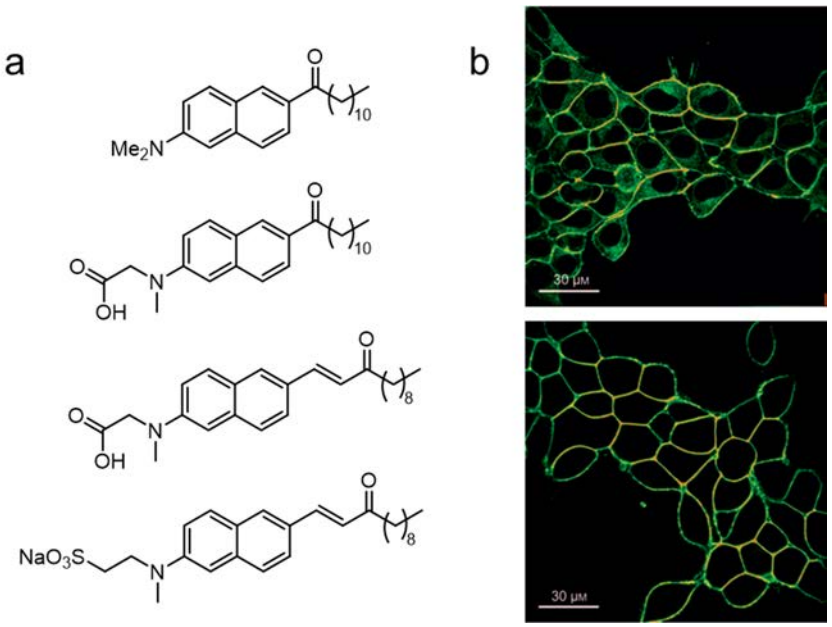

Fig. 27. (a) Structures of Laurdan (top compound) and new analogues.[123,125,126,223–225] (b) 2P-bioimaging of the last two compounds previously shown within 293T cells, respectively. Images reproduced with permission from reference [126].

At the other extreme, dyes that exhibit 2P-excited fluorescence sensitive to the presence of a particular chemical specie has notably stimulated the interest in the context of 2P bioimaging. A great number of 2P probes have been reported in the last years, which have been utilized for the detection of an immense variety of biological-relevant species present in those environments. Metal ions,[226–236] glucose,[237,238] or sulfides species[239–242] are just a few examples of a long list that could be made in this concern. Further information about this type of dyes will given at the introductions of **Chapter 3** and **4**., focusing in them on the use of 2P sensors for detection of reactive oxygen species and the monitoring of pH changes with this sort of tools, respectively.

2P-mediated release

As the 2P-induced photorelease of acid species is essential for some of the applications described in Section 1.2.1, much attention has been paid to the photodelivery or photodeprotection of functional molecules by biology and medicine fields. The use of 2PA facilitates the release in considerably small volumes, which in turn allows a selective and controlled targeting. Furthermore, most of the 2P-chromophores operate within the biological windows, avoiding thus light scattering and other similar interferences.

As it occurs in previous cases, the first studies about 2P-photolabile groups were performed with molecular scaffolds conceived to work under 1P conditions (**Fig. 28, top compounds**). However, these studies were done in the latter 90s, when the background knowledge about 2P-chromophores design was far advanced. Therefore, 2P-improved photolabile groups were rapidly devised, these mainly based on 7-hydroxycoumarins or 7-dimethylaminoquinoline analogues (**Fig. 28, bottom compounds**).[243–247]

Furthermore, these last-mentioned scaffolds have been used to photorelease a wide variety of species. These ranges from small moieties such as glutamate,[248] alcohols,[249] diols,[250,251] ketones/aldehydes,[252] or nitric oxide,[253] to larger entities like nucleobases,[254] nucleotides[255] or DNA/RNA.[256]

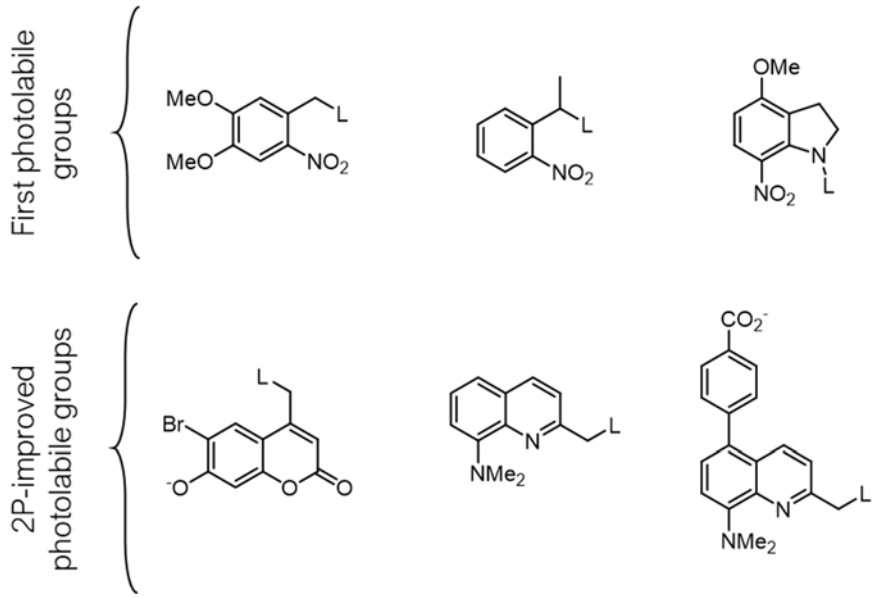

Fig. 28. Structures of some of the first photoremovable protecting groups used and a few examples of especially devised 2P-photolabile groups. In all cases, L represents the ligand to which these groups are attached.

Photodynamic therapy

The benefits of 2PA can also be brought to photodynamic therapy.[257] Through generation of cytotoxic singlet oxygen in a confined volume, the induced photodamage can be efficiently controlled. This technique has mainly been employed to treat skin cancers types and hollow organs.[258] The singlet oxygen is commonly generated by energy transfer from the first triplet excited state of a dye to the triplet ground state of molecular oxygen.

Taking into account that the lowest singlet state of molecular oxygen is 92.4 kJ mol^{-1} above the triplet ground state, the chromophores of interest should: 1) have a separation among the first triplet excited state and the singlet ground state larger than this energy quantity and 2) form the triplet excited state in a good yield on photoexcitation, that is, the dye should display an intersystem crossing rate that can compete with other processes that deactivate the first singlet excited state. 2P-induced singlet oxygen formation has been reported in a wide variety of chromophores with high 2PA cross-sections, such as compounds in Fig. 29)[71,259] among many others. Presumably due to the presence of the

heavy atom bromine, the replacement of the cyano groups of compound leads to an increased singlet oxygen formation quantum yield (noted as ϕ_Δ). Water-soluble analogues of these dyes have also been devised.[260] The production of singlet oxygen has been shown in other 2P-chromophores including dipolar fluorenes,[261,262] and porphyrin- and porphycene-based systems.[263–267]

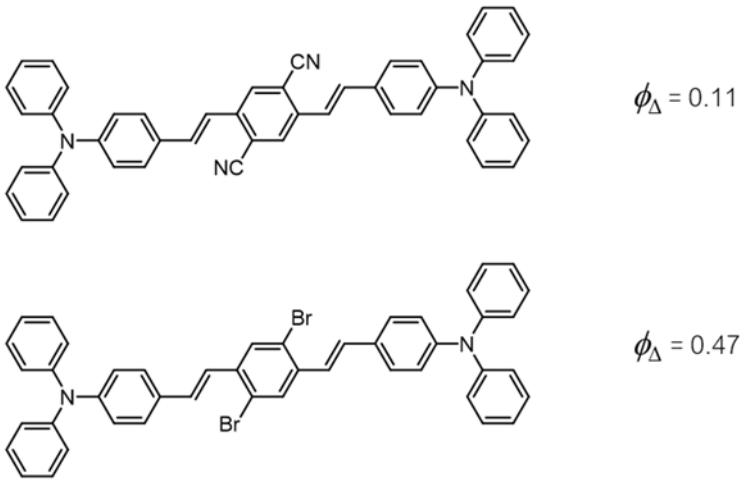

Fig. 29. Structures of some 2P-induced singlet oxygen photosensibilizators.[71,259]

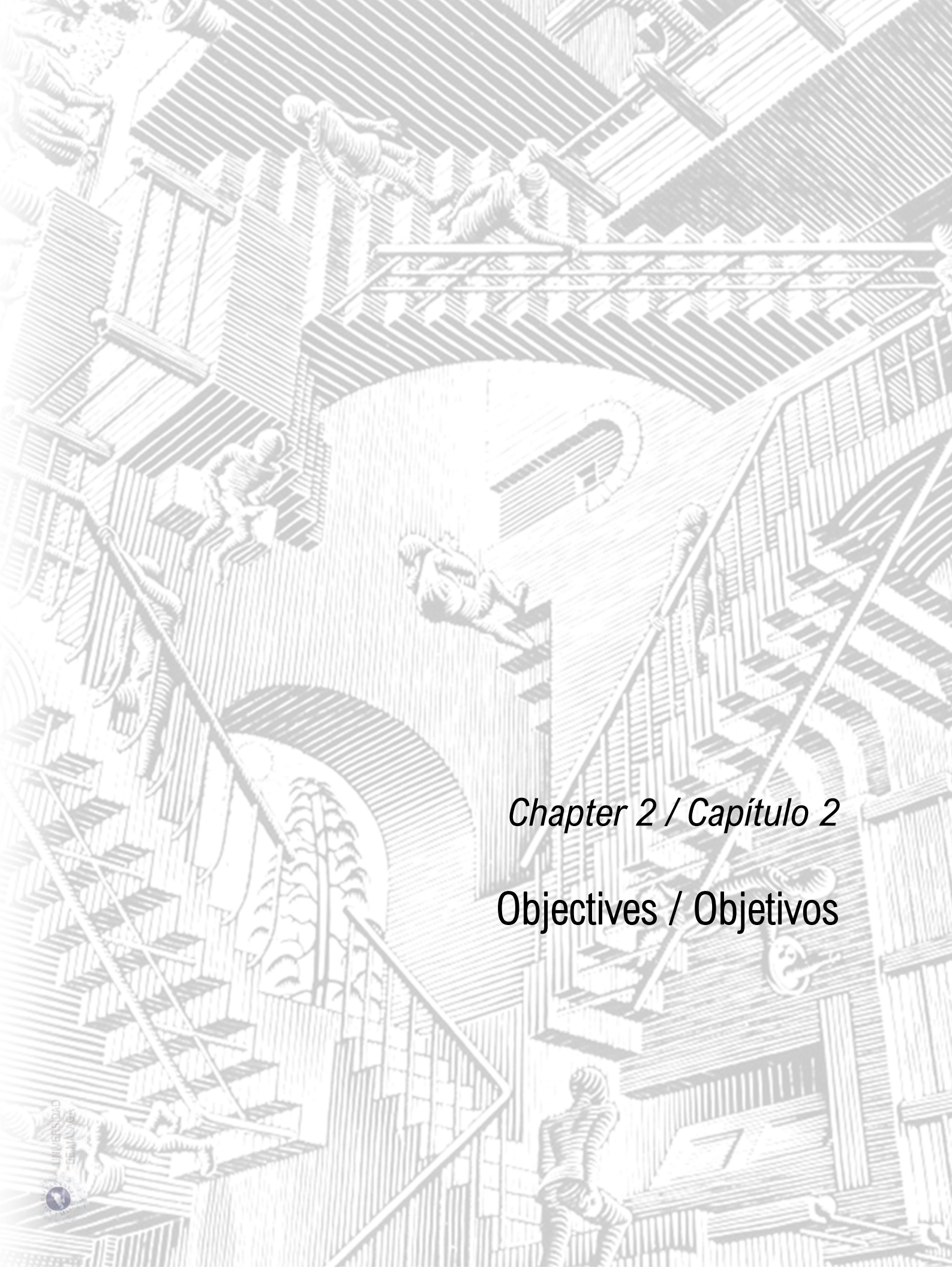

Chapter 2 / Capítulo 2

Objectives / Objetivos

English

This PhD thesis focuses on the 2PA process and more specifically, on the development of new organic molecular architectures for application in 2P bioimaging. Thereby, the first aim is to develop new 2P-optimized probes to sense chemical species that are frequent in the subcellular environment, as well as 2P-active trackers that identify cellular suburbs. To that end, new fluorophores based in indolenine and indolinium scaffolds will be developed (see **Fig. 30**).

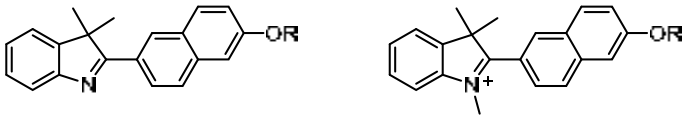

Fig. 30. General structures of indolenine- and indolinium-based 2P-chromophores developed in this thesis.

On the other hand, the spatial resolution of 2PM is a slight downside of this technique. Accordingly, the other topic to talk about in this thesis is the proof that the resolution of the 2PM technique can be improved by simply combining 2P-mediated processes. This approach would lead to a substantial upgrade in the field of 2P microscopy.

Accordingly, the specific objectives of the thesis are:

1. Design, synthesis, and characterization of a new 2P-fluorophore that can be adapted for the detection of Reactive Oxygen Species (ROS).
2. Design, synthesis, and characterization of a new *pH*-sensitive 2P-fluorophore scaffold; as well as its derivatization to control the subcellular targeting.
3. Design, synthesis, and characterization of new 2P-trackers for mitochondria.
4. Design and characterization of a new dyad system that operates through 2P-mediated processes.

Español

Esta tesis está centrada en el proceso de absorción de dos fotones y más específicamente, en el desarrollo de nuevas modelos orgánicos con propiedades de absorción de dos fotones para su aplicación en bioimagen. De este modo, el primero de los objetivos es desarrollar tanto nuevos sensores de especies frecuentes en entornos subcelulares optimizados para el proceso de 2PA, como nuevos marcadores con propiedades de 2PA para la identificación de elementos a nivel subcelular. Para ello, se desarrollarán nuevos fluoróforos basados en indolenina e indoleninio (ver **Fig. 30**). Por otro lado, la resolución espacial es un pequeño "talón de Aquiles" de la microscopía de 2P. El otro tema tratado en esta tesis es el estudio de la mejora de la resolución de la técnica a través de la combinación de dos procesos mediados por la absorción de 2P. Este modelo podría dar lugar a una mejora sustancial de la 2PM.

Los objetivos específicos de la tesis son:

1. Diseño, síntesis y caracterización de un nuevo fluoróforo con propiedades de absorción de 2P que pueda ser adaptado para la detección de especies reactivas de oxígeno (ROS).
2. Diseño, síntesis y caracterización de un nuevo fluoróforo con propiedades de absorción de 2P sensibles al *pH*, así como su derivatización para controlar la diana subcelular.
3. Diseño, síntesis y caracterización de nuevos marcadores para mitocondrias con propiedades de absorción de 2P.
4. Diseño y caracterización de una nueva díada que funcione a través de dos procesos mediados por absorción de 2P.

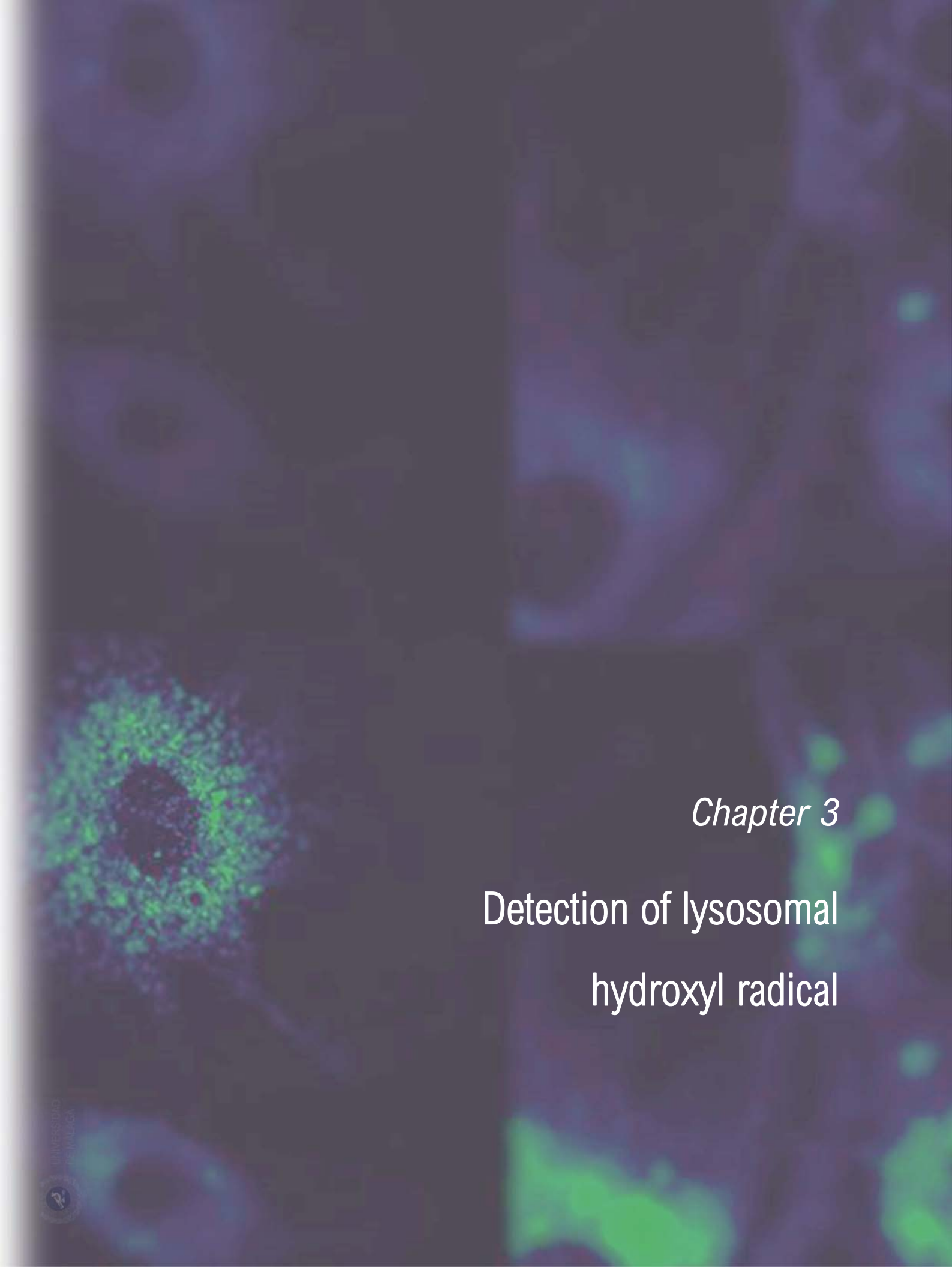

Chapter 3

Detection of lysosomal hydroxyl radical

3.1 INTRODUCTION

3.1.1 Reactive Oxygen Species (ROS)

Molecular oxygen is undoubtedly essential for cellular respiration in living aerobic organisms. Its triplet ground-state is responsible for almost its negligible reactivity with biomacromolecules. Nevertheless, certain derivatives of oxygen are highly toxic to cells. This was demonstrated for the first time back in the decade of 1950s, when Gerschman and coworkers reported the damage produced by oxygen-containing free radicals to aerobic organisms.[268,269] With the passage of time, terms such as ROS (reactive oxygen species), and RNS (reactive nitrogen species) have been used to define endogenous oxygen- and nitrogen-bearing molecules characterized for a high reactivity (see **Fig. 31**). These species are naturally generated to control cellular metabolism and signaling, as well as in response to certain pathological stimuli.[270–276] The imbalance between generation and elimination of ROS (and RNS), a mechanism known as oxidative stress,[277,278] is associated with the onset and development of multiple diseases, *e.g.*, cardiovascular diseases,[279] neurodegenerative diseases,[280] cancer,[281,282] rheumatoid arthritis,[280] allergies and other immune disfunctions.[283,284]

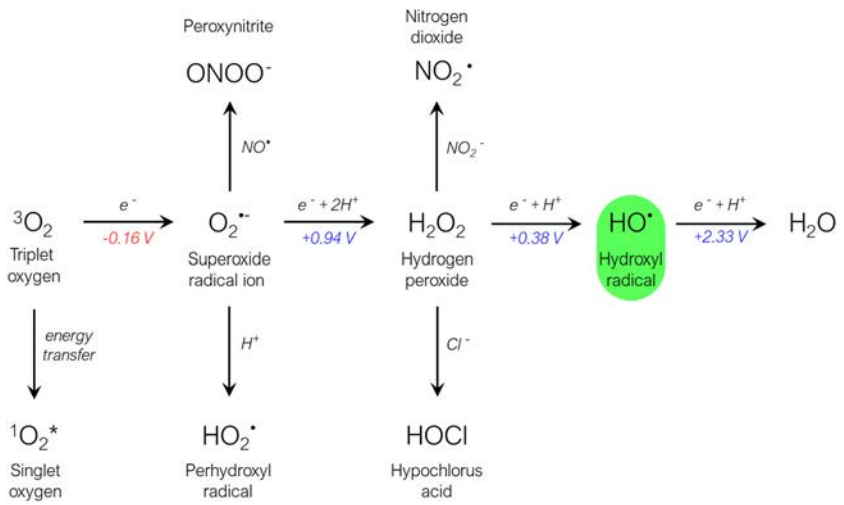

Fig. 31. Principal ROS and RNS species, and their formation mechanisms (mainly energy- and electron-transfer reactions).

As illustrated in **Fig. 31**, molecular oxygen is first derived in two different species: singlet oxygen and superoxide radical ion. While singlet oxygen is formed after energy transfer process, superoxide radical ion is produced by one-electron reduction. Both derivatives present considerable reactivity to organic molecules *versus* that of molecular oxygen. In addition, superoxide radical ion is in turn transformed into other oxygen-reactive molecules. Among them, hydrogen peroxide and hydroxyl radical are the most important. Hydrogen peroxide is characterized for its relative stability under physiological conditions despite of having positive electron reduction potentials: +0.38 V for one-electron process and +1.35 V for two-electron one.[285] In stark contrast, hydroxyl radical is the most powerful oxidant in the biological context, with a reduction potential of +2.33 V.[286] Consequently, this specie displays a high capacity to damage several biomacromolecules including lipids, proteins, and nucleic acids.[287]

Focusing on the intracellular sources of ROS, the most important are:

- **Cytoplasm:** cytosolic enzyme systems such as transmembrane nicotinamide adenine dinucleotide phosphate (NADPH) oxidases (NOX) are implicated in the generation of superoxide radical ion. There are various types of these enzymes, so different biological outcomes can be triggered.[288,289] The generation of singlet oxygen is also feasible in this environment. In particular, this derivative is produced in areas of inflammation through the action of phagocytes' NOX.[288]
- **Mitochondria:** these organelles are the major source of intracellular ROS. Superoxide radical ion is produced in the electron-transport chain.[290–293]
- **Lysosomes:** the formation of hydroxyl radical through Fenton reaction is substantially favored within these organelles, either from accumulated superoxide radical ion and/or hydrogen peroxide.[294–296] The acidic content (*pH* 4.5 – 5.0)[297] and the presence of multiple ferric proteins[298] in these subcellular compartments, provide the additional required ingredients for this reaction to occur. A high level of ROS is often translated into lysosomal membrane permeabilization, which implies the release of cathepsins into the extracellular space and is tightly associated with promotion and progression of tumors.[299,300]

3.1.2 Two-photon probes for detecting ROS

Several techniques have been employed to study the generation of ROS and the associated chemical processes, including high-performance liquid chromatography (HPLC), mass spectrometry or electron paramagnetic resonance (so-called EPR; only suitable if free radicals are implicated), among others.[301–303] These techniques offer information about the biological production of ROS by detecting oxidation products from protein, lipids, DNA, or other biomolecules. The major downside of these methods is their destructive character, that is, these are only adequate for *in vitro* measurements. Instead, fluorescence-based methods, such as confocal or two-photon fluorescence microscopy, enable for *in vivo* monitoring of ROS through the development of specific ROS-sensitive probes.[304–313] Even if there is a wide variety of this type of probes, not all of them are suitable for 2PM and there is still large room for improvement.

One of the classifications of fluorescent sensors most used is below and groups this type of compounds in two categories:

→ **Ratiometric probes:** the interaction of a molecular sensor with a certain compound of interest, produces a second form that presents a change in the photophysical properties in relation to the first one. Both derivatives are fluorescent under identical excitation conditions, but different emission bands are displayed. Thus, the target specie can be quantified through the quotient between the fluorescence intensities at each wavelength. An example of this type of probes is shown in **Fig. 32 a**, where the action of hydrogen peroxide produces the release of the carbamate group, and an improved π-conjugated system is attained. Consequently, the emission of the benzothiazole bearing the free methylamino group is red shifted from the blue to the yellow spectral region. Noteworthy, the incorporation of the triphenylphosphonium moiety provides the selective accumulation of this dye within mitochondria.[314]

→ **"On/off" - "off/on" probes:** unlike the previous, here only one of the forms is fluorescent under given excitation conditions. In most of the cases, it is desirable that the fluorescent form is the second one, *i.e.*, which results from the interaction

with the interest molecule. This class of sensors, more concretely the "off/on" ones, are characterized for minimizing the background signals. One of such probes is indicated in **Fig. 32 b**. Photoinduced electron transfer from the amino groups quenches the fluorescent of the primary form. The reaction of nitric oxide with these amino moieties implies the loss of this quenching process, and thus, 2P-excited emission is observed in the secondary form.[110,111]

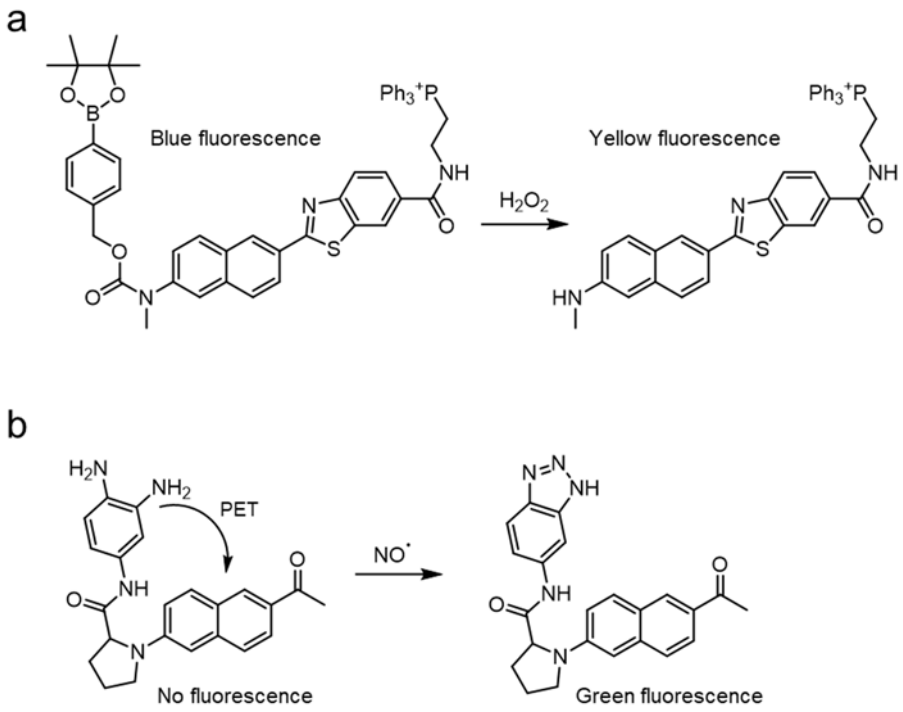

Fig. 32. Examples of 2P-probes based on Prodan's architecture for detection of (a) hydrogen peroxide[314] and (b) nitric oxide.[315]

3.2 MOLECULAR DESIGN AND SYNTHESIS

3.2.1 Structural elements and expected working principle

The control of hydroxyl radical as well as other ROS in lysosomes can provide valuable information for the development of some diseases. In order to achieve this objective, the

system represented in **Fig. 33** was originally envisioned for detecting, in principle, any type of lysosomal ROS.

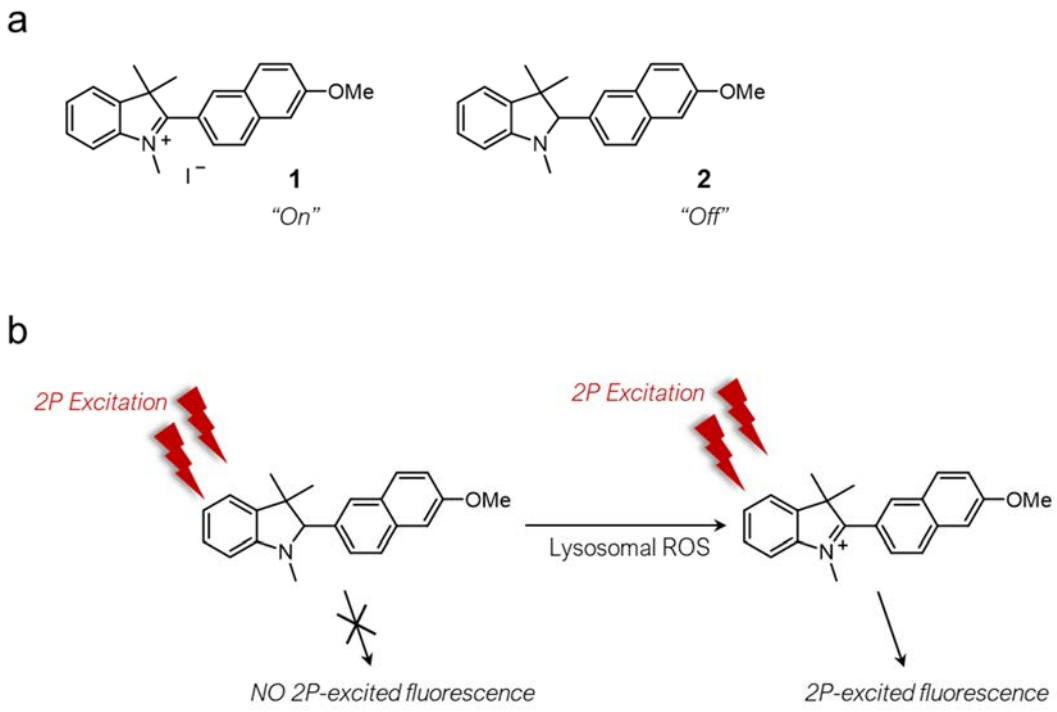

Fig. 33. (a) Structure of the target fluorophore **1** and potential ROS-sensor **2**, and (b) expected working principle for the system.

This molecular design of the fluorophore consists of the following structural elements:

→ **Naphthalene as central core:** the use of this π-conjugated system for constructing 2P-chromophores has been extensively reported in the literature. Prodan and its derivatives (*e.g.*, Laurdan and other compounds mentioned in the previous Chapter) are some of such examples.[120,142,143] The reason for applying this structural element is that endows an appropriate π-conjugation grade in a very concentrated molecular space, and consequently, good 2PA cross-sections are provided. Other cases of compounds bearing this structural element are those shown in **Fig. 32**, which were also devised for ROS sensing.[314,315] For these reasons, this group is incorporated within the structure of the target compound **2**. Unlike most of Prodan

derivatives, in this approach we have selected methoxy group instead of amino one as donor element. This choice pretends to avoid parallel processes frequently observed when using nitrogen-derivatives (*e.g.*, energy-transfer or protonation in acid environments).

→ **Use of 1,3,3-trimethyindolium as acceptor group:** this element is the one most used in cyanines and hemicyanines, which are recognized for being excellent dyes that include quaternary *N*-heterocycles as acceptor groups.[316] The reduction of the iminium group breaks the π-conjugation grade along the entire scaffold and results in a dramatic change in the photophysical properties. However, ROS-mediated oxidation would lead to recover this group and the starting optical features. There are a few examples of hydrocyanines displaying this performance in the literature.[317] Moreover, the reduction reaction yields a tertiary amine that could act as a lysosomotropic agent, as mentioned in Section 1.2.2.

Concerning to the expected working mechanism for the system, this can be deduced from the previous-made considerations: the reduction of the iminium group in **1** will result in a tertiary amine, being compound **2** the intended ROS-probe. If this is accumulated within lysosomes after being uptaken by cells, lysosomal ROS would oxidize compound **2** to the initial state **1**. The loss of the iminium group involves a reduction in the π-conjugation of the system and consequently, fluorescence under given excitation conditions for **1** is not expected in compound **2**. Thus, this system could be considered an "off/on" probe for lysosomal ROS.

3.2.2 Theoretical calculations

Prior to the synthesis, theoretical calculations were performed at the CAM-B3LYP/6-31+G(d) level for compound **1**. This calculation method was found to be good enough for other 2P-scaffolds that were previously studied in our research group.[318–320]

Regarding the electronic configurations, the HOMO is entirely located over the 6-methoxynapthalene group, while the LUMO is centered but slightly displaced toward the indolinium ring (**Fig. 34**). This electron density displacement suggests an ICT character in

this dye. Moreover, HOMO and LUMO are mainly implicated in the transition from ground to first excited state (**Fig. 34**). Hence, the electronic configurations of these states can be described through the above-mentioned frontier orbitals, respectively. Deepening more into the data, TD-DFT predicts that absorption will be located around 360 nm. This fact strongly suggests that the system could be studied in 2P-conditions (*i.e.*, when $\lambda_{exc,2P} = 2\lambda_{exc,1P}$) at one of the facilities that we had available.

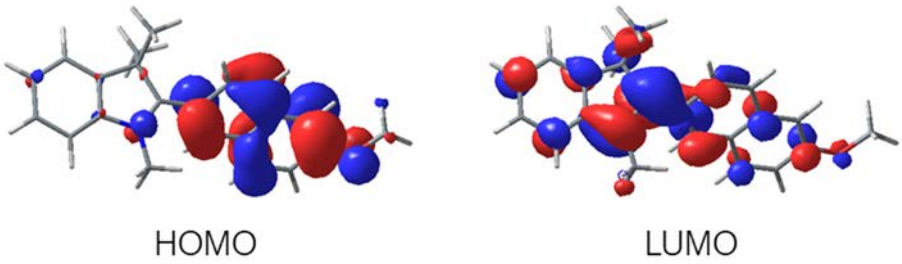

$S_0 \rightarrow S_1$ 3.40 eV (364 nm), $f_{0\rightarrow 1} = 0.5250$
Dominant component : HOMO $\rightarrow$ LUMO (92%)

$S_1 \rightarrow S_0$ 2.90 eV (427 nm), $f_{1\rightarrow 0} = 0.6524$
Dominant component : LUMO $\rightarrow$ HOMO (93%)

Fig. 34. Molecular frontier orbitals involved in the transitions between the ground (S_0) and excited (S_1) states, and representative data selected from the calculations (parameters for absorption ($S_0 \rightarrow S_1$) and emission ($S_1 \rightarrow S_0$) processes). All the calculations refer to compound **1**.

3.2.3 Synthetic approach

Having an orientation about the potential usefulness of the system, the following synthetic scheme (**Fig. 35**) was proposed and performed:

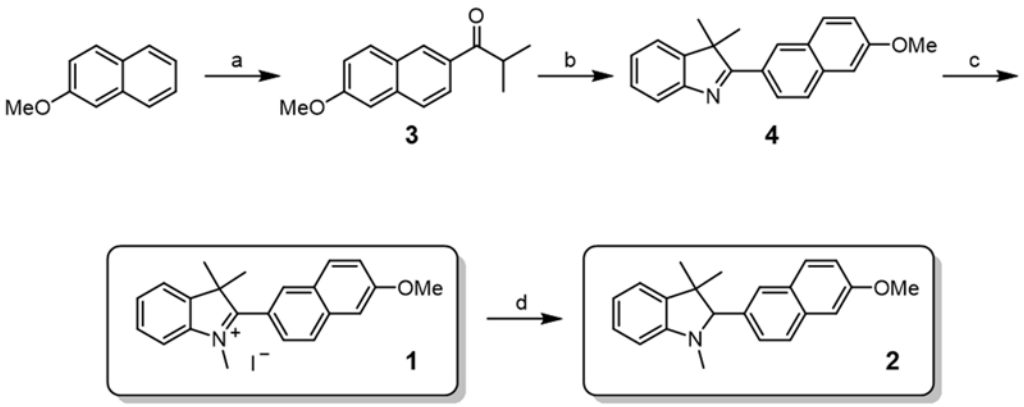

Fig. 35. Synthetic scheme for target compounds **1** and **2**. *Reagents and conditions:* (a) isobutyril chloride, $AlCl_3$, DCM,0 ºC → r.t., overnight; (b) phenylhydrazine hydrochloride, AcOH, reflux, 24h; (c) MeI, ACN, 80ºC, overnight; (d) $NaBH_4$, MeOH.

This sequence starts with a Friedel-Crafts reaction between 6-methoxynapthalene and isobutyril chloride. Ketone **3** is obtained from this reaction and with a yield of 73%. This compound is then subjected to a so-called "interrupted" Fischer-indole reaction[321] with phenylhydrazine. From this reaction, indolenine **4** is obtained in a slightly higher yield (80%). Methylation of the nitrogen of **4** conducts to the desired fluorophore **1**, this occurring quantitatively. Finally, the reduction of the iminium group of **1** is accomplished by reaction with sodium borohydride, and the ROS-sensor candidate **2** is obtained in a 96% yield.

The mechanism of the "interrupted" Fisher-indole synthesis is as distinct from the classical Fisher-indole synthesis, as illustrated in **Fig. 36**. Except for the last step, both processes share a common pathway. These start with the condensation between carbonyl and hydrazine groups. After several acid-base equilibriums take place, the intermediate species undergo a [3,3] sigmatropic rearrangement. The aromaticity is then recovered, and an amino group is formed. As good nucleophile, this moiety attacks to the iminium group and generates the five-member *N*-heterocycle. In the usual way, the proton at 3 (marked in red in **Fig. 36**) and a molecule of ammonia are simultaneously eliminated, giving rise to the double bond at position 2,3 typical of indole ring. The molecule of ammonia is

first released in the "interrupted" variant, and an iminium group at position 1,2 is formed. Finally, its deprotonation yields the *3H*-indole ring, also known as indolenine.

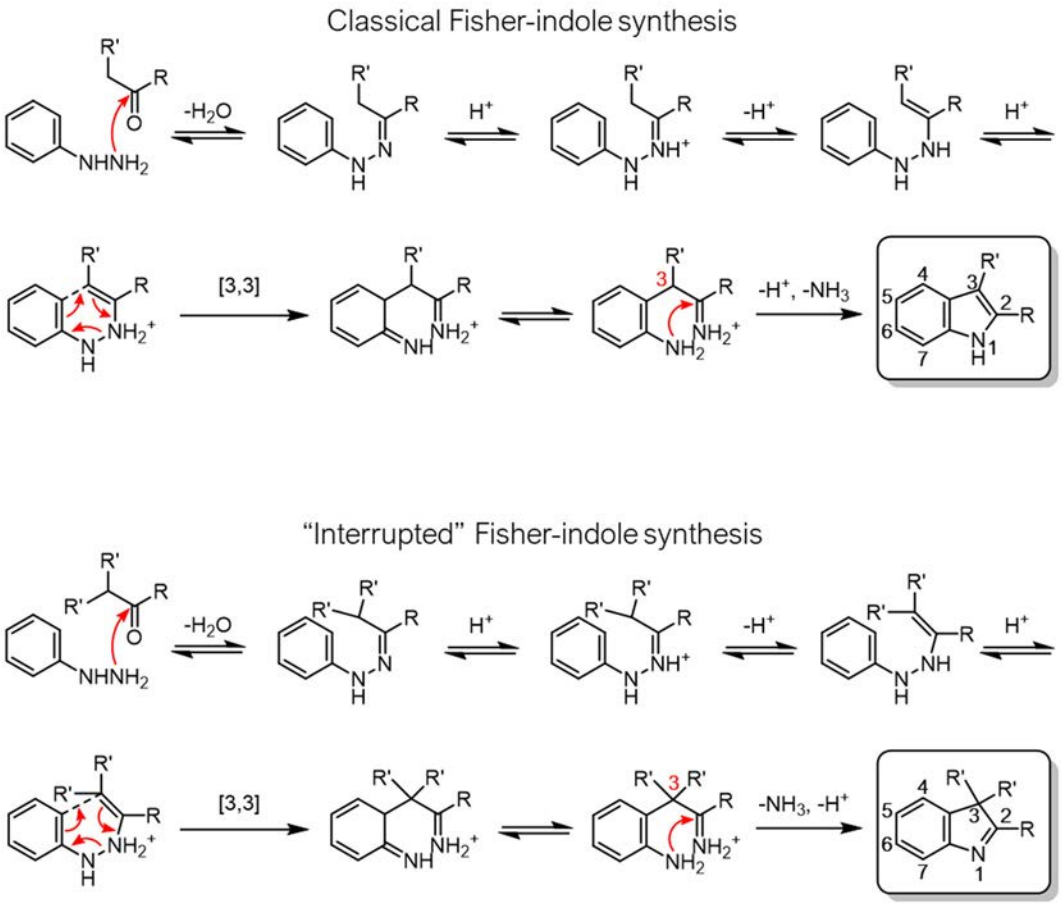

Fig. 36. Mechanisms of classical Fisher-indole synthesis (*top*) and "interrupted" Fisher-indole synthesis (*bottom*).

3.3 PHOTOPHYSICAL STUDIES

3.3.1 Characterization of compound 1

Optical properties under 1P conditions

Absorption and emission spectra were recorded in different solvents for compound **1**., these shown in **Fig. 37**. The relevant photophysical data are summarized in **Table 1**.

Table 1. Photophysical data of compound **1** in diverse solvents (10 μM air-equilibrated solutions).

Solvent	λ_{abs} (nm) [ε ($M^{-1}cm^{-1}$)]	λ_f (nm)	ϕ_f	$\Delta\upsilon$ (cm^{-1}) [$\Delta\lambda$ (nm)]
diethylether	365 [3600]	506	0.00	7634 [141]
chloroform	375 [9100]	510	0.01	7059 [135]
tetrahydrofuran	365 [10000]	521	0.02	8203 [156]
dichloromethane	390 [10400]	510	0.08	6033 [120]
acetone	358 [5600]	522	0.03	8776 [164]
acetonitrile	367 [8000]	517	0.03	7906 [150]
dimethylsulphoxide	355 [6100]	530	0.01	9301 [175]
water	361 [7000]	508	0.01	8016 [147]

Looking at the spectra of **1**, these are characterized for broad and structureless bands typical of push-pull based architectures. Absorption bands display their longest wavelength maxima (associated to $S_0 \rightarrow S_1$ transition) between 355 and 390 nm. On the other hand, the fluorescence maxima are centered at *ca.* 520 nm, within the green spectral region (see **Fig. 37**). Bathochromic shifts are observed as long as the solvent polarity increases in both absorption and emission. These moderate solvatochromic effects might be partially associated with the expected ICT character for the dye.

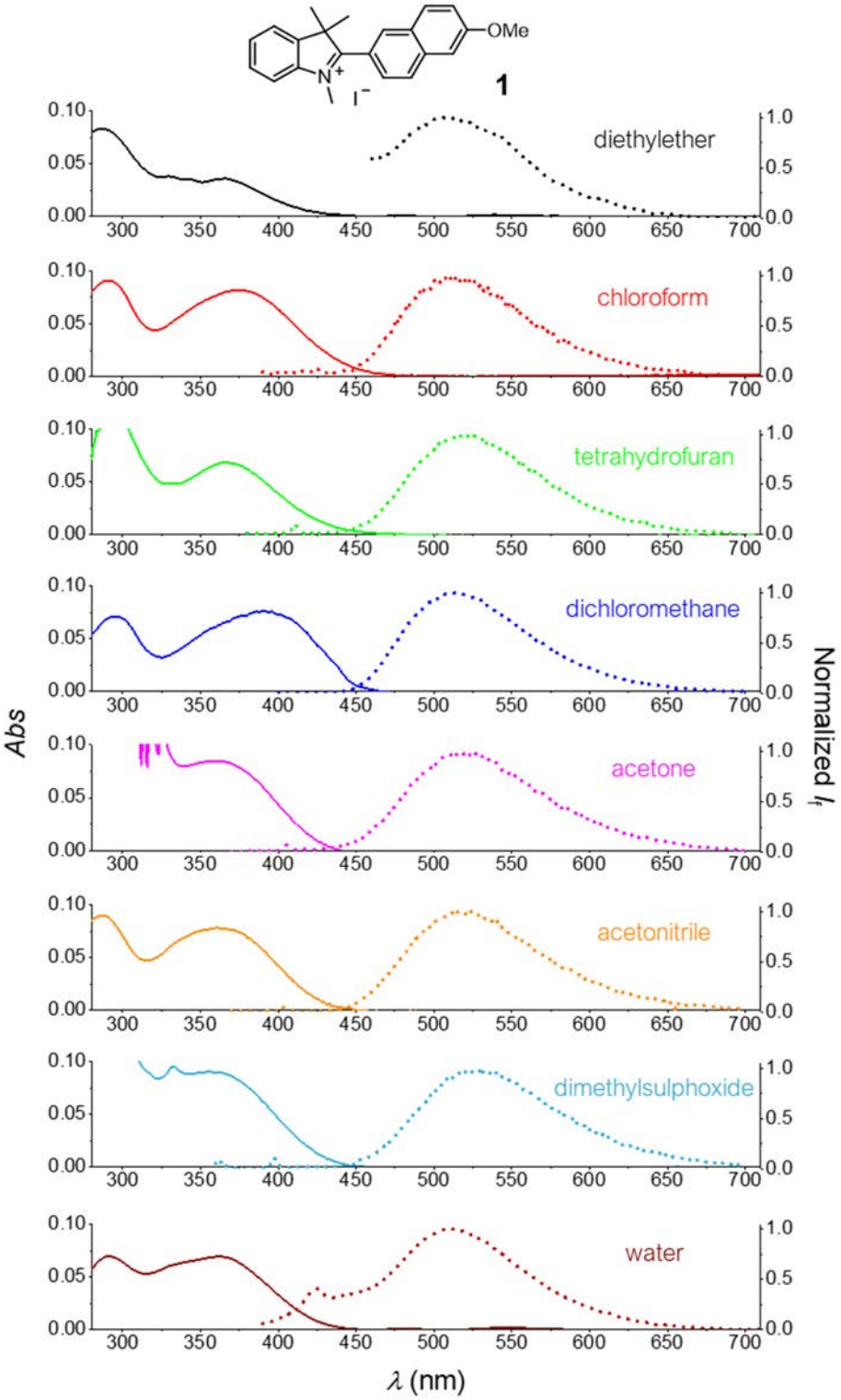

Fig. 37. Absorption (solid lines) and emission (dotted lines) spectra of compound 1 in different solvents indicated for each case (optically diluted air-equilibrated solutions).

The most intriguing optical feature of **1** is its Stokes shift ($\Delta\upsilon$), that regardless of the considered solvent is above 6000 cm^{-1}. In other terms, the separation among absorption and emission maxima ($\Delta\lambda$) is at least of 120 nm, suggesting potential application in biological contexts. Contrastingly, the fluorescence quantum yields are low to moderate (from *ca.* 0.01 to 0.08). This fact could be anticipated, since large Stokes shifts are associated with the occurrence of multiple non-radiative pathways. Furthermore, this compound has good photostability (its emission remained practically constant after continuous irradiation at $\lambda_{exc,1P}$ = 370 nm for 1 h).

Comparing the experimental data with those obtained in the theoretical calculations (**Section 3.2.2**), it is found that absorption energies can accurately be predicted for this type of molecules. On contrary, the calculation is not as precise for the emission ones. This calculation methodology is therefore mostly suitable for estimating the $S_0 \rightarrow S_1$ transition, which is useful to obtain a faithful orientation about whether the 2PA properties of the molecules could be or not studied according to the instrumental characteristics of the facilities.

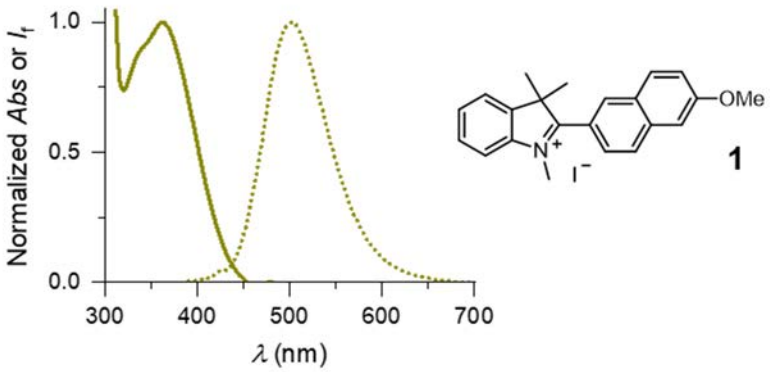

Fig. 38. Absorption (solid line) and emission (dotted line) spectra of **1** in aqueous 1% DMSO/glycine-HCl buffer (*pH* 2.4, 10 μM air-equilibrated solution).

As mentioned in **Chapter 1**, the innate properties of the compounds are important but also the situation where they are immersed.[97] Considering that this compound has been intended to work within lysosomes, their most significant characteristics were reproduced *in vitro*: high acid content (*pH* usually ranges between 4.5 – 5.0),[297] and large viscosity

(these organelles are considered the most viscous of all subcellular compartments).[322] To build the acidic environment, an aqueous glycine/hydrochloric acid buffer (pH 2.4) was employed as solvent, and the photophysical properties of **1** were examined. More importantly, no significant differences are observed between the features of the compound in this solvent and those determined in aqueous solution. This behavior is illustrated in **Fig. 38**, where the absorption and emission bands of **1** in acid solution are shown, which are seemingly identical to those obtained in aqueous solution (*cf.* **Fig. 37**).

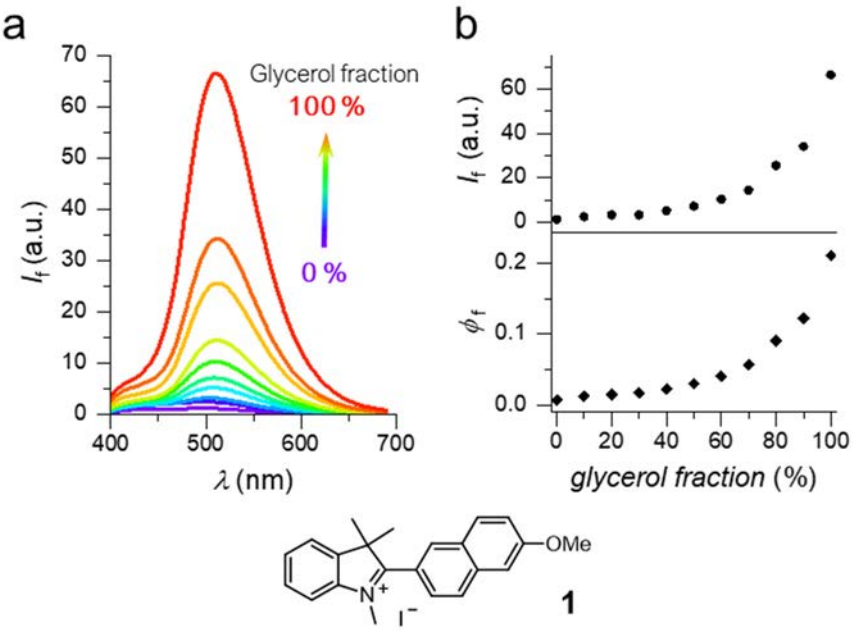

Fig. 39. (a) Emission spectra of **1** in different glycerol/water mixtures. These spectra were recorded upon excitation at 370 nm (10 μM air-equilibrated solution, 1% DMSO). (b) Changes in the emission maximum intensity and fluorescence quantum yield of **1** when increasing the viscosity of the medium.

In contrast with *pH* studies, the viscosity of the medium affects in a great extent to the photophysical properties of **1**. To that end, diverse water/glycerol mixtures were employed as solvent (**Fig. 39**). Since the two rings that compose the structure can rotate around the single bond that connect them, an increase in the emission intensity could be anticipated as long as the rotation is hindered by setting a more viscous medium. This is precisely observed when increasing the glycerol content in the medium (**Fig. 39**). It is noteworthy that the restriction of the movements does not only involves an increment in the

fluorescence intensity. Additionally, a 30-fold increase in the fluorescence quantum yield is determined, hence confirming that molecular motions are hampered by the high viscosity. Concerning the spectral position of the absorption and emission bands, these are only slightly affected, and the displacements are no significative.

2PA properties

The 2PA cross section (σ_{2PA}) of compound **1** was determined in acetonitrile solution by 2PEF method,[68] and is indicated in **Fig. 40**. The biphotonic nature of the electronic transitions under the given experimental conditions was confirmed through the dependence of the two-photon excited fluorescence on the laser power. The trend line's slope, quite close to the value of 2.0, corroborates the 2PA occurrence (inset of **Fig. 40**). This compound displays good σ_{2PA} values, addressing 25 GM when $\lambda_{exc,2P}$ = 740 nm.

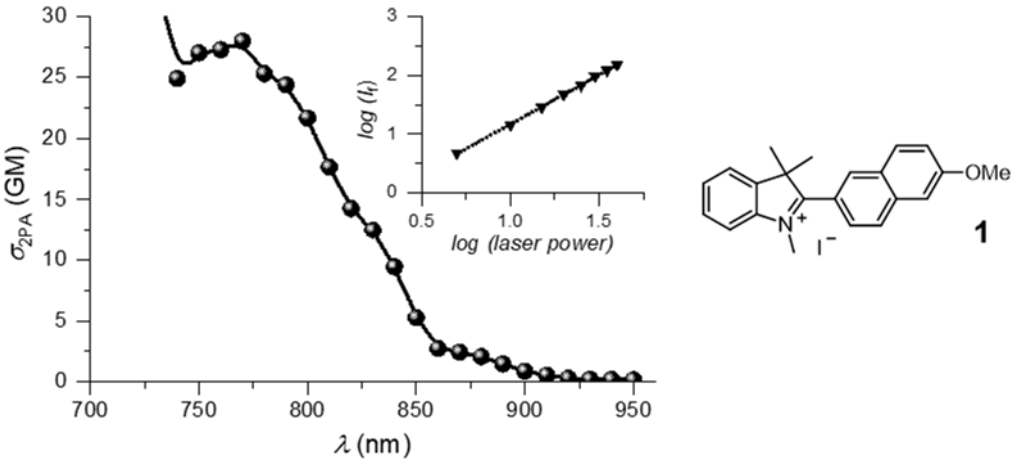

Fig. 40. 2PA cross section (σ_{2PA}) of compound **1** in acetonitrile (10 μM air-equilibrated solution). The inset shows the dependence of the fluorescence emission intensity on the excitation source intensity ($\lambda_{exc,2P}$ = 740 nm, slope: 1.7, R^2 = 0.9995).

The emission spectra are comparable regardless of the number of photons implied in the excitation process (**Fig. 41**). Moreover, the excitation wavelengths are essentially coincident, *i.e.*, $\lambda_{exc,2P} = 2\lambda_{exc,1P}$. It can thus be concluded that: a) the same excited electronic

state participates in both processes, and b) the first excited state participates in the electronic transitions that have been observed.

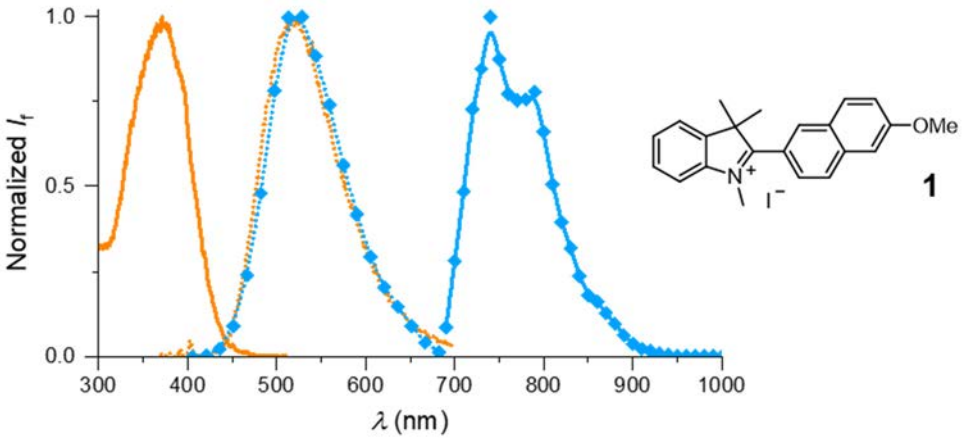

Fig. 41. Normalized excitation (solid lines) and emission (dotted lines) spectra of **1** in acetonitrile (10 μM air-equilibrated solution) under 1P (orange lines) and 2P (blue lines) conditions.

In consonance with the studies in 1P excitation conditions, the effect of a more restricted medium on the 2PA properties of **1** was evaluated. Accordingly, the σ_{2PA} of this dye was measured in different glycerol/water mixtures (**Fig. 42**). These measurements were also performed using water as unique solvent, but in these conditions the σ_{2PA} of **1** was too low and the data cannot be treated with enough confidence.

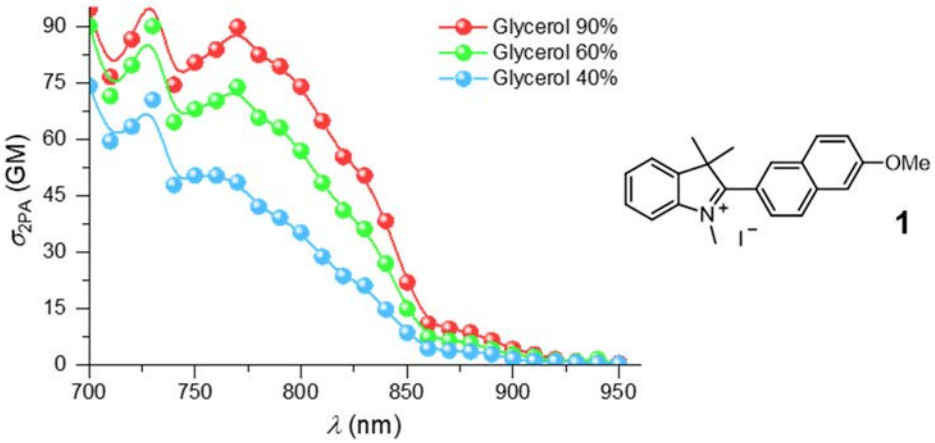

Fig. 42. 2PA cross section (σ_{2PA}) of compound **1** in diverse glycerol/water mixtures (10 μM air-equilibrated solution, 1% DMSO).

The increase of the viscosity clearly yields an enhancement of σ_{2PA} as well as it occurred with the fluorescence quantum yield. That is, the properties of **1** are tightly dependent on the restriction of the movements. Indeed, in the glycerol/water 9:1 solution, the σ_{2PA} value at $\lambda_{exc,2P}$ = 740 nm is of 75 GM, three times longer that the obtained in acetonitrile solution.

3.3.2 Characterization of compound 2

Optical properties under 1P conditions

The reduction of the iminium group to a tertiary amine entails unambiguously a considerable change in the optical properties of the fluorophore. Indeed, the π-conjugated system is dramatically altered and the ICT character of the dye is lost in compound **2**. The absorption spectrum of this dye clearly shows this issue (**Fig. 43 a**), where the band centered at 370 nm disappears. The changes in the structure also affect the emissive properties, and no fluorescence upon excitation at 370 nm is observed in a solution containing **2** (**Fig. 43 b**).

2PA properties

Owing that the longest wavelength absorption band of indolinium **1** is missed in **2**, it can be anticipated that this last is not going to be fluorescence-active under 2P-excitation at 740 nm. Furthermore, the 1P absorption of **2** is limited to the region below 350 nm, which excludes the possibility of exciting at other wavelengths in the range between 700 and 740 nm. Only compound **1** presents 2PA properties in the working range, and consequently, 2P-excited fluorescence (**Fig. 43 c**).

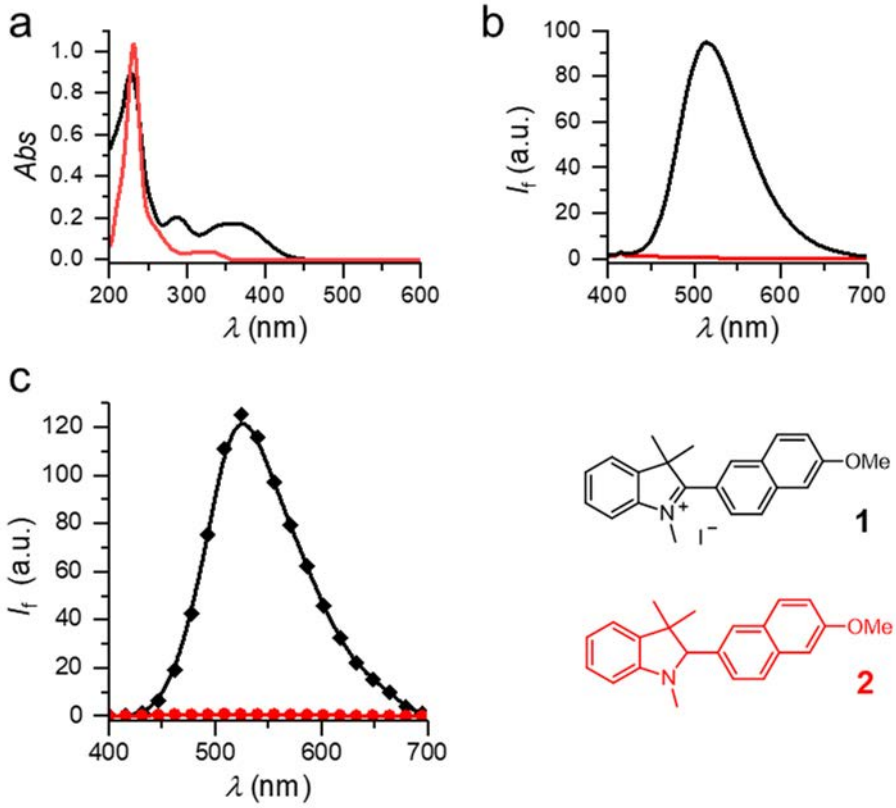

Fig. 43. (a) Absorption and (b) emission spectra of compounds **1** (black lines) and **2** (red lines) in acetonitrile (10 μM air-equilibrated solutions). Emission spectra were recorded upon excitation at $\lambda_{exc,1P}$ = 370 nm. (c) Emission spectra of compounds **2** (black line) and **1** (red line) in acetonitrile (10 μM air-equilibrated solutions) upon excitation at $\lambda_{exc,2P}$ = 740 nm

3.4 OXIDATION MECHANISM OF COMPOUND 2

Once examined the photophysical properties of compounds **1** and **2**, it was studied if the iminium group could be recovered by some reaction starting from **2**. In this case, this system effectively would be settled as an "off/on" probe.

3.4.1 Selectivity and sensitivity toward hydroxyl radical

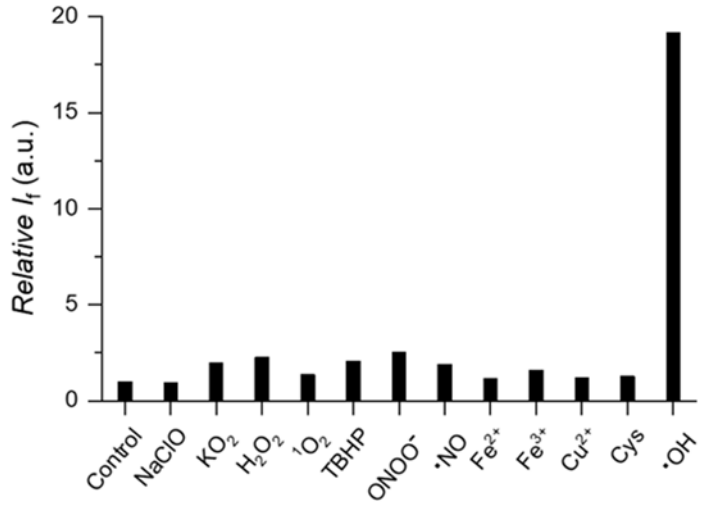

Fig. 44. Relative fluorescence response of **2** (10 μM in 1.0% DMSO/glycine-HCl buffer, *pH* = 2.4) to various oxidants ($\lambda_{exc,1P}$ = 370 nm, λ_{em} = 502 nm, oxidant concentrations: 50 μM. More details about the preparation of the oxidants are in **Chapter 8**).

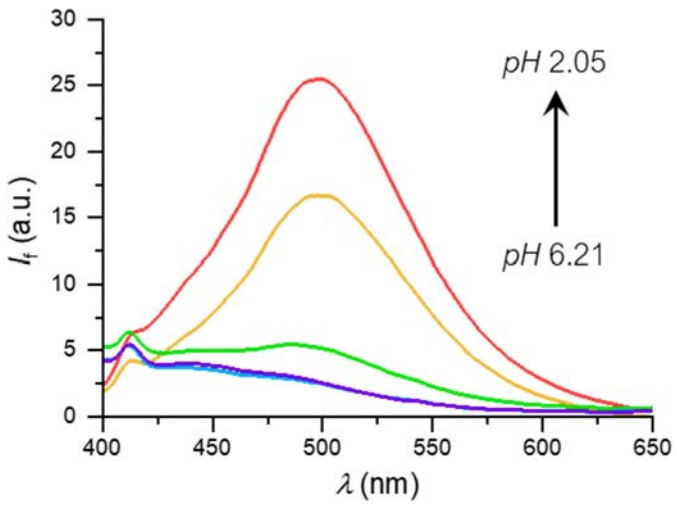

Fig. 45. Fluorescence response of **2** (10 μM in 1% DMSO in water with adjusted *pH*, $\lambda_{exc,1P}$ = 370 nm, λ_{em} = 502 nm) to hydroxyl radical (50 μM) at different pH values. Only at low pHs did hydroxyl radical-mediated oxidation yield compound **1** and increase fluorescence emissions.

First, the spectroscopic responses and selectivity of **2** ("off") toward different chemical species that could give rise to **1** ("on") were studied. The selection of these species includes a wide variety of ROS, RNS and some biologically relevant species. These studies were carried out under acid conditions, to simulate in part the lysosomal environment. As represented in (**Fig. 44**), compound **2** displays a high selectivity for hydroxyl radical *vs.* the other examined species. A significant enhancement of the relative fluorescence intensity upon excitation at 370 nm, of 20-fold, is only observed when employing this powerful oxidant agent. Moreover, this change is exclusive to acid environments (**Fig. 45**). The complete selectivity studies were repeated at different *pH* conditions, but the fluorescence response was only observed when combining the two mentioned ingredients: hydroxyl radical and low *pH*.

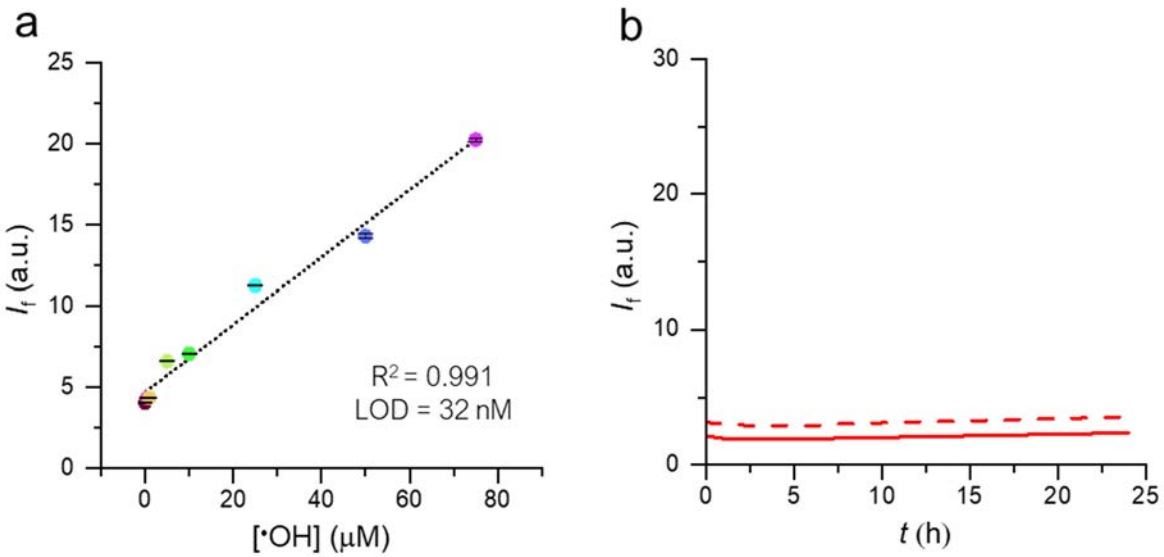

Fig. 46. (a) Fluorescence intensity of **2** in response to varying concentrations of •OH, (10 μM solution of **2** in 1% DMSO/glycine-HCl buffer, *pH* = 2.4; •OH obtained from a 1.5 mM solution in H_2O_2 and Fe^{2+}; $\lambda_{exc,1P}$ = 370 nm, λ_{em} = 502 nm). (b) Oxidation study of compound **2** (10 μM in 1% DMSO/glycine-HCl buffer (*pH* = 2.4) (dashed line, $\lambda_{exc,1P}$ = 370 nm, λ_{em} = 502 nm) and 10 μM in acetonitrile (solid line, $\lambda_{exc,1P}$ = 370 nm, λ_{em} = 520).

Next, the response of **2** to different amounts of hydroxyl radical was examined and fluorescence intensity was determined linear for •OH concentrations from 0.5 to 75 μM (**Fig. 46 a**). Oxidation of compound **2** is not only highly selective, but also displays outstanding sensitivity to the presence of hydroxyl radical at the nanomolar level. The limit of detection (LOD) of hydroxyl radical for **2** was determined in 32 nM, this calculated as 3.3 times the standard deviation of the blank measurements divided by the slope of the fitting curve. The stability of **2** to auto-oxidation was also evaluated by placing a solution of the probe in diverse solutions at room temperature and taking fluorescence measurements over time. As represented in **Fig. 46 b**, thermal oxidation of **2** is almost negligible.

3.4.2 Monitoring the Fenton's reaction by NMR

The oxidation of **2** with •OH was monitored also by ^{1}H-NMR, treating the probe with an equimolar concentration of Fenton's reagent and trifluoroacetic (TFA). Looking at the crude's spectra, the signals corresponding to **1** are clearly appreciable in both aromatic and aliphatic regions, where also those corresponding to **2** are barely present (see **Fig. 47 a** and **b**, respectively).

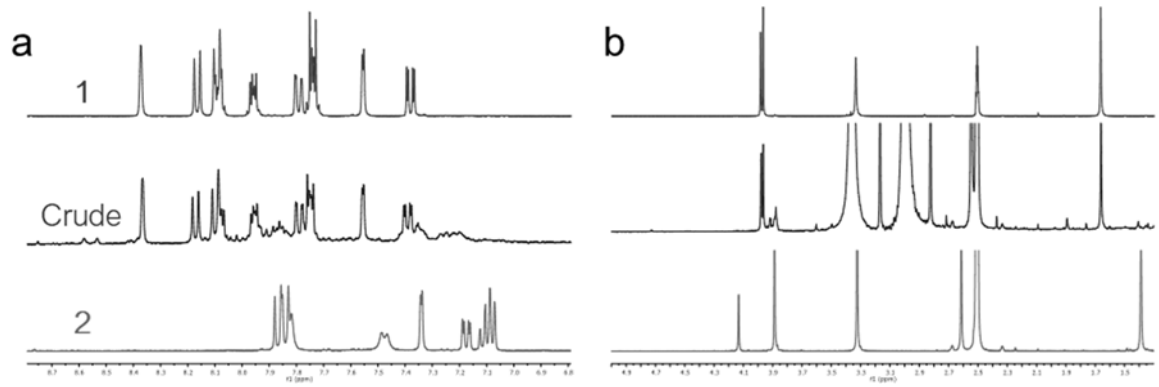

Fig. 47. Reaction of **2** and Fenton's reagent. Zoom-ins of the ^{1}H-NMR spectra of **1**, the crude reaction, and **2** in the (a) aromatic region (δ 8.8 – 6.8) and (b) aliphatic region (δ 5.0 – 1.3). All spectra were performed in DMSO-d_6.

To exclude other possible reactions, control experiments were conducted with Fe^{2+}, Fe^{3+} and H_2O_2 in acid conditions, and likewise followed by ^{1}H-NMR. The individual addition of these species did not address any change to the spectrum of **2**. Only when encountered with hydroxyl radicals, the spectrum changes toward that of **1**, corroborating thus the recovery of the initial chromophore structure after the oxidation process (**Fig. 48**).

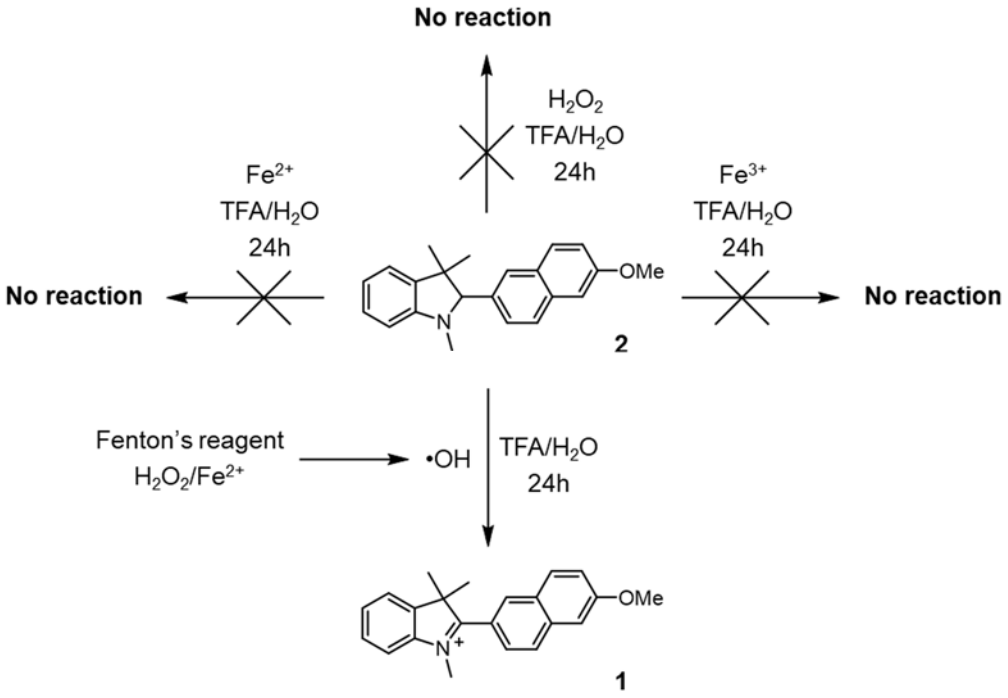

Fig. 48. Proposed oxidation mechanism of **2** to yield fluorophore **1**.

3.5 IN VIVO IMAGING

To explore the photophysical properties of **1** and the behavior of **2** as a potential ROS probe in living cells, mouse embryonic fibroblasts (MEFs) were used**.** MEF is a type of fibroblast isolated from mouse embryo. This cell line is limited, *i.e.*, cells senesce and dye after several transmissions. In other words, this cell line is a non-immortalized one. The studies below were performed in collaboration with the group of Prof. Dr. Jose Maria Perez-Pomares. Details concerning to the cell culture and the diverse treatments are in **Chapter 8**.

3.5.1 Cytotoxicity studies

Prior to the imaging experiments, cell viability in the presence of the potential ROS-sensor **2** was examined through a WST-1 assay. This colorimetric test consists in using a water-soluble tetrazolium salt. This compound is accumulated within the plasma membrane, where NADPH is responsible of its reduction if the cell maintain an optimal activity.[323] Thereby, the absorption band changes and cell viability is extrapolated from measuring the absorbance at 440 nm and referring these data to control experiments For compound **2**, significant cytotoxicity (*i.e.*, low cell viability) was observed only at concentrations of this probe over 0.1 μM (**Fig. 49**). Considering these results, the concentration employed in the below detailed bioimaging experiments was of 0.025 μM.

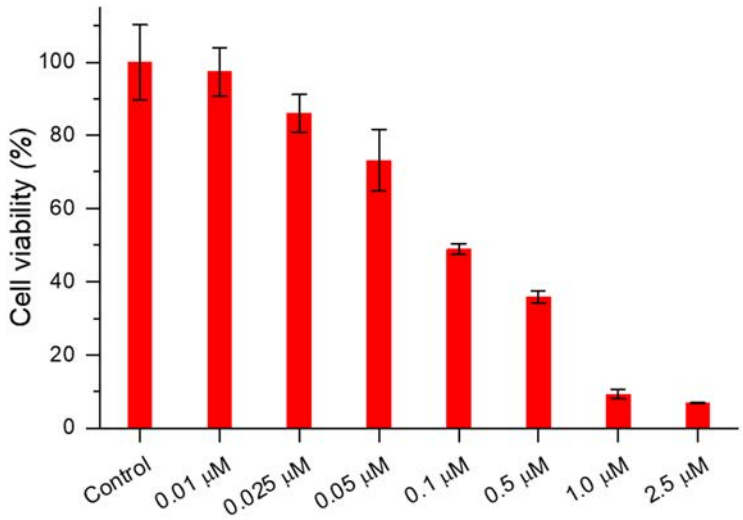

Fig. 49. Cytotoxicity of **2** on mouse embryonic fibroblast (MEF) cells. Data are expressed as mean values and standard error of the mean from three independent experiments (n=3).

3.5.2 Fluorescence imaging of compounds 1 and 2

Initially, compound **1** ("on" form) was applied to the cells to examine the behavior of fluorophore within cells. Fluorescence was recorded with appropriate excitation and emission settings, according to the photophysical properties of this compound ($\lambda_{exc,2P}$ = 740 nm, λ_{em} = 500-550 nm) (**Fig. 50**). Living MEFs treated with **1** display strong green

fluorescence spread along the cytoplasm, as observed in **Fig. 50 A1**. The overlap of the fluorescence image with the brightfield (**Fig. 50 A2**) indicates that compound was accumulated within cells, as no fluorescence is observed in areas outside the cells.

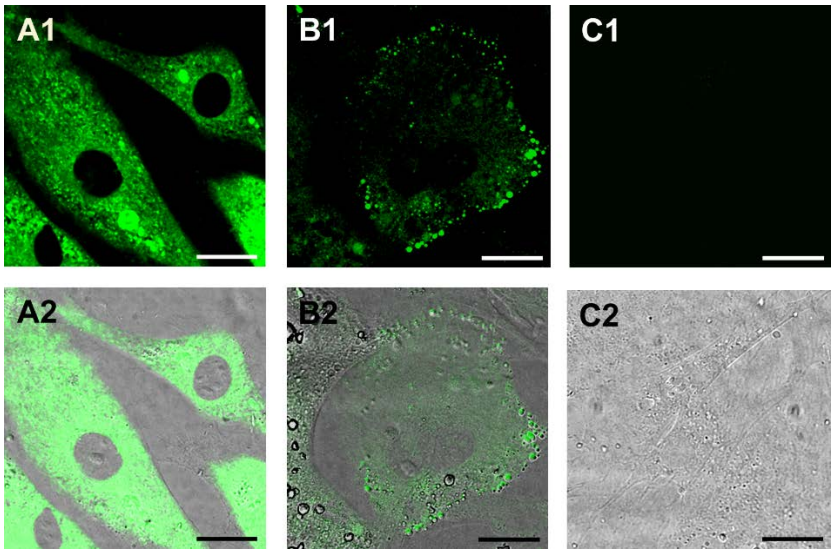

Fig. 50. MEF cells incubated for 24 h with 0.025 μM **1** (A1 and A2), 0.025 μM **2** (B1 and B2), and without any treatment (C1 and C2). Sample A was visualized with less laser power to compensate for the higher concentration of **1** inside the cells. Fluorescence was recorded between 500 and 550 nm upon $\lambda_{exc,2P}$ = 740 nm. Scale bars: 25 μm.

On the other hand, **2**-treated MEFs display fluorescence only in discrete punctuated cytoplasmic regions, seemingly lysosomes (**Fig. 50 B1 and B2**). Control cultures (without any compound-treatment, **Fig. 50 C1 and C2**) did not show significant fluorescence. In all cases, the recorded fluorescence was cytoplasmic rather than nuclear.

A more exhaustive analysis was performed to know how the fluorescence increases with time after treating cells with compound **2** (**Fig. 51**). At determined times, images registered during the timelapse experiment show a progressive increase of the fluorescence, which maintains in all cases its subcellular distribution (**Fig. 51 A-F**). An appropriate treatment of the data from these images confirms the increasing trend of the fluorescence with time

(**Fig. 51 G**, see **Chapter 8** for details about the calculation of the average spot fluorescence per cell from the images).

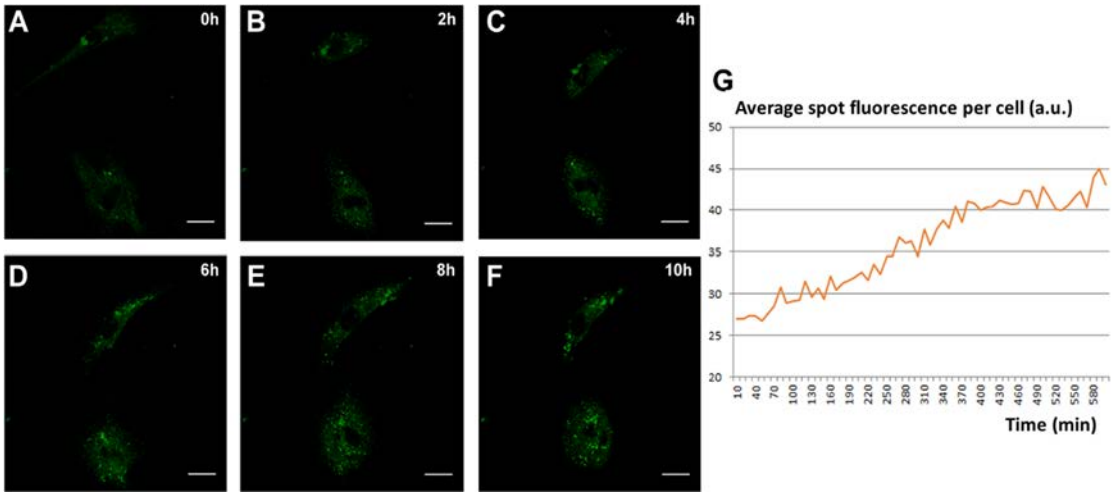

Fig. 51. Timelapse evaluation of 2 oxidation in living cells. Fluorescence emission was evaluated at 0h (A), 2h (B), 4h (C), 6h (D), 8h (E) and 10h (F) after treating the cells with 54. Average spot fluorescence per cell over time is also shown (G). Scale bar: 5 μm.

Colocalization experiments

Considering the characteristic and peculiar distribution of the "on" form within the cells after this being produced from compound **2**, two different specific and commercial fluorescent probes were employed to counterstain mitochondria (Mitotracker Red CMXRos, MTR) and lysosomes (Lysotracker Deep Red, LTDR).

After treating MEFs with **2** for 24 h, cultures counterstained with MTR probe did not display overlapping fluorescence (**Fig. 52 A**). For a better visualization, the area selected was magnified and the emission channels were separated (**Fig. 52 a1** and **a2**). The fluorescence registered from compound **1** generated *in situ* from **2** is shown in green in **Fig. 52 a1**, and the one from MTR is in red in **Fig. 52 a2**. The merge between these two channels is shown in **Fig. 52 a3**, where no orange points (resulting from the combination of green and red signals) are appreciated. Therefore, it seems that oxidation of compound **2** is not taking

place in a mitochondrial environment, since there is no colocalization between the emissive signals described.

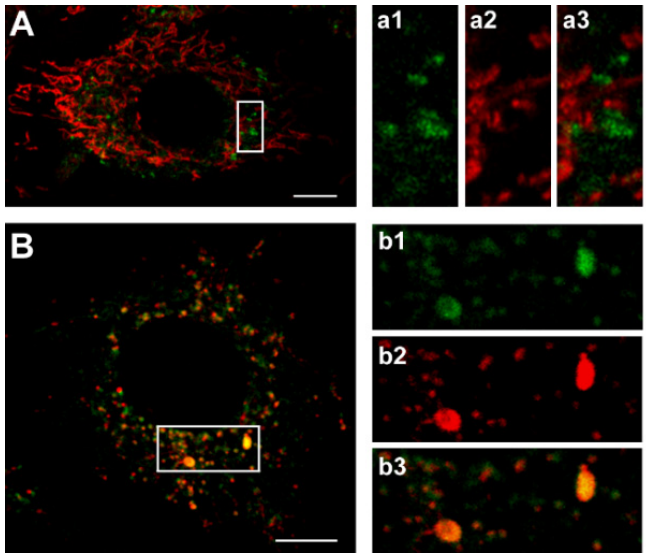

Fig. 52. MEF treated with 0.025 μM **2** (A–C, green, $\lambda_{exc,2P}$ = 740 nm, λ_{em} = 500-550 nm). Mitochondrial (A, MTR, red, $\lambda_{exc,\,1P}$ = 561 nm, λ_{em} = 600 - 640 nm) and lysosomal (B, LTDR, red, $\lambda_{exc,\,1P}$ = 633 nm, λ_{em} = 645 - 740 nm) counterstains were performed. Selected areas in A and B are magnified in a1-3 and b1-3, respectively.

Conversely, LTDR-counterstained cells display appreciable colocalization of the two emission signals, as illustrated in **Fig. 52 B** and more clearly in **Fig. 52 b1-b3**. Akin distribution is observed for both produced **1** and LTDR, shown in green and red in **Fig. 52 b1** and **b2** respectively. The overlap between these two signals, *i.e.*, the colocalization between **1** formed from **2** and LTDR is more evident in **Fig. 52 b3**. Practically all the discrete points are orange in this image.

As lysosomes are particularly mobile in MEFs, cells were also incubated with **2**, then treated with LTDR and finally fixed with 4% paraformaldehyde. The later analysis of the fixed cell images yielded a Pearson correlation coefficient (PCC, details about the calculations are in **Chapter 8**) between 0.83 (whole cell image, **Fig. 53 A** and **B**) and 0.87 (crop region, **Fig. 53 a-c**) (**Fig. 53**). Thus, it can be confirmed that these cytoplasmic vesicle regions are lysosomes.

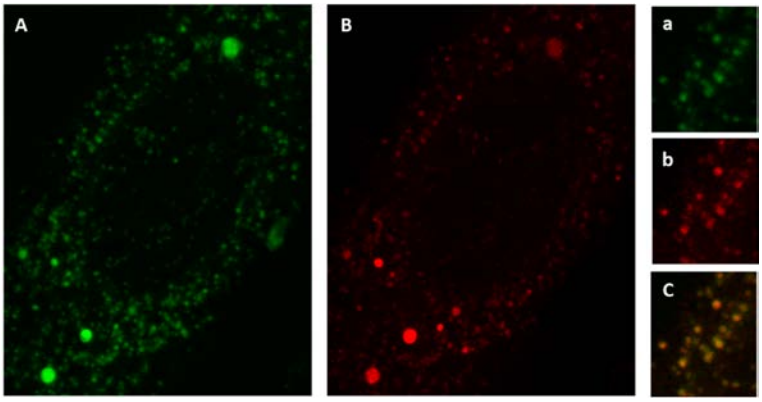

Fig. 53. Analysis in fixed cells of compound **2** with LTDR. Pearson Correlation Coefficient (PCC) values were obtained for **2** fluorescent signal (A, $\lambda_{exc,2P}$ = 740 nm, λ_{em} = 500-550 nm) *versus* LTDR (B, $\lambda_{exc,\ 1P}$ = 633 nm, λ_{em} = 645 - 740 nm) related fluorescence. Crop region of fluorescent signal of (a) **2** and (b) lysotracker and (c) combined images (a) and (b).

3.5.3 Monitoring induced oxidative stress

To prove that increased ROS is capable of promoting the oxidation of **2** to the fluorescent form **1**, MEFs were treated with **2** and then oxidative stress was induced in different vias.

The first agent for provoking this situation was ultraviolet (UV) light irradiation, which is a well-documented ROS generating agent.[324] This treatment results in a vast increment in fluorescence intensity, which can be noted when comparing **Fig. 54 A2** and **A3** (non-UV treated and post-UV treatment, respectively). This enhancement of the fluorescence signal is besides observed exclusively in living cells, *i.e.*, no significant increase of the fluorescence was found in fixed MEFs after UV irradiation (Fig. **54 B2** *vs.* **Fig. 54 B3**). Thus, upon UV exposure and resulting from a biological response to induced cell damage, •OH is generated and reacts with **2** ("off") yielding the **1** ("on") form.

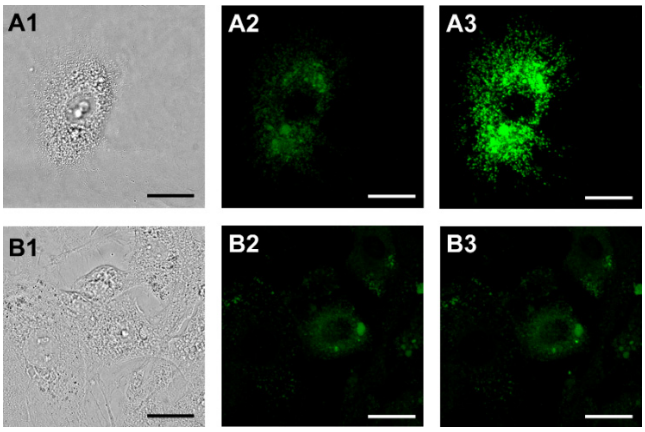

Fig. 54. Detection of endogenous ROS generation upon UV irradiation. MEF cells incubated for 24 h with 0.025 μM **2** before (A1, A2, B1, B2) and after UV irradiation (A3, B3). Cultures shown in B2 and B3 were fixed in 4% PFA. Fluorescence was recorded between 500 and 550 nm upon $\lambda_{exc,2P}$ = 740 nm. Scale bars: 25 μm.

Similar results, although not as gratifying as the previous, were obtained by treatment with other ROS-generating agents such as *tert*-Butyl hydroperoxide (TBHP), or 2-methoxyestradiol (**Fig. 55**). TBHP promotes oxidative stress by means of producing free radicals in the presence of cellular Fe^{2+}.[325] On the other hand, 2-methoxyestradiol is a superoxide dismutase (SOD) inhibitor which induces the •OH generation.

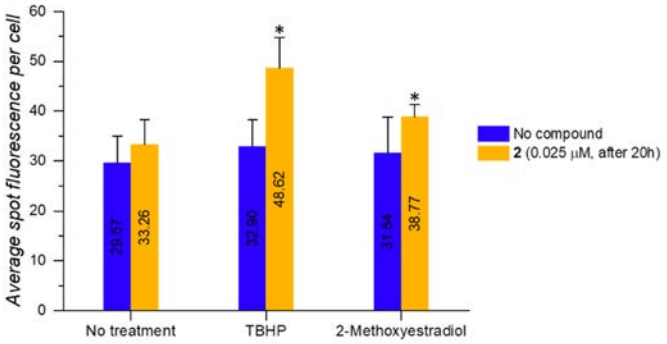

Fig. 55. ROS-inducing agents increase **2** oxidation increasing fluorescence in cultured living cells. Cells treated (with **2**/TBHP or **2**/2-Methoxyestradiol) significantly increase their fluorescence emission as compared to untreated cells as shown (Student's t-test; data represent mean ± SEM; *p<0.01, three independent experiments (n=3)). Measurement of mean spot fluorescence per cell are indicated for each case.

3.6 SUMMARY

A lysosome-targeting activatable probe, **2**, based on a small non-fluorescent naphthalene-indolenine molecule, has been developed. The oxidation of this probe within living cells lysosomes gives rise to the fluorescent state **1**, acting this system as an "off/on" fluorescent probe for hydroxyl radical detection in acid environments. This system demonstrates high sensitivity and selectivity for tracing •OH formation within living cells. The utility of **2** for detecting endogenous production of this specie as well as its generation by other agents affecting cellular oxidative stress in 2P microscopy has been demonstrated. This application is possible thanks to the good optical properties of **1**, which are besides enhanced in lysosome-like conditions. Hence, this system represents a powerful tool for a better comprehension about the role of •OH in biological processes.

Part of the results presented in this Chapter have been published in reference [326].

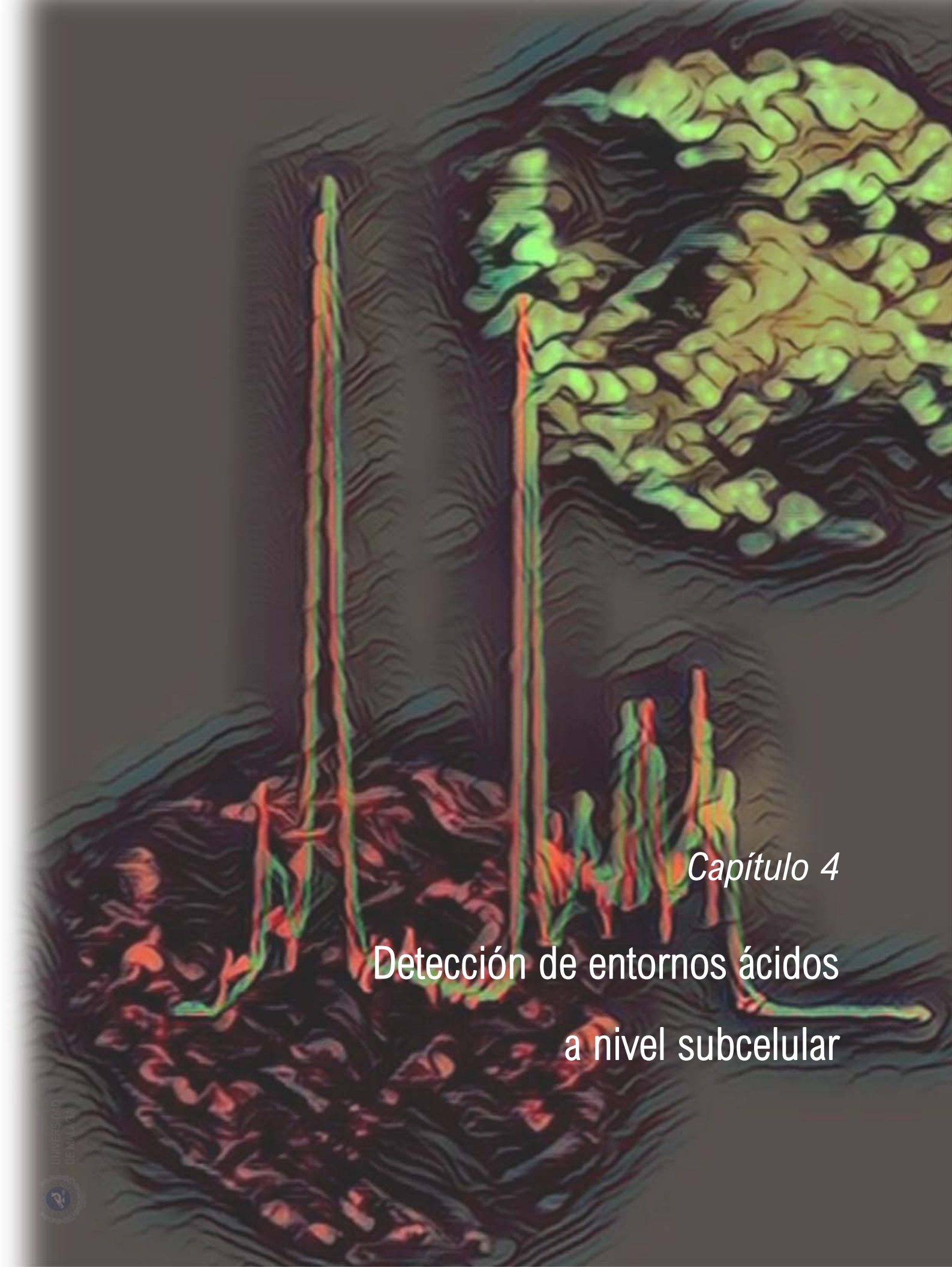

Capítulo 4

Detección de entornos ácidos a nivel subcelular

4.1 INTRODUCCIÓN

4.1.1 El papel y la importancia del *pH* en el organismo

El *pH* intracelular (pH_i) es un parámetro esencial en multitud de procesos biológicos, como son, entre otros, la proliferación celular,[327] la apoptosis,[328] la actividad enzimática,[329] la contracción muscular[330] o el transporte de iones.[331] El control del pH_i no solo es crucial para estas funciones, sino que la actividad de ciertos orgánulos subcelulares está altamente condicionada por la regulación de su *pH* local. Los valores óptimos de *pH* en los distintos entornos subcelulares[332] se encuentran indicados en la **Fig. 56**, donde se puede observar cómo los lisosomas son los orgánulos que poseen un valor de *pH* más bajo, normalmente entre 4.5 y 5.0 (en la figura se indica un valor medio).[297] Este valor de *pH* en lisosomas es fundamental para mantener el control de la homeostasis a nivel celular.

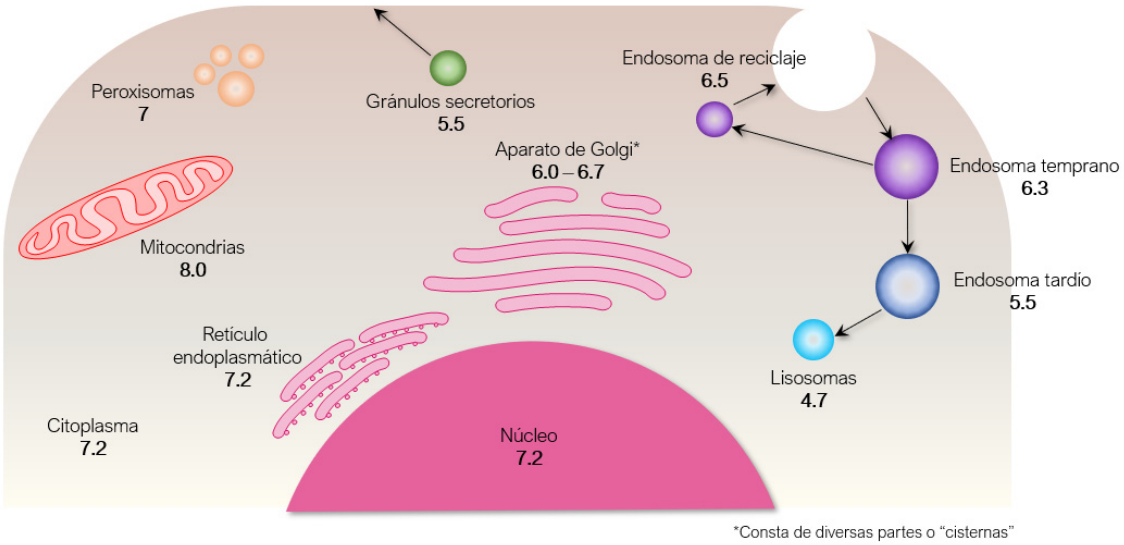

Fig. 56. Valores de pH en los diferentes compartimentos subcelulares.

Todo alejamiento de estos valores óptimos de *pH* implica una alteración severa en su correcto funcionamiento, afectando tanto al organismo como a las actividades subcelulares. De hecho, diversas enfermedades como el Alzheimer,[333] la fibrosis

quística,[334] el cáncer[335] o los desórdenes derivados del almacenamiento lisosomal[336] están relacionados con valores inusualmente bajos de *pH*. Por esta razón, el estudio de estos cambios de *pH* en el organismo puede proporcionar información de gran utilidad que ayude a comprender los desórdenes fisiológicos y procesos patológicos a los que están asociados.

La microscopía de fluorescencia es el método más empleado para observar y estudiar cambios en el pH_i y en orgánulos subcelulares. Esta técnica ha complementado y/o desbancado a métodos más tradicionales, como pudieran ser la resonancia magnética nuclear (RMN)[337] o los microelectrodos.[338] Las razones que motivan este hecho se pueden resumir en su simplicidad operacional, alta sensibilidad, alta resolución temporal y el carácter no invasivo que conlleva el empleo de la fluorescencia como medio de detección. Estas ventajas se incrementan si en el proceso de excitación se emplean dos fotones (2P) en lugar de uno solo (1P). De este modo, la microscopía de dos fotones (2PM), que conlleva el uso de longitudes de onda de excitación enmarcadas dentro de la primera ventana biológica (700-1000 nm),[207] incorpora a las ya mencionadas ventajas una menor dispersión de luz en muestras biológicas, una fototoxicidad más baja y una reducción de la autofluorescencia procedente de las estructuras biológicas.

4.1.2 Sensores de *pH* para 2PM descritos en la literatura

Debido al potencial de la microscopía de fluorescencia, se han desarrollado una variedad amplia de sensores de *pH* con aplicación en bioimagen, siendo los más frecuentes los diseñados para trabajar en condiciones de excitación de 1P.[339–341] No obstante, el auge que ha experimentado la 2PM en los últimos años ha hecho que se hayan desarrollado en paralelo nuevos sensores con propiedades de 2PA.[209,340,342–355]

Una posible clasificación de estos compuestos podría realizarse en función a la unidad sensible al *pH* dentro de la estructura molecular. Atendiendo a este criterio, encontramos que los más numerosos son los que disponen de un átomo de nitrógeno como centro básico [342,344,345,347,349,350,353–355], lo que implica en la mayoría de los casos que la sonda de *pH* sea del tipo "*on/off*". Por otro lado, cabe destacar a los derivados de 7-hidroxicumarina,

los cuales sustituyen el nitrógeno por oxígeno como centro de respuesta al *pH*.[343,347,351] Otros criterios o parámetros, como el rango de *pH* en el cual tienen capacidad de detección o la aplicación concreta, podrían ser empleados para agrupar estos compuestos.

En la **Tabla 2**, se presentan los compuestos para detección de cambios de *pH* en 2PM más similares en cuanto a características fotofísicas y ácido-base a los derivados que se plantean en este Capítulo, indicándose algunas de sus propiedades más relevantes.

El primero de ellos combina en su estructura una cumarina y un benzimidazol, dando lugar a una sonda *"off/on"* para el cambio de medio ácido a neutro y *"on/off"* para el paso de medio neutro a básico. Esta sonda está concebida para detectar estos cambios en las mitcondrías. La segunda sonda que se recoge es un derivado de 1,4-divinilbenceno decorado con grupos de piridina como centros básicos. La capacidad aceptora de los núcleos de piridina incorporados en esta molécula se ve incrementada tras el proceso de protonación, lo cual se traduce a nivel fotofísico en un desplazamiento batocrómico de las bandas de absorción y emisión. Esta sonda es del tipo ratiomérica en condiciones de excitación de 2P, y su aplicación reside en proporcionar información del pH_i. Aunque estos dos compuestos tienen un valor de *pKa* adecuado para el estudio del *pH* en lisosomas (4.5-5.0), ninguno de ellos tiene la capacidad para alcanzar selectivamente este orgánulo.

Tabla 2. Ejemplos de sensores de *pH* descritos para 2PM.

Compuesto	λ_f (nm)	σ_{2PA} (GM)	*pKa*	Intervalo de *pH* para su uso	Tipo de sonda y aplicación	Ref.
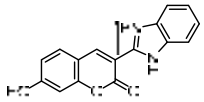	480	11 (800 nm)	4.20 7.20	3.30-5.40 6.50-8.30	*"on/off"* – *"off/on"*; estudio de *pH* mitocondrial	[347]
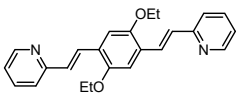	465	411 (700 nm)	3.85	2.99-5.28	Ratiométrica; mapeo de *pH*	[349]

4.2 DISEÑO MOLECULAR Y ESTUDIO DEL COMPUESTO MODELO (4)

Como punto de partida para el trabajo desarrollado dentro de este Capítulo se toma el compuesto **4** (**Fig. 57**). Durante la preparación de este compuesto, se observó una alta fluorescencia verde en el crudo de reacción, la cual desapareció al emplear carbonato sódico en la elaboración de la reacción. Este hecho, sugiere su potencial aplicación como sensor de *pH*. Al igual que **1**, el compuesto **4** presenta una estructura D-π-A o tipo *push-pull*. La protonación del nitrógeno del anillo de indolenina, que actúa como centro básico, implica un incremento en la capacidad aceptora (mayor deficiencia electrónica), lo que se traduce a nivel fotofísico en un desplazamiento sustancial de las bandas de absorción y emisión.

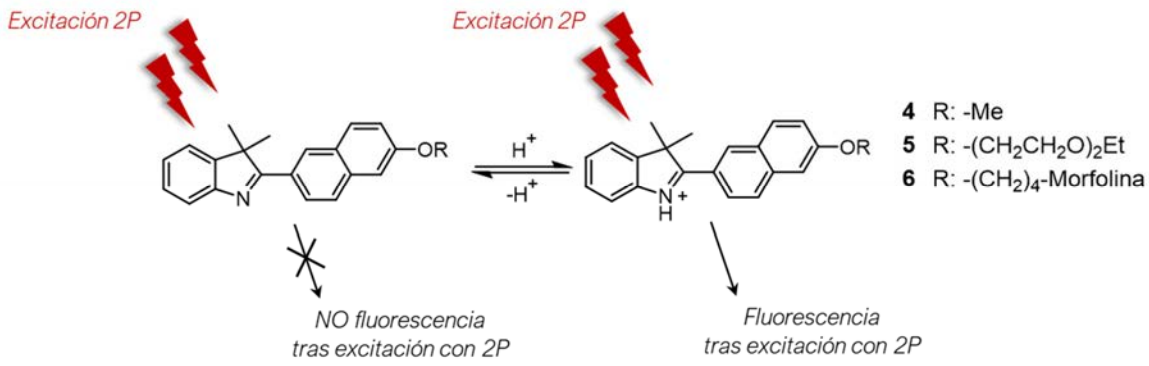

Fig. 57. Mecanismo para la detección de cambios de *pH* a través del empleo de derivados de indolenina y nuevos compuestos propuestos (**5** y **6**).

En base al compuesto **4**, se proponen dos nuevos derivados: **5** y **6** (**Fig. 57**). Las modificaciones sobre el modelo se realizarán sobre el sustituyente alcóxido. La variación del sustituyente en esta posición no debería conllevar cambios ni en las propiedades ópticas del cromóforo ni en las propiedades ácido-base de la molécula, dado que los cambios en esta posición no deberían tener una repercusión significativa sobre las unidades aceptoras y dadoras de la estructura. Teniendo esto en cuenta, las siguientes modificaciones se plantean con objeto de guiar la sonda de *pH* a nivel subcelular:

→ **Incorporación del grupo carbitol en 5**: esta unidad no tiene una diana definida a nivel subcelular, siendo incorporada para mejorar la solubilidad y favorecer su ubicuidad dentro del entorno celular. Esto permitirá el empleo de **5** como sonda general de pH_i.

→ **Incorporación de *N*-alquilmorfolina en 6**: este grupo es un agente lisosomotrópico, es decir, contribuye a la acumulación selectiva del fluoróforo dentro de los lisosomas. Tras protonarse este resto básico, el derivado **6** quedará confinado.[212,215–217] El *pH* ácido de los lisosomas dará posteriormente lugar a la forma fluorescente. Es decir, este compuesto será un sensor de lisosomas.

4.2.1 Estudio preliminar de las propiedades de 4

En primer lugar, se lleva a cabo el estudio de las propiedades fotofísicas del compuesto modelo (**4**) en distintos disolventes, quedando los resultados recogidos en la **Tabla 3**. Los espectros de absorción y emisión se muestran en la **Fig. 58**.

Tabla 3. Propiedades fotofísicas de **4** en diferentes disolventes (disoluciones 10 μM, sin desoxigenar).

Compuesto	Disolvente	λ_{abs} (nm) [ε ($M^{-1}\,cm^{-1}$)]	λ_f (nm)	ϕ_f	$\Delta\upsilon$ (cm^{-1}) [$\Delta\lambda$ (nm)]
4	tetrahidrofurano	338 [23300]	413	0.02	5373 [75]
	diclorometano	333 [24800]	415	0.03	5934 [82]
	metanol	337 [23200]	422	0.02	5977 [85]
	agua	337 [22300]	438	0.14	6843 [101]
4H	HCl_{aq} (*pH* 1.22)	401 [25100]	502	0.37	5017 [101]

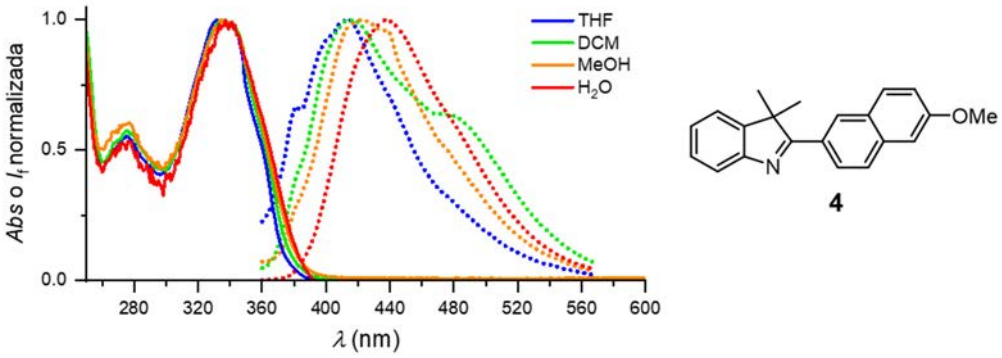

Fig. 58. Espectros de absorción (líneas sólidas) y emisión (líneas punteadas) del compuesto **4** en distintos disolventes (disoluciones 10 μM, sin desoxigenar).

Como se puede apreciar, las bandas de absorción de **4** se encuentran en una región espectral relativamente pequeña, centradas entre 332 y 338 nm y fuera del rango de trabajo del microscopio de 2P. Las variaciones en la emisión, en cambio, son más acentuadas y los máximos se encuentran localizados entre 412 y 438 nm acorde a la polaridad del disolvente (**Fig. 58**). Este efecto fluorosolvatocrómico positivo apunta a un mayor momento dipolar en el estado excitado, hecho que justifica por qué las bandas de emisión se ven más afectadas por la polaridad que las de absorción. Ello, a su vez, se podría trasladar a la posible presencia de una transferencia de carga intramolecular (ICT) en estas moléculas. Por otro lado, de entre sus propiedades fotofísicas cabe destacar los altos desplazamientos de Stokes de hasta 6843 cm^{-1}, que además están acompañados de rendimientos cuánticos de fluorescencia moderados (0.14 en disolución acuosa, **Tabla 3**).

Con objeto de estudiar la respuesta óptica al *pH* del compuesto **4**, los espectros de absorción y emisión se registran en condiciones ácidas (HCl_{aq} *pH* 1.22). Los datos fotofísicos están recogidos también en la **Tabla 3**, mientras que la comparación de los espectros en registrados en condiciones ácidas y neutras se encuentra en la **Fig. 59**.

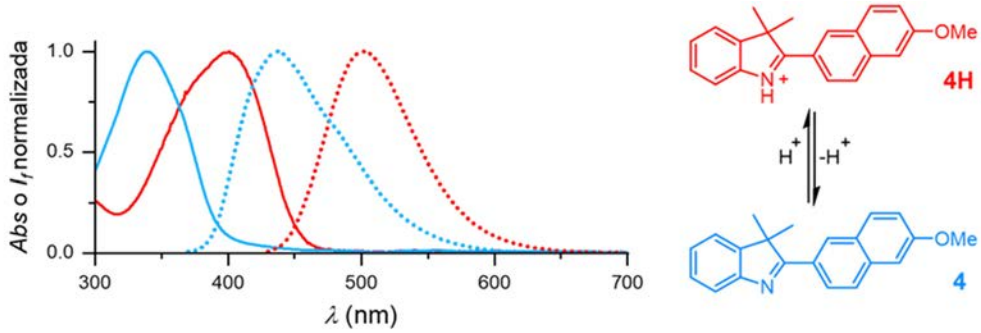

Fig. 59. Espectros de absorción (líneas sólidas) y de emisión (líneas punteadas) del compuesto **4** (*pH* 7.00, líneas azules), y su respectiva forma protonada **4H** (*pH* 1.22, líneas rojas). La emisión fue registrada tras excitar en los respectivos máximos de absorción ($\lambda_{exc,\,1P}$ = 340 y 401 nm para las formas neutra y protonada, respectivamente; disoluciones 10 μM, sin desoxigenar).

Como se mencionaba antes, en condiciones neutras la absorción del compuesto **4**, independientemente del disolvente que se considere, no es idónea para su aplicación en 2PM. La situación es notablemente distinta tras la protonación, observándose un cambio brusco en las propiedades de la forma protonada **4H** a consecuencia de la mejora en el proceso de ICT que gobierna la transición electrónica $S_0 \rightarrow S_1$. Concretamente, el máximo de la banda de absorción sufre un desplazamiento desde 340 nm en el compuesto **4** hasta 401 nm en la forma **4H** (**Fig 59** y **Tabla 3**). Este desplazamiento batocrómico tan acusado habilita la aplicación en 2PM del sistema **4**/**4H** como sonda de *pH* tipo "*off/on*". Al igual que la absorción, la emisión experimenta un cambio en una extensión similar a causa de la formación del indolinio, desplazándose desde 437 hasta 502 nm. Es importante destacar que el proceso de protonación conlleva un aumento del rendimiento cuántico de aproximadamente tres veces, conservando además la forma protonada un desplazamiento de Stokes grande (5017 cm^{-1}).

Para profundizar en las propiedades ácido-base del compuesto **4**, la absorción y la emisión del compuesto se registran en disoluciones de distinto *pH* comprendidas entre 2.32 y 4.38 (**Fig. 60 a**). A partir de estos espectros, el *pKa* se calcula tanto en el estado fundamental como en el estado excitado mediante la ecuación de Henderson-Hasselbach [**Eq. (5)**]:

$$pH = \log\left(\frac{I_{max} - I}{I - I_{min}}\right) + pKa \qquad \textbf{Eq. (5)}$$

donde I_{max} y I_{min} son los valores más altos y bajos registrados en los espectros de absorción y emisión para una longitud de onda, asociada en este caso a las bandas relativas a la forma protonada. Por otro lado, I es la absorbancia o intensidad de fluorescencia medida al *pH* considerado.

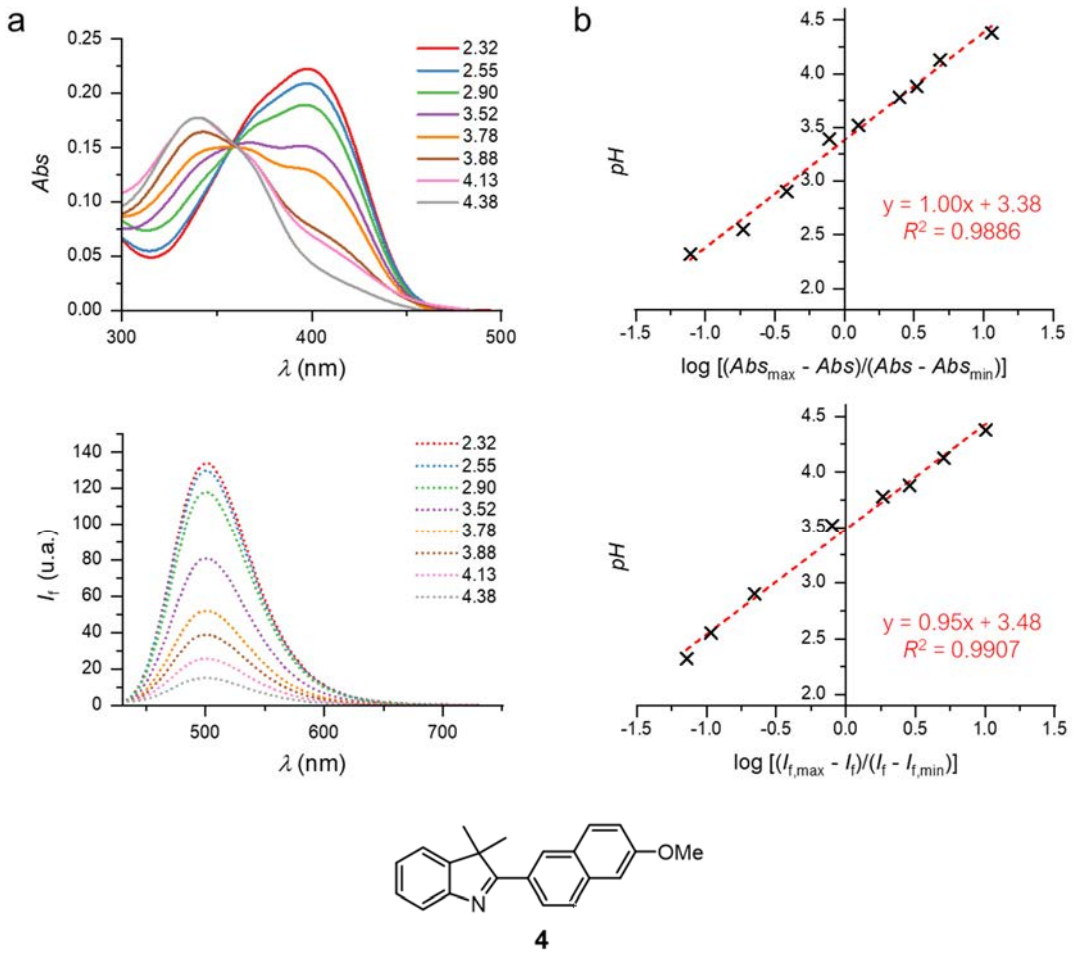

Fig. 60. (a) Cambios en los espectros de absorción (parte superior) y de emisión (parte inferior) del compuesto **4** causados por la variación de *pH* de la disolución (rango de estudio: 2.32-4.38; los espectros de emisión fueron registrados tras $\lambda_{exc,\,1P}$ = 400 nm, 10 μM). (b) Representación de la **Eq. (5)** en base a los valores de absorción a 400 nm (parte superior) y los de emisión a 500 nm tras $\lambda_{exc,\,1P}$ = 400 nm (parte inferior) para el compuesto **4**.

De la introducción de los respectivos valores en la **Eq. (5)** se obtienen valores de *pKa* de 3.38 para el estado fundamental y 3.48 para el estado excitado (**Fig. 60 b**). Aunque existe una diferencia entre los valores obtenidos, esta no es significativa. Por ello, se puede concluir que tanto estado fundamental como excitado presentan el mismo comportamiento ácido-base, lo cual ha sido descrito en *N*-heterociclos.[356,357]

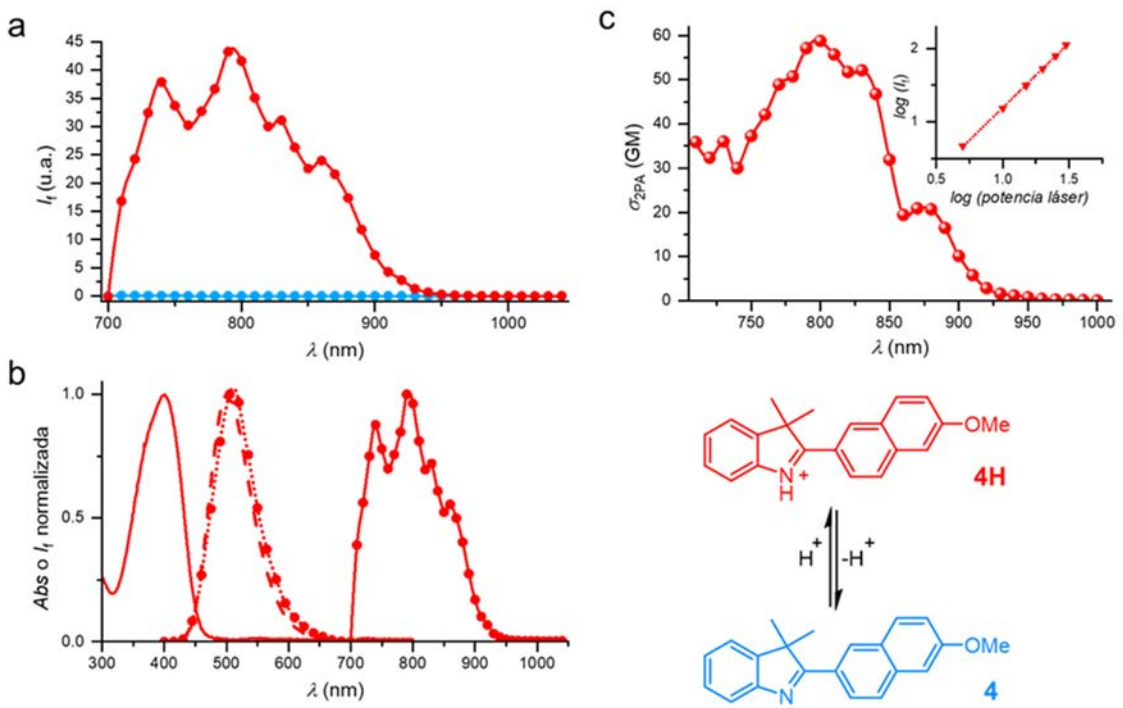

Fig. 61. (a) Espectros de excitación en 2P de **4** (azul, disolución acuosa a *pH* 7.00) y de **4H** (rojo, disolución acuosa a *pH* 1.22). (b) Espectro de absorción en condiciones de 1P (línea sólida roja), espectro de excitación (línea sólida roja con círculos) y espectros de emisión en las distintas condiciones de excitación (línea sesgada para 1P y línea punteada con círculos para 2P) de la forma protonada **4H**. (c) σ_{2PA} de **4H** (disolución acuosa a *pH* 1.22, 10 μM). La representación en la esquina superior derecha muestra la relación logarítmica entre la intensidad de fluorescencia y la potencia del láser incidente ($\lambda_{exc,2P}$ = 800 nm, pendiente: 1.8, R^2= 0.9996).

El comportamiento de **4** en régimen de excitación de 2P se recoge en la **Fig. 61**. Bajo estas condiciones y como se anticipaba antes, solo la forma protonada **4H** presenta emisión tras la excitación con 2P (**Fig. 61 a**). Esta emisión es además coincidente con la registrada en condiciones de excitación de 1P, con lo cual, se puede confirmar que se cumple la regla

de Kasha (**Fig. 61 b**) y la emisión se produce en ambos casos desde el estado S_1. Finalmente, se calculó σ_{2PA} para la forma **4H** mediante el método 2PEF.[68] Esta presenta un máximo de 59 GM a 800 nm (**Fig 61 c**), longitud de onda equivalente a la cual se observa la transición $S_0 \rightarrow S_1$ en condiciones de 1P (véase **Fig. 61 a**). La dependencia cuadrática de la intensidad de emisión con la potencia del láser (**Fig 61 c**) demuestra la excitación bifotónica en estas condiciones.

4.2.2 Cálculos teóricos

Tras optimizar las geometrías del estado fundamental (S_0) y excitado (S_1) mediante DFT y usando el funcional CAM-B3LYP[358] junto con la base 6-31+G(d), se calculan las energías de absorción y emisión mediante TD-DFT. El disolvente se tiene en cuenta mediante el empleo del modelo de polarización continua (*polarizable continuum model, PCM*).[359] Los resultados obtenidos están recogidos en la (**Tabla 4**), en la que se además de incluyen los datos experimentales obtenidos.

Tabla 4. Datos calculados mediante TD-DFT para la indolenina neutra (**4**) y el indolinio resultante de la protonación (**4H**) al nivel PCM(H_2O)/CAM-B3LYP/6-31+G(d).

	Transición (*f*)	E_{calc}[a] eV (nm)	E_{exp} eV (nm)	Componente dominante[b] (%)	Diferencia HOMO-LUMO eV
Absorción					
4	$S_0 \rightarrow S_1$ (1.108)	3.70 (335.09)	3.65 (340)	HOMO → LUMO (94)	6.22
4H	$S_0 \rightarrow S_1$ (1.133)	3.14 (394.85)	3.09 (401)	HOMO → LUMO (95)	5.57
Emisión					
4	$S_1 \rightarrow S_0$ (1.211)	2.77 (447.60)	2.84 (437)	LUMO → HOMO (97)	
4H	$S_1 \rightarrow S_0$ (1.223)	2.62 (473.22)	2.47 (502)	LUMO → HOMO (97)	

[a] Obtenidos como respuesta lineal (*linear response (LR) approach*).

[b] Componentes con una contribución a la transición mayor del 10%.

Mientras que el cálculo muestra una gran precisión para la estimación de las energías de absorción, los errores son mayores en cuanto a las energías de emisión. No obstante, las diferencias entre las energías experimentales y teóricas para el proceso de emisión -sobrestimada en el caso de la molécula neutra y subestimada para la forma protonada - se encuentran dentro del margen de error de esta metodología de cálculo (0.25 eV), y, lo que es más importante, la tendencia observada es reproducida. En ambos procesos electrónicos los orbitales moleculares implicados son exclusivamente HOMO y LUMO.

La disminución de la diferencia de energía entre HOMO y LUMO tras el proceso de protonación está relacionada con el desplazamiento batocrómico observado tanto en la absorción como en la emisión. En líneas generales, se podría concluir que este modelo de cálculo es válido para este tipo de compuestos, especialmente para la predicción de las energías de absorción.

4.3 SÍNTESIS Y CARACTERIZACIÓN DE LOS NUEVOS DERIVADOS 5 Y 6

4.3.1 Síntesis de los derivados 5 y 6

Para la obtención de los nuevos derivados propuestos se plantea el esquema sintético ilustrado en la Fig. 62. En este, se parte del compuesto **3,** previamente sintetizado. La desmetilación del oxígeno anclado al anillo de naftaleno se realiza con HBr_{aq}/AcOH, dando lugar al derivado de naftol **7** con un rendimiento del 86%.

Desde **7**, el compuesto **5** se obtiene en dos pasos: 1) la introducción mediante síntesis de Williamson del grupo carbitol en la estructura a partir de su derivado tosilado, obteniéndose la cetona **8** con un rendimiento del 82%; y 2) la transformación del grupo carbonilo de **8** en el anillo de indolenina mediante la síntesis "interrumpida" de indoles de Fisher. Esta última reacción conduce al compuesto **5** con un rendimiento del 74%.

Por otro lado, la síntesis del compuesto **6** requiere de tres etapas. La primera de ellas parte del naftol **7**, que se hace reaccionar en condiciones de alta dilución con 1,4-dibromobutano, obteniéndose la cetona **9** con un rendimiento del 81%. A partir de esta cetona se obtiene la indolenina **10** (82%). Finalmente se alcanza el compuesto deseado **6** tras la sustitución nucleófila en la cadena alquílica de **10** empleando morfolina (86%).

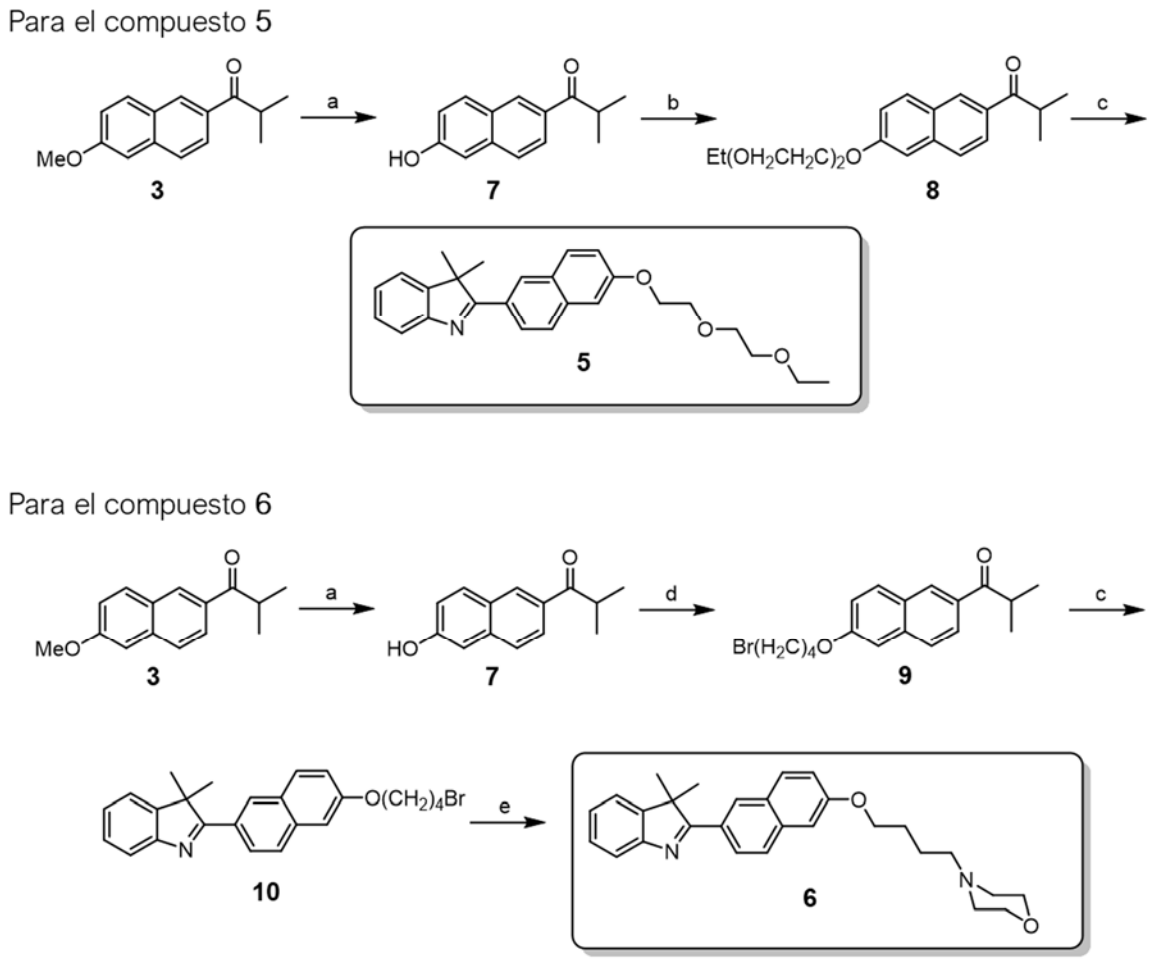

Fig. 62. Esquema sintético para la obtención de los derivados **5** y **6**. *Reactivos y condiciones*: (a) $HBr_{aq,\ conc.}$, AcOH, reflujo, 24h; (b) 4-metilbencenosulfonato de 2-(2-etoxietoxi)-etilo, KI, K_2CO_3, DMF, 80 ºC, 12h; (c) fenilhidrazina, AcOH, reflujo, 24h; (d) 1. KOH, MeOH, reflujo, 1h; 2. 1,4-dibromobutano, ACN, 80ºC, 5h; y (e) morfolina, KI, K_2CO_3, DMF, 12h.

4.3.1 Propiedades fotofísicas de los derivados 5 y 6

Para corroborar que los sustituyentes incorporados no afectan a las propiedades fotofísicas del cromóforo, se registran en primer lugar los espectros de absorción y emisión de los nuevos compuestos en distintos disolventes. Los datos obtenidos están recogidos en la **Tabla 5**, mientras que los espectros quedan ilustrados en la **Fig. 63**.

Tabla 5. Propiedades fotofísicas de **5** y **6** en diferentes disolventes (disoluciones 10 μM, sin desoxigenar).

Compuesto	Disolvente	λ_{abs} (nm) [ε (M^{-1} cm^{-1})]	λ_f (nm)	ϕ_f	$\Delta\upsilon$ (cm^{-1}) [$\Delta\lambda$ (nm)]
5	tetrahidrofurano	338 [20300]	413	0.01	5373 [74]
	diclorometano	332 [27400]	415	0.02	6024 [83]
	metanol	337 [23600]	423	0.02	6033 [86]
	agua	337 [17400]	438	0.10	6843 [101]
5H	HCl_{aq} (pH 1.22)	402 [21300]	500	0.35	4876 [98]
6	tetrahidrofurano	338 [29300]	412	0.02	5314 [74]
	diclorometano	332 [28300]	415	0.03	6024 [82]
	metanol	337 [27700]	423	0.03	6033 [86]
	agua	337 [24500]	437	0.14	6790 [100]
6H	HCl_{aq} (pH 1.22)	401 [25200]	500	0.41	4938 [99]

De la comparación de estos datos y espectros con los registrados para el modelo **4** (**Tabla 3** y **Fig. 58**), se concluye que el cromóforo efectivamente permanece inalterado tras los cambios estructurales introducidos. No solo no se observan cambios entre las propiedades de estos compuestos, sino que además estas son esencialmente idénticas a las determinadas para **4**.

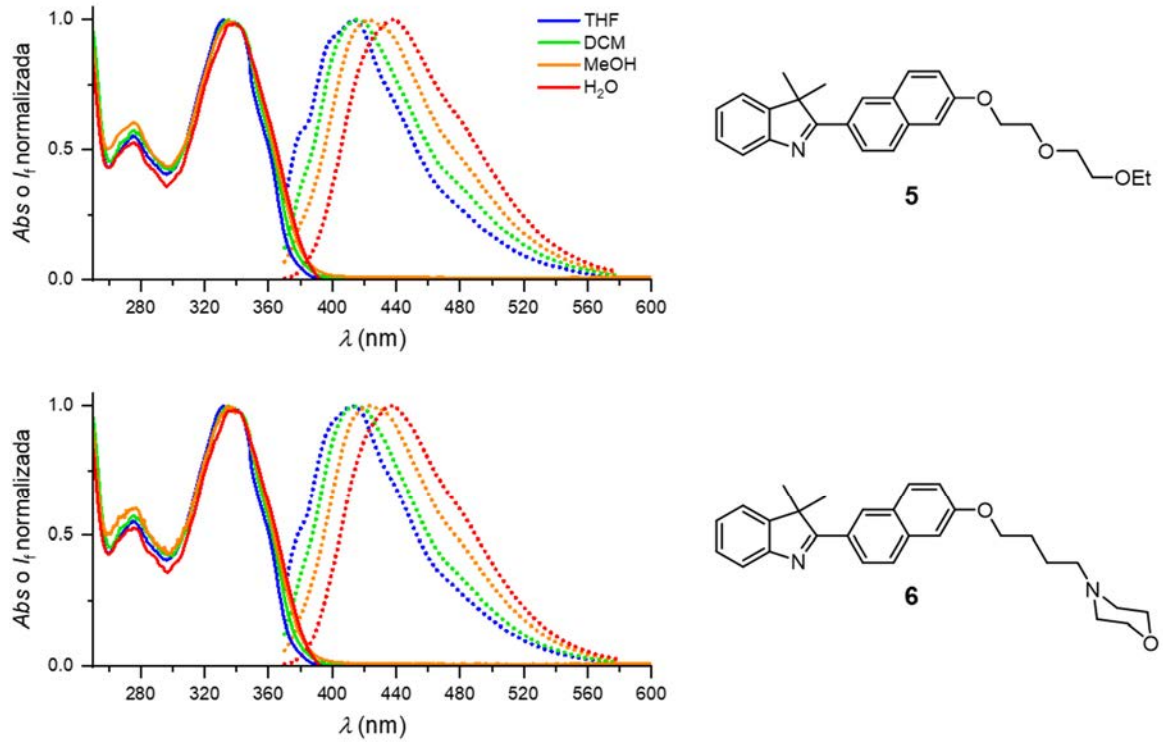

Fig. 63. Espectros de absorción (líneas sólidas) y emisión (líneas punteadas) de los compuestos 5 y 6 en distintos disolventes (disoluciones 10 μM).

Ambos derivados muestran también una respuesta análoga al cambio de *pH*, tal y como se aprecia en la **Fig. 64** y como queda recogido en la **Tabla 5**, donde también están indicadas las propiedades fotofísicas de las formas protonadas. Al igual que ocurre en el compuesto modelo, la absorción y la emisión en estos derivados experimenta un desplazamiento hacia el rojo tras el proceso de protonación. También se aprecia un aumento importante en el rendimiento cuántico junto a buen desplazamiento de Stokes.

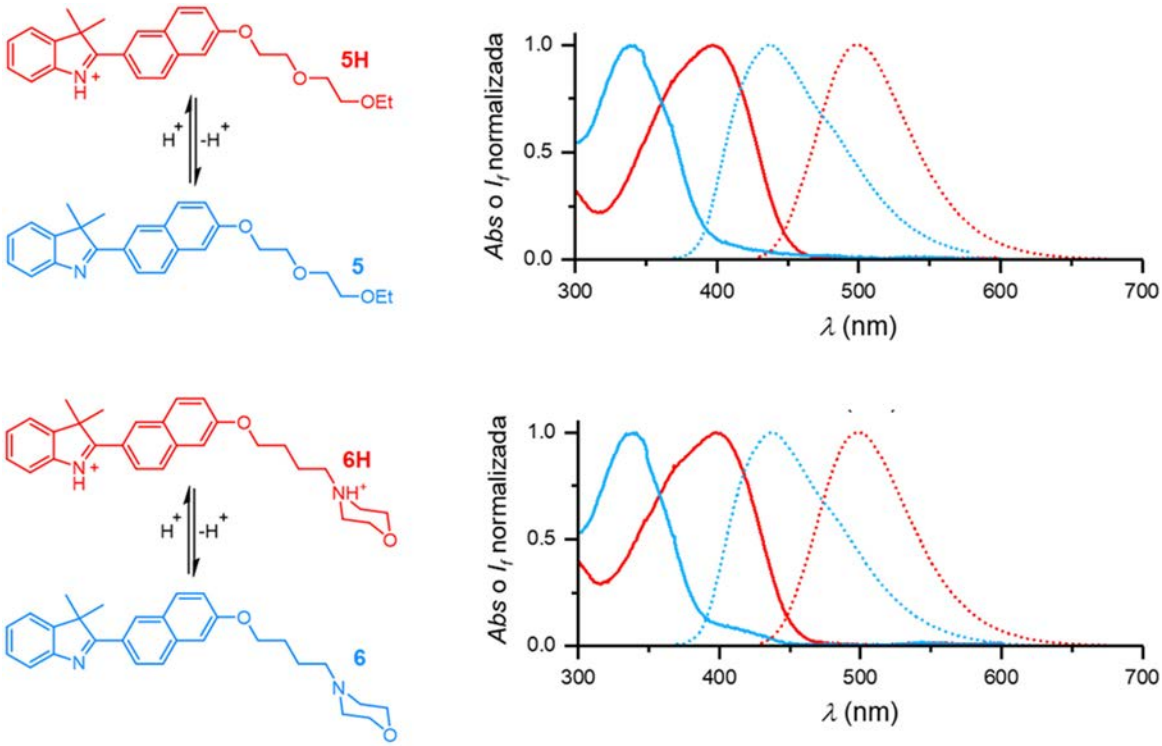

Fig. 64. Espectros de absorción (líneas sólidas) y de emisión de los compuestos **5** y **6** (*pH* 7.00, líneas azules), y sus respectivas formas protonadas **5H** y **6H** (*pH* 1.22, líneas rojas). La emisión fue registrada tras excitar en los respectivos máximos de absorción ($\lambda_{exc,\,1P}$ = 340 y 401 nm para las formas neutra y protonada, respectivamente; disoluciones 10 μM).

Un estudio pormenorizado de las propiedades ácido-base se recoge en la **Fig. 65** para estos compuestos. A partir de los datos de los espectros de absorción y emisión recogidos a distintos *pH*s (**Fig. 65 a**) y mediante la aplicación de la **Eq. (5)** (**Fig. 65 c**), los valores de *pKa* obtenidos son 3.52 y 3.61 para el compuesto **5**, y 3.53 y 3.65 para el **6** (estado fundamental y excitado, respectivamente). De nuevo, no se observan diferencias significativas en los valores de *pKa*, es decir, las cadenas introducidas tampoco repercuten en las propiedades ácido-base del grupo imina del anillo de indolenina. Las curvas de valoración de la **Fig. 65 b** apuntan que además solo hay un centro básico cuya protonación (o deprotonación) afecte a la fotofísica del cromóforo.

5

6

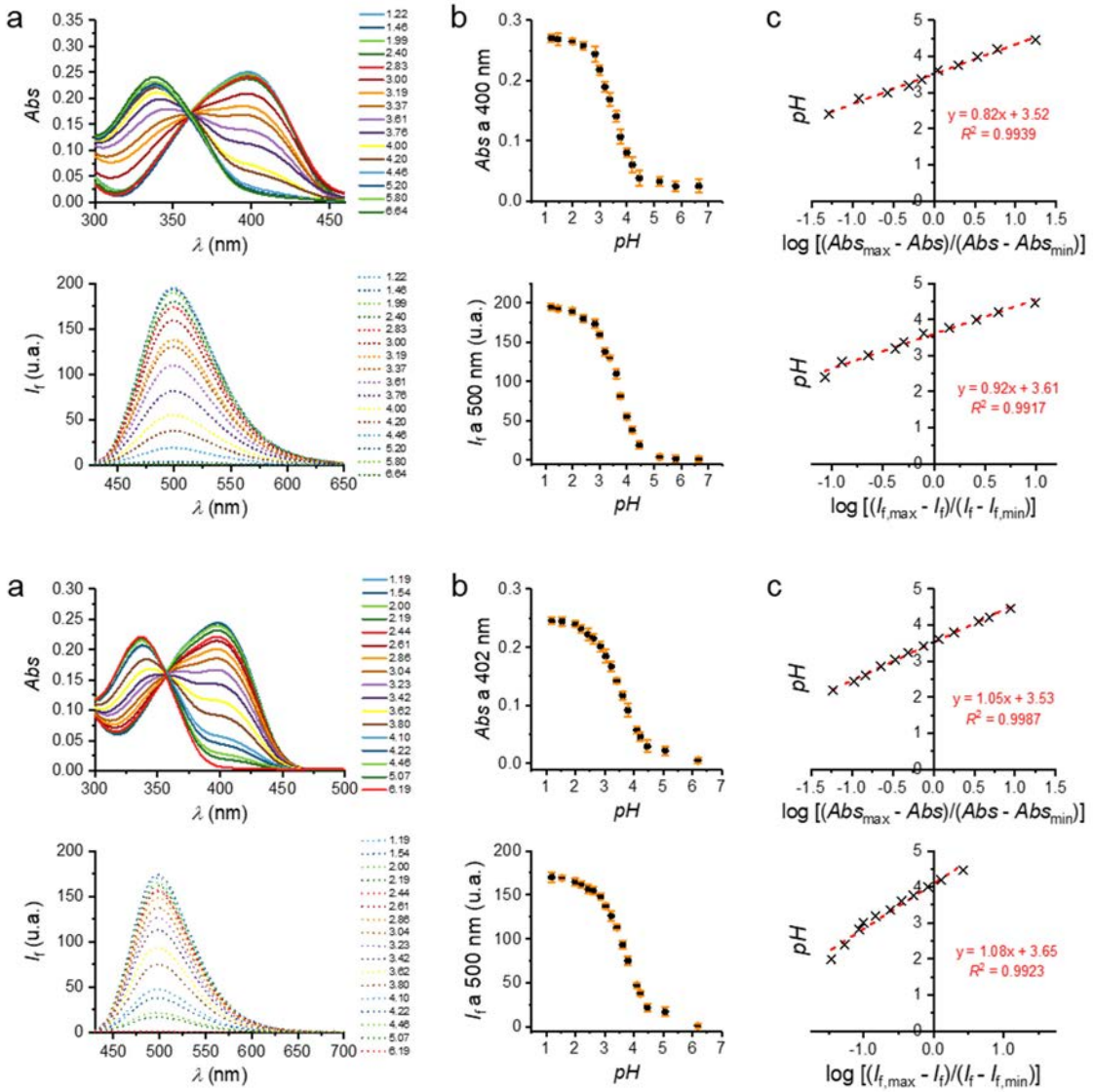

Fig. 65. (a) Cambios en los espectros de absorción (parte superior) y de emisión (parte inferior) de los compuestos **5** y **6** causados por la variación de *pH* de la disolución (rangos de *pH*: 1.22-6.64 y 1.19-6.19 respectivamente; los espectros de emisión fueron registrados tras $\lambda_{exc,\,1P}$ = 400 nm; 10 μM). (b) Curvas de valoración en función de los datos de absorción (parte superior) y de los de emisión (parte inferior) para estos derivados. (c) Representación de la **Eq. (5)** en base a los valores de absorción a 400 nm (parte superior) y los de emisión a 500 nm tras $\lambda_{exc,\,1P}$ = 400 nm (parte inferior) para estos compuestos.

Para conectar los cambios en las propiedades ópticas antes descritos con la protonación del anillo de indolenina, se registran los cambios en los espectros de protón (RMN-^{1}H) de **5** y **6** tras la adición de distintos equivalentes de ácido trifluoroacético (TFA).

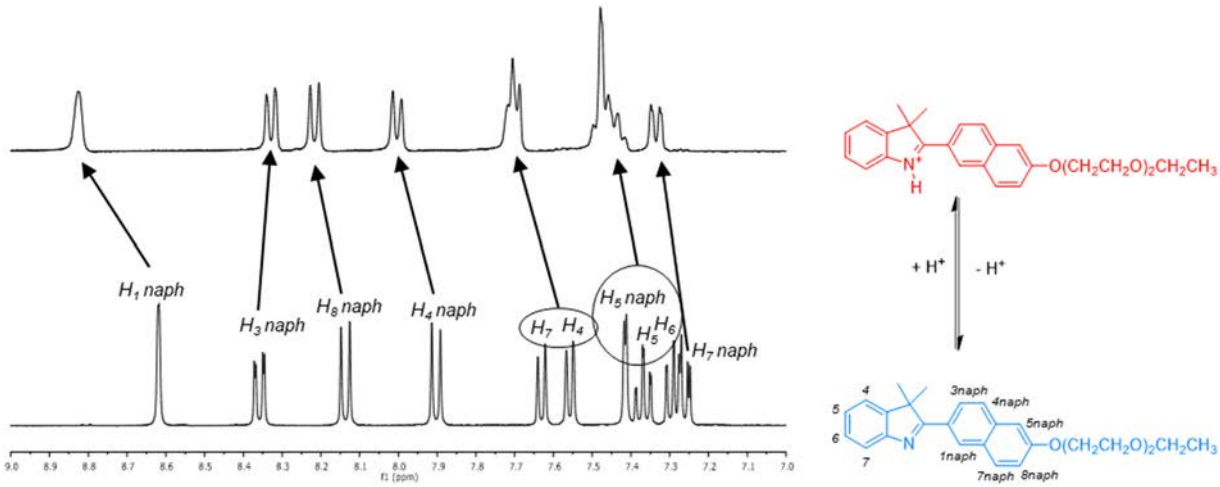

Fig. 66. Variaciones en el espectro RMN-^{1}H (DMSO-d_6) del compuesto **5** tras la adición de TFA (ampliación de la parte aromática).

En la **Fig. 66** se muestran los cambios en el espectro de **5** tras la adición de un equivalente de TFA. En líneas generales, la protonación conlleva un desapantallamiento de todas las señales aromáticas. Particularmente, el $H_{1\ naph}$ es la señal más afectada, cuyo desplazamiento varía desde 8.6 ppm en la forma neutra hasta aproximadamente 8.9 ppm en la protonada. Otras señales convenientemente señaladas en la **Fig. 66** pasan de estar resueltas a agruparse tras la protonación del anillo de indolenina. La adición de más equivalentes de TFA no produce ningún cambio adicional, demostrándose que el centro básico responsable del cambio en las propiedades fotocrómicas de **5** es el nitrógeno de la indolenina. En la parte alifática no se observan cambios apreciables.

El compuesto **6** se diferencia del **5** en cuanto a la incorporación de un grupo básico adicional al de la indolenina: el resto de *N*-alquilmorfolina, el cual además tiene un mayor carácter básico. La protonación de esta unidad transcurre por tanto en primer lugar, lo cual se traduce en una restricción conformacional que implica desdoblamiento de señales que antes eran equivalentes y estaban asociadas a los metilenos pertenecientes al anillo de morfolina (**Fig. 67**). Las modificaciones en esta parte de la estructura no conllevan cambios en la parte aromática, y es necesaria la adición de un segundo equivalente de

TFA para observar cambios de las señales aromáticas. El desplazamiento a campo bajo de estas señales es similar al descrito para el compuesto **6**.

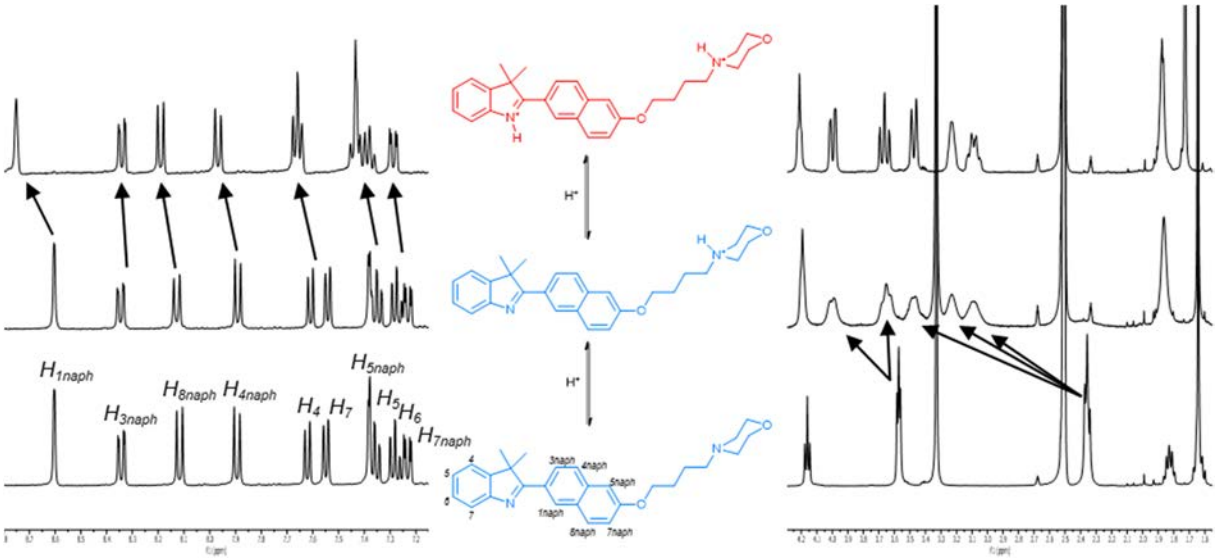

Fig. 67. Variaciones en el espectro RMN-^{1}H (DMSO-d_6) del compuesto **6** tras la adición de TFA.

Para finalizar la caracterización a nivel fotofísico de los nuevos compuestos, se procede al estudio de las propiedades de absorción de dos fotones. Los espectros de excitación de 2P, en los que se registra la emisión entre 400 y 655 nm y se excitó desde 700 hasta 1040 nm, aseguran que en ambos compuestos solo las formas protonadas son activas en condiciones de excitación de 2P (**Fig. 68**).

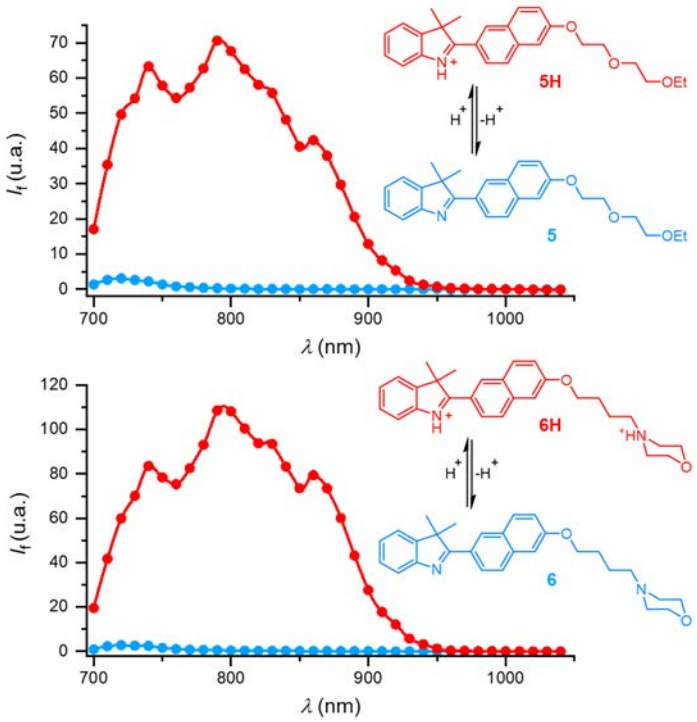

Fig. 68. Espectros de excitación en 2P de **5** y **6** (azul, disolución acuosa a *pH* 7.00) y de **5H** y **6H** (rojo, disolución acuosa a *pH* 1.22). Teniendo en cuenta el *pKa* de la *N*-metilmorfolina (7.38), el resto *N*-alquilmorfolina incorporado en **6** podría estar parcialmente protonado a *pH* 7.00. No obstante, la protonación en esta posición no tiene repercusión en las propiedades fotofofísicas, y por ello se ha representado en la forma totalmente deprotonada.

Por otra parte, la comparación de espectros de emisión y excitación realizada en la **Fig. 69 a** nos permite afirmar que al igual que el modelo **4H**, las formas protonadas de los nuevos compuestos cumplen con la regla de Kasha. Finalmente, se determina la σ_{2PA} en el rango de longitudes de onda comprendido entre 710 y 1000 nm (**Fig. 69 b**). El máximo del espectro de absorción de dos fotones se registra en ambos casos a 800 nm, siendo los valores de *cross section* de 57 y 61 GM para **5H** y **6H**, respectivamente. La dependencia cuadrática de la intensidad de fluorescencia con la intensidad de la luz incidente, representada junto a los espectros de absorción de dos fotones, corrobora la ocurrencia del fenómeno bifotónico en las condiciones de estudio.

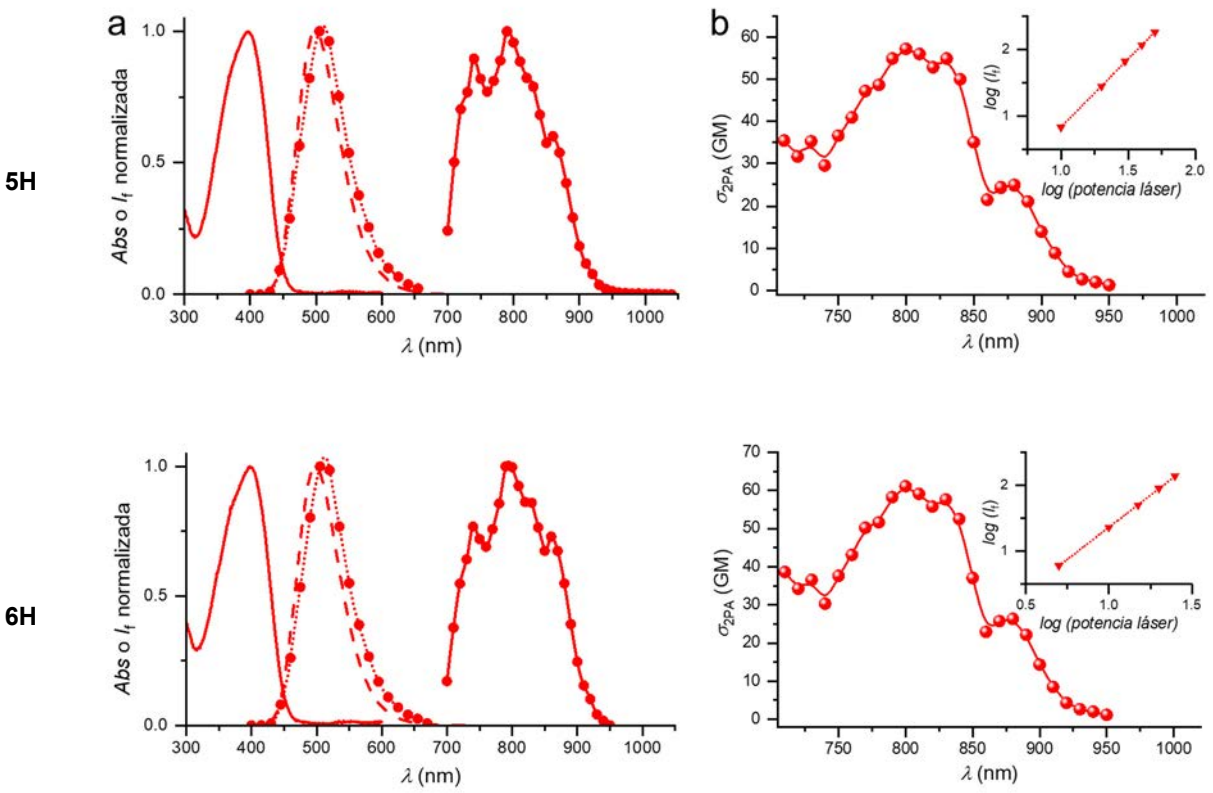

Fig. 69. (a) Espectro de absorción en condiciones de 1P (línea sólida roja), espectro de excitación (línea sólida roja con círculos) y espectros de emisión en las distintas condiciones de excitación (línea sesgada para 1P y línea punteada con círculos para 2P) de las formas protonadas **5H** y **6H**. (c) σ_{2PA} de **5H** y **6H** (disolución acuosa a *pH* 1.22, 10 μM). La representación en la esquina superior derecha muestra la relación logarítmica entre la intensidad de fluorescencia y la potencia del láser incidente ($\lambda_{exc,2P}$ = 800 nm; pendientes: 2.0 y 1.9, respectivamente; R^2= 0.9996 en ambos casos).

4.4 ESTUDIOS FOTOFÍSICOS ADICIONALES

Tras estudiar el comportamiento óptico de los nuevos derivados frente a los cambios de *pH*, los siguientes estudios se enfocan a comprobar la selectividad y sensibilidad de estos compuestos para la detección el protón frente a otras especies con importancia a nivel biológico y presencia considerable en el entorno celular. Además, se examina la fatiga de estos compuestos tanto a nivel de reversibilidad, como de estabilidad frente a la exposición de luz.

4.4.1 Estudio de selectividad de los derivados 5 y 6

La existencia de múltiples especies cargadas positivamente (fundamentalmente metales) en el entorno celular que puedan actuar como interferencias en la respuesta luminiscente de los compuestos **5** y **6**, hace que sea necesario un estudio de la selectividad. Para ello, ambos compuestos se exponen a algunas de las especies de este tipo más abundantes en el entorno subcelular tanto a *pH* neutro (7.00) como a *pH* ácido (1.22), mostrándose los resultados en la **Fig. 70**. Para medir los cambios en la fluorescencia a la presencia de metales, las muestras se excitan a 400 nm y la emisión se mide en 500 nm.

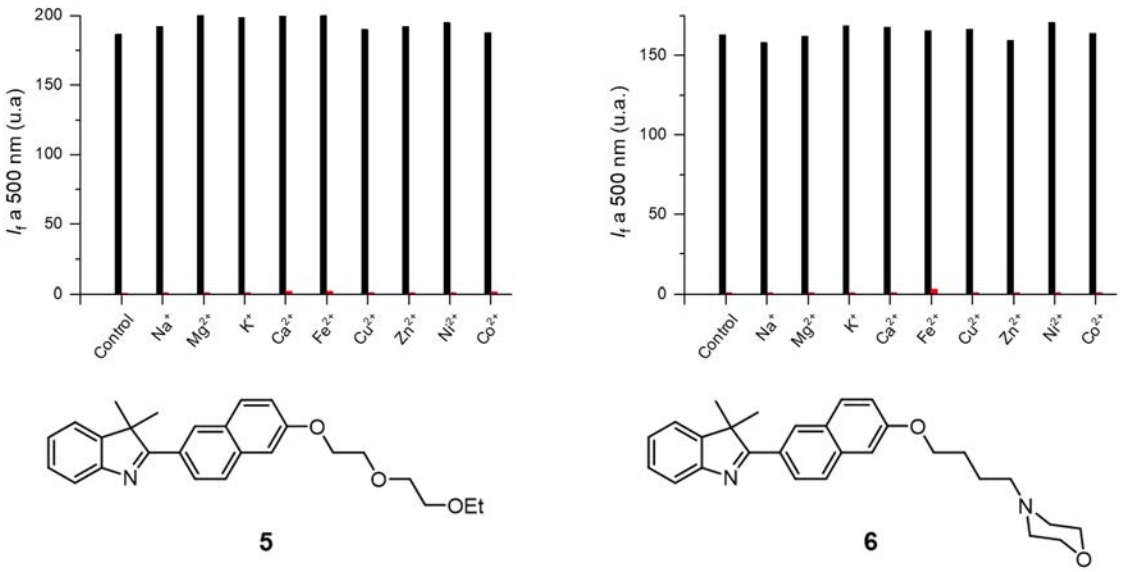

Fig. 70. Estudios de selectividad de protón frente a otras especies con carga positiva e importancia biológica para los compuestos **5** y **6**. Las mediciones de fluorescencia fueron realizadas a *pH* 1.22 (barras negras) y a *pH* 7.00 (barras rojas). La fluorescencia fue registrada a 500 nm tras excitar a 400 nm. Concentración de los compuestos de interés: 10 μM (1% DMSO en disolución acuosa); concentración de los distintos iones: 100 mM.

Ambos derivados presentan una alta selectividad y sensibilidad a la presencia de entornos ácidos, con un incremento en la fluorescencia de más de 100 veces en cualquiera de los casos presentados **Fig. 70**. En caso de que pudieran dar lugar a complejos con algunos de los metales examinados, el prácticamente inapreciable tamaño de las barras rojas

asociadas a los experimentos en medio neutro indica que la formación de estos no tiene ninguna repercusión en las propiedades fotofísicas del cromóforo.

4.4.2 Estudio de la reversibilidad de los derivados 5 y 6

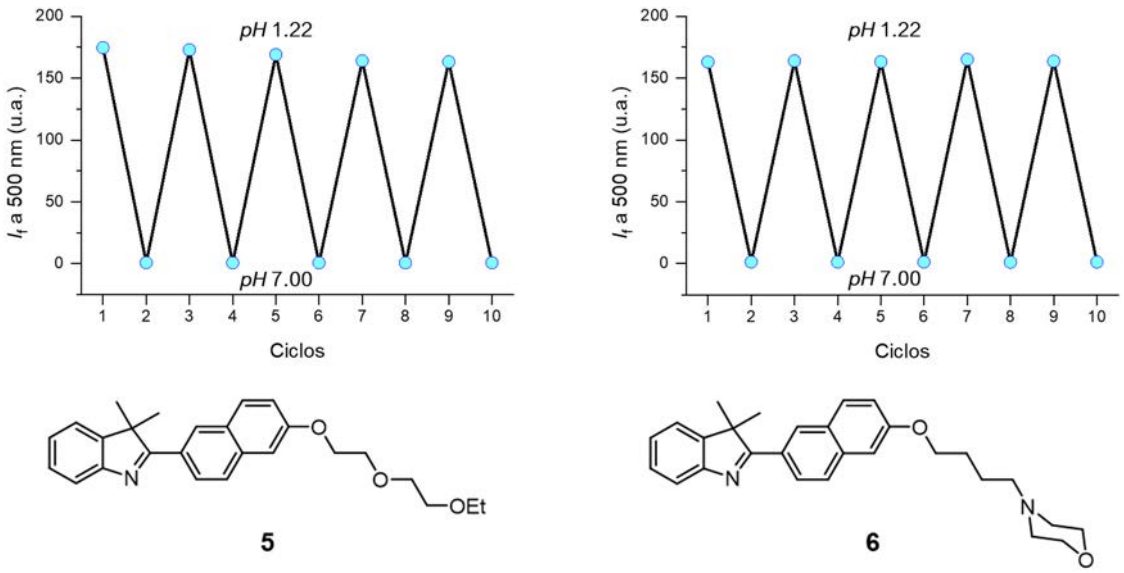

Fig. 71. Estudios de reversibilidad de los compuestos 5 y 6. a fluorescencia fue registrada a 500 nm tras excitar a 400 nm. Concentración de los compuestos de interés: 10 μM (1% DMSO en disolución acuosa)

La resistencia de estos compuestos a diversos ciclos de protonación-deprotonación en disolución es examinada en la **Fig. 71**. Para ello, el *pH* se cambia desde 1.22 hasta 7.00 en múltiples ocasiones. Estos compuestos presentan una buena resistencia a los cambios de *pH* del medio.

4.4.3 Estudio de la fotoestabilidad de los derivados 5 y 6

Finalmente, se estudia la fotoestabilidad de los nuevos derivados en disolución acuosa tanto a *pH* neutro (7.00) como a *pH* ácido (1.22) (**Fig. 72**). En condiciones ácidas, se demuestra una buena estabilidad ante la irradiación continua a 400 nm. Por otra parte aunque la dimerización entre indoleninas es un proceso que podría darse *via* fotoquímica,[360] en medio neutro no se observa ninguna interferencia.

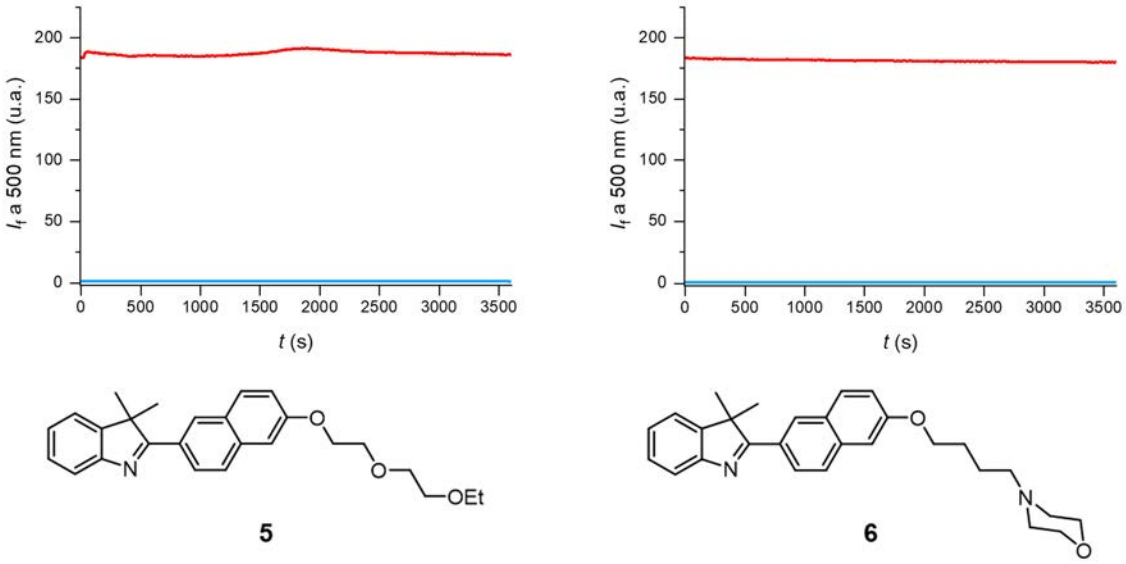

Fig. 72. Estudios de fotoestabilidad de los compuestos **5** y **6** a *pH* 1.22 (rojo) y a *pH* 7.00 (azul). La fluorescencia fue registrada a 500 nm tras excitar a 400 nm. Concentración de los compuestos de interés: 10 μM (1% DMSO en disolución acuosa).

4.5 ESTUDIOS CON CÉLULAS EN MICROSCOPÍA DE DOS FOTONES

Una vez concluida la caracterización química y fotofísica de los derivados **5** y **6**, se procedió a su ensayo en medio biológico. Estos estudios fueron realizados en colaboración con el grupo del Prof. Dr. D. José María Pérez-Pomares. Para los estudios de este capítulo se usan fibroblastos de embriones de ratón (*mouse embryonic fibroblast*, MEF).

4.5.1 Estudios de citotoxicidad

De manera preliminar a los ensayos de bioimagen y para determinar la concentración más adecuada para realizar estos experimentos, se utiliza el test de citotoxidad WST-1 (más detalles acerca de este test se encuentran en la Sección 3.5.1). Los resultados de este ensayo, recogidos en la **Fig. 73**, indican que la citotoxidad de ambos compuestos **5** y **6** es baja en el rango de concentraciones en el que se emplea. A raíz de estos datos, se determina 10 μM como una concentración adecuada para los siguientes estudios.

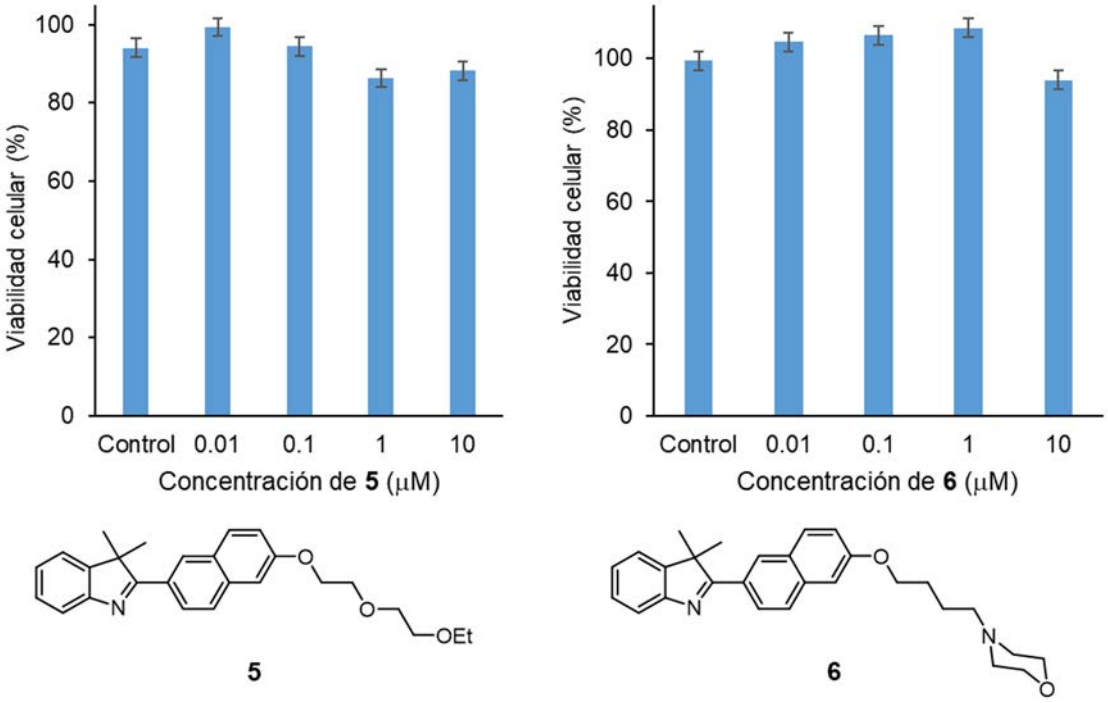

Fig. 73. Test de citotoxicidad WST-1 para los derivados **5** y **6** a diversas concentraciones.

4.5.2 Estudios de bioimagen con 5

Los primeros estudios se realizan incubando las células con el compuesto **5** durante una hora en PBS a *pH* 7.4, observándose tras este tiempo señal fluorescente regiones discretas y punteadas dentro del citoplasma (**Fig. 74 a y a'**), las cuales podrían ser relacionados con lisosomas. Toda la señal obtenida se limita a estas regiones, es decir, no se observa fluorescencia en el resto del citoplasma. El compuesto **5** requiere de un entorno ácido (pH < 4.5) para dar lugar a la forma fluorescente **5H**, con lo cual a pH_i 7.4, solo en orgánulos ácidos (lisosomas) podemos disponer de las condiciones adecuadas para dar lugar al proceso de protonación.

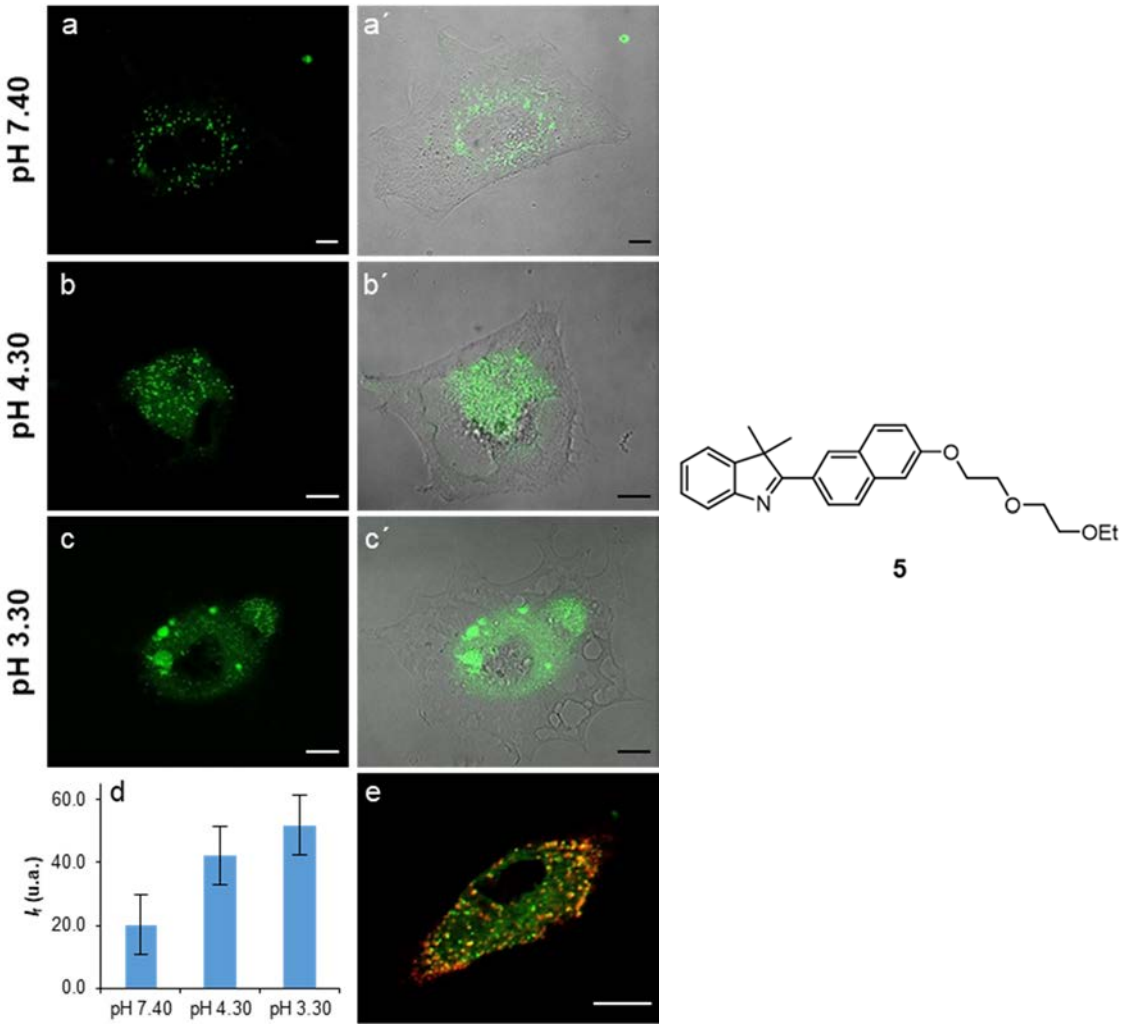

Fig. 74. (a–c) Imágenes de fluorescencia del compuesto **5** (10 μM, $\lambda_{exc,2P}$ = 800 nm, λ_{em} = 500-550 nm) e (a'–c') imágenes de fluorescencia combinadas con campo claro en células MEF a diferentes pH (7.4, 4.3 y 3.3). (d) Intensidad de fluorescencia media determinada a partir de seis medidas independientes. (e) Imágenes de colocalización entre **5** y LDTR a *pH* 4.3 (50 nM, $\lambda_{exc,\ 1P}$ = 633 nm, λ_{em} = 645 - 740 nm). Barras de escala: 10 μm.

Dado que el propósito de la incorporación del grupo carbitol en el compuesto **5** es facilitar su distribución a nivel subcelular para así actuar como sensor de pH_i, se emplean nigericina (10 nM) y KCl (140 mM) para modificar este parámetro.[361,362] Estos estudios se realizan además a dos valores de *pH* distintos: 4.30 (**Fig. 74 b y b'**) y 3.30 (**Fig. 74 c y c'**).

En primer lugar, a pH_i 4.30 se observa un incremento en la señal procedente del citoplasma, mientras que las regiones discretas y más brillantes se hacen más numerosas. A pH_i 3.30, el aumento en la fluorescencia en toda la célula es más notable. Estos incrementos en la intensidad de fluorescencia en paralelo a la bajada de *pH* se encuentran ilustrados en la **Fig. 74 d**, indicando la utilidad del compuesto **5** como sonda para pH_i.

Para identificar las regiones antes mencionadas, se realiza un ensayo de colocalización entre el compuesto **5** y LTDR (**Fig. 74 e**) en condiciones de *pH* 4.30. La presencia de puntos de color amarillento casi naranja en esta imagen, resultantes de la combinación de verde (señal del compuesto 5 en su forma protonada) y rojo (señal procedente del LTDR), indica que estas regiones discretas y vesiculadas observadas son lisosomas. En la región citoplasmática, por el contrario, no se da colocalización entre ambas señales.

4.5.3 Estudios de bioimagen con 6

Para examinar la utilidad de **6** como sensor de lisosomas, se lleva a cabo una incubación en las mismas condiciones que se han descrito anteriormente para el compuesto **5** y a *pH* 7.4. En este caso, se puede observar con una mayor claridad las regiones vesiculadas dentro del citoplasma (**Fig. 75 a**). Posteriormente, se realiza el ensayo de colocalización, empleándose de nuevo LTDR (**Fig. 75 b y c**). El solapamiento entre las señales procedentes de los dos canales de emisión resulta evidente en la **Fig. 75 c**, donde se aprecia que prácticamente la fluorescencia de las imágenes anteriores coindice. El coeficiente de correlación de Pearson a partir de estas imágenes se determina en 0.84. Esta buena colocalización se comprueba además a través del perfil lineal que se muestra **Fig. 75 d**, donde existe una buena coincidencia entre las señales. Estos resultados demuestran la utilidad de **6** como sensor de lisosomas.

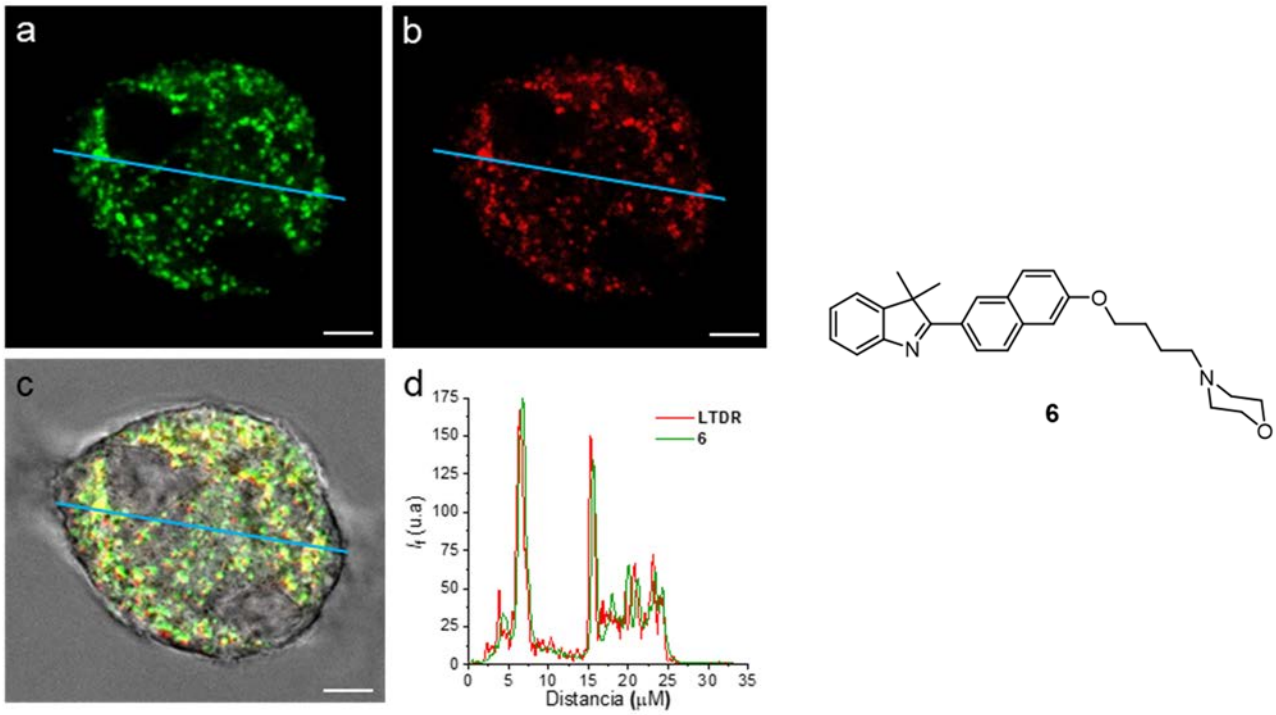

Fig. 75. Imágenes de colocalización en células MEF tratadas con (a) **6** (10 μM, $\lambda_{exc,2P}$ = 800 nm, λ_{em} = 500-550 nm) y (b) LTDR (50 nM, $\lambda_{exc,\ 1P}$ = 633 nm, λ_{em} = 645 - 740 nm). (c) Superposición entre a, b y el campo claro. (d) Perfil de intensidad de la emisión de ambos fluoróforos a lo largo de la línea azul trazada en la célula. Barra de escala: 10 μm

4.6 RESUMEN

En primer lugar, se ha realizado un estudio detallado de las propiedades ópticas y fisicoquímicas del compuesto **4** como modelo para nuevos sensores de *pH*. En base a este, dos nuevos derivados (**5** y **6**) han sido diseñados, sintetizados de manera eficiente y caracterizados en profundidad. Los cambios estructurales planteados en estos compuestos no han conllevado variaciones en las buenas propiedades fotofísicas del modelo, las cuales además son sustancialmente mejoradas cuando se expone a un entorno ácido. La presencia de ácido en el medio implica el desplazamiento batocrómico tanto de la absorción como de la emisión, siendo especialmente destacable el cambio en la absorción y que permite constituir una sonda "*off/on*" en régimen de excitación de dos

fotones. De entre las propiedades fotofísicas de las formas protonadas, destacan una considerable eficiencia cuántica, que oscila en torno a 0.40, que además está acompañada de desplazamientos de Stokes grandes (~4900 cm^{-1}). Sus valores de *cross-section*, de aproximadamente 60 GM, junto con los antes detallados, aseguran su aplicación en 2PM. Estos derivados, además, presentan una buena sensibilidad y selectividad por el protón frente a otras especies con carga positiva, así como una buena fotoestabilidad y una alta resistencia a diversos ciclos de protonación-desprotonación. Ambas modificaciones estructurales han cumplido con sus cometidos, es decir, mientras que **5** muestra una ubicación general dentro de la célula, **6** queda confinado selectivamente en lisosomas. Por último, cabe destacar que la fotofísica observada a nivel celular es la misma que ha sido estudiada en cubeta para las formas protonadas.

Parte de los resultados presentados en este Capítulo han sido publicados en la referencia [363].

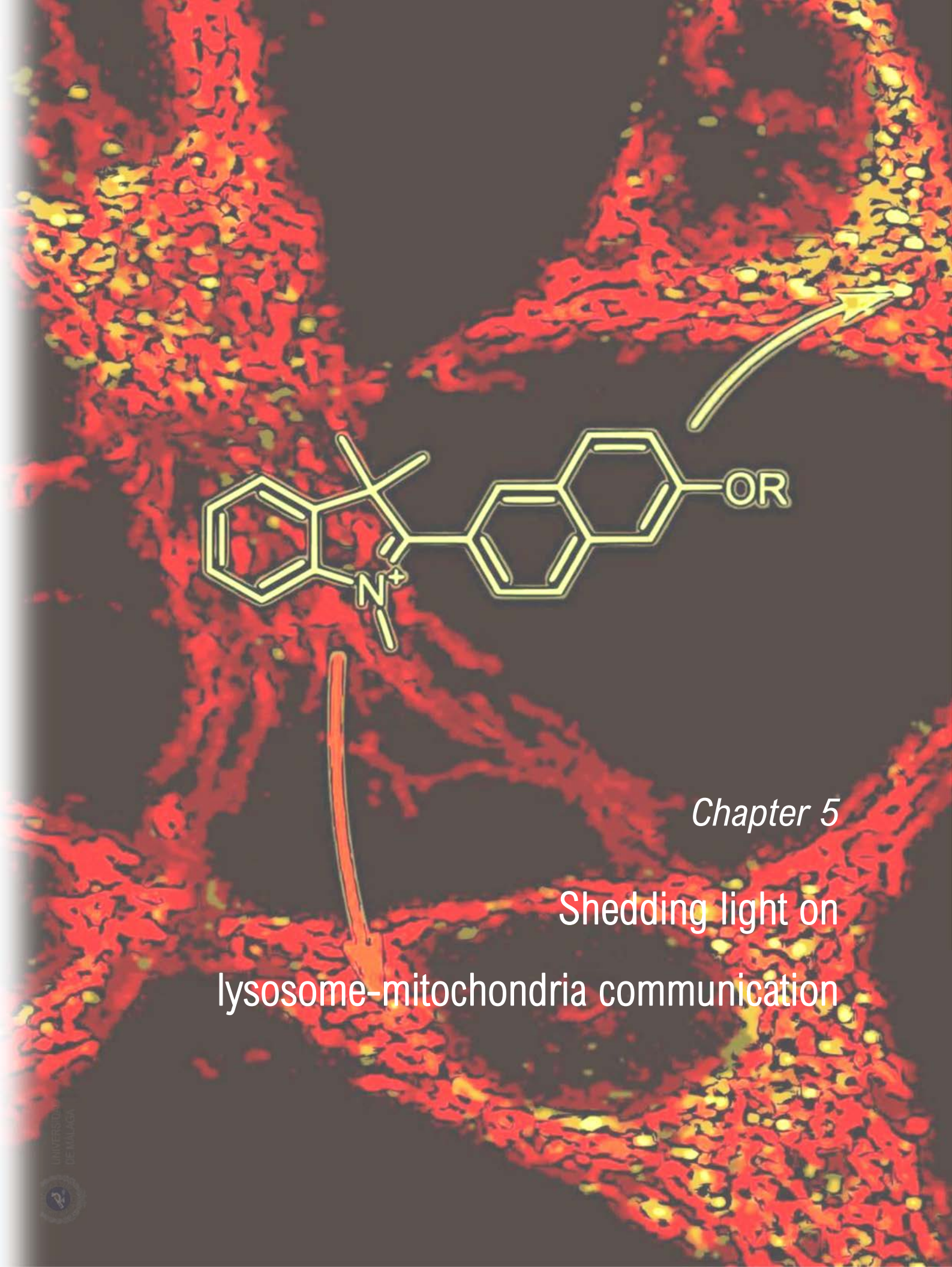

Chapter 5

Shedding light on lysosome-mitochondria communication

5.1 INTRODUCTION

5.1.1 Lysosomes and mitochondria: an intricate relationship

Subcellular organelles, far from acting as isolated entities, establish complex functional networks. Consequently, the cellular activity lies on the controlled and synchronized labors of the different organelles.[364,365] Among these, lysosome-mitochondria communication plays a crucial role for cellular homeostasis and indeed, the dysfunction of one or both organelles is tightly associated with some human diseases.[366–369]

As mentioned in the previous Chapter, lysosomes are characterized for hosting a high acidic content (*pH* 4.5-5.0)[297] as well as numerous enzymes, which together are essential for the degradation of endocytosed and endogenous intracellular materials. It is worth noting that these subcellular compartments are also the most viscous of all cellular organelles.[370,371] On the other hand, mitochondria are responsible for managing the cellular energy supply. Adenosine triphosphate (ATP) is generated within these subcellular "powerhouses", which requires the action of diverse proton pumps to remove the consequent proton excess. Because of this, the double membrane that surrounds these organelles is polarized, and the subsequent mitochondrial membrane potential (around 180 mV; commonly noted as $\Delta\Psi_m$)[372] determines the pass through this structure and is related with the selective accumulation of positive charged species within mitochondria.[211–215] Besides, these organelles are one of the most important source of ROS at cellular level.[373] However, this issue implies a gradual oxidative damage to mitochondria often associated with aging, cancer and neurodegenerative diseases.[374–376]

Hence, it can be drawn that preserving the quality and quantity of mitochondria population is crucial for cell survival. This requires periodic removal and subsequent recycling of damaged and/or excess mitochondria in a process so-called mitophagy. In this mechanism, the role of lysosomes is fundamental for breaking down the mitochondrial components.[377–380] This process can occurs in two *vias*, as illustrated in **Fig. 76 a**: 1) lysosomes wrap the damaged mitochondria, or 2) the injured parts are released in form of mitochondria-derived vesicles (MDVs), which are then engulfed by lysosomes.

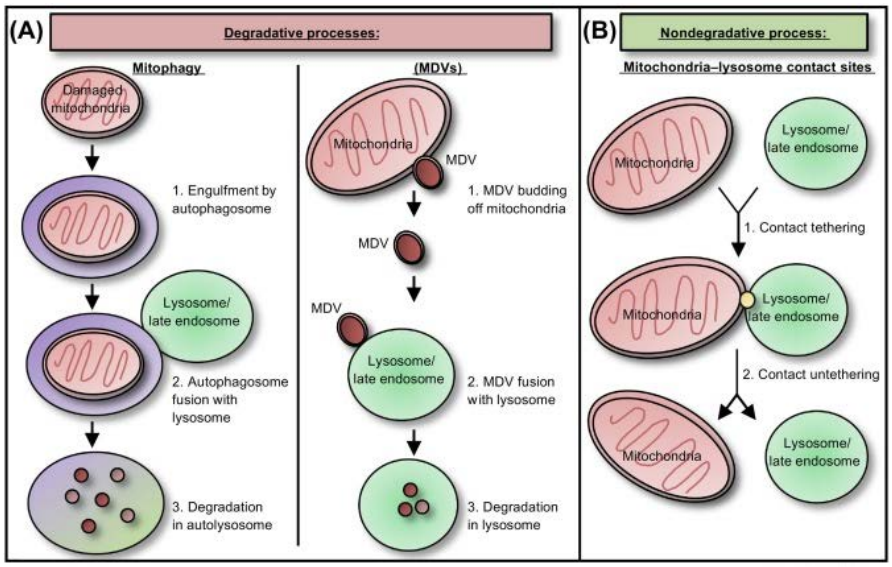

Fig. 76. Schematic illustration of the different lysosome-mitochondria interactions: (a) degradative and (b) non-degradative processes. Image reproduced from ref. [369]

Despite of these organelles are known for a long time, non-degradative interactions beyond mitophagy have been recently described in healthy cells.[369,381] It is represented in **Fig. 76 b**, that both organelles establish contact between their membranes and later, some content is transferred from each to other.

5.1.2 Simultaneous and dual-color organelle trackers

Although confocal and 2PM offer a wide number of advantages for live imaging of cellular processes, individual small fluorescent molecules capable to specifically stain multiple subcellular regions with organelle-specific photophysical properties are all but unknown. Thus, this task is practically limited to the use of multiple fluorescent labels, which is in turn limited by the availability of photophysically-compatible dyes that allow simultaneous visualization of organelle-specific dynamics.

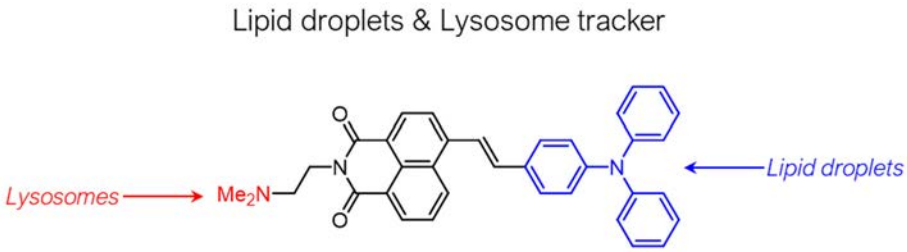

Fig. 77. Structure of the only one dual-color and simultaneous tracker described in literature to date.

To date, only one example of specific multi-organelle probe has been described in the literature, this represented in **Fig. 77**. This compound was devised to gain insights into lipid droplets and lysosome interactions, and its ability to reach these organelles is based on incorporating two well-known targeting groups in its structure: a tertiary amine, responsible for the storage of the dye within lysosomes; and the triphenylamine as hydrophobic moiety that facilitates the accumulation in lipid droplets. The different polarities of these organelles and the strong solvathochromic character of this dye are responsible for the dual-color tracking.[382]

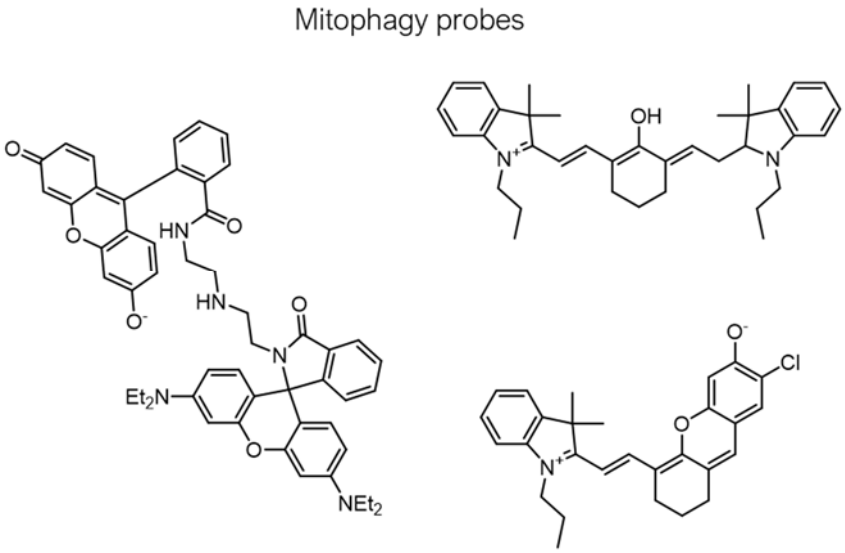

Fig. 78. Structures of some representative probes for monitoring mitophagy.

Regarding lysosome-mitochondria dual labeling, this is only accessible by means of two photophysically distinguishable dyes as yet.[383] Although some probes have been

developed for monitoring mitophagy (a few representative examples are indicated in **Fig. 78**),[384–391] the use of a single small molecule capable of separately labeling both organelles simultaneously has never been reported. The functioning of most of mitophagy probes lays on the different *pH* within these organelles. Thereby, these compounds are first accumulated in mitochondria, where they display a certain photophysical features. When they reach lysosomes after mitophagy takes place, the protonation of the structures induces a different optical behavior to that previously exhibited.

5.2 MOLECULAR DESIGN AND SYNTHESIS

5.2.1 Structural composition of the new derivatives 11 and 12

Two new derivatives (**11** and **12**, **Fig. 79**) were devised in this Chapter combining different organelle-tracker moieties in a single scaffold.

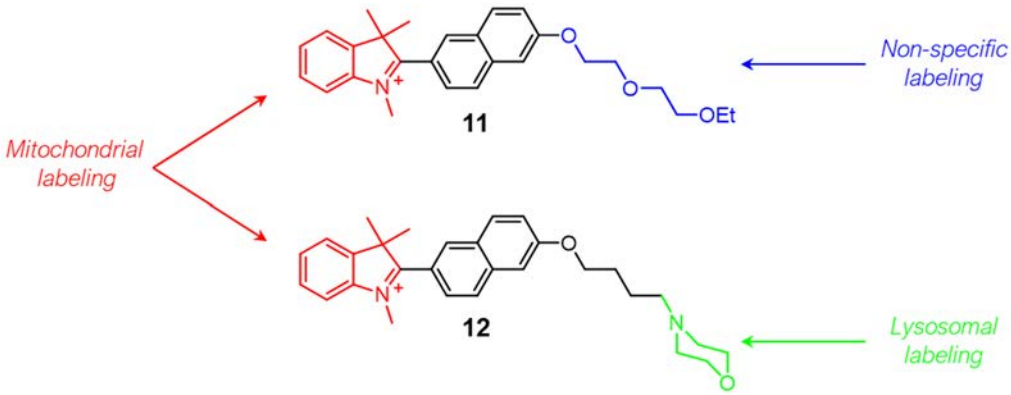

Fig. 79. Structure of the target compounds **11** and **12**.

Although these compounds are inspired by the ones developed in **Chapter 4**, the presence of the indolinium group in compounds **11** and **12** implies two significant differences:

→ As they dispose of the same fluorophore composition that compound **1**, it is anticipated that these compounds will be 2P-active without depending on secondary processes such as protonation or oxidation. That is, these dyes are conceived as trackers instead of sensors.

→ There are lipophilic cationic species containing an indolinium moiety that have been described in literature to stain selectively mitochondria.[392] Moreover, it has previously been informed about *J*-aggregation phenomena in some cyanine dyes within these same organelles.[393] Considering this, it might be possible that the proposed derivatives display a different optical feature if reaching these cellular suburbs.

On the other hand, the selection of the alkoxy substituents builds on similar principles to that applied in the previous Chapter:

→ **Incorporation of carbitol chain in compound 11:** this moiety is known for being a non-specific organelle-targeting group that facilitates the pass through the cellular membranes and improves molecular solubility. This group was selected with the aim of achieving a mitochondrial localization.

→ **Incorporation of *N*-alkylmorpholine chain in compound 12:** this group is a well-documented lysosomotropic agent.[212,215–217] As this compound bears a positive charge in the indolinium ring yet, this moiety was envisioned to provide the scaffold of a dual-organelle tracker ability.

5.2.1 Synthetic approach

For these new compounds, the synthetic scheme shown in **Fig. 80** was proposed and performed. Compound **11** was obtained through the methylation of the previously prepared **5** (61% yield). For the insertion of the morpholine moiety in **12**, two synthetic steps were required: 1) the methylation of previously prepared **10** that quantitatively yields indolinium **13** and 2) the nucleophilic substitution of iodide per morpholine obtained in this last one. After this reaction, the desired compound **12** was achieved with a 58% yield as the hydroiodide **12H**. As it will be detailed below, the protonation of the morpholine ring has not influence on the photophysical properties of the chromophore. That is, both forms (**12** and **12H**) exhibit the same optical features.

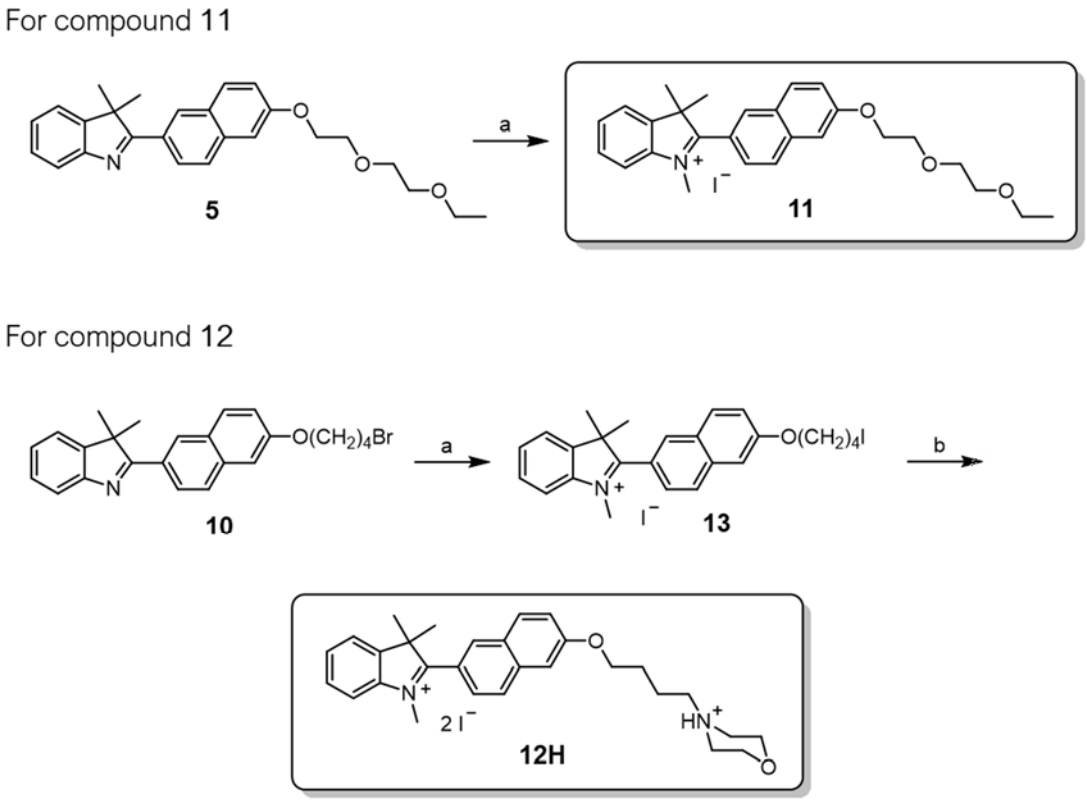

Fig. 80. Synthetic scheme for the obtention of compounds 11 and 12H (please note that H in compound 12 indicates that its morpholine moiety is protonated). *Reagents and conditions:* (a) MeI, ACN, 80ºC, 24h; (b) morpholine, acetonitrile, reflux, overnight.

5.3 PHOTOPHYSICAL PRELIMINARY STUDIES

5.3.1 Characterization of compounds 11 and 12

The new derivatives **11** and **12** dispose the same fluorophore moiety that compound **1**, whose photophysical properties were thoroughly studied in **Chapter 3**. In order to compare the optical features of the new dyes with the ones of the model **1**, these analogues were photophysically characterized in acetonitrile solution. The corresponding data are summarized in **Table 6**, and the absorption and emission spectra are in **Fig. 81**.

Table 6. Photophysical data of compounds **1**, **11** and **12H** in acetonitrile (10 μM air-equilibrated solutions).

Compound	λ_{abs} (nm) [ε (M^{-1} cm^{-1})]	λ_f (nm)	ϕ_f	$\Delta\upsilon$ (cm^{-1}) [$\Delta\lambda$ (nm)]
1	367 [8000]	517	0.03	7612 [146]
11	361 [10500]	517	0.04	8358 [156]
12H[a]	361 [10200]	515	0.04	8283 [154]

[a] Please note that the properties of **12** and **12H** are comparable.

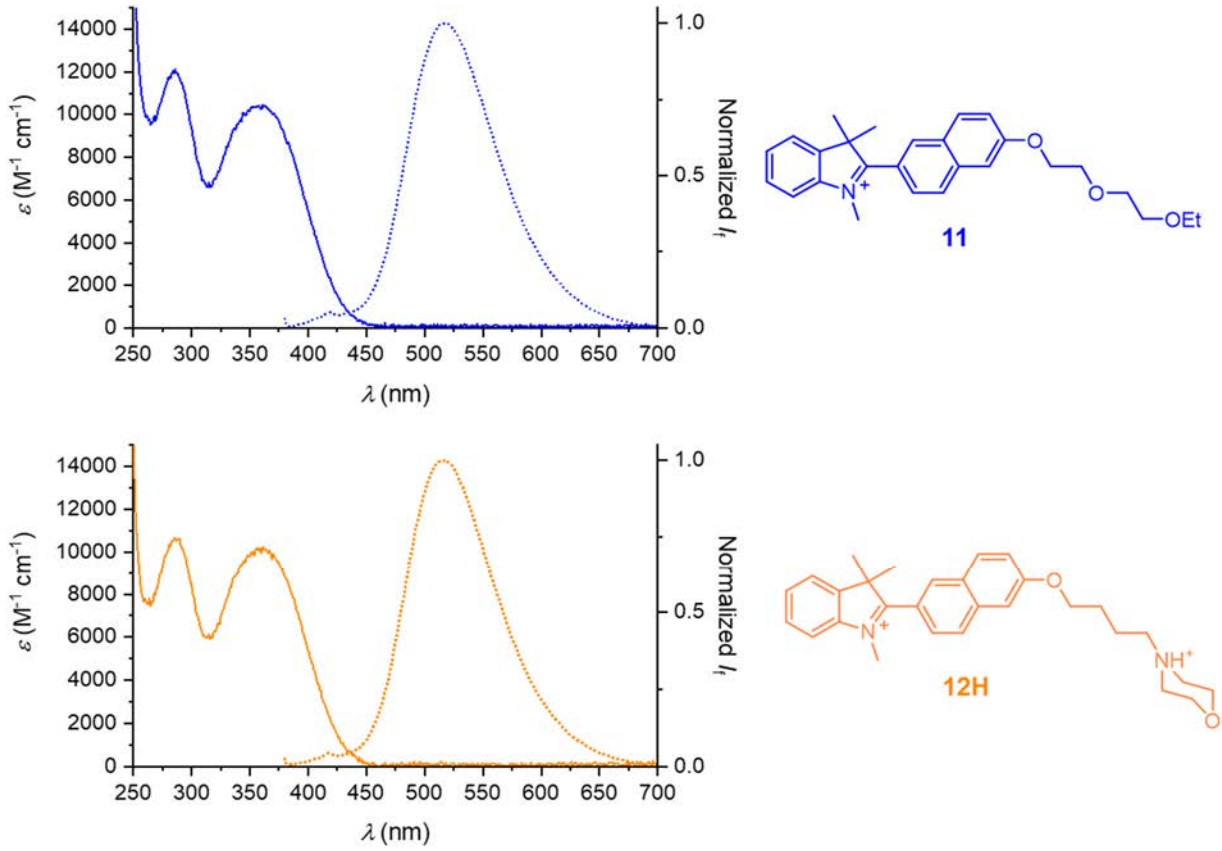

Fig. 81. Absorption (solid lines) and emission (dotted lines) spectra of compounds **11** (blue lines) and **12H** (orange lines) in acetonitrile (10 μM air-equilibrated solutions).

Both absorption and emission bands are seemingly identical for these derivatives. First, absorption bands displayed their maxima at 361 nm with molar extinction coefficients above 10000 M^{-1} cm^{-1}. Moreover, broad and structureless emission bands were registered, these centered around 516 nm. More importantly, these data are similar to those observed in the model compound **1** (see **Table 6**). The great separation between the absorption and the emission bands (above 150 nm) yields considerable large Stokes shifts of around 8300 cm^{-1}. The fluorescence quantum yields determined were also close to that of the model reference: ~0.04 in these analogues *vs.* ~0.03 in the model. Although these values could be considered moderate-to-low at first sight, it was demonstrated that for **1** the fluorescence quantum yield is dramatically enhanced (30-fold) by increasing the viscosity of the environment (**Fig. 39**, **Chapter 3**). Judging from these data, it seems clear that alkoxy moiety has almost a negligible effect on the chromophore's features. Hence, a similar response toward viscosity displayed by **1** can be expected in these compounds.

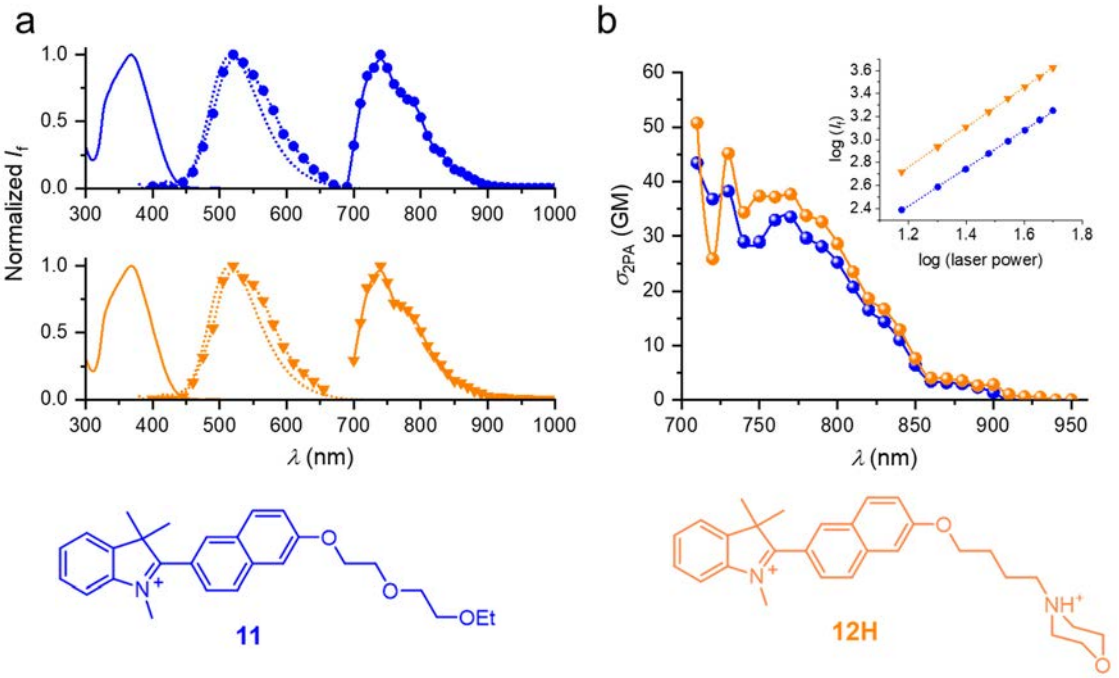

Fig. 82. (a) Excitation (solid lines) and emission (dotted lines) spectra of compounds **11** (blue) and **12H** (orange) under 1P (lines) and 2P (lines and symbols) excitation conditions. (b) σ_{2PA} of **11** and **12H** (blue and orange lines respectively). Inset shows laser power dependency of 2P excited fluorescence. All the spectra were recorded in acetonitrile (10 μM, air-equilibrated solutions).

Next, the 2PA properties of these compounds were examined *via* 2P-excited fluorescence.[394] As illustrated in **Fig. 82 a**, the emission spectra registered are comparable regardless of the nature of the excitation source, indicating thus that the same electronic states are involved ($S_0 \rightarrow S_1$ transition). Moreover, both compounds displayed very similar spectra in terms of shape and spectral position. In **Fig. 82 b** it can be appreciated that the 2PA spectra are also similar, where σ_{2PA} at $\lambda_{exc,2P}$ = 740 nm were determined at 38 and 45 GM for **11** and **12** respectively. All in all, it can be safely assumed that only the oxygen participates as donor group in the dipolar D-π-A structure, and that changes on the structure does not have consequences on the 2PA properties of the fluorophore moiety.

5.3.2 Photostability and interference studies

Additionally, the photostability of these compounds was examined, as represented in **Fig. 83 a**. Despite a slight decrease in the emission intensity at 515 nm upon excitation at 370 nm for 1 hour, photobleaching can be considered low (the emission barely decreases from 6.5 to 6.0 a.u.). Both compounds not only demonstrated a notable robustness to the continuous irradiation, but also the attained fluorescence intensity levels were similar. These results also corroborate the absence of non-desired photochemical processes which could alter the fluorescence properties.

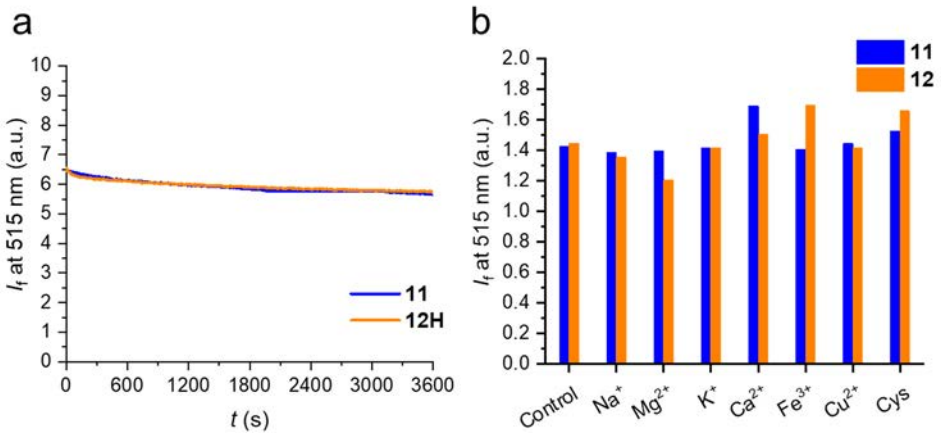

Fig. 83. (a) Photostability of **11** and **12H** in acetonitrile (10 μM, air-equilibrated solutions). Compounds were excited continuously at 370 nm for 1 hour and the emission was monitored at 515 nm. (b) Interference studies of dyes **11** and **12** towards physiologically important species. The solutions were prepared in distilled water (10 μM for our derivatives and 1 mM for the other chemical species).

The possible interferences with some of the most common biological cations were also evaluated. Furthermore, the possible interaction with cysteine, considering the electrophile character of the indolinium ring, was also examined (**Fig. 83 b**). The differences observed in optical behavior of these derivatives towards the tested species are not significant in all cases.

5.4 CELL STUDIES

The studies with living cells were carried out employing HeLa cells. This cell line consists of immortal cancer cells. Interestingly, these cells were taken for the first time in February 1951 from the cervical cancer that suffered Henrietta Lacks, who passed away that same year.[395] This cell line is the most extensively used in scientific studies. Cell studies in this Chapter were performed in the U28 Unit of the ICTS "NANBIOSIS" hosted at the Andalusian Centre for Nanomedicine & Biotechnology (Bionand).

5.4.1 Cytotoxicity studies

Prior to the imaging experiments, the cytotoxicity of these compounds was evaluated to determine the optimal concentration to incubate the cells. In this case and taking into account the possible interferences, we performed a "Live/Dead" test, which consists of determining the number of live and dead cells. This is feasible through staining cells with propidium iodide, which passes through the disordered areas of the nuclear membrane of dead cells, thus allowing the differentiation of live from dead cells. This dye, once it has reached the cellular nucleus, intercalates with the DNA of the nuclei and emits red fluorescence light.[396] The results obtained are shown in **Fig. 84**. These data point out that these dyes, at the concentrations tested, are practically harmless to cells (please note that compounds are considered toxic when cell survival is below 80% by this method, according to ISO 10993-5:2009). Considering the results, the selected concentration for the biomaging studies was 10 μM.

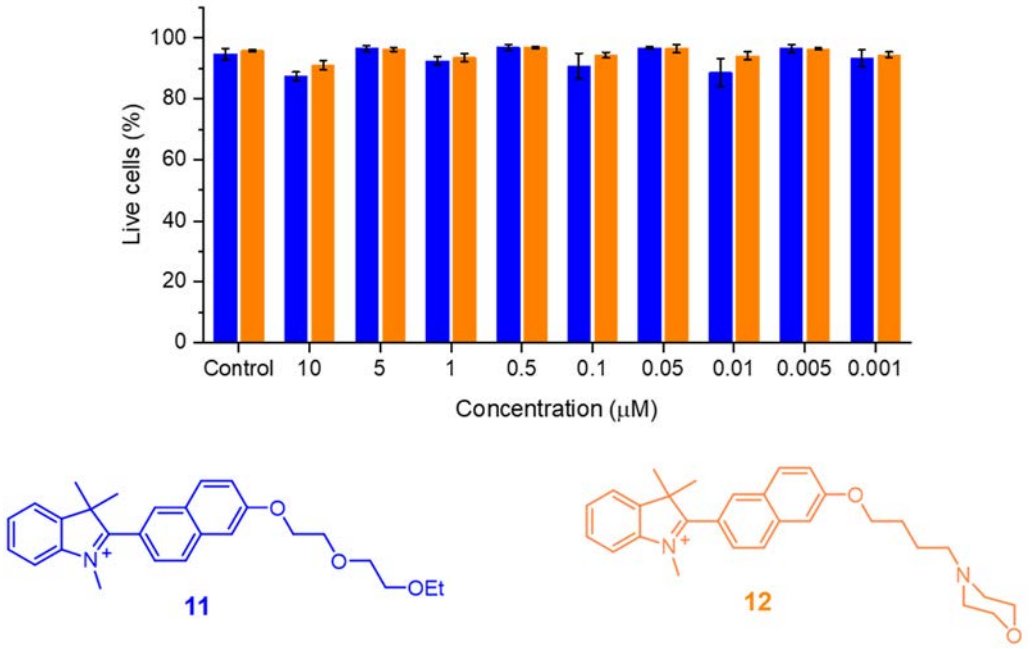

Fig. 84. Cytotoxicity of **11** and **12** on HeLa cells. Data are expressed as mean values and standard error of the mean from four independent experiments (n=4).

5.4.2 Bioimaging studies with compound 11

The initial cells studies with compound **11** revealed an unexpected behavior upon 2P-excitation at 740 nm: an apparently dual emission was observed. Noteworthy, the emissions were separated in two channels: one that ranges from 450 to 520 nm ("green") and other that covers from 580 to 700 nm ("red"). Interestingly, it was observed that these emissions were localized at different subcellular localizations, *i.e.*, the typical filamentous pattern of mitochondria was drawn in the red channel whereas the green one presented multiple and discrete vesicles, likely lysosomes, spread along the cytoplasm.

Different 1P- and 2P-excitation conditions in the microscope were tested to gain insights into this behavior, being attained a selective manner to observe the different described emissions: fluorescence at the green channel can be obtained upon 2P excitation at 740 nm, and the red one can be selectively triggered by 1P excitation at 514 nm (hereinafter

noted as Ind^{Green} and Ind^{Red}, respectively). These results point thus to two emissive species at the subcellular level (**Fig. 85**). Since the observed emissions after 2h of incubation were clearly appreciable (**Fig. 85 a**), the culture medium was then replaced by fresh one without containing compound **11**. This was performed with the aim of examining the evolution of the fluorescence signals. Please note that the emissions observed hereupon outcome from the dye that has been accumulated during the 2h incubation. Images of experiments at long-time expose a decrease in the emission of both channels (**Fig. 85 b**). Furthermore, the merge of fluorescence and brightfield images confirms that no fluorescence signal is observed in other subcellular areas rather than the previous mentioned at any conditions (**Fig. 85 a'** and **b'**).

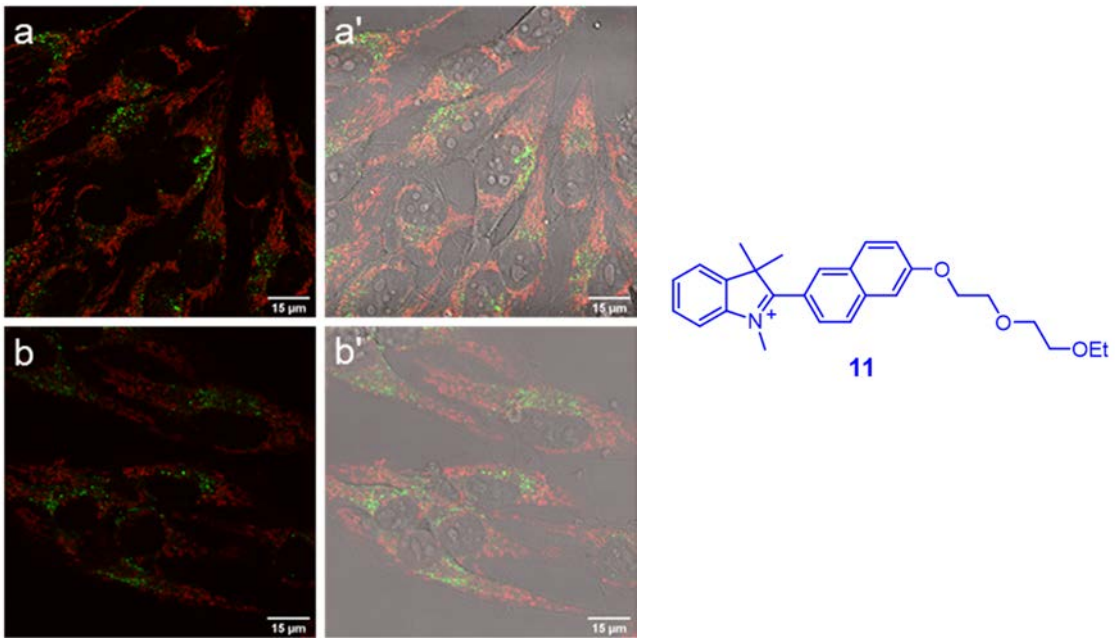

Fig. 85. Fluorescence images within living HeLa cells after incubation with **11** (10 µM in complete medium). Emissions were recorded in two different channels: $\lambda_{exc,\ 2P}$ = 740 nm, λ_{em} = 450 - 520 nm (shown in green, hereinafter noted as Ind^{Green}) and $\lambda_{exc,\ 1P}$ = 514 nm, λ_{em} = 580 - 700 nm (shown in red, hereinafter noted as Ind^{Red}). Images were taken (a) after 2h of incubation and (b) 24h post-incubation. Merged fluorescence/brightfield images are presented in (a') and (b').

In order to ascertain the identity of the subcellular distributions, colocalization experiments were carried out with two photophysically-compatible commercial trackers: Lysotracker

Deep Red (LTDR) was selected to counterstain lysosomes, and Mitotracker Green FM (MTG) to examine the mitochondrial localization. The images obtained are indicated in **Fig. 86** and **87** for the counterstaining of **11** with LTDR and MTG, respectively. These experiments were conducted at short and long-time conditions, and PCCs were determined for the most evident signal combinations.

In **Fig. 86 a** and **b,** the different emissions from the indolinium derivative are represented in green (Ind^{Green}) and red (Ind^{Red}) respectively, being clearly reflected the well-differentiated subcellular distributions. LTDR channel (magenta) is represented in **Fig. 86 c**. All these images were taken at short time experiences. The combination of these three channels is illustrated in **Fig. 86 d**, where small and discrete whitish points, resulting from the sum of green and magenta signals, are detected.

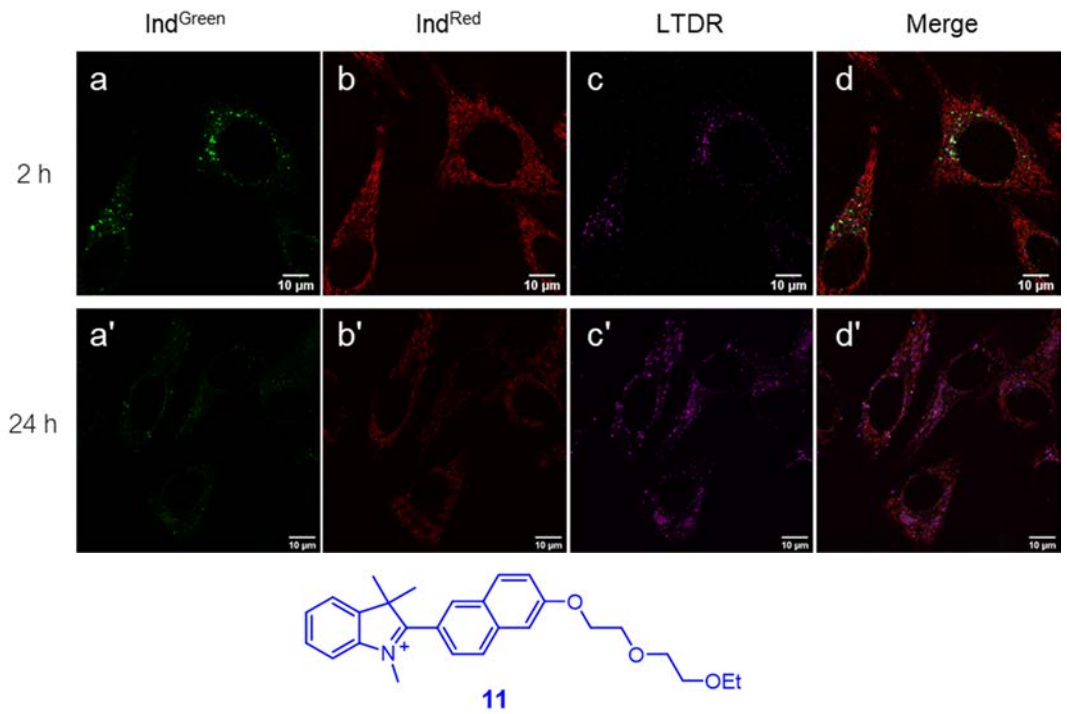

Fig. 86. Colocalization between **11** with LTDR. The following fluorescence channels are shown: (a) Ind^{Green} : $\lambda_{exc,\ 2P}$ = 740 nm, λ_{em} = 450 - 520 nm; (b) Ind^{Red} : $\lambda_{exc,\ 1P}$ = 514 nm, λ_{em} = 580 - 700 nm; (c) LTDR (shown in magenta) = $\lambda_{exc,\ 1P}$ = 633 nm, λ_{em} = 645 - 740 nm. Images were taken (a-d) after 2h of incubation and (a'-d') 24h post-incubation. The fourth column of each panel (d and d') represents a merged overlay of the three separate channels shown in each row.

It is important to note long time experiments, where the lysosomal localization of **11** is practically loss (**Fig. 86 a'**). Consequently, the overlap between Ind^{Green} and LTDR is not appreciable in **Fig. 86 d'**. On the other hand, the mitochondrial distribution is maintained, but showing a marked decrease in the intensity of the Ind^{Red} signal (**Fig. 86 b'**).

The counterstaining with MTG and **11** is represented in **Fig. 87**, where the two different emissions that arise from **11** are in **Fig. 87 a** and **b** (Ind^{Green} and Ind^{Red}, correspondingly), and **Fig. 87 c** refers to MTG (magenta). The overlap in short time experience, shown in **Fig. 87 d**, results in the filamentous pattern of mitochondria totally pink-colored. This fact indicates that red and magenta signals are in good coincidence.

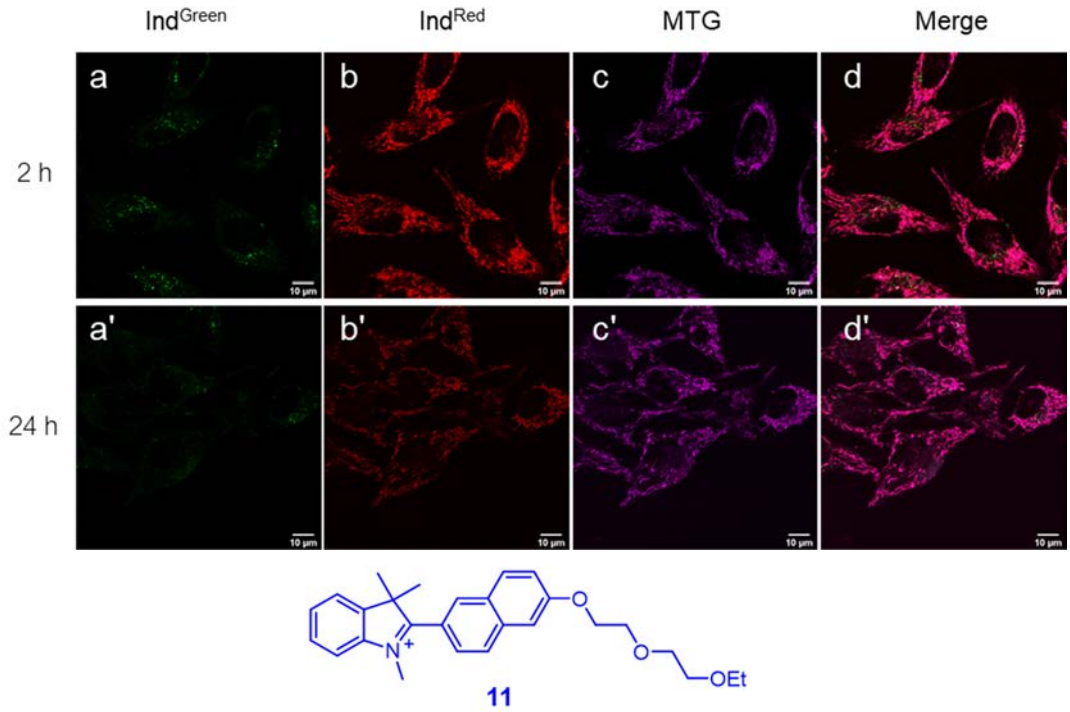

Fig. 87. Colocalization between **11** with MTG. The following fluorescence channels are shown: (a) Ind^{Green} : $\lambda_{exc,\ 2P}$ = 740 nm, (b) λ_{em} = 450 - 520 nm; Ind^{Red} : $\lambda_{exc,\ 1P}$ = 514 nm, λ_{em} = 580 - 700 nm; (c) MTG (shown in magenta) = $\lambda_{exc,\ 1P}$ = 458 nm, λ_{em} = 470 – 560 nm. Images were taken (a-d) after 2h of incubation and (a'-d') 24h post-incubation. The fourth column of each panel (d and d') represents a merged overlay of the three separate channels shown in each row.

In turn, the Pearson Correlation Coefficient (PCC) for **11** and the different commercial trackers are determined in the different experiences. Thereby, PCCs for **11** *vs.* LTDR are calculated from **Fig. 86 d** (short time) and **Fig. 86 d'** (long time) in 0.72 and 0.33, correspondingly. For the mitochondrial localization, the PCCs of MTG *vs.* **11** obtained from **Fig. 87 d** (short time) and **Fig. 87 d'** (long time) are of 0.78 and 0.87, respectively. These data support the previous-made observations over the images, that is, the staining of lysosomes with **11** is not preserved with time. On the contrary, compound **11** displays a good ability to track mitochondria regardless of the time considered.

5.4.3 Bioimaging studies with compound 12

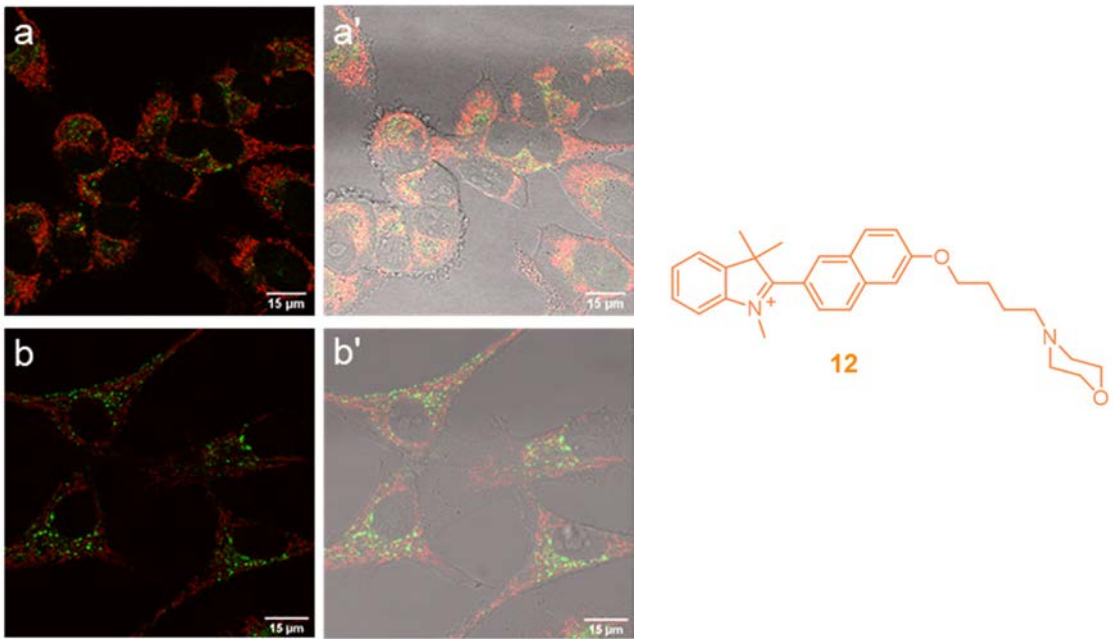

Fig. 88. Fluorescence images within living HeLa cells after incubation with **12** (10 µM in complete medium). Emissions were recorded in two different channels: Ind^{Green} : $\lambda_{exc,\ 2P}$ = 740 nm, λ_{em} = 450 - 520 nm; Ind^{Red} : $\lambda_{exc,\ 1P}$ = 514 nm, λ_{em} = 580 - 700 nm. Images were taken (a) after 2h of incubation and (b) 24h post-incubation. Merged fluorescence/brightfield images are presented in (a') and (b').

Alike **11**, compound **12** displayed an apparent dual emission when incubated in HeLa cells, these located at the same spectral regions and showing similar subcellular distribution (**Fig. 88**). At short time, multiple and discrete points are depicted in Ind^{Green} (**Fig. 88 a**), and Ind^{Red}

appears as a stretched red pattern (**Fig. 88 b**). As intended, **12** seems to exhibit an enhanced lysosome-targeting ability. This is more notable in long-time experiments, in which the number of green spots and their intensity has increased particularly (**Fig. 88 b**) if comparing to those barely observed when using **11** in comparable conditions (*cf.* **Fig. 85 b**). The Ind^{Red} signal, although somewhat reduced, is also visible after 24h post-incubation in **Fig. 88 b**. As it occurs with **11**, fluorescence that outcomes from **12** is not detected at the cytoplasm after merging fluorescence and brightfield images for each time considered (**Fig. 88 a'** and **b'**).

The subcellular localization of **12** was investigated, being the counterstaining of this dye with LTDR or MTG shown in **Fig. 89** and **90**, correspondingly.

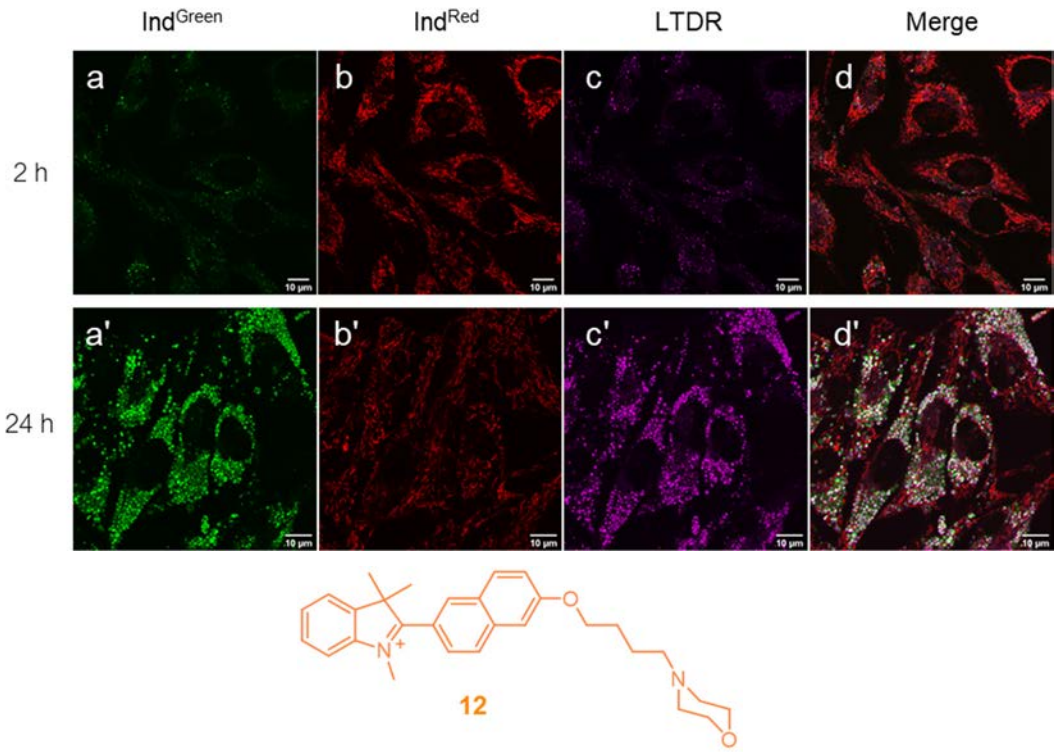

Fig. 89. Colocalization between **12** with LTDR. The following fluorescence channels are shown: (a) Ind^{Green} : $\lambda_{exc,\ 2P}$ = 740 nm, λ_{em} = 450 - 520 nm; (b) Ind^{Red} : $\lambda_{exc,\ 1P}$ = 514 nm, λ_{em} = 580 - 700 nm; (c) LTDR (shown in magenta) = $\lambda_{exc,\ 1P}$ = 633 nm, λ_{em} = 645 - 740 nm. Images were taken (a-d) after 2h of incubation and (a'-d') 24h post-incubation. The fourth column of each panel (d and d') represents a merged overlay of the three separate channels shown in each row.

When examining the lysosomal localization of **12**, it is found that the overlap of Ind^{Green} with LTDR (magenta) is considerable in both short and long-time conditions (**Fig. 89 d** and **d'**, respectively), although it is more evident with the passage of time (**Fig. 89 d'**). In this last image, numerous white discrete points are easily recognized.

Moreover, compound **12** shows a similar performance to label mitochondria to that displayed by **11**. This is illustrated in **Fig. 90 d** and **d'** for short- and long-time conditions, respectively. In both images mitochondria are labelled in pink, which results from the sum of Ind^{Red} and MTG channels.

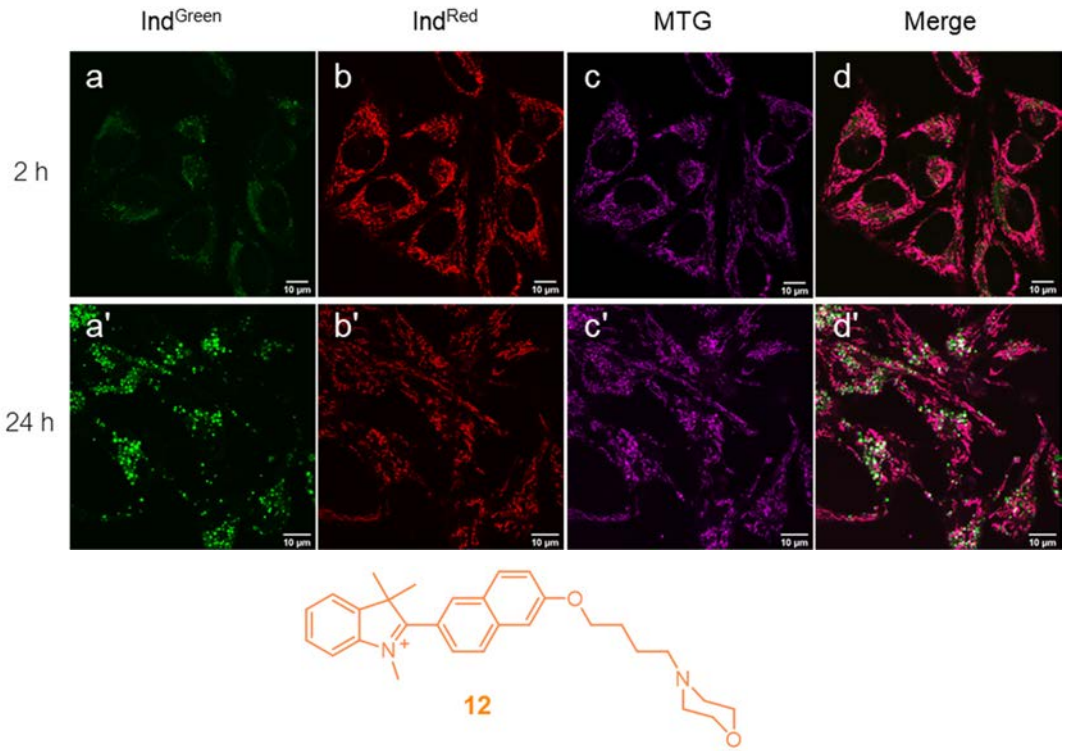

Fig. 90. Colocalization between **12** with MTG. The following fluorescence channels are shown: (a) Ind^{Green} : $\lambda_{exc,\ 2P}$ = 740 nm, (b) λ_{em} = 450 - 520 nm; Ind^{Red} : $\lambda_{exc,\ 1P}$ = 514 nm, λ_{em} = 580 - 700 nm; (c) MTG (shown in magenta) = $\lambda_{exc,\ 1P}$ = 458 nm, λ_{em} = 470 – 560 nm. Images were taken (a-d) after 2h of incubation and (a'-d') 24h post-incubation. The fourth column of each panel (d and d') represents a merged overlay of the three separate channels shown in each row.

As previously indicated, with time, a similar behavior from the displayed by **11** is appreciated in the Ind^{Red} signal from **12**. When comparing **Fig. 89 b** *vs.* **89 b'** and **Fig. 90 b** *vs.* **90 b'**, long-time conditions are translated into a decrease of the fluorescence detected from mitochondria. In stark contrast, the Ind^{Green} signal from **12** increases with time, which indicates this dye as a better dual tracker for lysosomes and mitochondria (see **Fig. 89 a** *vs.* **89 a'** and **Fig. 90 a** *vs.* **90 a'**).

Then PCCs are calculated for each experience. The PCCs for **12** *vs.* LTDR obtained from **Fig. 89 d** (short time) and **Fig. 89 d'** (long time) were of 0.74 and 0.77, respectively. Likewise, PCCs of MTG *vs.* **12** were determined from **Fig. 90 d** (short time) and **Fig. 90 d'** (long time) in 0.93 and 0.79, respectively. These values support the visual analysis performed over the images.

When comparing the PCCs for mitochondrial **12** *vs.* MTG, it is however noticed that this decreases with time. This fact is contradictory with the observed in the merged Ind^{Red} and MTG (magenta) images at long time experiences (**Fig. 90 d'**), where the overlap is clearly reflected through the pink pattern. Nevertheless, in this image a considerable amount of discrete whitish points can also be detected. These white points are resulting from the sum of the green **12** and MTG (magenta) signals. That is, it seems that there is a population of lysosomes that probably contain MTG within them.

Indeed, MTG can label both healthy mitochondria as well as injured ones (both MDVs or mitochondria being engulfed by lysosomes), and has been used to study mitophagy process.[397–399] Thus, these white points could be ascribed to mitochondria being degraded by lysosomes. A more detailed image analysis was performed to deepen in this behavior (**Fig. 91**). This analysis was realized over the long-time experiment images **Fig. 90 a'-d'**.

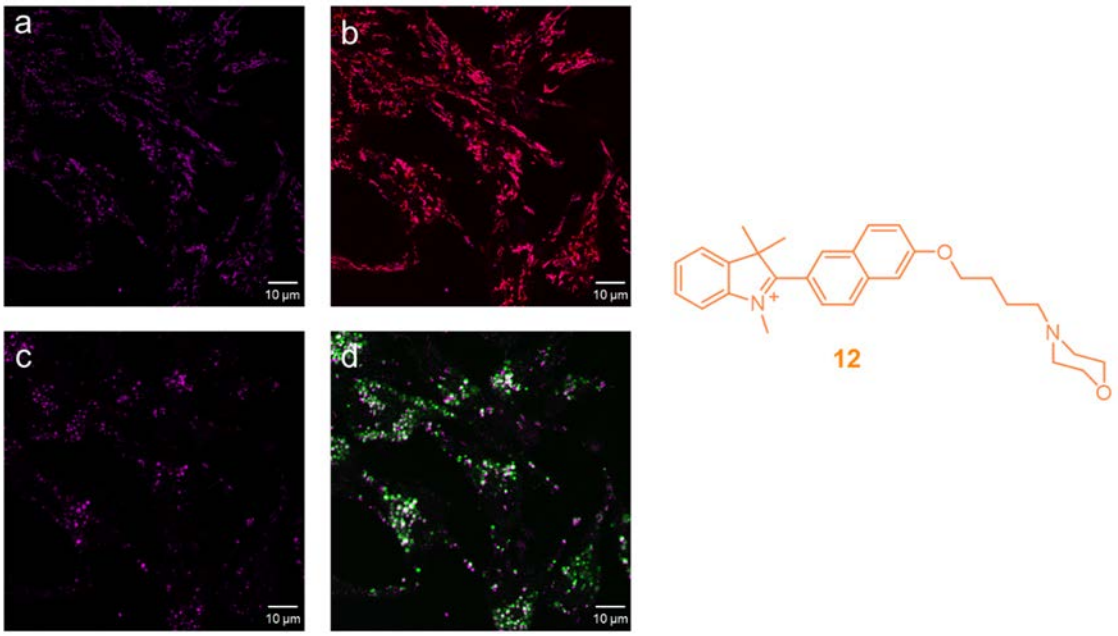

Fig. 91. Analysis of the images from counterstaining MTG vs. **12** in long-time conditions (Fig. 90 a'-c'). The following operations were performed: (a) subtraction of Ind^{Green} from **12** to MTG signal (**Fig. 90c'** *minus* **Fig. 90 a'**), (b) merge between (a) and Ind^{Red} (**Fig. 91 a** *plus* **Fig. 90 b'**); (c) subtraction of Ind^{Red} from **12** to MTG signal (**Fig. 90c'** *minus* **Fig. 90 b'**); and (d) merge between (c) and Ind^{Green} (**Fig. 91 a** *plus* **Fig. 90 a'**)

When subtracting the lysosomal emission from **12** to MTG signal (*i.e.*, **Fig. 90 c'** *minus* **Fig. 90 a'**) an interesting result is addressed: the remaining signal from MTG shows a clear filamentous distribution. Please note that in **Fig. 90 c'**, discrete magenta points are also appreciated. The merge of this resulting image (**Fig. 91 a**) with the mitochondrial emission from **12** (**Fig. 90 b'**) is in good coincidence, as displayed in **Fig. 91 b**. Thus, this observation suggests that the observed points at **Fig. 90 c'** are like lysosomes or mitochondria being engulfed by the former.

Additionally, the emission from mitochondrial **12** emission (**Fig. 90 b'**) is subtracted to MTG fluorescence (**Fig. 90 c'**). In the resulting image **Fig. 91 c**, multiple discrete points are now appreciated. Moreover, these points are partially overlapped with the green emission of **12**, as regards to the presence of white points in **Fig. 91 d** in which **Fig. 91 c** and **Fig. 90 a'** (lysosomal emission from **12**) are overlapped.

All in all, the points observed in **Fig. 91 c** could be mitochondria being degraded. Although further experiments are required to deepen in this issue, these observations point compound **12** as a good candidate for tracking mitophagy.

5.5 UNDERSTANDING THE WORKING PRINCIPLE: ADDITIONAL PHOTOPHYSICAL STUDIES

Considering that subcellular environments are responsible of the observed optical properties for these compounds, additional photophysical studies were performed to deepen in the behavior of these dyes. Although it is practically impossible to faithfully reproduce organelles conditions *in vitro* considering that numerous biological and processes are participating in the function of these suburbs, we attempted to gain insights into how the different properties of lysosomes and mitochondria (mainly *pH* and viscosity),[322,400] are linked to the unexpected photophysical behaviors of these dyes *in vivo*. Please note that some environmental factors and its influence on the optical properties have yet been examined. In Section 5.3.2, it was studied the interaction of these compounds with diverse biologically relevant species in diluted aqueous solutions, without these addressing significant changes to the optical properties. Moreover, it was demonstrated in **Chapter 3** that viscosity only affects to the emission intensity and the fluorescence quantum efficiency of the fluorophore moiety, but not to the spectral position of the bands.

5.5.1 pH titrations

The possible effect of *pH* over the fluorophore was studied, being the results obtained represented in **Fig. 92**. Looking at this figure, it is observed that fluorescence emission is maintained at acid to neutral conditions (*pH*s 4 and 6), where both compounds exhibit the same optical features. However, a considerable decrease is observed at *pH* 8, where both emission and absorptions bands are halved. At more basic conditions (*pH* 10), these bands suffer a dramatic decrease. Otherwise, this behavior is expected if taken into account that the nucleophilic character of the hydroxyl ion and the electrophile one from the indolinium

ring. The disappearance of the emission band is very likely due to loss of the π-conjugated system as a result of a nucleophilic addition.

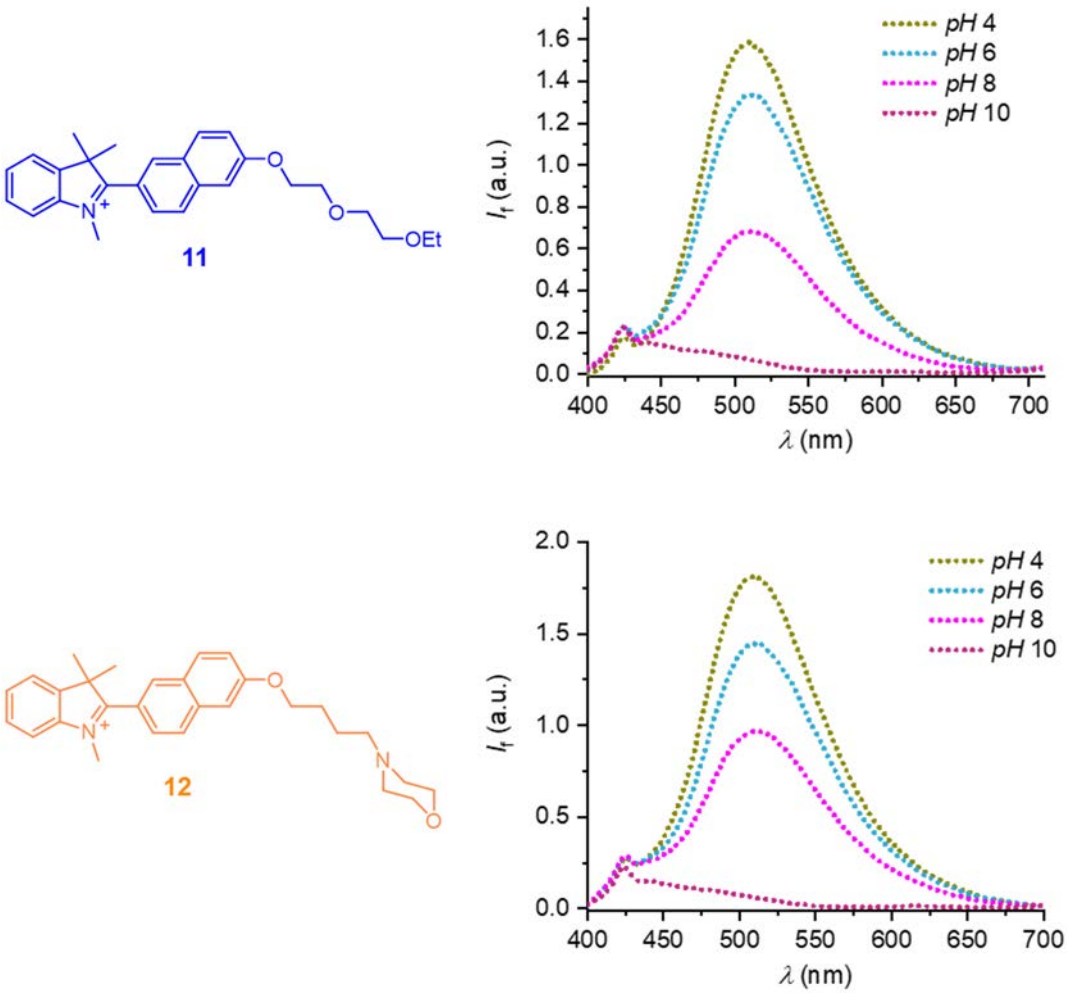

Fig. 92. Absorption (left) and emission (right) spectra of **11** and **12** at different pH (10 μM air-equilibrated distilled water solutions). *pH* was adjusted by adding NaOH 1M or HCl 1M while measuring with a calibrated *pH*-meter. Emission was recorded upon excitation at 370 nm.

5.5.2 Aggregation studies: optical properties of the aggregates

As pH alone (as well as viscosity) seems unlikely to be sufficient to mediate these differential emissions, we investigated self-assembly effects by increasing the compounds

concentration from 10^{-5} M to 10^{-2} M in acetonitrile solutions (**Fig. 93**). These studies lay on a) *J*-aggregation phenomena has previously been reported to some cyanine dyes within mitochondria[393] and b) the changes in the optical properties caused by the formation of this type of assemblies are very similar to the ones demonstrated by our derivatives. That is, *J*-aggregate's formation entails red-shifts in both excitation and emission spectra, being more pronounced in the excitation ones. These trends are certainly the ones exhibited by **11** and **12** within cells. Gratifyingly, in **Fig. 93** it can be appreciated how both emission and excitation are red-shifted when increasing the concentration of the compound.

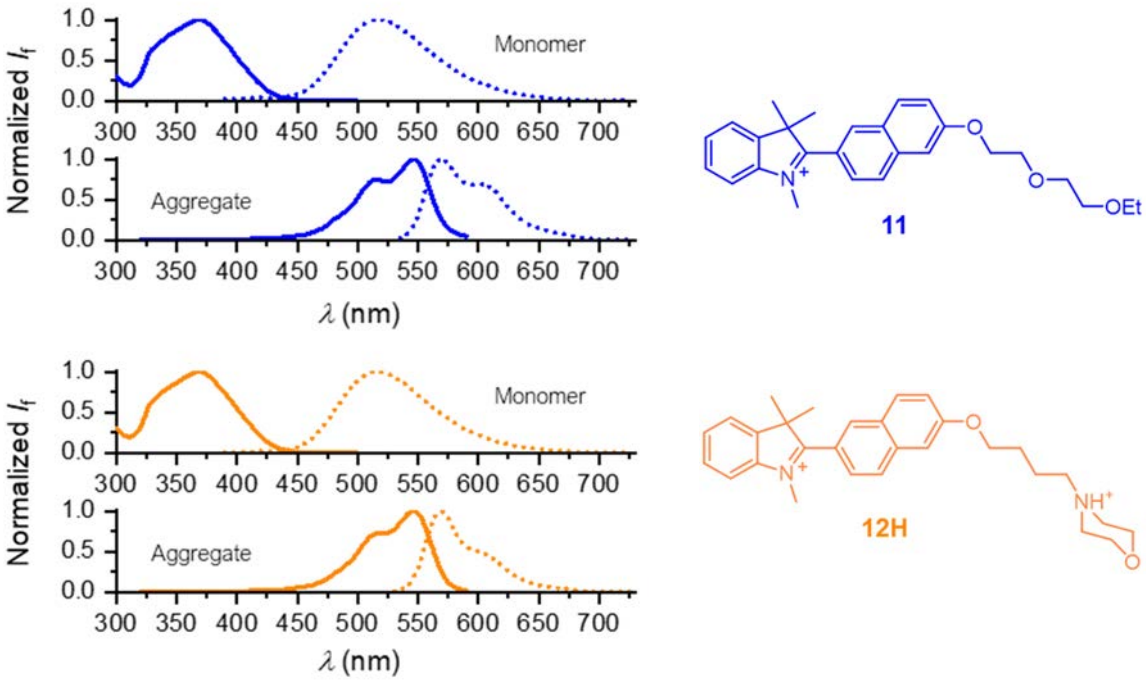

Fig. 93. Emission (dotted lines) and excitation (solid lines) of **11** (blue lines) and **12H** (orange lines) at 10^{-5} M (monomer) and 10^{-2} M (aggregate) in acetonitrile solution.

More specifically, the excitation bands move from 370 nm in high diluted conditions to ~540 nm in the aggregated state. Further, the change in the emission is not as pronounced, and the maxima of the bands are approximately displaced from 515 to 580 nm. Noteworthy, both compounds exhibited similar trends and these are coincident with the optical properties observed in mitochondria, which strongly suggests that self-assembling is

substantially favored in this organelle. The absence of aggregation-quenching effects on emission intensities is also consistent with the formation of these high-ordered structures.

Additionally, the absence of secondary photochemical processes when these structures are formed was assessed, *i.e.*, these assemblies neither they suffer from photobleaching when they are continuously irradiated (**Fig. 94**).

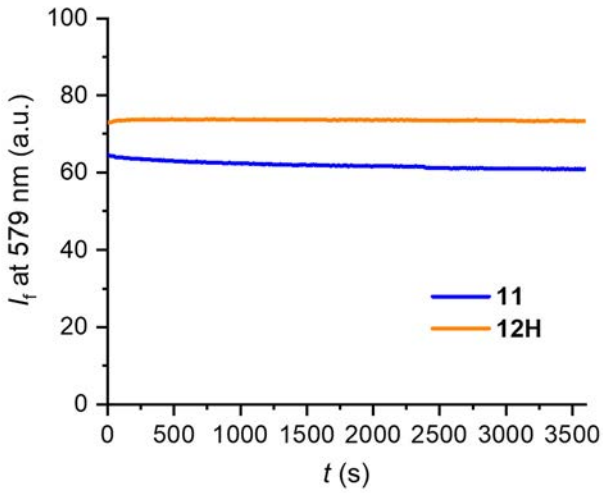

Fig. 94. Photostability of **11** and **12H** in acetonitrile (10^{-2} M, air-equilibrated solutions). Compounds were excited continuously at 540 nm for 1 hour and the emission registered at 580 nm.

Finally, it was examined how *pH* and viscosity can affect self-assembly phenomena for a closer approximation to the *in vivo* situation. These studies were carried out combining these parameters by means of different *pH* adjusted water/glycerine mixtures (**Fig. 95**). A similar behavior is observed in both acid and basic non-viscous conditions (**Fig. 95 a** and **c**, respectively), where the emission from the aggregate state is superior to that of the monomer one. Only when placing high viscosity and acid *pH,* (**Fig. 95 b**) the monomer emission bands are favored over those of the aggregates, being these conditions closer to lysosomal environment. The combination of basic and viscous conditions results in the loss of the emission of both monomers and aggregates (**Fig. 95 d**), which can be ascribed to the formation of a precipitate in the cuvette. All together, these data indicate that *pH* and viscosity could partially support as why aggregate formation is not occurring in lysosomes.

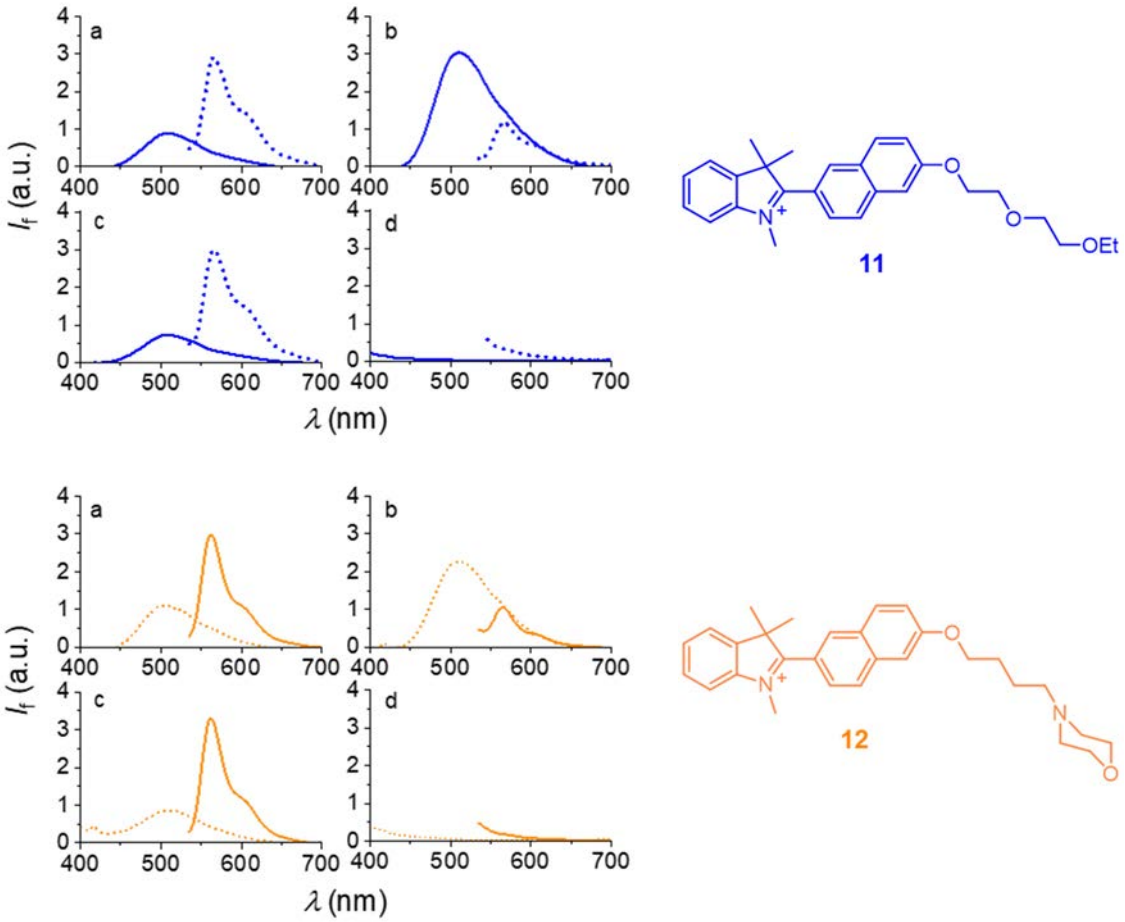

Fig. 95. Emission of compound **11** and **12** (10^{-2} M air-equilibrated solution) upon excitation at 370 nm (solid lines) and at 520 nm (solid lines). The solvent systems employed were: (a) *pH* 4 aqueous solution, (b) *pH* 4 aqueous solution/glycerin mixture (1:1), (c) *pH* 8 aqueous solution and (d) *pH* 8 aqueous solution/glycerin mixture (1:1).

5.5.3 Bioimaging studies at different concentrations

Further studies were performed at the subcellular level to evaluate the *J*-aggregation phenomena observed in mitochondria. Since **12** demonstrates an enhanced ability for the dual staining, we decided to perform this experiment only using this dye. Considering that the concentration of the dye is critical for this process to occur,[401,402] **12** was incubated at different concentrations for two hours as illustrated in **Fig. 96**.

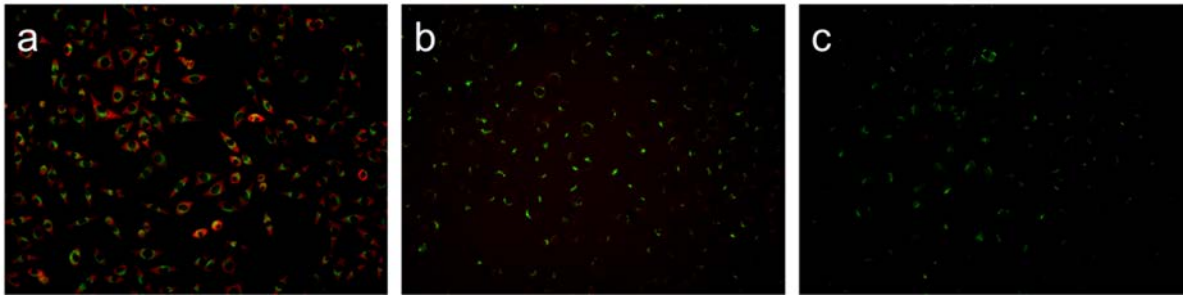

Fig. 96. Fluorescence images within living HeLa cells after 2h incubation with **12** at different concentrations: (a) 10 μM, (b) 5 μM and (c) 1μM. The following fluorescence channels are shown: (a) Ind^{Green} : $\lambda_{exc,\ 2P}$ = 740 nm, (b) λ_{em} = 450 - 520 nm; Ind^{Red} : $\lambda_{exc,\ 1P}$ = 514 nm, λ_{em} = 580 - 700 nm.

Whereas the lysosomal staining is apparently independent of the concentration employed, the signal that outcomes from mitochondria seems to be extremely dependent on the concentration of the compound. Thereby, it can be appreciated how the red signal is practically lost when incubating with a complete medium solution containing 5 μM (**Fig. 96 b**) of **12** instead of 10 μM (**Fig. 96 a**). At lower concentrations (1 μM, **Fig. 96 c**), this trend is consistent, that is, no emission is observed in the red channel.

5.6 SUMMARY

Two different indolinium-based compounds (**11** and **12**) have been developed. As these dyes incorporate the same chromophoric moiety, comparable photophysical properties are attained. These derivatives offer the interesting possibility of dual-color and simultaneous labelling of mitochondria and lysosomes, especially compound **12**. The performance of these compounds is not solely compromised on the mitophagy occurrence, and the double staining is observed even if looking at short time incubation experiences. This selective difference seems to be related to aggregation processes, which in turn builds on a junction of different subcellular conditions. Although further studies will be required to demonstrate the potential of these compounds, compound **12** seems track mitophagy. It is very likely that these compounds could play a key role in providing biorelevant knowledge about the interactions between the mitochondria and lysosomes, facilitating information about the biological processes in which these organelles participate.

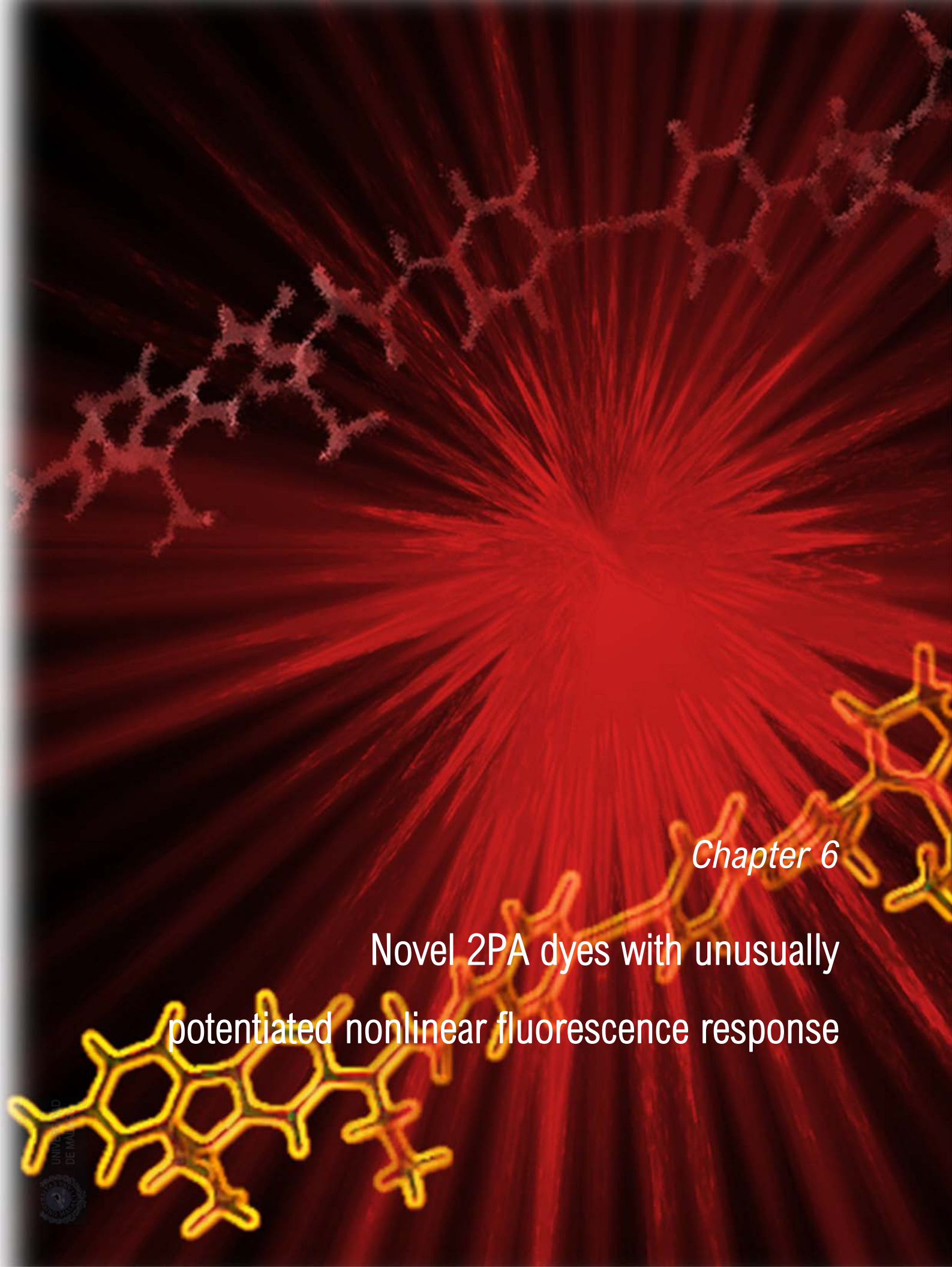

Chapter 6

Novel 2PA dyes with unusually potentiated nonlinear fluorescence response

6.1 INTRODUCTION

6.1.1 Photochromic molecules: an overview

Photochromism is a reversible transformation between two isomers of a chemical species having different absorption spectra, which can be induced in one or both directions by electromagnetic irradiation.[403–405] Some of the most representative examples of photochromic compounds are represented in Fig. 97.

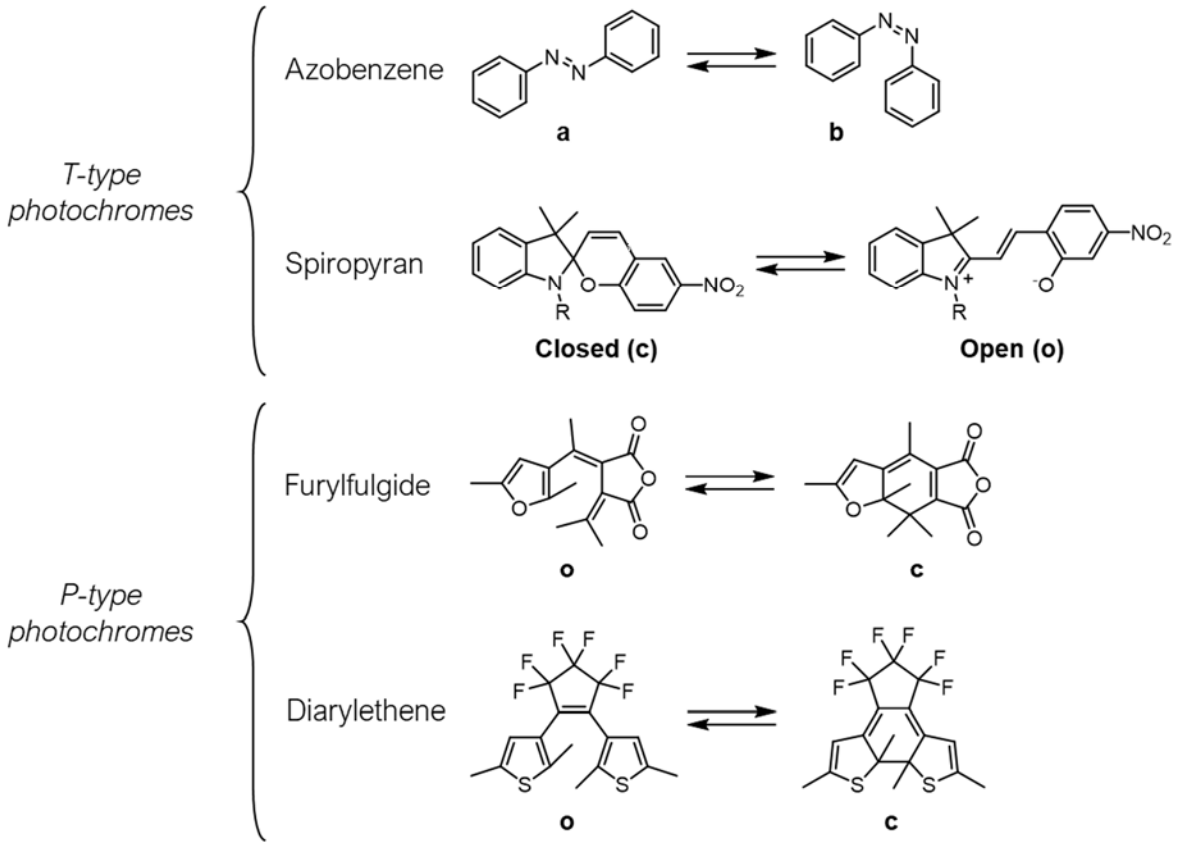

Fig. 97. Representative examples of photochromic molecules

The most common classification of photochromic molecules attends to the thermal reversibility or not. Thereby, two main groups are distinguished:

→ **T-type photochromic molecules**: the majority of the reported photochromes correspond to this type. Among them, azobenzenes and spiropyrans are the most investigated. Such compounds are characterized for being thermally reversible, *i.e.*, one of the isomers is thermally unstable and photoisomerization process is reverted to the action of temperature (and time). Particularizing at the azobenzene example, the so-called "a" form is colorless. UV light prompts the formation of the colored "b" form. However, when keeping this isomer in the dark at room temperature, the color is loss due to the thermal isomerization that provides the initial "a" form.

→ **P-type photochromic molecules:** in contrast to the previous one, the photoisomerization between the two isomers is thermally irreversible but photochemically reversible in these dyes. In other words, both isomers are thermally stable, and the use of different wavelength lights conduct to the formation of one of these structures. The number of families of compounds with this behavior is however relatively limited, and furylfulgide and diarylethene are the most common ones. In both shown cases in **Fig. 97**, irradiation with UV light achieves the closed (c) forms. This chemical transformation is characterized for involving the establishment of a six-member ring with subsequent reorganization of the π-conjugated system. In consequence, the absorption bands of the "c" forms are red-shifted respect to those of the open (o) forms. Thus, visible light is responsible for the photoisomerization from "c" to "o".

Although the choice of one or other type of photochromes depends on the intended use, thermal irreversibility is crucial for their application in photonic devices, as for example, optical memories, switches or molecular machines. Besides, other features are highly desired for such applications: 1) fatigue-resistance property, 2) high sensitivity and 3) rapid response. Among the derivatives presented in **Fig. 97**, well-designed diarylethene dyes fulfill all these requirements, and especially dithienylethenes (DTEs).[406,407] The best performance of DTEs includes:

→ Both isomers display a half-life time of thermal isomerization at room temperature greater than 400000 years.

→ Ring-closing or -opening cycles can be repeated more than 10000 times.

→ Isomerization reactions occur in a picosecond time region, and usually displaying good isomerization quantum yield for the closing reaction.

This project detailed below was performed in residence at Chalmers University of Technology under the supervision of Prof. Dr. Joakim Andréasson. All the compounds presented in this study were kindly provided by his research group.

6.2 MOLECULAR DESIGN

6.2.1 Working principle

The system proposed in this Chapter (**Fig. 98**) combines a 2PA dye with a photochromic system within a single scaffold. Although the structural components are intentionally electronically decoupled as detailed below, they can communicate each other by Förster resonance energy transfer (FRET). Please note that for FRET to occur efficiently, it is required a) an optimal donor-acceptor distance, and b) a prominent spectral overlap between the emission from the donor and the absorption of the acceptor. Thus, the design criteria for the system **14o**/**14c** are oriented to fulfill the Förster theory. The system can be described as below:

→ **A FRET acceptor**: a DTE photoswitch, highlighted in red in **Fig. 98.**

→ **A FRET donor**: a fluorene derivative, marked in blue in **Fig. 98**. This unit was selected for procuring a suitable overlap integral (J) between its emission and the longest absorption wavelength of DTE. As well, this type of fluorophores demonstrated suitable 2PA properties.[142]

→ **A fine-designed spacer:** the insulating spacer should limit the conformational freedom without disturbing the photophysical properties of the two abovementioned components. The selected bridge also provides of a restricted geometry, allowing the knowledge of the distance between the donor and the acceptor and thus, an accurate treatment of the photophysical events.

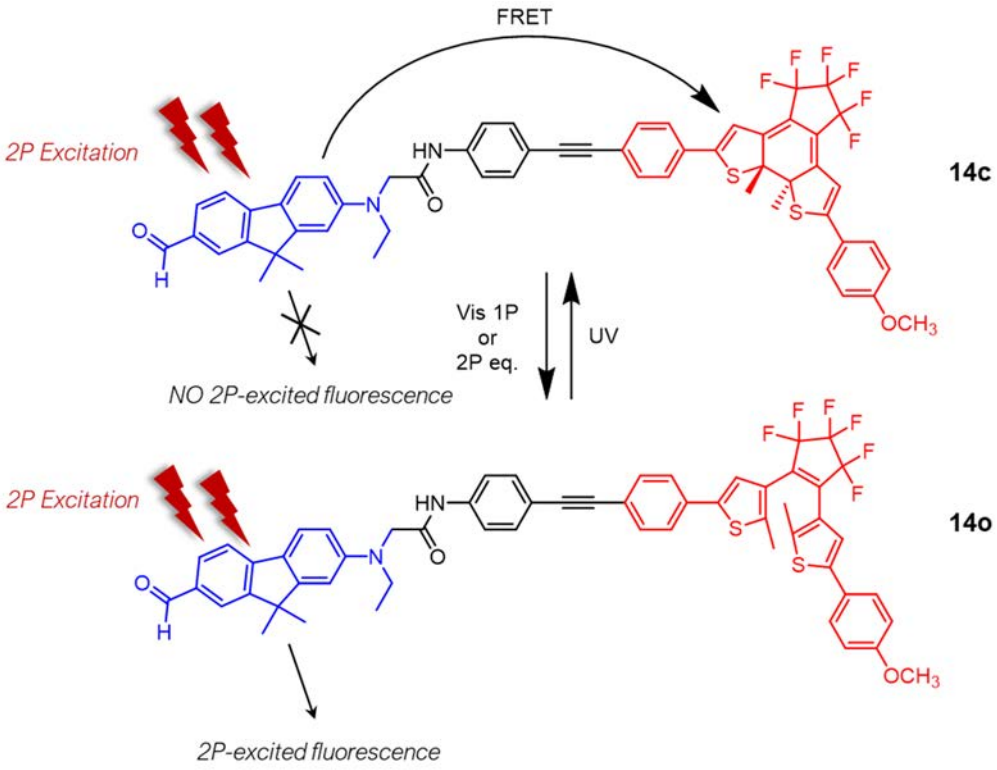

Fig. 98. Working principle of a photochromic dyad (**14**) having a DTE appended to a 2PA dye. The FRET acceptor, FRET donor and the used bridge are distinguished in red, blue, and black, respectively.

In our specific case, FRET would imply the closed form but not the colorless open one. Thereby, the fluorescence from the fluorene unit would be quenched by FRET in the **14c** isomer. This FRET process would sensitize the isomerization to the **14o** form, in which the 2P-excited fluorescence from the fluorene would arise. The combination of these two two-photon induced processes, that is, a) FRET sensitized isomerization that yields the emissive form of the dyad and b) the 2P-excited fluorescence, will affect directly to the emission intensity dependence on the laser power.

Under ideal conditions, the fluorescence of the considered system will respond to **Eq. (6)**,

$$I_f = I_{f,\infty} (1 - e^{kt}) \qquad \textbf{Eq. (6)}$$

where t is the time, I_f is the fluorescence, $I_{f,\infty}$ is the fluorescence at infinite, and k is the rate of the isomerization process.

Since the coupled processes are 2P-mediated, the effect on duplicate the intensity of the laser would be translated into a 4-fold increase in both $I_{f,\infty}$ and k owing to the quadratic dependence of the fluorescence intensity on the laser power. Thus, two different situations can be figured: one at half intensity of the laser power, and other one when using the full intensity (**Fig. 99 a**). The dynamic range among these conditions (*i.e.*, the quotient between the associated curves) would lead to a quartic dependence for the first instances of the photochromic conversion, obtaining a difference up to 16 times at time zero as represented in **Fig. 98**. Once all **14c** is converted, the usual quadratic dependence, arising from two-photon-excited fluorescence, would apply for (**Fig. 99 b**).

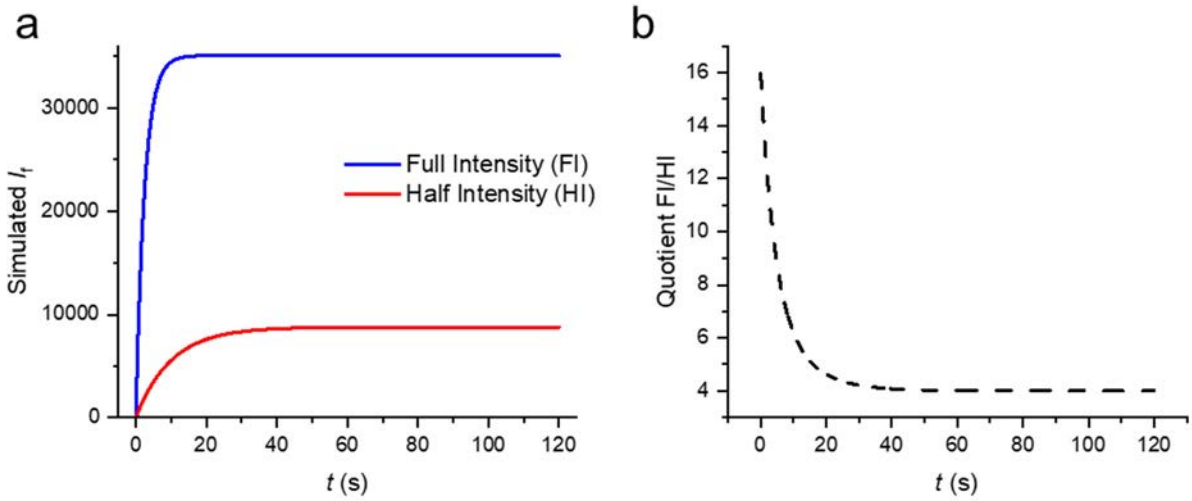

Fig. 99. (a) Modeling of the FI and HI conditions according to **Eq. (6)** and (b) dynamic range between FI and HI.

This quartic dependence is typically observed in systems absorbing simultaneously four photons. Considering that the occurrence of the multiphotonic absorption process is confined to a smaller space as long as photons are simultaneously involved, this novel dyad system, displaying a similar performance that a 4PA dye, would achieve a dramatic improvement of the spatial resolution by combining two two-photon mediated processes. Thereby, the applications in which 2PA process is essential and whose major downside is the three-dimensional resolution, would be improved by this novel strategy.

6.3 PHOTOPHYSICAL STUDIES

6.3.1 Characterization of the model compounds

Prior to the synthesis of the dyad, the optical properties of the isolated models that compose the system were studied. Their structures are indicated in **Fig. 100**.

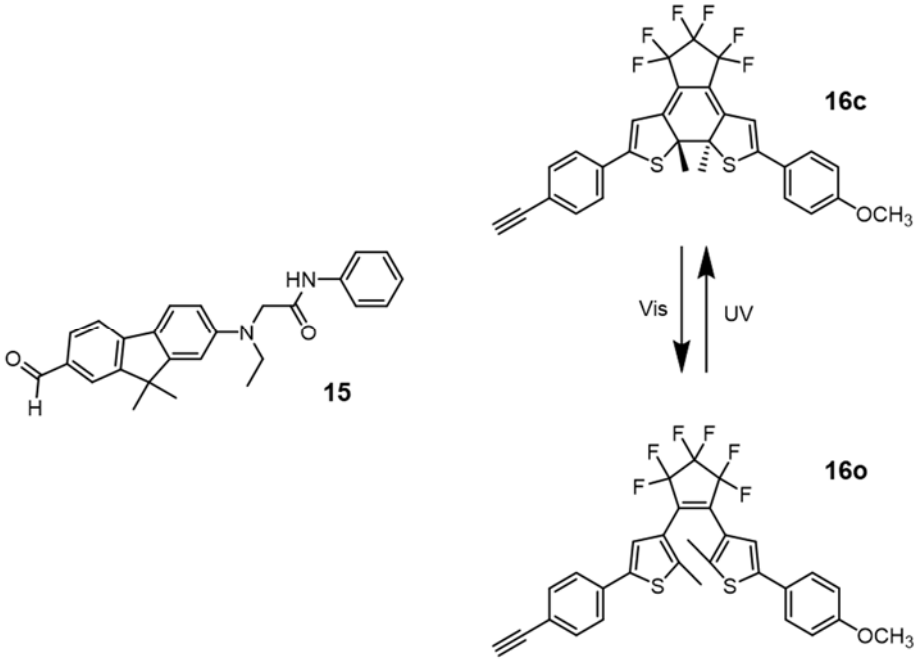

Fig. 100. Structure of the model fluorene (**15**) and DTE (**16**).

In stark contrast to most of DAEs, fluorenes such as the one employed in this Chapter exhibit prominent solvatochromism. Thereby, the solvent is critical for the system to function, and methanol was considered appropriate attending to the previous reported data for a similar fluorene and those of the model DTE.[142,403,408] In this solvent, **15** displays a structureless absorption band at 377 nm (**Fig. 101**). The excitation at this wavelength leads to a broad intramolecular charge-transfer band in the emission spectrum, with maximum at 555 nm (ϕ_f = 0.36, fluorescence lifetime (τ_f) = 2.4 ns).

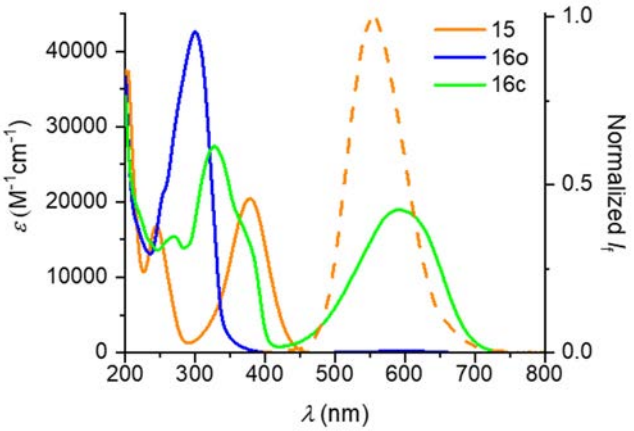

Fig. 101. Absorption spectra (solid lines) of the model compounds in methanol (**15**, orange line; **16o**, blue line; **16c**, green line; 10 μM aerated solutions). In addition, the emission spectrum of **15** is shown as dashed orange line.

Table 7. Photophysical relevant data of the models **15** and **16** in methanol (10 μM aerated solution).

Compound	λ_{abs} (nm) [ε ($M^{-1}cm^{-1}$)]	λ_f (nm)	ϕ_f	τ_f (ns)
15	336 [34900]	555	0.36	2.4
16o	302 [49600]	n.d.[b]	n.d.[b]	n.d.[b]
16c [a]	592 [18700]	n.d.[b]	n.d.[b]	n.d.[b]

[a] It actually refers to the observed properties at the Photostationary State (PSS), which mainly consist of **16c**.[408]

[b] n.d.: not determined.

On the other hand, **16o** exhibits an absorption band with maximum at 302 nm. Note that no absorption is appreciated in wavelengths larger than 400 nm for this molecule in **Fig. 101**, dismissing thus any possibility of FRET between **15** and **16o**. The treatment of **16o** with UV light (302 nm) efficiently leads to a blue solution through the enrichment in the closed isomer **16c**. Although the main component at the Photostationary State (PSS) is certainly the closed isomeric form, both photoisomers are present in the solution at this stage. All the same, when comparing the absorption spectrum of the PSS with that of isolated **16o**, it can be confirmed that the lower energy band (centered at 592 nm, **Fig. 101**) corresponds exclusively to **16c**. All these data are duly summarized in **Table 7**.

Moreover, with this data and following Förster theory,[409] the overlap integral [$J(\lambda)$] for the pair **15**/**16c** was calculated as 1.54 x 10^{15} nm^4 $(M\ cm)^{-1}$ by using a|e - UV-Vis-IR Spectral Software.[410] This value results from the spectral overlap between the emission from the donor and the absorption of the acceptor, and was determined according to **Eq. (7)**:

$$J(\lambda) = \int_0^\infty \varepsilon_A(\lambda)\, \lambda^4\, F_D(\lambda)\, d\lambda \qquad \textbf{Eq. (7)}$$

where ε_A is the extinction coefficient spectrum of the acceptor in units of $M^{-1}cm^{-1}$, λ is the wavelength in nm and F_D is the wavelength dependent donor emission spectrum normalized to an area of 1.

The critical Förster radius (R_0), that is, the maximal length between donor and acceptor molecules under which resonance energy transfer yet to occur, was calculated as 47 Å by means of **Eq. (8)**:

$$R_0 = 0.211 \left[\frac{\kappa^2\ \phi_{f,D}\ J(\lambda)}{n^4}\right]^{1/6} \qquad \textbf{Eq. (8)}$$

where κ^2 is an orientation factor between the donor and acceptor (assumed as 2/3), n is the refractive index, and $\phi_{f,D}$ is the fluorescence quantum yield of the donor in absence of the acceptor.

Furthermore, the 2PA properties of **15** were examined *via* 2P induced fluorescence between 700 nm and 1000 nm.[394] Looking at **Fig. 102 a**, it has been founded that the 2PA spectrum features a maximum at 770 nm with a significant 2PA cross section (σ_{2PA}) of 156 GM. Moreover, this spectrum resembles the 1P absorption when the wavelength scale is conveniently adapted, *i.e.*, $\lambda_{2PA} \approx 2\lambda_{1PA}$. Likewise, the 2P-excited fluorescence essentially coincides with the registered under 1P conditions, confirming that the same excited state is involved in either process. The double logarithmic plot, shown in **Fig. 102 b**, confirms the two-photon absorption occurrence because the closeness to 2 of the slope.

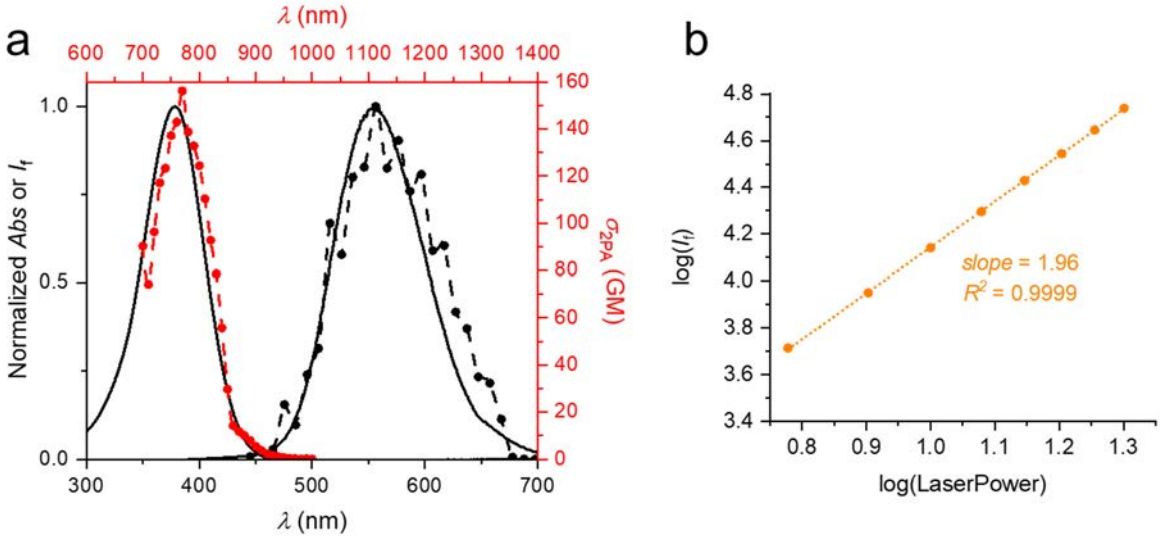

Fig. 102. (a) One-photon absorption (left) and fluorescence (right) spectra of **15** (black solid lines), and energy-scaled two-photon absorption spectrum (red dashed line and red points) and the two-photon-excited fluorescence spectrum (black dashed line and black points); 10 μM in methanol. (b) Double-logarithmic plot of the emission maximum intensity versus laser power for **15**. The dashed line represents the linear regression fittings.

6.3.2 Characterization of the dyad

Once having studied the properties of the isolated model compounds, the photophysical properties of the dyad **14**, in both isomeric forms, were examined.

Table 8. Photophysical relevant data of the dyad **14** in methanol (10 μM aerated solution).

Compound	λ_{abs} (nm) [ε (M^{-1} cm^{-1})]	λ_f (nm)	ϕ_f	τ_f (ns)
14o	378 [20400]	555	0.36	2.4
14c[a]	600 [49600]	-[b]	-[b]	-[b]

[a] It actually refers to the observed properties at the Photostationary State (PSS), see details below.

[b] Some residual fluorescence is observed due to the presence **14o** in the photostationary state, see details below.

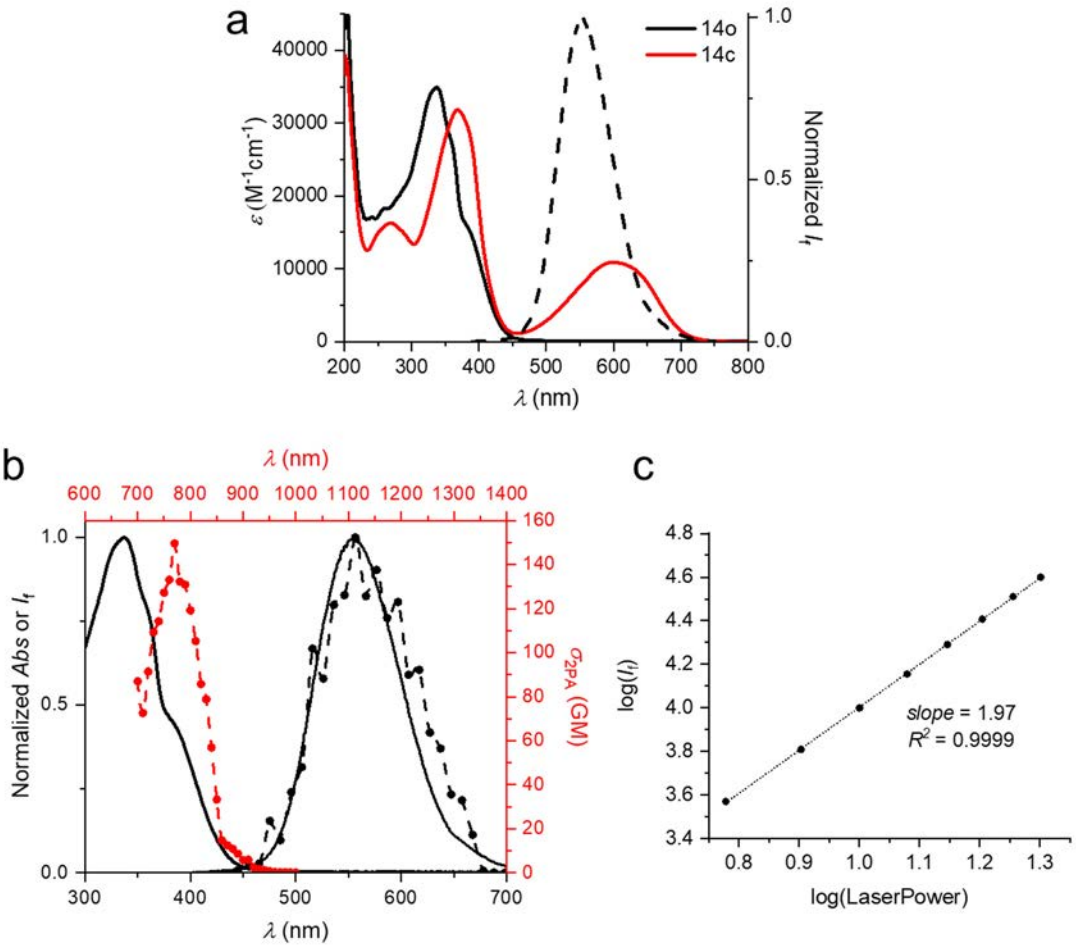

Fig. 103. (a) Absorption spectra (solid lines) of the dyad in both isomeric forms in methanol (**14o**, black line; **14c**, red line). The **14o** emission spectrum is shown as dashed black line. (b) One-photon absorption (left) and fluorescence (right) spectra of **14o** (black solid lines), and energy-scaled two-photon absorption spectrum (red dashed line and red points) and the two-photon-excited fluorescence spectrum (black dashed line and black points); 10 μM in methanol. (c) Double-logarithmic plot of the emission maximum intensity versus laser power for **14o**. The dashed line represents the linear regression fittings.

When looking at the open form (**14o**), regardless of the excitation conditions, it is noteworthy that similar optical features to that of the model **15** were observed. Briefly, the absorption band of the fluorene appears together with the one from the DTE, looking like a shoulder at *ca.* 384 nm. The excitation at this wavelength leads to a very similar fluorescence in terms of spectral features (spectral position, maximum and shape of the

band) and of spectroscopical parameters (fluorescence quantum yield and lifetime) (**Fig. 103 a** and **Table 8**). Under 2P regime, the properties were also comparable. **14o** showed a maximum σ_{2PA} of 150 GM at $\lambda_{exc,2P}$ = 770 nm, as **15** did (**Fig. 103 b**). Hence, as stated above, it can be confirmed that no FRET is present when fluorene is encountered with the open DTE in the dyad, that is, there is no electronic communication in this photoisomer. The quadratic fluorescence intensity dependence on the laser power, confirms the 2PA occurrence (**Fig. 103 c**).

In turn, pure **14o** was irradiated with 302 nm light until reaching the PSS, where the photophysical properties were examined. At this point, some residual fluorescence with identical shape, spectral position, and fluorescence lifetime to that of **14o** (and **15**) was observed, which seems to indicate that a small portion of the open isomer is still present at the PSS. ^{1}H-NMR and the model DTE were employed to confirm this hypothesis, assuming that there are no significant changes in the properties of the isolated DTE *vs.* when incorporated in the dyad (**Fig. 104**). Through this experiment, the composition of the PSS was determined in 94/6 for closed/open isomers.

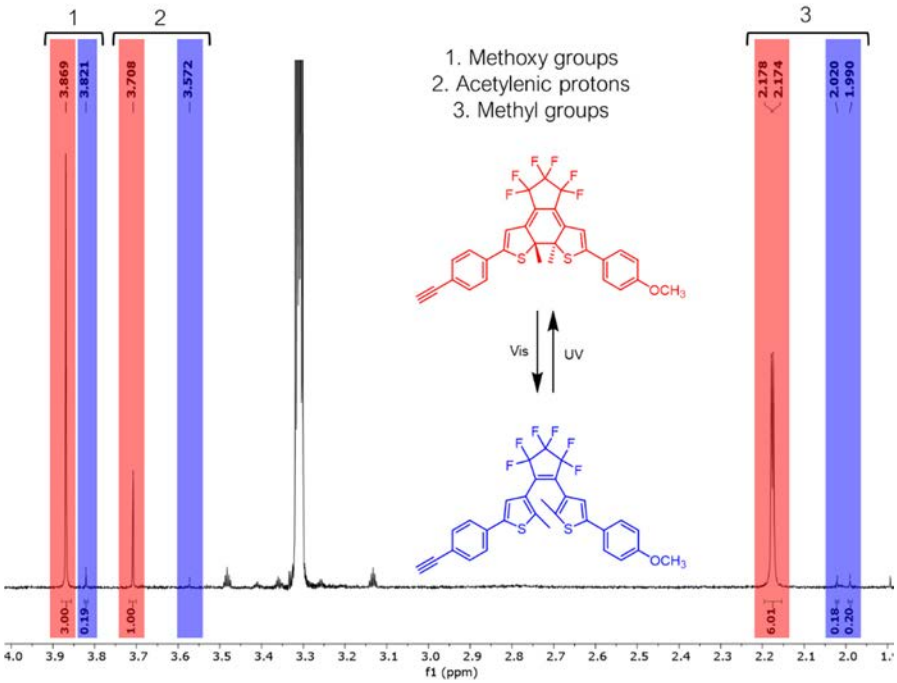

Fig. 104. ^{1}H-NMR in methanol-d_4 of the PSS attained by irradiating **16o** with 302 nm light (δ 4.0 – 1.5). The signals corresponding to **16c** are highlighted in red, and those of **16o** in blue.

In light of these results, we could evaluate that the observed residual fluorescence outcomes from open isomer at the PSS. However, this would only be right if FRET were practically quantitative. To corroborate this, we carried out theoretical calculations that aid us to gain insights into the behavior of the system. **14c** geometrical parameters at the ground state (S_0) were optimized using DFT, and employing the CAM-B3LYP[358] functional with the 6-31+G(d) basis set. The solvent effects, methanol in this case, were taken into account by including the PCM.[359] From this optimized structure, the center-to-center distance between the two chromophores within the dyad was determined as 22 Å (**Fig. 105**).

$$\text{FRET efficiency } (\Phi_{FRET}) = \frac{R_{0,\,theo}^6}{R_{0,\,theo}^6 + R_{0,\,exp}^6} \qquad \textbf{Eq. (9)}$$

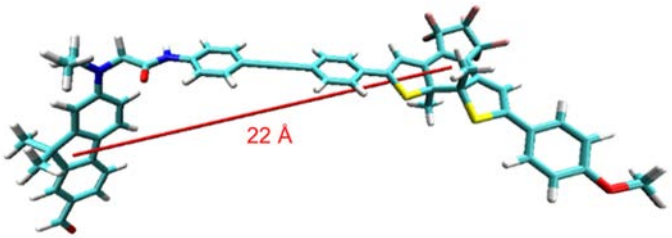

Fig. 105. Optimized structure of the **14c** dyad.

Considering that the experimentally determined R_0 in Section 6.3.1, the FRET efficiency [**Eq. (9)**] was estimated as practically quantitative in the dyad (ϕ_{FRET} = 0.99), which ensures that the fluorescence observed at the PSS corresponds effectively to the open isomer.

Additionally, the absorption energies for both isomers of **14** were computed at the PCM(MeOH)/CAM-B3LYP/6-311+G(d,p) level for the first ten excited states, using the linear-response (LR) approach with the TD-DFT.[108] Natural Transition Orbitals (NTOs),[43] which better describe the electronic transitions, are represented in **Fig. 106**.

In the **14o** form, the transitions to the first (S_1) and the fourth (S_4) excited states are assigned to the absorptions of fluorene and DTEo units, respectively. A similar analysis can

be performed at the transitions of the closed **14c**, where the transitions to the first (S_1) and the third (S_3) excited states correspond to those of DTEc and fluorene components, correspondingly (**Fig. 106**). It is very encouraging the accuracy of the calculations performed, as it can be appreciated in the tables included in this figure where the theoretical and experimental values are compared.

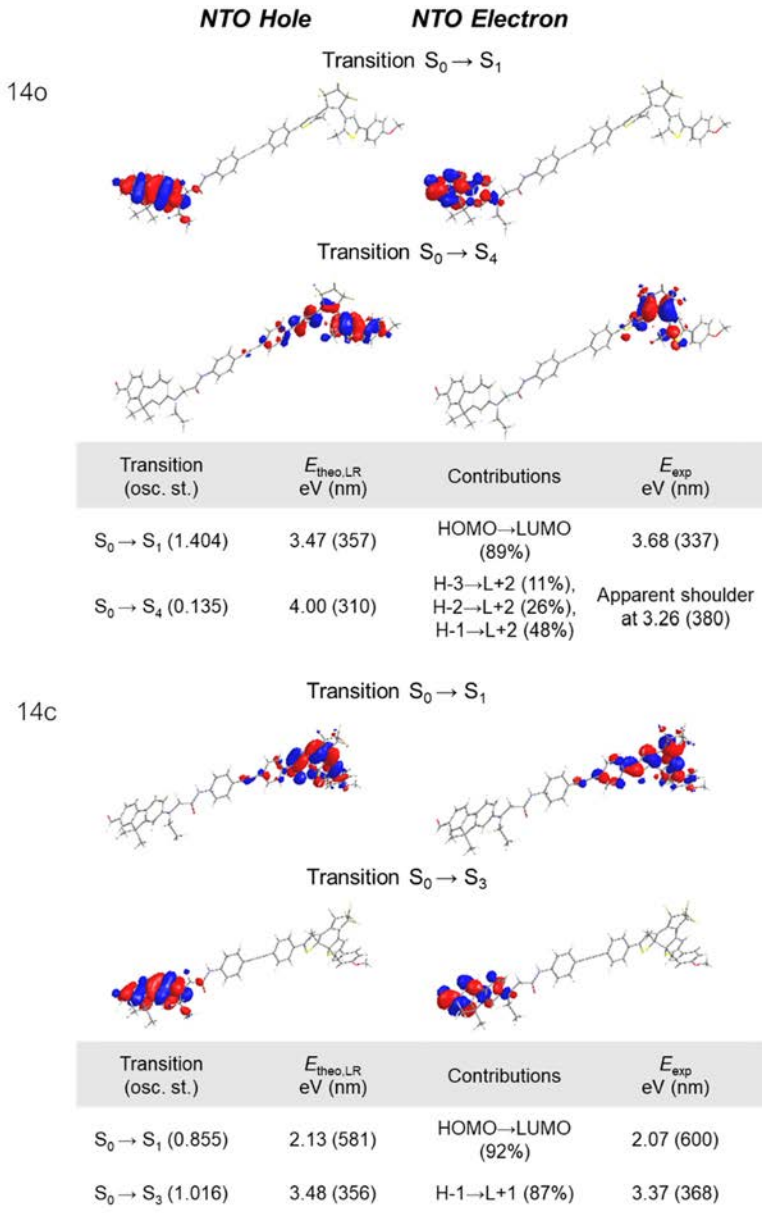

Transition (osc. st.)	$E_{theo.LR}$ eV (nm)	Contributions	E_{exp} eV (nm)
$S_0 \rightarrow S_1$ (1.404)	3.47 (357)	HOMO→LUMO (89%)	3.68 (337)
$S_0 \rightarrow S_4$ (0.135)	4.00 (310)	H-3→L+2 (11%), H-2→L+2 (26%), H-1→L+2 (48%)	Apparent shoulder at 3.26 (380)

Transition (osc. st.)	$E_{theo.LR}$ eV (nm)	Contributions	E_{exp} eV (nm)
$S_0 \rightarrow S_1$ (0.855)	2.13 (581)	HOMO→LUMO (92%)	2.07 (600)
$S_0 \rightarrow S_3$ (1.016)	3.48 (356)	H-1→L+1 (87%)	3.37 (368)

Fig. 106. NTOs of the photoisomers of **14**. Representative data for the transitions depicted are further indicated.

Furthermore, from the transitions of **14c**, the dipole moment transitions (*M*) can be used to better approximate κ^2. This can be calculated following **Eq. (10)**:

$$\kappa^2 = (\cos\theta_{AD} - 3\cos\theta_A \cos\theta_D)^2 \qquad \textbf{Eq. (10)}$$

In this expression, θ_D and θ_A are the angles between the donor-acceptor geometric center-to-center vector and the transition dipoles moments of these units, respectively; θ_{AD} refers to the angle between the transition dipole moments implicated. The transition dipole moments are represented in **Fig. 107** together with the angles' values.

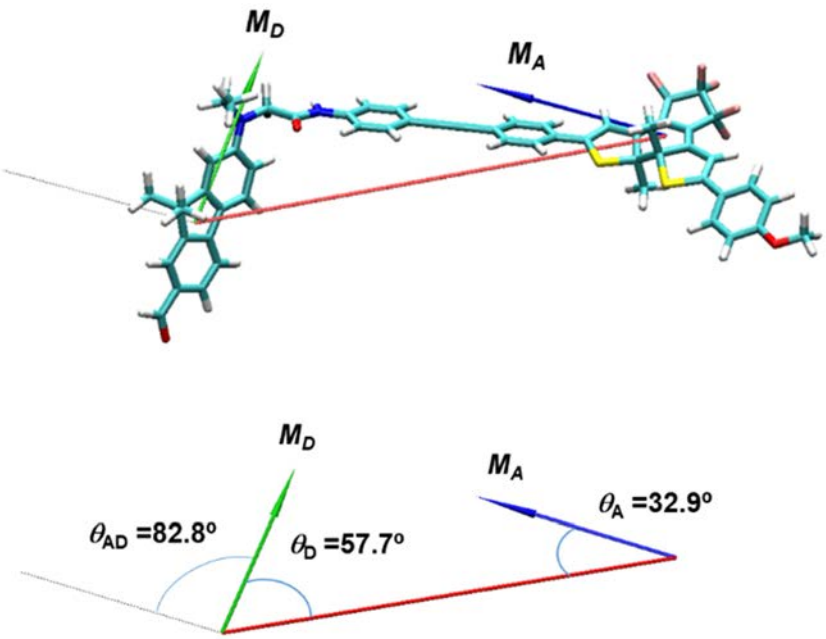

Fig. 107. Dipole transitions moments abovementioned for **14c** (upper panel) and respective angles (bottom panel) with the center-to-center vector.

Accordingly, κ^2 was estimated as of 1.48. This more precise orientation factor gives rise to a slightly higher and more accurate critical Förster radius of 53 Å, although it does not involve any substantial change to the prediction of a quantitative FRET ($\Phi_{FRET} = 1$).

Furthermore, the isomerization quantum yields were determined according to a comparative method (similar to the one employed for the fluorescence quantum yield or

the 2PA cross-section determination) by using furylfulgide as reference.[411–413] The ring-opening reactions were triggered using 523 nm, whereas the closing ones were carried out with a 302 nm light. As usually observed in DTE derivatives, the isomerization quantum yield for the closing process was as efficient as $\phi_{o\rightarrow c}$ = 0.50. The opening reaction, in contrast, showed a relative lower efficiency of $\phi_{c\rightarrow o}$ = 0.008, but yielding quantitatively the open isomer.

6.3.3 Kinetic studies under 2P excitation conditions

To bring about these studies, we started from a solution enriched in the closed isomer **14c**. Considering the observed optical features and having established the FRET behavior of the dyad, 820 nm was selected as excitation source because: a) at half of this wavelength, *i.e.*, 410 nm, the DTE photochrome exhibits a considerable low absorption in both isomeric forms (below 1000 M^{-1} cm^{-1} for **16c** and zero for **16o**), and b) model **15** bears a suitable 2PA cross-section of 86 GM at this wavelength.

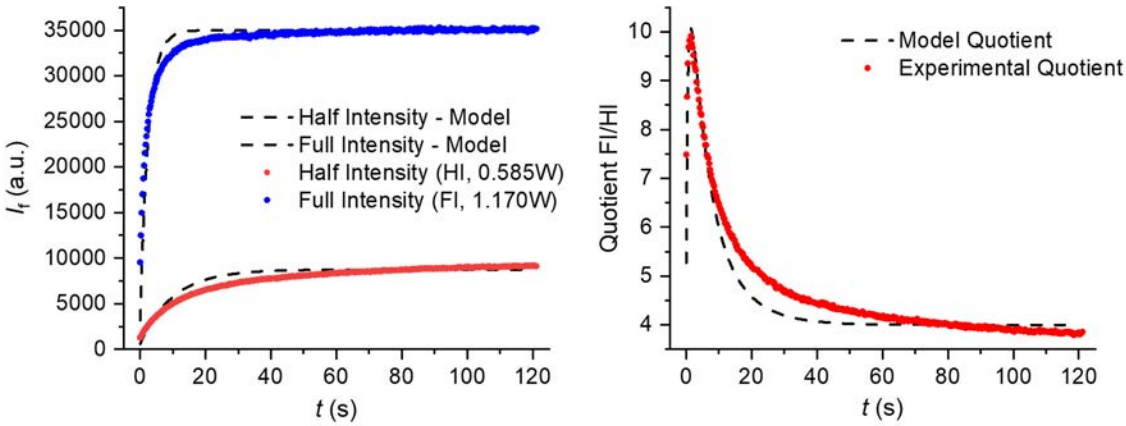

Fig. 108. (*Left*) Kinetics of fluorescence build-up on irradiation of **14c** (10 μM in aerated methanol) with 820 nm laser light at full intensity (FI, blue points) and at half intensity (HI, red points). Modeling of these conditions, introducing the initial 6% of the open isomer in **Eq. (5)**, are included as dashed black lines. (*Right*) Ratio of time-dependent fluorescence intensities shown at the left, these including the theoretical curves.

The irradiation of the PSS enriched in **14c** with this light prompted a fast increase of the 2P-excited fluorescence, as illustrated in **Fig. 108**. Two laser powers were also employed,

being the ratio of the fast kinetic components, ascribed to FRET-induced isomerization, of 4.3. It is very encouraging to notice that for a quartic dependence the ratio is expected to be 4 ($k_{obs,FI}$ = 0.483 s^{-1}, $k_{obs,HI}$ = 0.112 s^{-1}). The quotient between the curves, however, addressed a value of *ca.* 10, which is lower than that expected for a "pure" quartic dependence, *i.e.*, of 16 (*cf.* **Fig. 99**). Gratifyingly, this deviation from the ideal assumptions can be anticipated, since the modelling performed above did not contemplate the presence of already 6% **14o** in the initial solution, corresponding to the value experimentally observed for the PSS of the open-to-close reaction. When introducing this 6% at time zero in the modeling [**Eq. (6)**], the quotient yielded a maximum of 10.1, being in line with the experimental observations and corroborating thus this proof-of-principle (see **Fig. 108**).

6.4 SUMMARY

It is proposed an innovative approach toward dye systems that conducts to a dramatic improvement of the dependence of the fluorescence signal on the excitation light intensity. By combining a conventional two-photon absorbing fluorophores and photochromic system that can be switched by two-photon-initiated FRET, two 2PA processes are entangled, and consequently, this system practically performs as a 3PA dye. Although originally a quartic dependence was expected, the characteristics of the studied system are responsible for originating a deviation from the ideal theoretical models. However, this strategy would effectively lead to a quartic dependence for a photochromic system with quantitative conversion. Hence, the presented approach enables to overcome the photophysically imposed limitations of 2PA dyes, while maintaining the technological benefits of working under 2P-excitation regime. Noteworthy, this structurally modular approach, i.e., the nonconjugative combination of the two functional units, allows the merge of any 2PA dye with a FRET-efficient photochromic system to yield the phenomenon described.

Part of the results presented in this Chapter have been published in reference [414].

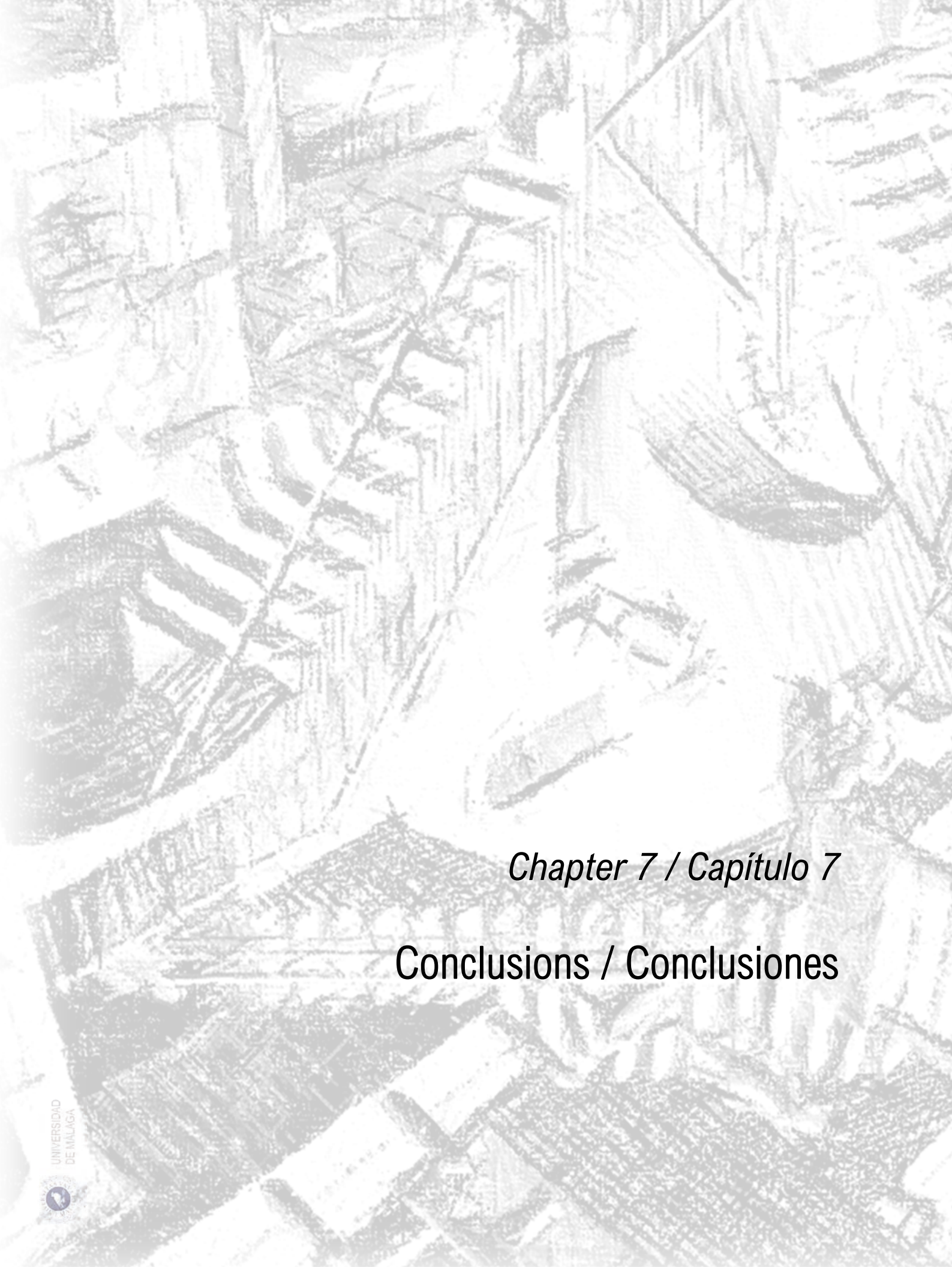

Chapter 7 / Capítulo 7

Conclusions / Conclusiones

English

In relation to Objective 1

A new "off/on" 2P-probe has been devised to detect hydroxyl radical in acid environments. When applied into cells, the presence of a tertiary amine in **2** was responsible of its selective accumulation within lysosomes, where the fluorescent form **1** was produced. The utility of **2** for detecting endogenous production of lysosomal hydroxyl radical as well as its generation by other agents affecting cellular oxidative stress in 2PM has been proved.

In relation to Objective 2

The appropriate decoration of compound **4** has resulted in two new-indolenine-based *pH* sensors with different intended uses: compound **5** as a pH_i-probe, and compound **6** as a lysosensor. Their application in cellular contexts has been demonstrated.

In relation to Objective 3

Compounds **11** and **12** presented two emissive forms at the subcellular level: monomer and *J*-aggregates, which have been observed in lysosomes and mitochondria, respectively. These species displayed different photophysical properties, and in consequence, **11** and **12** offered the interesting possibility of dual-color and simultaneous labelling of these organelles. Compound **12** has demonstrated to serve for tracking mitophagy.

In relation to Objective 4

The combination of two two-photon processes in a dyad system (2PA and FRET sensitized by 2P-excited fluorescence) has resulted in a system that practically perform as a 3PA dye. Although under ideal conditions for the system, it was expected a quartic dependence of the fluorescence on the excitation source., the observed behavior was reproduced when contemplating the experimental characteristics of the dyad within the model. This strategy

allows literally matching any 2PA dye with a FRET-efficient photochromic system, and conducts to a superior 3D-resolution than the one of the 2PA process *per se*.

Español

En relación con el Objetivo 1

Se ha desarrollado una nueva sonda "off/on" con propiedades de absorción de 2P para la detección de radical hidroxilo en entornos ácidos. La presencia de una amina terciaria en **2** propicia su acumulación selectiva dentro de lisosomas, donde se da lugar a la forma fluorescente **1**. La utilidad de **2** para detectar radical hidroxilo en lisosomas (ya sea este producido de forma endógena o estimulada por otros agentes que aumente el estrés oxidativo) en 2PM ha sido demostrada.

En relación con el Objetivo 2

La modificación del compuesto **4** ha dado lugar a dos nuevos sensores de *pH* basados en indoleninas con diferentes usos: el compuesto **5** como sensor de *pH*$_i$, y el compuesto **6** como sensor de lisosomas. Su aplicación en células ha sido probada.

En relación con el Objetivo 3

Los compuestos **11** y **12** presentaron dos formas emisivas a nivel subcelular: monómero y agregados tipo J en lisosomas y mitocondrias, respectivamente. Estas especies mostraron propiedad fotofísicas diferentes, lo que permite el marcaje de ambos orgánulos de manera simultánea y diferenciada a través del uso estos derivados. El compuesto **12** ha demostrado servir para monitorizar el proceso de mitofagia.

En relación con el Objetivo 4

La combinación de dos procesos mediados por 2PA en una diada (la propia 2PA y la FRET sensibilizada por fluorescencia obtenida por excitación con 2P) da lugar a un sistema se comporta prácticamente como un compuesto con capacidad de absorción de 3P. Aunque

para este sistema se esperaba una respuesta cuártica de la intensidad de fluorescencia con la intensidad del láser, el comportamiento experimental se puede justificar cuando se tienen en cuenta las características de la díada en el modelo teórico. Esta estrategia permite la combinación de cualquier compuesto con propiedades de absorción de dos fotones y un sistema fotocrómico con una alta eficiencia para FRET, proporcionando además una mayor resolución tridimensional que la que se obtiene con el proceso de 2PA.

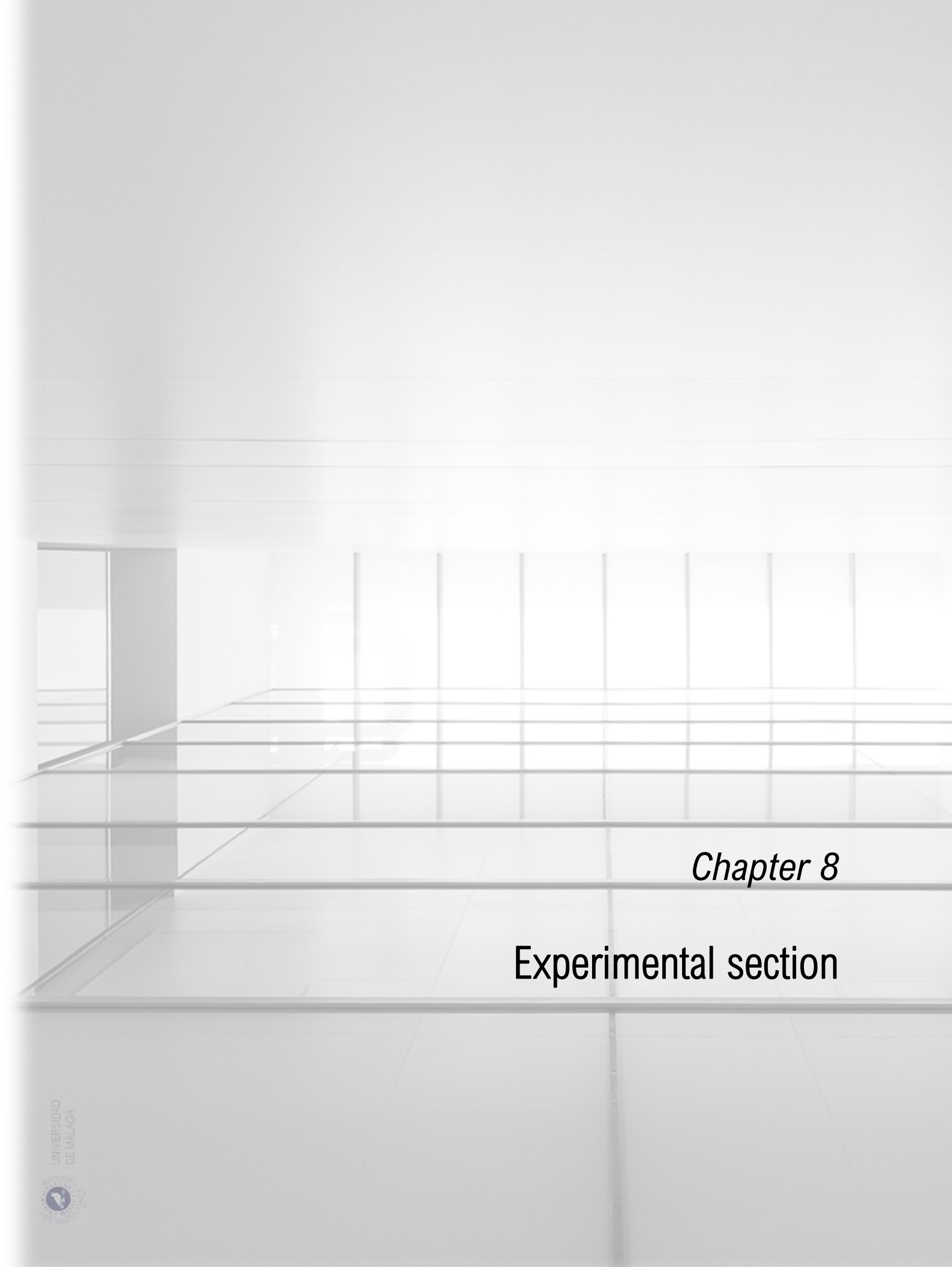

Chapter 8

Experimental section

8.1 GENERAL CONSIDERATIONS AND TECHNIQUES

8.1.1 Reagents and solvents for synthesis

Commercially available reagents and solvents were purchased and used as supplied.

Thin layer chromatography (TLC) was performed using silica gel 60 F_{254} plates. Visualization was performed by exposure to UV light (254 nm). Occasionally, chemical revealing agents, such as potassium permanganate, were further used. Purification *via* column chromatography was carried out with silica gel 60 (230-400 mesh). Solvents are indicated for each case.

The synthetic procedures of **Chapters 3**, **4** and **5** are described according to the routes represented in **Fig. 35**, **62** and **80**, respectively. Compounds studied in **Chapter 6** were synthesized and characterized by Prof. Dr. Joakim Andréasson group.

8.1.2 Nuclear magnetic resonance

In Chapters 3, 4 and 5, NMR spectra were collected on a Bruker Advance III Ascend 400 MHz spectrometer at 25 ºC. In Chapter 6, NMR were recorded on an Agilent 400 spectrometer at 25 ºC.

^{1}H NMR and ^{13}C NMR chemical shifts (δ) are expressed in parts per million (ppm).

In ^{1}H NMR the signals are referred to the residual protic solvent: CHD_5SO at 2.50 ppm in DMSO-d_6, $CHCl_3$ at 7.26 ppm in $CDCl_3$ and CHD_2OH at 3.31 ppm in MeOH-d_4. Coupling constants are expressed in Hertzs (Hz), and multiplicity of the signals is indicated with the following abbreviations: (s) singlet, (d) doublet, (t) triplet, (quint) quintuplet, (hept) heptuplet, (dd) double doublet, (td) triple doublet, (m) multiplet. The chemical shifts of ^{13}C NMR are calibrated respect to the signals of the carbon resonance: 39.5 ppm for DMSO-d_6, and 77.0 ppm for $CDCl_3$.

Total assignment of the NMR shifts was accomplished using 2D NMR experiments (COSY, HSQC, HMBC) as appropriate.

8.1.3 High Resolution Mass Spectrometry

High resolution electrospray ionization (ESI) mass spectra were obtained on a Thermo Fisher high resolution mass spectrometer Orbitrap.

8.1.4 Infrared spectra

Infrared spectra were recorded on a JASCO FT/IR-4100. Representative data are indicated as appropriate.

8.1.5 Melting point determination

Melting points (m.p.) were measured using an Electrothermal IA-9300 melting point apparatus. The determined values were not corrected.

8.1.6 UV/vis and fluorescence measurements

Spectroscopic grade solvents were employed for all the photophysical measurements, including studies under 2P-excitation conditions (Section 8.1.7).

Experiments were performed at room temperature, using air-equilibrated solutions contained in a 1 cm pathlength quartz cuvettes. Compound's solutions were prepared to a final concentration of 10 μM or optically diluted (*Abs* of the longest wavelength band < 0.1), indicated for each case.

In **Chapters 3, 4** and **5**, absorption spectra were recorded on a Cary 100 Bio UV-Vis Spectrophotometer, and both emission and excitation spectra on a JASCO FP-750 Spectrofluorometer. In **Chapter 6**, absorption spectra were registered on a Varian CaryBio 50 UV/vis spectrophotometer and steady-state fluorescent measurements on a SPEX Fluorolog-3 spectrofluorometer or a Varian Cary Eclipse spectrofluorometer.

Fluorescence quantum yields (ϕ_f) were determined according to a published procedure.[67] The expression used is **Eq. (11)**, where *s* refers to the sample and *r* to the reference compound; *F* notes the area of the fluorescence spectrum; *f* is calculated as $1\text{-}10^{-Abs}$, where *Abs* is the absorbance value at the excitation wavelength used; and n_D is the refractive index of the solvent used.

$$\phi_f^s = \frac{F^s \; f_s \; n_{D,s}^2}{F^r \; f_s \; n_{D,r}^2} \; \phi_f^r \qquad \textbf{Eq. (11)}$$

Taking into account the fluorescent spectra of the species, quinine sulphate in sulphuric acid 0.5M (ϕ_f = 0.546) or coumarine 153 in ethanol (ϕ_f = 0.38) were used as references.

More details about specific photophysical experiments of each Chapter (such as *pH* titrations or the preparation of aqueous solutions) are duly indicated in the Sections below.

8.1.7 Studies under two-photon excitation conditions

Two-photon absorption (2PA) cross-sections (σ_{2PA}) were determined using the two-photon-excited-fluorescence method.[394,415] Rhodamine B (0.1 or 5 μM in methanol) was employed as reference under experimentally identical conditions, assuming that fluorescence quantum yield is independent of the excitation regime. Compounds were diluted to 10 μM, and spectra were measured in a laser power regime where the fluorescence was proportional to the square of the laser excitation power. All solutions were contained in 0.1 cm pathlength quartz cuvettes. σ_{2PA} was calculated for each wavelength using a similar expression to that of the fluorescence quantum yield:

$$\sigma_{2PA,s} = \sigma_{2PA,r} \; \frac{C_r \, n_{D,r} \, \phi_{f,r} \, F_s}{C_s \, n_{D,s} \, \phi_{f,s} \, F_r} \qquad \textbf{Eq. (4)}$$

where s refers to the sample and r to the reference compound, σ_{2PA} is the 2PA cross-section, *C* is the concentration of the specie, ϕ_f is the fluorescence quantum yield, n_D is the refractive index of the used solvent and *F* is the area under the emission spectrum.

In **Chapters 3, 4** and **5**, the fluorescence properties of the compounds were analyzed using an inverted Leica SP5 MP confocal and multiphoton microscope hosted at the Andalusian Center for Nanomedicine and Biotechnology (Bionand). This microscope is equipped with a MaiTai Ti:Sapphire HP laser (Spectra-Physics, Inc.) tunable between 690 and 1040 nm. Imaging was performed using a 10x Plan APO objective (NA 0.4) focused at the air/liquid boundary, allowing for simultaneous detection of sample and background fluorescence. Emission and excitation spectra data for compound and background regions of interest (ROIs) were registered using Leica LAS AF software. Emission spectra were measured using a dynamic 15 nm wide emission detection window moving in 20 steps from 400 to 700 nm. In **Chapter 6**, a ZEISS LSM710 NLO MP/Confocal Microscope at the Centre of Cellular Imaging at Gothenburg University was employed. This microscope is equipped with an InSight DS+ laser (Spectra-Physics) tunable between 680 nm and 1300 nm. The provided pulse width was 100 ps. Imaging was performed using a Plan-Apochromat 10x objective (NA 0.45) focused at the air/liquid boundary, which enables simultaneous detection of sample and background fluorescence. Emission spectral data for compound and background ROIs were registered using ImageJ software. Emission spectra were measured using a dynamic 10 nm wide emission detection window moving in 25 steps between 445 and 700 nm.

8.1.8 Theoretical calculations

Calculations were performed with Gaussian 16A03 software.[416] Geometrical parameters at the ground (S_0) and excited (S_1) states were determined by density-functional theory (DFT), using the Coulomb-attenuated CAM-B3LYP[417] functional and the 6-31+G(d) basis set. The absence of negative frequencies in analytical Hessian calculations corroborated the nature of the minima. Solvent effects were accounted generally, by using the polarizable continuum model (PCM).[418] Energy parameters were calculated as vertical electronic excitations from the minima of the S_0 or S_1 structures using the linear response (LR) approach and the time-dependent density functional response theory (TD-DFT).[108] These calculations was carried out for the ten first excited states.

8.2 EXPERIMENTAL PROCEDURES IN CHAPTER 3

8.2.1 Synthesis of 1-(6-methoxynaphthalen-2-yl)-2-methylpropan-1-one (3)

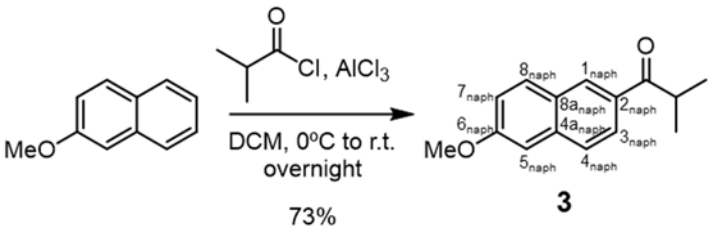

2-Methoxynaphtalene (3.00 g, 18.8 mmol) and $AlCl_3$ (3.29 g, 24.6 mmol) were dissolved in 10 mL of dichloromethane in a 50 mL two-neck round bottom flask. Nitrobenzene (0.6 mL, 59.0 mmol) was then added, maintaining the temperature at 20ºC. Finally, isobutyryl chloride (2.3 mL, 21.1 mmol) was dropwise added to the previous solution. The reaction was followed by TLC using dichloromethane/hexane 8:2 as eluent. Once the reaction was finished, the solution was poured into a water-ice mixture at 0ºC. The mixture was then extracted using dichloromethane (3x10 mL). The combined extracts were washed with 10% $NaHCO_3$ (2x15 mL) and brine (2x15 mL), dried over anhydrous $MgSO_4$ and concentrated *in vacuo*. The crude product obtained was purified by column chromatography using dichloromethane/hexane 8:2 as eluent, obtaining a colourless solid (3.14 g, 73% yield).

m.p.: 54-56ºC.

^{1}H-NMR (400 MHz, $CDCl_3$, δ ppm): 8.43 (d, *J*=1.6Hz, 1H, $H_{1\ naph}$), 8.04 (dd, *J*=8.7, 1.6Hz, 1H, $H_{3\ naph}$), 7.88 (d, *J*=8.9Hz, 1H, $H_{8\ naph}$), 7.80 (d, *J*=8.7Hz, 1H, $H_{4\ naph}$), 7.23 (dd, *J*=8.9, 2.5Hz, 1H, $H_{7\ naph}$), 7.18 (d, *J*=2.5Hz, 1H, $H_{5\ naph}$), 3.97 (s, 3H, CH_3O), 3.73 (hept, *J*=6.8Hz, $CH(CH_3)_2$), 1.30 (d, 6H, *J*=6.8Hz, $CH(CH_3)_2$).

^{13}C-NMR (101 MHz, $CDCl_3$, δ ppm): 204.2 (*C=O*), 159.7 ($C_{6\ naph}$), 137.2 ($C_{4a\ naph}$), 131.6 ($C_{2\ naph}$), 131.2 ($C_{8\ naph}$), 129.6 ($C_{1\ naph}$), 127.9 ($C_{8a\ naph}$), 127.2 ($C_{4\ naph}$), 125.1 ($C_{3\ naph}$), 119.7 ($C_{7\ naph}$), 105.7 ($C_{5\ naph}$), 55.4 (*CH*$_3$O), 35.2 (*CH*(CH$_3$)$_2$), 19.4 (CH(*CH*$_3$)$_2$).

IR (υ cm^{-1}): 2971, 2930, 2872, 2848, 1675, 1618, 1502, 1088, 1016.

8.2.3 Synthesis of 2-(6-methoxynaphthalen-2-yl)-3,3-dimethyl-3*H*-indole (4)

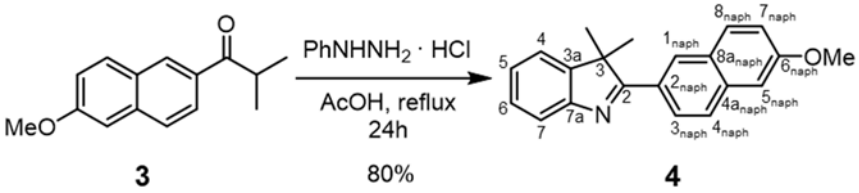

3 **4**

Compound **4** (0.80 g, 3.5 mmol) and phenylhydrazine hydrochloride (0.51 g, 3.5 mmol) were dissolved in 6 mL of glacial acetic acid in a 25 mL round-bottom flask. The mixture was heated to reflux and temperature maintained for 24 hours. The reaction was followed by TLC using hexane/dichloromethane/EtOAc 8:1:1 as eluent. The crude reaction was then concentrated *in vacuo* and resolved in 25 mL of dichloromethane. The solution was washed with Na_2CO_3conc. (2x15 mL) and brine (2x15 mL). Finally, the organic layer was dried over anhydrous $MgSO_4$ and concentrated *in vacuo*. The crude product was purified by column chromatography using *n*-hexane/dichloromethane/EtOAc 8:1:1 as eluent, obtaining a yellow solid (0.94 g, 80% yield).

m.p.: 152-155ºC.

^{1}H-NMR (400 MHz, $CDCl_3$, δ ppm): 8.53 (d, *J*=1.6Hz, 1H, $H_{1\ naph}$), 8.41 (dd, *J*=8.7, 1.6Hz, 1H, $H_{3\ naph}$), 7.90 (d, *J*=8.9Hz, 1H, $H_{8\ naph}$), 7.86 (d, *J*=8.6Hz, 1H, $H_{4\ naph}$), 7.79 (dd, *J*=7.6, 0.7Hz, 1H, H_7), 7.42 (td, *J*=7.6, 0.7Hz, 1H, H_6), 7.40 (dd, *J*=7.6, 0.7Hz, 1H, H_4), 7.32 (td, *J*=7.6, 0.7Hz, 1H, H_5), 7.24 (dd, *J*=8.9, 2.5Hz, 1H, $H_{7\ naph}$), 7.20 (d, *J*=2.5Hz, 1H, $H_{5\ naph}$), 3.97 (s, 3H, *CH*$_3$O), 1.72 (s, 6H, C(*CH*$_3$)$_2$).

^{13}C-NMR (101 MHz, $CDCl_3$, δ ppm): 183.1 (*C_2*), 159.0 (*$C_{6\ naph}$*), 153.3 (*C_{7a}*), 147.8 (*C_{3a}*), 135.8 (*$C_{4a\ naph}$*), 130.6 (*$C_{8\ naph}$*), 128.6 (*$C_{8a\ naph}$*), 128.4 (*$C_{1\ naph}$*), 127.8 (*C_6*), 127.2 (*$C_{4\ naph}$*), 126.2 (*$C_{3\ naph}$*), 125.8 (*C_5*), 121.0 (*C_7*), 120.8 (*C_4*),119.4 (*$C_{7\ naph}$*), 105.8 (*$C_{5\ naph}$*), 55.4 (*CH_3*O), 53.5 (*C*$(CH_3)_2$), 25.2 (C*$(CH_3)_2$*).

IR (υ cm^{-1}): 3061, 3042, 3009, 2965, 2929, 2867, 1736, 1719, 1673, 1622, 1606, 1518, 1480, 1454, 1439, 1394, 1378, 1363, 1336, 1310, 1271, 1258, 1205, 1107, 1085, 1023.

HRMS (ESI): calculated mass for $C_{21}H_{20}N_1O_1$ ($M+H^+$): 302.1539, found: 302.1540.

8.2.4 Synthesis of 2-(6-methoxynaphthalen-2-yl)-1,3,3-trimethyl-3*H*-indol-1-ium iodide (1)

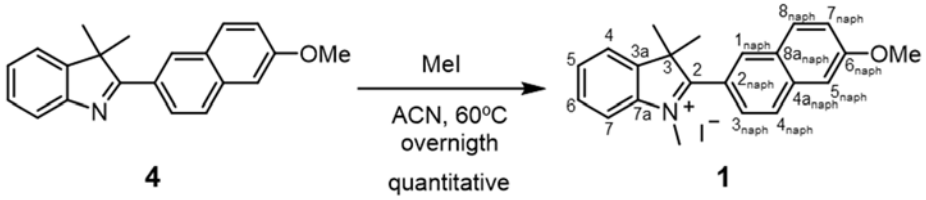

Compound **4** (0.300g, 0.996mmol) was dissolved in 15 mL of acetonitrile. Methyl iodide was then added (0.1mL, 1.494mmol) and the solution heated to 60ºC in a sealed tube. The reaction was followed by TLC using *n*-hexane/dichloromethane/EtOAc 8:1:1 as eluent. When the reaction had finished, the crude product was concentrated *in vacuo* and washed with cold diethyl ether. The desired compound was obtained without further purification as an orange solid (0.44 g, quantitative yield).

m.p.: 197-200ºC.

^{1}H-NMR (400 MHz, DMSO-d_6, δ ppm): 8.37 (d, *J*=1.6Hz, 1H, *$H_{1\ naph}$*), 8.16 (d, *J*=8.7Hz, 1H, *$H_{4\ naph}$*), 8.09 (d, *J*=8.9Hz, 1H, *$H_{8\ naph}$*), 8.09-8.06 (m, 1H, *H_7*), 7.97-7.93 (m, 1H, *H_4*), 7.79 (dd, *J*=8.6, 1.6Hz, 1H, *$H_{3\ naph}$*), 7.77-7.70 (m, 2H, *H_5* and *H_6*), 7.55 (d, *J*=2.5Hz, 1H, *$H_{5\ naph}$*), 7.37 (dd, *J*=8.9, 1H,1.6Hz, *$H_{7\ naph}$*), 3.98 (s, 3H, N*CH_3*), 3.96 (s, 3H, O*CH_3*), 1.66 (s, 6H, C*$(CH_3)_2$*).

^{13}C-NMR (101 MHz, DMSO-d_6, δ ppm): 189.8 (*C*$_{2}$), 159.8 (*C*$_{6\ naph}$), 142.3 (*C*$_{7a}$), 142.2 (*C*$_{3a}$), 136.3 (*C*$_{4a\ naph}$), 131.0 (*C*$_{8\ naph}$), 130.1 (*C*$_{5}$), 129.7 (*C*$_{1\ naph}$), 129.1 (*C*$_{6}$), 127.9 (*C*$_{4\ naph}$), 127.3 (*C*$_{8a\ naph}$), 124.5 (*C*$_{3\ naph}$), 123.4 (*C*$_{4}$), 120.5 (*C*$_{2\ naph}$), 120.4 (*C*$_{7\ naph}$), 116.1 (*C*$_{7}$), 106.3 (*C*$_{5\ naph}$), 55.6 (O*C*H$_3$), 55.1 (N*C*H$_3$), 36.8 (C*(C*H$_3$)$_2$), 22.2 (*C*(CH$_3$)$_2$).

IR (υ cm^{-1}): 3039, 3012, 2967, 2935, 2859, 1994, 1948, 1870, 1847, 1827, 1793, 1739, 1686, 1601, 1586, 1543, 1522, 1485, 1457, 1180, 1128, 1047.

HRMS (ESI): calculated mass for $C_{22}H_{22}N_1O_1$ (M+H$^+$): 316.1697, found: 316.1696.

8.2.5 Synthesis of 2-(6-methoxynaphthalen-2-yl)-1,3,3-trimethylindoline (2)

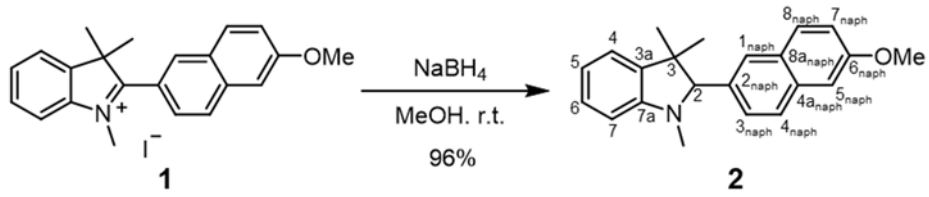

Compound **1** (0.38g, 0.113mmol) was dissolved in 10 mL of methanol in a round-bottom flask. Sodium borohydride (0.043 g, 1.13 mmol) was added as a solid in small fractions. The reaction was followed by TLC using *n*-hexane/dichloromethane/EtOAc 8:1:1 as eluent. Once completed, the crude product was concentrated *in vacuo* and resolved in 15 mL of dichloromethane. The organic layer was washed with water (2x15 mL). The aqueous layer was extracted with dichloromethane (2x10 mL) and organic layers combined and concentrated *in vacuo*. The final product was obtained without further purification as a colorless solid (0.26g, 96% yield).

m.p.: 144-146ºC.

^{1}H-NMR (400 MHz, DMSO-d_6, δ ppm): 7.87-7.81(m, 3H, *H*$_{8\ naph}$, *H*$_{4\ naph}$, *H*$_{1\ naph}$), 7.47 (d, *J*=7.7Hz, 1H, *H*$_{3\ naph}$), 7.34 (d, *J*=2.4Hz, 1H, *H*$_{5\ naph}$), 7.16 (dd, *J*=8.9, 2.4Hz, 1H, *H*$_{7\ naph}$), 7.11 (d, *J*=7.4Hz, 1H, *H*$_{4}$), 7.08 (t, *J*=7.4Hz, 1H, *H*$_{6}$), 6.73 (t, *J*=7.4Hz, 1H, *H*$_{5}$), 6.68 (d, *J*=7.4Hz,

1H, *H7*), 4.13 (s, 1H, *H2*), 3.87 (s, 3H, *OCH3*), 2.62 (s, 3H, N*CH3*), 1.38(s, 3H, C*(CH3)2*), 0.64 (s, 3H, C*(CH3)2*).

^{13}C-NMR (101 MHz, DMSO-d_6, δ ppm): 157.2 (*C6 naph*), 151.5 (*C7a*), 138.2 (*C3a*), 133.9 (*C8a naph*), 132.7 (*C2 naph*), 129.3 (*C8 naph*), 128.3 (*C4a naph*), 127.4 (*C4*), 126.5 (*C1 naph and C3 naph*), 121.8 (*C6*), 118.7 (*C7 naph*), 118.5 (C_5), 108.1 (C_7), 105.8 (C_5 *naph*), 81.6 (C_2), 55.2 (O*CH3*), 44.1 (C_3), 34.6 (N*CH3*), 26.0 (*C(CH3)2*), 25.1 (*C(CH3)2*).

IR (υ cm^{-1}): 3042, 2995, 2964, 2934, 2902, 1633, 1542, 1521, 1505, 1482, 1457, 1436, 1422.

HRMS (ESI): calculated mass for $C_{22}H_{24}N_1O_1$ ($M+H^+$): 318.1852, founded: 318.1852.

8.2.5 Optical studies

Aqueous solutions were prepared from a 1 mM stock solution in DMSO of the interest compounds (**1** and **2**). The resulting concentration of DMSO in these solutions was *ca.* 1%, which has negligible effect on the photophysical properties.

8.2.6 Selectivity and sensitivity studies. Preparation of ROS and RNS species *in-cuvette*

ROS and RNS were added to 3 mL of **2** solution (10 μM in 1% DMSO/Gly-HCl buffer, pH=2.4) from 1.5 mM stock solutions to obtain a 50 μM final concentration of each ROS/RNS agent. Stock solutions were prepared as follows:

- → KO_2 was dissolved in DMSO.
- → H_2O_2, TBHP and NaClO were diluted in ultrapure water.
- → •OH was generated *in situ*, adding the appropriate quantity of H_2O_2 to a solution containing an equimolar concentration of Fe^{2+} and 10 μM **2**.
- → $^1O_2$ was generated by adding H_2O_2 to a solution that contained NaClO and **2** at a 10:1 concentration ratio.

→ •NO was released from sodium nitroprusside [$Na_2Fe(CN)_5NO{\cdot}2H_2O$]. This salt was dissolved and then storage for 3 h before using.[419]

On the other hand, metallic ions were provided from their commercially available inorganic salts: $FeSO_4{\cdot}7H_2O$, $FeCl_3{\cdot}6H_2O$ and $CuCl_2{\cdot}2H_2O$ for Fe^{2+}, Fe^{3+} and Cu^{2+}, respectively. These salts were dissolved in water to a concentration of 1.5 mM. A proper quantity of these solutions was added to one containing 3 mL of 10 μM **2** to obtain a 50 μM final concentration of each metallic ion. A similar protocol was followed to examine the possible influence of cysteine.

8.2.7 Cell studies

These studies were performed in collaboration with the group of Prof. Dr. Jose Maria Perez-Pomares, who provided the used cells and carried out the below-detailed experiments.

Cell culture and incubation with compounds 1 and 2

MEF cells were isolated from 14.5 old mouse embryos following standard protocols,[420] and were cultured in complete medium (DMEM + 10% FBS + 1% Penicillin-Streptomycin + 2 mM L-Glutamine) at 37°C in a humidified environment with 5% CO_2. For microscopy experiments, MEF cells were grown in 35 mm glass-bottomed dishes (Ibidi) suitable for optical microscopy to approximately 50% confluency prior to starting the experiment. Unless otherwise stated, compounds **1** and **2** were added to cells diluted 0.025 μM in complete medium.

Cell cytotoxicity assay

A standard Cell Proliferation Reagent WST-1 assay was used to test the cytotoxicity of **2** in mouse embryonic fibroblasts (MEFs). Cells were cultured in a 96-well microplate to a total volume of 100 μL per well with a density of 6×10^5 cells per mL at 37ºC in a 5% CO_2 atmosphere. After 24 h, **2** at 0.01 μM, 0.025 μM, 0.05 μM, 0.1 μM, 0.5 μM, 1 μM, 2.5 μM concentrations was incubated with MEFs for 12 h in fresh medium. Cells cultured without

2 were used as a negative control. After incubating the cells for 12 h with **2**, 10 µL of Cell Proliferation Reagent WST-1 was added into each well of the 96-well microplate for another 6 h. Finally, wells' absorbance was measured at 440 nm and cell viability calculated using the following equation [**Eq. (12)**]:

$$\% \textit{ viability} = \frac{\sum \left({}^{A_i}/_{A_{control}} \right) \times 100}{n} \qquad \textbf{Eq. (12)}$$

where A_i is the experimental absorbance value and $A_{control}$ is the average absorbance of the control wells. Three replicas were performed for each sample (n = 3).

Visualization of intracellular fluorescence in 2PM from 1

Intracellular fluorescence and distribution following incubation with compounds **1** and **2** were analyzed using the above-mentioned inverted Leica SP5 MP confocal microscope. For cell studies, a 63x PLAN APO NA 1.4 oil immersion objective was used. Optimal conditions were maintained throughout the imaging process with an integrated microscope enclosure keeping cells at 37°C and 5% CO_2.

Compound **1** (either as is or *in situ* generated from **2**) was visualized with two-photon excitation at 740 nm and fluorescence detection between 500-550 nm using a HyD non-descanned detector. Brightfield images were captured independently using a 405 nm laser as light source. For timelapse experiments, 3D image stacks were captured every 10 minutes for 10 hours, with each timepoint composed of 6 images separated by 1.25-micron intervals.

Colocalization experiments

After cells being incubated with **2** for 5 hours, colocalization experiments were performed by adding Lysotracker Deep Red (LTDR, Thermofisher Scientific Cat. No. L12492; 50 nM final concentration) or Mitotracker Red CMXRos (MTR, Thermofisher Scientific Cat. No. M7512; final concentration 250 nM) to the cell culture media approximately 30 minutes

prior to visualization by microscopy. MTR and LTDR were visualized using single photon excitation: $\lambda_{exc,\,1P}$ = 561 nm, λ_{em} = 600 - 640 nm and $\lambda_{exc,\,1P}$ = 633 nm, λ_{em} = 645 - 740 nm respectively. These configurations were selected to avoid signal contamination between markers. The generated-by-oxidation **1** was detected sequentially using the two-photon configuration described above. As lysosomes and mitochondria are extremely mobile in MEF cells, images were captured at high speed to minimize the time delay between confocal and two photon acquisitions (<1 s). Identical laser power and gain settings were used for all samples within each experiment.

Treatments for inducing oxidative stress at the subcellular level

Once MEF cells had been cultured with **2** for 5 hours, different physical (UV) or chemical treatments (*tert*-Butyl hydroperoxide "TBHP", 2-methoxyestradiol) that produce reactive oxygen species (ROS) were added to the culture medium to study the oxidizing effect that they produce on the cells. For TBHP and 2-methoxyestradiol treatments, cells were first incubated with compound **2** as described above followed by the addition of complete medium supplemented with 0.001 mM TBHP or 0.001 mmol 2-methoxyestradiol. For UV treatment, cells were identified with a Leica DMI6000 microscope and a 63x PLAN APO oil immersion objective (NA 1.4). Pre-treatment brightfield and two-photon microscopy images were captured before applying a 10 second UV exposure using a conventional mercury lamp light source (Leica EL6000 fitted with an OSRAM 120 W short arc bulb) with a Leica "A" filter cube resulting in UV treatment between 340-380 nm. Post UV exposure two-photon microscopy images were captured using identical settings to the pre-treatment images.

Image analysis and quantification

Cell fluorescence following incubation with compound **2** combined with different treatments was quantified in terms of average spot fluorescence per cell. Spots were detected automatically using Imaris version 7.6 (Bitplane Inc.) to detect spots with a 1-micron size and a minimal intensity threshold of 20. Images were analyzed without preprocessing other than to select individual cells for analysis. To determine if a given

treatment had a statistically significant effect on spot fluorescence, the Student's T-test was used to perform pairwise comparisons with and without each treatment and determine a *p*-value for each case. Quantification of average spot fluorescence of compound **1** during the timelapse experiment was performed using the same spot detection methodology described above for each timepoint.

Colocalization analysis comparing MTR and LTDR with compound **2** was carried out using the "Coloc 2" module of the image processing package ImageJ.[421,422] In living cells, thresholds were normalized based on selecting the top 15% of pixels of each channel analyzed. Using these thresholds, Pearson Correlation Coefficient (PCC) values were obtained for compound **2** *versus* MTR and compound **2** *versus* LTDR. In fixed cells, PCC values were obtained for compound **2** *versus* lysotracker using maxima projections of the images.

8.3 EXPERIMENTAL PROCEDURES IN CHAPTER 4

8.3.1 Synthesis of 1-(6-hydroxynaphthalen-2-yl)-2-methylpropan-1-one (7)

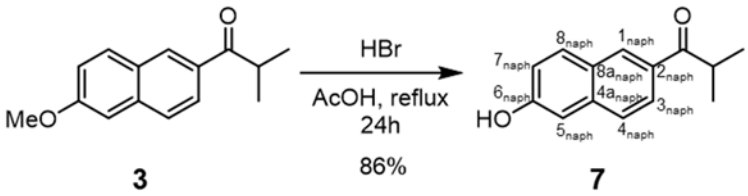

3 **7**

Compound **3** (5.0 g, 21.9 mmol) and HBr 48% (25.0 mL, 219.0 mmol) were dissolved in 75 mL of glacial acetic acid in a 250 mL round bottom flask. The mixture was heated to reflux for 24 hours. The reaction was followed by TLC (DCM/*n*-hexane 9:1). Then was concentrated *in vacuo*, dissolved in 100 mL of EtAcO. and washed with 10% $NaHCO_3$ (2 x 75 mL) and brine (75 mL). The organic layer was dried over anhydrous $MgSO_4$ and concentrated *in vacuo*. The product was purified by column chromatography using DCM/*n*-hexane (9:1) to DCM as eluent, obtaining compound **7** as a brown oil (3.25 g, 86% yield).

^{1}H-NMR (400 MHz, $CDCl_3$, δ ppm): 8.42 (d, J = 1.5 Hz, 1H, *H_1*), 7.99 (dd, J = 8.7, 1.5 Hz, 1H, *H_3*), 7.87 (d, J = 8.5 Hz, 1H, *H_7*), 7.71 (d, J = 8.7 Hz, 1H, *H_4*), 7.23–7.17 (m, 2H, *H_8 and H_5*), 3.73 (hept, J = 6.9 Hz, 1H, *$\underline{CH}(CH_3)_2$*), 1.28 (d, J = 6.9 Hz, 6H, *$CH(\underline{CH_3})_2$*).

^{13}C-NMR (101 MHz, $CDCl_3$, δ ppm): 205.0 (*C=O*), 156.0 (*C_6*), 137.2 (*C_{4a}*), 131.7 (*C_7*), 131.4 (*C_2*), 130.0 (*C_1*), 127.8 (*C_{8a}*), 126.9 (*C_4*), 125.1 (*C_3*), 118.9 (*C_8*), 109.6 (*C_5*), 35.3 (*$\underline{CH}(CH_3)_2$*), 19.4 (*$CH(\underline{CH_3})_2$*).

IR (υ cm^{-1}): 3311, 2966, 2918, 2867, 1655, 1616, 1559, 1477, 1280, 1239, 1154, 935, 799, 664.

8.3.2 Synthesis of 1-(6-(2-(2-ethoxyethoxy)ethoxy)naphthalen-2-yl)-2-methylpropan-1-one (8)

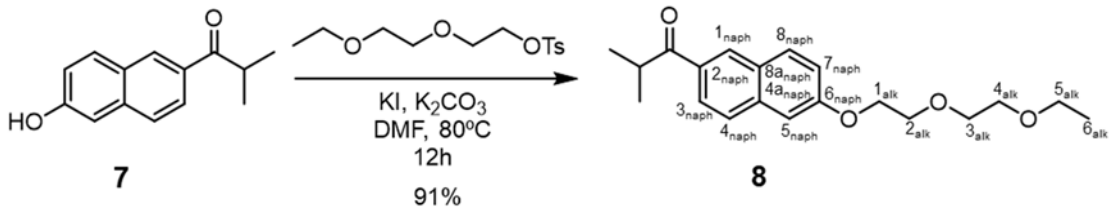

Compound **7** (0.65 g, 3.03 mmol) and 2-(2-ethoxyethoxy)ethyl 4-methylbenzenesulfonate (0.67 g, 2.33 mmol) were dissolved in 5 mL of DMF in a 25 mL round bottom flask. K_2CO_3 (0.84 g, 6.06 mmol) and KI (0.13 g, 0.76 mmol) were added to the mixture, which was heated to 80ºC overnight (*ca.* 12h). The reaction was followed by TLC using DCM/EtAcO (95:5) as eluent. Then, 50 mL of EtAcO were added and washed with saturated $NaHCO_3$ (2 x 15 mL) and 10% Na_2CO_3 (15 mL). The organic layer was dried over anhydrous $MgSO_4$ and concentrated *in vacuo*. The syrup obtained was purified by column chromatography using DCM/EtAcO (95:5) as eluent, obtaining ketone **8** as a brown oil (0.70 g, 91% yield).

^{1}H-NMR (400 MHz, $CDCl_3$, δ ppm): 8.32 (d, J = 1.8 Hz, 1H, *H_1*), 7.92 (dd, J = 8.6, 1.8 Hz, 1H, *H_3*), 7.77 (d, J = 9.0 Hz, 1H, *H_8*), 7.68 (d, J = 8.6 Hz, 1H, *H_4*), 7.16 (dd, J = 9.0, 2.5 Hz, 1H, *H_7*), 7.08 (d, J = 2.5 Hz, 1H, *H_5*), 4.21 (t, J = 4.8 Hz, 2H, *$H_{1\ alk}$*), 3.87 (d, J = 4.8 Hz, 2H, *$H_{2\ alk}$*), 3.68 (d, J = 5.0 Hz, 2H, *$H_{3\ alk}$*), 3.62 (hept, J = 6.8 Hz, 1H, *$\underline{CH}(CH_3)_2$*), 3.56 (t, J = 5.0

Hz, 2H, $H_{4\ alk}$), 3.47 (q, J = 6.9 Hz, 2H, $H_{5\ alk}$), 1.19 (d, J = 6.9 Hz, 6H, $CH(\underline{CH_3})_2$), 1.14 (t, J = 7.0 Hz, 3H, $H_{6\ alk}$).

^{13}C-NMR (101 MHz, $CDCl_3$, δ ppm): 204.2 (*C=O*), 158.8 (C_6), 137.1 (C_{4a}), 131.6 (C_2), 131.1 (C_8), 129.6 (C_1), 128.0 (C_{8a}), 127.2 (C_4), 125.1 (C_3), 119.9 (C_7), 106.6 (C_5), 71.0 ($C_{3\ alk}$), 69.9 ($C_{4\ alk}$), 69.6 ($C_{2\ alk}$), 67.6 ($C_{1\ alk}$), 66.7 ($C_{5\ alk}$), 35.2 ($\underline{CH}(CH_3)_2$), 19.4 ($CH(\underline{CH_3})_2$), 15.2 ($C_{6\ alk}$).

IR (υ cm^{-1}): 3061, 2968, 2928, 2871, 2359, 1672, 1621, 1470, 1383, 1349, 1262, 1196, 1151, 990, 856, 813, 743.

HRMS (ESI, m/z): calculated mass for $C_{20}H_{27}O_4$ ($M+H^+$): 331.1904; found, 331.1903.

8.3.3 Synthesis of 2-(6-(2-(2-ethoxyethoxy)ethoxy)naphthalen-2-yl)-3,3-dimethyl-3*H*-indole (5)

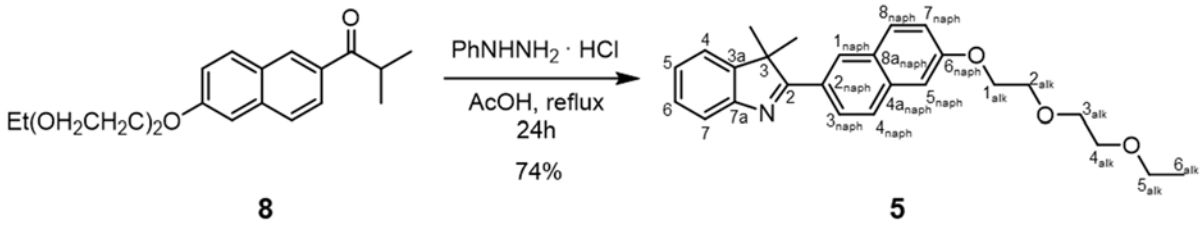

8 **5**

Compound **8** (0.77 g, 2.33 mmol) and phenylhydrazine hydrochloride (0.34 g, 2.33 mmol) were dissolved in 10mL of glacial AcOH in a 25 mL round bottom flask. The mixture was heated to reflux for 24 hours. The reaction was followed by TLC using DCM/EtAcO (95:5) as eluent. The reaction was concentrated *in vacuo*, dissolved in 25 mL of DCM and washed with Na_2CO_3conc. (2 x 15 mL) and brine (2 x 15 mL). Finally, the organic layer was dried over anhydrous $MgSO_4$ and concentrated in vacuo. The product was purified by column chromatography using DCM/EtAcO (95:5) as eluent, obtaining compound **5** as a brownish oil (0.69 g, 74% yield).

^{1}H-NMR (400 MHz, DMSO-d_6, δ ppm): 8.62 (d, J=1.7 Hz, 1H, $H_{1\ naph}$), 8.36 (dd, J = 8.8, 1.7 Hz, 1H, $H_{3\ naph}$), 8.14 (d, J = 8.9 Hz, 1H, $H_{8\ naph}$), 7.90 (d, J = 8.8 Hz, 1H, $H_{4\ naph}$), 7.63 (d, J = 7.5 Hz, 1H, H_4), 7.56 (d, J = 6.9 Hz, 1H, H_7), 7.41 (d, J = 2.4 Hz, 1H, $H_{5\ naph}$), 7.37 (td, J =

7.5, 1.2 Hz, 1H, H_5), 7.29 (td, J = 6.9, 0.8 Hz, 1H, H_6), 7.26 (dd, J = 8.9, 2.4 Hz, 1H, $H_{7\ naph}$), 4.27 (t, J= 4.8 Hz, 2H, $H_{1\ alk}$), 3.84 (t, J= 4.8Hz, 2H, $H_{2\ alk}$), 3.63 (t, J = 5.8 Hz, 2H, $H_{3\ alk}$), 3.52 (t, J=5.8 Hz, 2H, $H_{4\ alk}$), 3.45 (q, J = 7.0 Hz, 2H, $H_{5\ alk}$), 1.64 (s, 6H, $C(CH_3)_2$) 1.11 (t, J = 7.0 Hz, 3H, $H_{6\ alk}$).

^{13}C-NMR (101 MHz, DMSO-d_6, δ ppm): 182.8 (C_2), 158.3 ($C_{6\ naph}$), 153.2 (C_{3a}), 148.5 (C_{7a}), 135.9 ($C_{4a\ naph}$), 131.4 ($C_{8\ naph}$), 128.8 ($C_{1\ naph}$), 128.5 ($C_{2\ naph}$), 128.1 ($C_{8a\ naph}$), 128.1 (C_5), 127.6 ($C_{4\ naph}$), 126.2 ($C_{3\ naph}$), 126.2 (C_6), 121.9 (C_7), 120.7 (C_4), 119.6 ($C_{7\ naph}$), 107.3 ($C_{5\ naph}$), 70.5 ($C_{3\ alk}$), 69.7 ($C_{4\ alk}$), 69.3 ($C_{2\ alk}$), 67.8 ($C_{1\ alk}$), 66.1 ($C_{5\ alk}$), 53.4 ($\underline{C}(CH_3)_2$), 25.0 ($C(\underline{CH_3})_2$), 15.6 ($C_{6\ alk}$).

IR (υ cm^{-1}): 3060, 2969, 2925, 2866, 1625, 1602, 1519, 1453, 1272, 1255, 1206, 1107, 752.

HRMS (ESI, m/z): calculated mass for $C_{26}H_{30}N_1O_3$ ($M+H^+$): 404.2220; found, 404.2219.

8.3.4 Synthesis of 1-(6-(4-bromobutoxy)naphthalen-2-yl)-2-methylpropan-1-one (9)

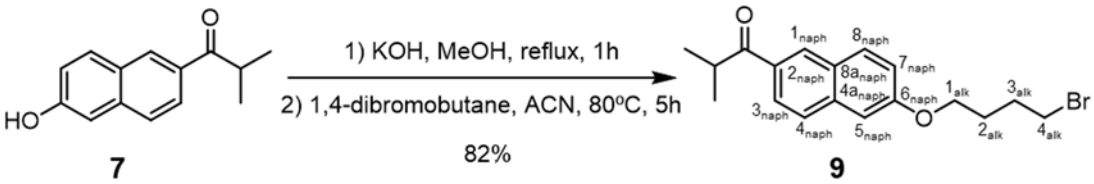

7 9

Compound **7** (2.60 g, 12.13 mmol) was dissolved in MeOH and KOH (0.88 g, 13.34 mmol) was added. This mixture was heated until reflux for one hour. Then, the resulting alkoxide salt was concentrated *in vacuo*. In a 250 mL two-neck round bottom flask, 1,4-dibromobutane (1.88 mL, 15.77 mmol) was solved in 100 mL of ACN and heated at 80 ºC. The alkoxide salt was dispersed in 20 mL of ACN and slowly added to the two-neck round bottom flask through a dropping funnel. After finishing the addition, the temperature was maintained for 2 hours. The reaction was followed by TLC using DCM/*n*-hexane 8:2 as eluent. When the reaction finished, was concentrated *in vacuo* and dissolved in 50 mL of DCM. The solution was washed with 10 % $NaHCO_3$ (2 x 50 mL) and water (50 mL). The

organic layer was dried over anhydrous $MgSO_4$ and concentrated *in vacuo*. The product was purified by column chromatography using DCM/*n*-hexane (8:2) to afford compound **9** as a brown oil (3.45 g, 82% yield).

^{1}H-NMR (400 MHz, $CDCl_3$, δ ppm): 8.42 (d, J = 1.7 Hz, 1H, *H*$_1$), 8.03 (dd, J = 8.7, 1.7 Hz, 1H, *H*$_3$), 7.88 (d, J = 8.9 Hz, 1H, *H*$_8$), 7.78 (d, J = 8.7 Hz, 1H, *H*$_4$), 7.21 (dd, J = 8.9, 2.5 Hz, 1H, *H*$_7$), 7.17 (d, J = 2.5 Hz, 1H, *H*$_5$), 4.17 (t, J = 6.5 Hz, 2H, *H*$_{1\ alk}$), 3.73 (hept, J = 6.8 Hz, 1H, *CH*$(CH_3)_2$), 3.55 (t, J = 6.5 Hz, 2H, $H_{4\ alk}$), 2.15 (quint, J = 6.5 Hz, 2H, *H*$_{2\ alk}$), 2.06 (quint, J = 6.5 Hz, 2H, *H*$_{3\ alk}$), 1.30 (d, J = 6.8 Hz, 6H, *CH*$(CH_3)_2$).

^{13}C-NMR (101 MHz, $CDCl_3$, δ ppm): 204.2 (*C=O*), 158. 9 (*C*$_6$), 137.1 (*C*$_{4a}$), 131.6 (*C*$_7$), 131.2 (*C*$_2$), 129.6 (*C*$_1$), 128.0 (*C*$_{8a}$), 127.1 (*C*$_4$), 125.1 (*C*$_3$), 119.8 (*C*$_8$), 106.4 (*C*$_5$), 67.0 (*C*$_{1\ alk}$), 35.2 (*CH*$(CH_3)_2$), 33.4 (*C*$_{4\ alk}$), 29.5 (*C*$_{2\ alk}$), 27.8 (*C*$_{3\ alk}$), 19.4 (*CH*$(CH_3)_2$).

IR (υ cm^{-1}): 3059, 2966, 2931, 2871, 1671, 1620, 1468, 1383, 1261, 1195, 1174, 1016, 989, 855, 811, 743, 648.

HRMS (ESI, m/z): calculated mass for $C_{18}H_{22}O_2Br_1$ ($M+H^+$): 349.0798; found 349.0799.

8.3.5 Synthesis of 2-(6-(4-bromobutoxy)naphthalen-2-yl)-3,3-dimethyl-3*H*-indole (10)

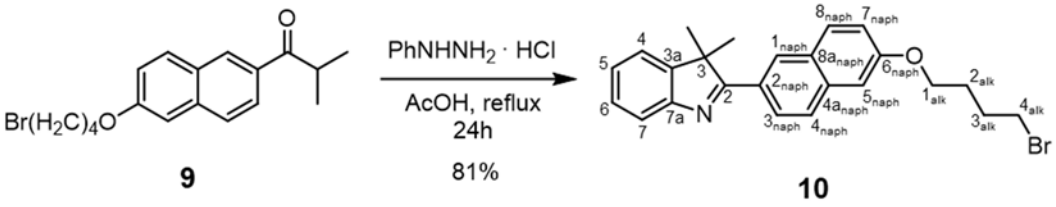

9 **10**

Compound **9** (3.40 g, 9.74 mmol) and phenylhydrazine hydrochloride (1.41 g, 9.74 mmol) were dissolved in 20 mL of glacial AcOH in a 50 mL round bottom flask. The mixture was heated to reflux for 24 hours. The reaction was followed by TLC using DCM as eluent. The reaction was then concentrated *in vacuo*, redissolved in 50 mL of DCM and washed with saturated Na_2CO_3 (2 x 30 mL) and brine (2 x 30 mL). Finally, the organic layer was dried

over anhydrous $MgSO_4$ and concentrated *in vacuo*. The product was purified by column chromatography using DCM as eluent, obtaining the compound **10** as a yellow solid (3.34 g, 81% yield).

m.p.: 132-133 ºC.

^{1}H-NMR (400 MHz, DMSO-*d*$_6$, δ ppm): 8.60 (d, J = 1.8 Hz, 1H, $H_{1\ naph}$), 8.35 (dd, J = 8.7, 1.8 Hz, 1H, $H_{3\ naph}$), 8.12 (d, J = 9.0 Hz, 1H, $H_{8\ naph}$), 7.90 (d, J = 8.7 Hz, 1H, $H_{4\ naph}$), 7.63 (d, J = 7.5 Hz, 1H, H_4), 7.55 (d, J = 7.1 Hz, 1H, H_7), 7.40 (d, J = 2.5 Hz, 1H, $H_{5\ naph}$), 7.37 (td, J = 7.5, 1.2 Hz, 1H, H_5), 7.29 (td, J = 7.1, 0.8 Hz, 1H, H_6), 7.25 (dd, J = 9.0, 2.5 Hz, 1H, $H_{7\ naph}$), 4.20 (t, J = 6.1 Hz, 2H, $H_{1\ alk}$), 3.76 (d, J = 6.3 Hz, 1H, $H_{4\ alk}$), 3.65 (t, J = 6.6 Hz, 1H, $H_{4\ alk}$), 2.08–1.88 (m, 4H, $H_{2\ alk}$ and $H_{3\ alk}$), 1.64 (s, 6H, $C(CH_3)_2$).

^{13}C-NMR (101 MHz, DMSO-*d*$_6$, δ ppm): 182.8 (C_2), 158.4 ($C_{6\ naph}$), 153.2 (C_{3a}), 148.5 (C_{7a}), 135.9 ($C_{4a\ naph}$), 131.4 ($C_{8\ naph}$), 128.8 ($C_{1\ naph}$), 128.5 ($C_{2\ naph}$), 128.1 ($C_{8a\ naph}$ and C_5), 127.5 ($C_{4\ naph}$), 126.2 ($C_{3\ naph}$), 126.1 (C_6), 121.9 (C_7), 120.7 (C_4), 119.6 ($C_{7\ naph}$), 107.3 ($C_{5\ naph}$), 67.4 ($C_{1\ alk}$), 67.3 ($C_{1\ alk}$), 53.4 ($C(CH_3)_2$), 45.7 ($C_{4\ alk}$), 35.3 ($C_{4\ alk}$), 29.6, 29.4, 27.8 and 26.6 ($C_{2\ alk}$ and $C_{3\ alk}$), 25.0 ($C(\underline{CH_3})_2$).

IR (υ cm^{-1}): 3059, 2950, 2927, 2871, 1627, 1609, 1522, 1472, 1455, 1393, 1205, 1173, 1019, 887, 865, 810, 773, 756, 650.

HRMS (ESI, m/z): calculated mass for $C_{24}H_{25}N_1O_1Br_1$ ($M+H^+$): 422.1114; found, 422.1112.

8.3.6 Synthesis of 2-(6-(4-morpholinobutoxy)naphthalen-2-yl)-3,3-dimethyl-3*H*-indole (6)

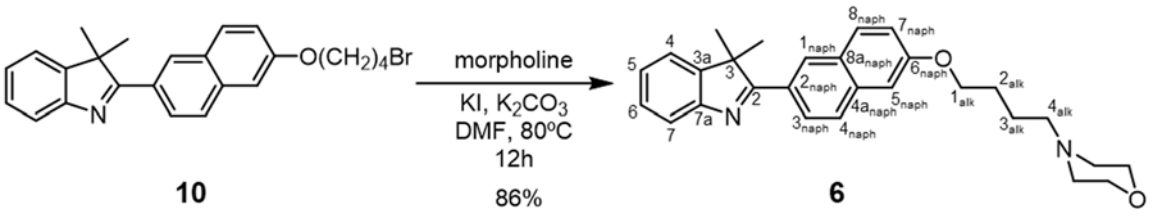

Compound **10** (0.30 g, 0.71 mmol), KI (0.03 g, 0.18 mmol) and K_2CO_3 (0.10 g, 0.75 mmol) were added to a 25 mL round bottom flask, then DMF (5 mL) and morpholine (0.20 mL, 2.24 mmol). The mixture was heated to 80 ºC overnight (*ca.* 12h). The reaction was followed by TLC using DCM/MeOH (95:5) as eluent. When the reaction was finished, 40 mL of DCM were added and washed with HCl_{aq} 2M (2 x 40 mL). The aqueous layer was neutralised with NaOH 2M (90 mL). Then, the aqueous layer was extracted with DCM (2 x 50 mL). Finally, the organic layer was dried over anhydrous $MgSO_4$ and concentrated *in vacuo* obtaining compound **6** as a yellow solid (0.26 g, 86% yield).

m.p.: 104-105 ºC.

^{1}H-NMR (400 MHz, DMSO-d_6, δ ppm): 8.61 (d, J=1.7 Hz, 1H, $H_{1\ naph}$), 8.35 (dd, J = 8.7, 1.7 Hz, 1H, $H_{3\ naph}$), 8.12 (d, J = 9.0 Hz, 1H, $H_{8\ naph}$), 7.90 (d, J = 8.7 Hz, 1H, $H_{4\ naph}$), 7.63 (d, J = 7.5 Hz, 1H, H_4), 7.56 (d, J = 7.1 Hz, 1H, H_7), 7.39 (d, J = 2.3 Hz, 1H, $H_{5\ naph}$), 7.37 (td, J = 7.5, 1.2 Hz, 1H, H_5), 7.29 (td, J = 7.1, 0.8 Hz, 1H, H_6), 7.24 (dd, J = 9.0, 2.3 Hz, 1H, $H_{7\ naph}$), 4.16 (t, J = 6.5 Hz, 2H, $H_{1\ alk}$), 3.57 (t, J = 4.6 Hz, 4H, $O\text{-}(CH_2)_{2\ morph}$), 2.36 (t, J = 7.1 Hz, 6H $N\text{-}(CH_2)_{2\ morph}$ and $H_{4\ alk}$), 1.83 (quint, J = 6.5 Hz, 2H, $H_{2\ alk}$), 1.68–1.59 (m, 8H, $C(\underline{C}H_3)_2$ and $H_{3\ alk}$).

^{13}C-NMR (101 MHz, DMSO-d_6, δ ppm): 182.8 (C_2), 158.5 ($C_{6\ naph}$), 153.2 (C_{3a}), 148.5 (C_{7a}), 135.9 ($C_{4a\ naph}$), 131.4 ($C_{8\ naph}$), 128.8 ($C_{1\ naph}$), 128.4 ($C_{2\ naph}$), 128.1 ($C_{8a\ naph}$), 128.0 (C_5), 127.5 ($C_{4\ naph}$), 126.2 ($C_{3\ naph}$), 121.9 (C_7), 120.6 (C_4), 119.7 ($C_{7\ naph}$), 107.2 ($C_{5\ naph}$), 68.0 ($C_{1\ alk}$), 66.7 ($O\text{-}(CH_2)_{2\ morph}$), 58.3 ($\underline{C}(CH_3)_2$), 53.8 and 53.4 ($N\text{-}(CH_2)_{2\ morph}$ and $C_{4\ alk}$), 27.0 ($C_{2\ alk}$), 25.0 ($C(\underline{C}H_3)_2$), 22.9 ($C_{3\ alk}$).

IR (υ cm^{-1}): 3061, 2928, 2847, 2800, 2763, 1626, 1608, 1519, 1454, 1273, 1256, 1116, 979, 867, 813, 751, 652.

HRMS (ESI, m/z): calculated mass for $C_{28}H_{32}N_2O_2$ ($M+H^+$): 429.2537; found, 429.2535.

8.3.7 Optical studies

Aqueous solutions were prepared from a 1 mM stock solution in DMSO of the interest compounds (**4**, **5** and **6**). The resulting concentration of DMSO in these solutions was *ca.* 1%, which has negligible effect on the photophysical properties.

Aqueous *pH*-adjusted solutions were prepared by addition of HCl or NaOH 1M to ultrapure water, controlling *pH* value with a well-calibrated *pH*-meter.

For interference studies, metallic ions were provided from their commercially available inorganic salts: NaCl, $MgCl_2$, KCl, $CaCl_2$, $FeSO_4 \cdot 7H_2O$, $CuCl_2 \cdot 2H_2O$, $ZnCl_2$, $NiCl_2 \cdot 6H_2O$ and $CoCl_2 \cdot 6H_2O$ for Na^+, Mg^{2+}, K+, Ca^{2+}, Fe^{2+}, Cu^{2+}, Zn^{2+}, Ni^{2+} and Co^{2+} respectively. These salts were added to 3 mL of 10 μM *pH*-adjusted aqueous solutions of **5** or **6**, to obtain a final concentration of the ions of 1 mM.

8.3.8 Cell studies

As in Chapter 3, cell studies were performed in collaboration with the group of Prof. Dr. Jose Maria Perez-Pomares.

Cell culture and incubation with compounds 5 and 6

Cell cultures details are identical to those explained in Section 8.2.7.

Different incubation treatments were applied. MEF cells were treated with 10 μM **5** or **6** in PBS *pH* 7.4 for one hour. To equilibrate the pH_i with external *pH*, cells were then incubated in citric acid/phosphate buffer adjusted to various pHs (7.40, 4.30 and 3.30). These buffers were supplemented with 10 nM nigericin (a well-known K^+/H^+ ionophore) and 140 mM KCl.[361]

Cell cytotoxicity assay

WST-1 assay was again used to test the cytotoxicity of compounds **5** and **6** in MEF cells. The protocols followed were analogous to those described in Section 8.2.7, excepting the employed concentrations of the compounds. These dyes were incubated at 0.01 μM, 0.1 μM, M, 1.0 μM, and 10.0 μM concentrations with MEF cells in fresh medium. Three replicas were performed for each sample (n=3).

Visualization of intracellular fluorescence in 2PM from protonated 5 or 6

Intracellular fluorescence and distribution following incubation with compounds **5** and **6** (in their protonated forms) were analyzed following the procedures detailed in Section 8.2.7. Different excitation and emission settings were utilized: 800 nm light was employed for 2P-excitation, and fluorescence was detected between 450 and 550 nm.

Colocalization experiments

To examine the lysosomal localization, LTDR was used as a counterstain to **5H**/**6H**. Details about the image acquisition and the colocalization analysis are identical to those of Section 8.2.7. Please note that excitation and emission wavelengths for visualizing **5H**/**6H** are mentioned above.

8.4 EXPERIMENTAL PROCEDURES IN CHAPTER 5

8.4.1 Synthesis of 2-(6-(2-(2-ethoxyethoxy)ethoxy)naphthalen-2-yl)-1,3,3-trimethyl-3*H*-indol-1-ium iodide (11)

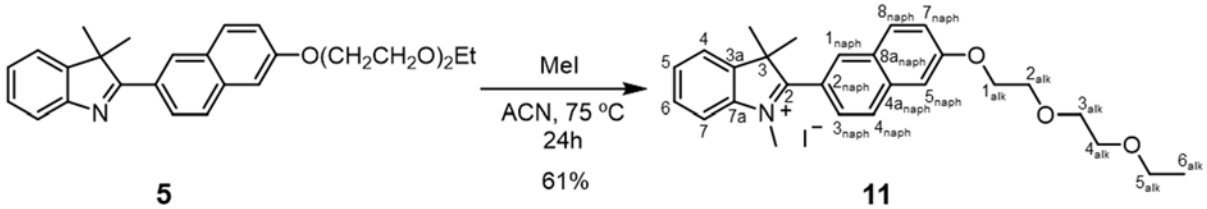

5 **11**

In a 20 mL sealed tube, compound **5** (0.190 g, 0.47 mmol) was dissolved in 5 mL of ACN. Methyl iodide was then added (0.09 mL, 1.45 mmol) and the mixture heated to 75 °C for 24 hours. The reaction was followed by TLC using DCM/MeOH 98:2 as eluent. The crude product was concentrated *in vacuo* and purified by column chromatography using DCM/MeOH (98:2 to 95:5) as eluent. Compound **11** was obtained as a red viscous oil (0.157 g, 61% yield).

^{1}H-NMR (400 MHz, DMSO-d_6, δ ppm): 8.36 (d, J = 1.8 Hz, 1H, $H_{1\ naph}$), 8.13 (d, J = 8.7 Hz, 1H, $H_{4\ naph}$), 8.12 - 8.03 (m, 2H, $H_{8\ naph}$ and H_7), 8.00 - 7.91 (m, 1H, H_4), 7.78 (dd, J = 8.7, 1.8 Hz, 1H, $H_{3\ naph}$), 7.78 - 7.69 (m, 2H, H_5 and H_6), 7.56 (d, J = 2.5 Hz, 1H, $H_{5\ naph}$), 7.39 (dd, J = 9.0, 2.5 Hz, 1H, $H_{7\ naph}$), 4.33 - 4.28 (m, 2H, $H_{1\ alk}$), 3.98 (s, 3H, NCH_3), 3.88 - 3.81 (m, 2H, $H_{2\ alk}$), 3.63 (dd, J = 5.9, 3.6 Hz, 2H, $H_{3\ alk}$), 3.52 (dd, J = 5.9, 3.6 Hz, 2H, $H_{4\ alk}$), 3.44 (q, J = 7.0 Hz, 2H, $H_{5\ alk}$), 1.65 (s, 6H, $C(\underline{CH_3})_2$), 1.10 (t, J = 7.0 Hz, 3H, $H_{6\ alk}$).

^{13}C-NMR (101 MHz, DMSO-d_6, δ ppm): 189.8 (C_2), 159.0 ($C_{6\ naph}$), 142.3 (C_{7a}), 142.2 (C_{3a}), 136.3 ($C_{4a\ naph}$), 131.0 ($C_{8\ naph}$), 130.1 (C_5), 129.7 ($C_{1\ naph}$), 129.1 (C_6), 127.9 ($C_{4\ naph}$), 127.3 ($C_{8a\ naph}$), 124.5 ($C_{3\ naph}$), 123.4 (C_4), 120.6 ($C_{7\ naph}$), 120.5 ($C_{2\ naph}$), 116.1 (C_7), 107.0 ($C_{5\ naph}$), 70.1 ($C_{3\ alk}$), 69.3 ($C_{4\ alk}$), 68.8 ($C_{2\ alk}$), 67.6 ($C_{1\ alk}$), 65.6 ($C_{5\ alk}$), 55.1 ($\underline{C}(CH_3)_2$), 36.8 (NCH_3), 22.2 ($C(\underline{CH_3})_2$), 15.1 ($C_{6\ alk}$).

IR (υ cm^{-1}): 3369, 2972, 2924, 2866, 2361, 2339, 1620, 1601, 1582, 1517, 1484, 1457, 1395, 1349, 1271, 1249, 1211, 1184, 1105, 1051, 971, 939, 925, 861, 817, 765, 720, 690, 669, 650, 630.

HRMS (ESI, m/z): calculated mass for $C_{27}H_{32}N_1O_3$ (M^+): 418.2377, found: 418.2375.

8.4.2 Synthesis of 2-(6-(4-iodobutoxy)naphthalen-2-yl)-1,3,3-trimethyl-3*H*-indol-1-ium iodide (13)

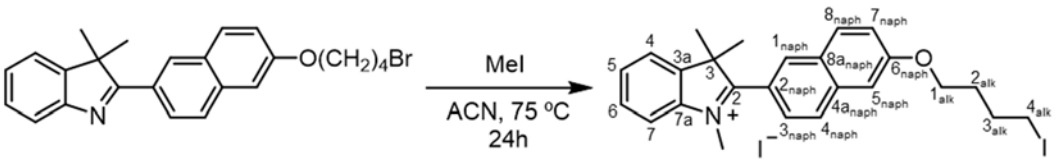

10 **13**

In a 20 mL sealed tube, compound **10** (0.400 g, 0.95 mmol) was dissolved in 5 mL of ACN. Methyl iodide was then added (0.18 mL, 2.89 mmol) and the mixture was heated to 75 °C for 24 hours. The reaction was monitored by TLC using dichloromethane/methanol (98:2) as eluent. Once the reaction was completed, the crude product was concentrated *in vacuo* and thoroughly washed with approximately 20 mL of cold diethyl ether/EtOH (95:5). **13** was obtained as an orange solid (0.580 g, quantitative yield) and used without further purification.

m.p.: 136 °C.

^{1}H-NMR (400 MHz, DMSO-d_6, δ ppm): 8.35 (s, 1H, $H_{1\ naph}$), 8.13 (d, J = 8.7 Hz, 1H, $H_{4\ naph}$), 8.11 - 8.04 (m, 2H, $H_{8\ naph}$ and H_7), 7.98 - 7.92 (m, 1H, H_4), 7.77 (d, J = 8.7 Hz, 1H, $H_{3\ naph}$), 7.75 - 7.68 (m, 2H, H_5 and H_6), 7.55 (d, J = 2.5 Hz, 1H, $H_{5\ naph}$), 7.37 (dd, J = 8.9, 2.5 Hz, 1H, $H_{7\ naph}$), 4.22 (t, J = 6.2 Hz, 2H, $H_{1\ alk}$), 3.40 (t, J = 6.7 Hz, 2H, $H_{4\ alk}$), 2.04 - 1.95 (m, 2H, $H_{3\ alk}$), 1.95 - 1.88 (m, 2H, $H_{2\ alk}$), 1.65 (s, 6H, $C(CH_3)_2$).

^{13}C-NMR (101 MHz, DMSO-d_6, δ ppm): 189.8 (C_2), 159.1 ($C_{6\ naph}$), 142.3 (C_{7a}), 142.2 (C_{3a}), 136.3 ($C_{4a\ naph}$), 131.0 ($C_{8\ naph}$), 130.1 (C_5), 129.7 ($C_{1\ naph}$), 129.1 (C_6), 127.9 ($C_{4\ naph}$), 127.2 ($C_{8a\ naph}$), 124.5 ($C_{3\ naph}$), 123.4 (C_4), 120.6 ($C_{7\ naph}$), 120.4 ($C_{2\ naph}$), 116.1 (C_7), 107.0 ($C_{5\ naph}$), 66.9 ($C_{1\ alk}$), 55.1 ($\underline{C}(CH_3)_2$), 36.8 (NCH_3), 29.7 ($C_{3\ alk}$), 29.5 ($C_{2\ alk}$), 22.2 ($C(\underline{CH_3})_2$), 8.4 ($C_{4\ alk}$).

IR (υ cm^{-1}): 3020, 2928, 2869, 1620, 1602, 1560, 1484, 1461, 1418, 1389, 1271, 1209, 1182, 1129, 1045, 1015, 936, 918, 857, 814, 760, 670, 650, 634.

HRMS (ESI, m/z): calculated mass for $C_{25}H_{27}N_1O_1I_1$ (M^+): 484.1132, found: 484.1133.

8.4.3 Synthesis of 2-(6-(4-morpholino-4-ium)naphthalen-2-yl)-1,3,3-trimethyl-3*H*-indol-1-ium iodide (12)

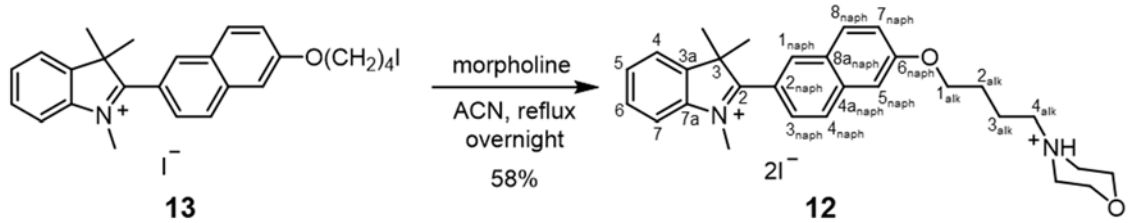

Compound **13** (0.383 g, 0.63 mmol) was dissolved in 5 mL of ACN in a 25 mL round bottom flask. Morpholine (0.08 mL, 0.92 mmol) was added, and the mixture heated to reflux overnight (*ca.* 12h). The reaction was followed by TLC using DCM/MeOH 98:2 as eluent. The crude product was concentrated *in vacuo* and purified by column chromatography using DCM/MeOH (98:2 to 95:5) as eluent. Compound **12** was obtained as a red viscous oil (0.253 g, 58% yield).

^{1}H-NMR (400 MHz, DMSO-*d*$_6$, δ ppm): 10.76 (s, 1H, NH_{morph}), 8.36 (d, J = 1.8 Hz, 1H, $H_{1\ naph}$), 8.14 (d, J = 8.7 Hz, 1H, $H_{4\ naph}$), 8.11 - 8.05 (m, 2H, $H_{8\ naph}$ and H_7), 7.98 - 7.93 (m, 1H, H_4), 7.78 (dd, J = 8.7, 1.8 Hz, 1H, $H_{3\ naph}$), 7.76 - 7.71 (m, 2H, H_5 and H_6), 7.55 (d, J = 2.5 Hz, 1H, $H_{5\ naph}$), 7.37 (dd, J = 9.0, 2.5 Hz, 1H, $H_{7\ naph}$), 4.25 - 4.19 (m, 2H, $H_{1\ alk}$), 4.00 - 3.93 (m, 5H, NCH_3 and $OCH_{2\ morph}$), 3.83 - 3.76 (m, 2H, $OCH_{2\ morph}$), 3.45 - 3.40 (m, 2H, $NCH_{2\ morph}$, under residual water signal), 3.21 - 3.15 (m, 2H, $H_{4\ alk}$), 3.10 - 3.02 (m, 2H, $NCH_{2\ morph}$), 1.94 - 1.84 (m, 4H, $H_{2\ alk}$ and $H_{3\ alk}$), 1.65 (s, 6H, $C(CH_3)_2$).

^{13}C-NMR (101 MHz, DMSO-*d*$_6$, δ ppm): 189.8 (C_2), 159.0 ($C_{6\ naph}$), 142.3 (C_{7a}), 142.2 (C_{3a}), 136.3 ($C_{4a\ naph}$), 131.0 ($C_{8\ naph}$), 130.1 (C_5), 129.7 ($C_{1\ naph}$), 129.1 (C_6), 127.9 ($C_{4\ naph}$), 127.3 ($C_{8a\ naph}$), 124.5 ($C_{3\ naph}$), 123.4 (C_4), 120.6 ($C_{7\ naph}$), 120.5 ($C_{2\ naph}$), 116.2 (C_7), 107.0 ($C_{5\ naph}$),

67.3 (*$C_{1\ alk}$*), 63.2 (*relative to both $O(\underline{CH_2})_{2\ morph}$*), 55.6 (*$C_{4\ alk}$*), 55.1 (*$\underline{C}(CH_3)_2$*), 50.9 (*relative to both $N(\underline{CH_2})_{2\ morph}$*), 36.8 (*$NCH_3$*), 22.2 (*$C(\underline{CH_3})_2$*), 25.8 and 19.8 (*$C_{2\ alk}$* and *$C_{3\ alk}$*).

IR (υ cm^{-1}): 3377, 2934, 2870, 2601, 2470, 1620, 1577, 1485, 1462, 1395, 1270, 1210, 1184, 1133, 1108, 1048, 1017, 969, 918, 868, 821, 766, 717, 669, 620, 616.

HRMS (ESI, m/z): calculated mass for $C_{29}H_{36}N_2O_2$ (M^{2+}): 222.1383, found: 222.1383.

8.4.4 Interference studies

Metallic ions were provided from their commercially available inorganic salts: NaCl, $MgCl_2$, KCl, $CaCl_2$, $FeCl_3 \cdot 6H_2O$ and $CuCl_2 \cdot 2H_2O$ for Na^+, Mg^{2+}, K+, Ca^{2+}, $Fe^{3+}$and Cu^{2+} respectively. These salts were added to 3 mL of 10 μM aqueous **11** or **12** to get a final concentration of the ions of 1 mM. Cysteine interference was examined in the same manner.

8.4.5 Cell studies

Cell studies were carried out by Dr. John R. Pearson, from the U28 Unit of the ICTS "NANBIOSIS" hosted at the Andalusian Centre for Nanomedicine & Biotechnology (Bionand).

Cell culture and incubation with compounds 11 and 12

HeLa cells were cultured in complete medium at 37°C in a humidified environment with 5% CO_2. For microscopy experiments cells were grown on 8-well chambered slides suitable for optical microscopy to approximately 50% confluency. Cells were pre-incubated with 10 μM solutions of the **11** or **12** in complete medium for 2 hours. Prior to fluorescence imaging, media was replaced with fresh unlabeled complete medium. Images were recorded at 0- and 24-hours post-incubation.

Cell cytotoxicity assay

"Live/dead" assay was used to test the cytotoxicity of **11** and **12** in HeLa cells. This assay consists in determining live and dead cells, which are differentially labeled by using propidium iodide. This compound only passes through the disordered areas of the nuclear membrane of dead cells.

Cells were cultured in complete medium (DMEM + 10% FBS + 1% Penicillin-Streptomycin + 2 mM L-Glutamine) in a 96-well microplate to a total volume of 100 µL per well. Wells were seeded with ~10000 cells and grown under optimal conditions (37 ºC and 5% CO_2 atmosphere) until reaching ~50-60% confluency (~2.0-2.2 x 10^4 cells/well), typically after 24h. Compounds **11** or **12** were then added at different concentrations: 0.001 µM, 0.005 µM, 0.01 µM, 0.05 µM, 0.1 µM, 0.5 µM,1 µM, 5 µM and 10.0 µM. After incubating for 24 hours, propidium iodide was added (10 µL), and cells (living and dead ones) were counted in a Perkin Elmer Operetta High Content Screening (HCS) system. Accounting the total number of cells for each well, the percentage of living cells was calculated. Four replicas for each condition were performed, and the results refer to the average. Cells without any compound were used as negative controls.

Visualization of intracellular fluorescence from 11 or 12

The fluorescence properties of derivatives **11** and **12** in HeLa cells were analyzed using Leica SP5 confocal/multiphoton microscope mentioned previously. Cell imaging was performed using a 63x PLAN APO NA 1.4 oil immersion objective. Dye visualization was performed by combining Confocal and 2P microscopy. Emission was recorded in two different channels with different excitation sources and emission windows: a green channel ($\lambda_{exc,\,2P}$ = 740 nm, λ_{em} = 450 - 520 nm) and a red channel ($\lambda_{exc,\,1P}$ = 514 nm, λ_{em} = 580 - 700 nm). Brightfield transmitted light images were captured at the same time. Negative control cells, without **11** or **12**, did not show significant background fluorescence.

Colocalization experiments

Colocalization experiments were performed by adding LTDR (Thermofisher Scientific Cat. No. L12492; 50 nM final concentration) or Mitotracker Green FM (MTG, Thermofisher Scientific Cat. No. M7514; 20 nM final concentration) to the cell culture media approximately 30 minutes prior to visualization by microscopy. The commercial dyes were visualized using single photon excitation: $\lambda_{exc,\ 1P}$ = 633 nm, λ_{em} = 645 - 740 nm for LTDR, and $\lambda_{exc,\ 1P}$ = 458 nm, λ_{em} = 470 – 560 nm for MTG. These configurations were selected to avoid signal contamination between markers. Compounds **11** or **12** were detected sequentially using the two-photon configuration described above. As lysosomes and mitochondria are extremely mobile in MEF cells, images were captured at high speed to minimize the time delay between confocal and two photon acquisitions (<1 s). Identical laser power and gain settings were used for all samples within each experiment.

Colocalization analysis comparing MTG and LTDR with compound **11** and **12**, were carried out using the "Coloc 2" module of the image processing package ImageJ.[421,422] PCC values were obtained for the different combinations between the compounds channels *vs.* MTG or LTDR, as indicated in the corresponding figures to colocalization experiments.

8.4.5 Additional photophysical studies

pH titrations

Aqueous *pH*-adjusted solutions were prepared by addition of HCl or NaOH 1M to ultrapure water, controlling *pH* value with a well-calibrated *pH*-meter. Compounds 11 and 12 were added from a 10^{-3} M stock solution in DMSO.

Aggregation studies

Self-assembly effects were studied by increasing the compounds concentration from 10^{-5} M to 10^{-2} M in acetonitrile solution.

Studies of the optical properties of the aggregates in pH-viscosity combined conditions

Diverse mixtures of *pH*-adjusted and glycerine were prepared in 1:1 proportion of aqueous solution/glycerine. Two *pH* conditions were examined: 4.0 and 8.0. Compounds were directly dissolved in these solutions. As well, the effect of pH alone was examined in a similar manner.

8.5 EXPERIMENTAL PROCEDURES IN CHAPTER 6

8.5.1 Optical studies

Fluorescence lifetimes for compounds in this Chapter were determined using a time-correlated single-photon-counting (TC-SPC) setup. The excitation light (λ_{exc} = 377 nm) was provided at a repetition rate of 20 MHz by a diode laser (LDH-P-C-375) powered by a PDL 800B pulsed diode driver (Picoquant, GmbH Germany). The emitted photons were collected at the magic angle (54.7°) at around the emission maxima by a thermoelectrically cooled microchannel plate photomultiplier tube (R3809U-50, Hamamatsu). The signal was digitalized using a multi-channel analyzer with 4096 channels (SPC-300, Edinburgh Analytical Instruments) and to ensure good statistics 10000 counts were recorded in the top channel. The measured fluorescence decays were fitted after deconvolution of the data with the instrument response function (IRF).

The isomerization quantum yields were determined according to standard procedures by using furylfulgide (Aberchrome 540™) as actinometer. [411–413] The ring-opening reactions were triggered using 523 nm from a LED (LZ4-00G108-0000). The closing reactions were carried out with a 302 nm handheld lamp (UVP 34004401). The absorbance changes in the dyad were monitored at 592 nm and compared to those of the reference compound at 494 nm under identical irradiation power/geometries. The molar absorption coefficients of either the dyad and the reference compound, at 302 nm for the open isomers and at 523 nm for the closed isomers, were used to correct the isomerization quantum yields of the closing and the opening reactions, respectively.

8.5.2 Kinetic studies under 2P-excitation conditions

A **14o** solution (10 μM in methanol) was irradiated with 302 nm light until the photostationary state was reached, being this process followed by UV/vis absorption. Approximately less than 1 μL of this solution was introduced inside 5 μL microcapillary tubes (Hirschmann). Theses tubes were employed in order to avoid as much as possible any diffusion phenomena. The capillaries were then sealed to avoid evaporation of the solvent. The isomerization process was followed by recording 500 images during 120 seconds, *i.e.*, 1 image each 240 msec. Excitation at 820 nm was carried out at half intensity and full intensity of the laser power at this wavelength.

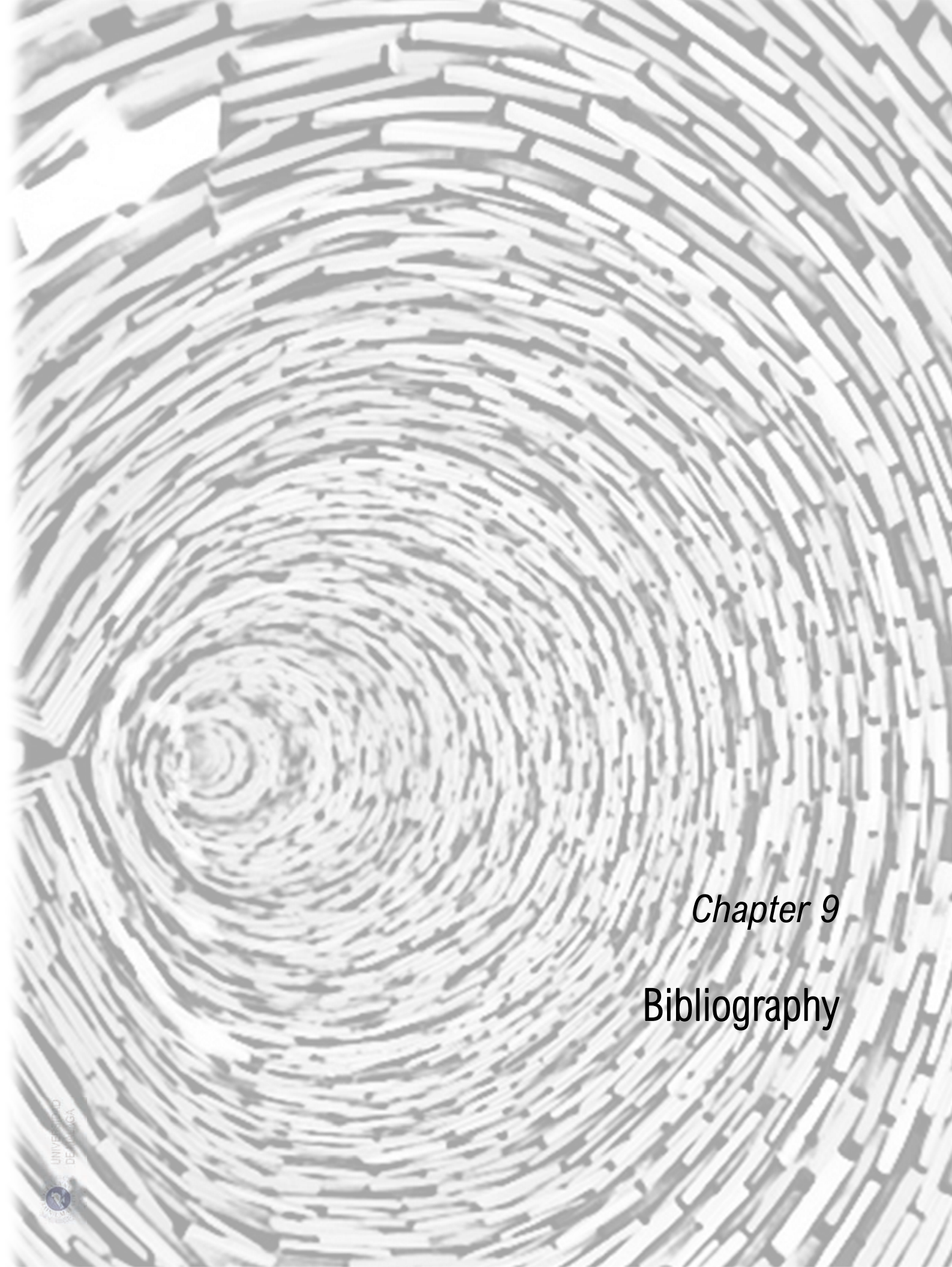

Chapter 9

Bibliography

(1) Göppert-Mayer, M. Über Elementarakte Mit Zwei Quantensprüngen. *Ann. Phys.* **1931**, *401* (3), 273–294. https://doi.org/10.1002/andp.19314010303.

(2) Göppert-Mayer, M. On Closed Shells in Nuclei. II. *Phys. Rev.* **1949**, *75* (12), 1969–1970. https://doi.org/10.1103/PhysRev.75.1969.

(3) Dombey, N. The Nobel Prize in Physics 1963 https://www.nobelprize.org/prizes/physics/1963/summary/ (accessed Feb 4, 2021). https://doi.org/10.1038/300106a0.

(4) Kaiser, W.; Garrett, C. G. B. Two-Photon Excitation in CaF2: Eu2+. *Phys. Rev. Lett.* **1961**, *7* (6), 229–231. https://doi.org/10.1103/PhysRevLett.7.229.

(5) Gould, G. The LASER, Light Amplification by Stimulated Emission of Radiation. In *The Ann Arbor conference on optical pumping*; University of Michigan, Ed.; 1959.

(6) He, G. S.; Reinhardt, B. A.; Bhawalkar, J. D.; Prasad, P. N. Three-Photon-Absorption-Induced Fluorescence and Optical Limiting Effects in an Organic Compound. *Opt. Lett.* **1995**, *20* (14), 1524. https://doi.org/10.1364/ol.20.001524.

(7) Szmacinski, H.; Gryczynski, I.; Lakowicz, J. R. Three-Photon Induced Fluorescence of the Calcium Probe Indo-1. *Biophys. J.* **1996**, *70* (1), 547–555. https://doi.org/10.1016/S0006-3495(96)79601-7.

(8) Lakowicz, J. R.; Gryczynski, I.; Malak, H.; Schrader, M.; Engelhardt, P.; Kano, H.; Hell, S. W. Time-Resolved Fluorescence Spectroscopy and Imaging of DNA Labeled with DAPI and Hoechst 33342 Using Three-Photon Excitation. *Biophys. J.* **1997**, *72* (2 I), 567–578. https://doi.org/10.1016/S0006-3495(97)78696-X.

(9) Maiti, S.; Shear, J. B.; Williams, R. M.; Zipfel, W. R.; Webb, W. W. Measuring Serotonin Distribution in Live Cells with Three-Photon Excitation. *Science (80-.).* **1997**, *275* (5299), 530–532. https://doi.org/10.1126/science.275.5299.530.

(10) He, G. S.; Markowicz, P.; Lin, T. C.; Prasad, P. N. Observation of Stimulated Emission by Direct Three-Photon Excitation. *Nature* **2002**, *415* (6873), 767–770. https://doi.org/10.1038/415767a.

(11) Hernández, F. E.; Belfield, K. D.; Cohanoschi, I.; Balu, M.; Schafer, K. J. Three- and Four-Photon Absorption of a Multiphoton Absorbing Fluorescent Probe. *Appl. Opt.* **2004**, *43* (28), 5394–5398. https://doi.org/10.1364/AO.43.005394.

(12) Wu, P. L.; Feng, X. J.; Tam, H. L.; Wong, M. S.; Cheah, K. W. Efficient Three-Photon Excited Deep Blue Photoluminescence and Lasing of Diphenylamino and 1,2,4-Triazole Endcapped Oligofluorenes. *J. Am. Chem. Soc.* **2009**, *131* (3), 886–887. https://doi.org/10.1021/ja806703v.

(13) Fan, H. H.; Guo, L.; Li, K. F.; Wong, M. S.; Cheah, K. W. Exceptionally Strong Multiphoton-Excited Blue Photoluminescence and Lasing from Ladder-Type Oligo(p -Phenylene)S. *J. Am. Chem. Soc.* **2012**, *134* (17), 7297–7300. https://doi.org/10.1021/ja302085q.

(14) Horton, N. G.; Wang, K.; Kobat, D.; Clark, C. G.; Wise, F. W.; Schaffer, C. B.; Xu, C. In Vivo Three-Photon Microscopy of Subcortical Structures within an Intact Mouse Brain. *Nat. Photonics* **2013**, *7* (3), 205–209. https://doi.org/10.1038/nphoton.2012.336.

(15) Gryczynski, I.; Piszczek, G.; Gryczynski, Z.; Lakowicz, J. R. Four-Photon Excitation of 2,2′-Dimethyl-p-Terphenyl. *J. Phys. Chem. A* **2002**, *106* (5), 754–759. https://doi.org/10.1021/jp012860n.

(16) Markowicz, P. P.; He, G. S.; Prasad, P. N. Direct Four-Photon Excitation of Amplified Spontaneous Emission in a Nonlinear Organic Chromophore. *Opt. Lett.* **2005**, *30* (11), 1369. https://doi.org/10.1364/ol.30.001369.

(17) Zheng, Q.; Zhu, H.; Chen, S. C.; Tang, C.; Ma, E.; Chen, X. Frequency-Upconverted Stimulated Emission by Simultaneous Five-Photon Absorption. *Nat. Photonics* **2013**, *7* (3), 234–239. https://doi.org/10.1038/nphoton.2012.344.

(18) Chen, W.; Bhaumik, S.; Veldhuis, S. A.; Xing, G.; Xu, Q.; Grätzel, M.; Mhaisalkar, S.; Mathews, N.; Sum, T. C. Giant Five-Photon Absorption from Multidimensional Core-Shell Halide Perovskite Colloidal Nanocrystals. *Nat. Commun.* **2017**, *8* (3), 1–9. https://doi.org/10.1038/ncomms15198.

(19) Lakowicz, J. R. *Principles of Fluorescence Spectroscopy*; 2006. https://doi.org/10.1007/978-0-387-46312-4.

(20) Peticolas, W. L. Multiphoton Spectroscopy. *Annu. Rev. Phys. Chem.* **1967**, *18* (1), 233–260. https://doi.org/10.1146/annurev.pc.18.100167.001313.

(21) McClain, W. M. Two-Photon Molecular Spectroscopy. *Acc. Chem. Res.* **1974**, *7* (5), 129–135. https://doi.org/10.1021/ar50077a001.

(22) Xu, C.; Webb, W. W. Multiphoton Excitation of Molecular Fluorophores and Nonlinear Laser Microscopy. In *Topics in Fluorescence Spectroscopy*; Springer US: Boston, MA, 2002; pp 471–540. https://doi.org/10.1007/0-306-47070-5_11.

(23) Monson, P. R.; McClain, W. M. Polarization Dependence of the Two-Photon Absorption of Tumbling Molecules with Application to Liquid 1-Chloronaphthalene and Benzene. *J. Chem. Phys.* **1970**, *53* (1), 29–37. https://doi.org/10.1063/1.1673778.

(24) Mcclain, W. M. Excited State Symmetry Assignment through Polarized Two-Photon Absorption Studies of Fluids. *J. Chem. Phys.* **1971**, *55* (6), 2789–2796. https://doi.org/10.1063/1.1676494.

(25) Dick, B.; Hohlneicher, G. Importance of Initial and Final States as Intermediate States in Two-Photon Spectroscopy of Polar Molecules. *J. Chem. Phys.* **1981**, *76* (12), 5755–5760. https://doi.org/10.1063/1.442971.

(26) Mortensen, O. S.; Svendsen, E. N. Initial and Final Molecular States as “Virtual States” in Two-Photon Processes. *J. Chem. Phys.* **1981**, *74* (6), 3185–3189. https://doi.org/10.1063/1.441512.

(27) Parthenopoulos, D. A.; Rentzepis, P. M. Three-Dimensional Optical Storage Memory. *Science (80-.).* **1989**, *245* (4920), 843–845. https://doi.org/10.1126/science.245.4920.843.

(28) Dvornikov, A. S.; Rentzepis, P. M. Novel Organic ROM Materials for Optical 3D Memory Devices. *Opt. Commun.* **1997**, *136* (1–2), 1–6. https://doi.org/10.1016/S0030-4018(96)00645-1.

(29) Loudon, R.; von Foerster, T. *The Quantum Theory of Light*, Third Edit.; Oxford University Press, 1973. https://doi.org/10.1119/1.1987930.

(30) Butcher, P. N.; Cotter, D. *The Elements of Nonlinear Optics*; Cambridge University Press, 1990. https://doi.org/10.1017/cbo9781139167994.

(31) Boyd, R. *Nonlinear Optics*, 2nd Editio.; Elsevier, 2002.

(32) Meath, W. J.; Power, E. A. On the Importance of Permanent Moments in Multiphoton Absorption Using Perturbation Theory. *J. Phys. B At. Mol. Phys.* **1984**, *17* (5), 763–781.

https://doi.org/10.1088/0022-3700/17/5/017.

(33) Birge, R. R. One-Photon and Two-Photon Excitation Spectroscopy. In *Ultrasensitive Laser Spectroscopy*, Academic Press, 1983; pp 109–174. https://doi.org/10.1016/b978-0-12-414980-9.50007-8.

(34) Karplus, M. Contact Electron-Spin Coupling of Nuclear Magnetic Moments. *J. Chem. Phys.* **1959**, *30* (1), 11–15. https://doi.org/10.1063/1.1729860.

(35) Karplus, M. Vicinal Proton Coupling in Nuclear Magnetic Resonance. *J. Am. Chem. Soc.* **1963**, *85* (18), 2870–2871. https://doi.org/10.1021/ja00901a059.

(36) Parrill, A. L.; Lipkowitz, K. B. *Reviews in Computational Chemistry*; Reviews in Computational Chemistry; Wiley, 1990. https://doi.org/10.1002/9781119518068.

(37) Cramer, C. J. *Essentials of Computational Chemistry: Theories and Models, 2nd Edition | Wiley*, 2nd ed.; Wiley, 2004.

(38) Levine, I. N. *Quantum Chemistry*, 7th ed.; Pearson, 2014.

(39) Bachrach, S. M. *Computational Organic Chemistry*, 2nd ed.; Bachrach, S. M., Ed.; Wiley, 2014.

(40) Jensen, F. *Introduction to Computational Chemistry*, 3rd ed.; Wiley, 2017.

(41) Albota, M.; Beljonne, D.; Brédas, J. L.; Ehrlich, J. E.; Fu, J. Y.; Heikal, A. A.; Hess, S. E.; Kogej, T.; Levin, M. D.; Marder, S. R.; McCord-Maughon, D.; Perry, J. W.; Röckel, H.; Rumi, M.; Subramaniam, G.; Webb, W. W.; Wu, X. L.; Xu, C. Design of Organic Molecules with Large Two-Photon Absorption Cross Sections. *Science (80-.).* **1998**, *281* (5383), 1653–1656. https://doi.org/10.1126/science.281.5383.1653.

(42) Rumi, M.; Ehrlich, J. E.; Heikal, A. A.; Perry, J. W.; Barlow, S.; Hu, Z.; McCord-Maughon, D.; Parker, T. C.; Röckel, H.; Thayumanavan, S.; Marder, S. R.; Beljonne, D.; Brédas, J. L. Structure - Property Relationships for Two-Photon Absorbing Chromophores: Bis-Donor Diphenylpolyene and Bis(Styryl)Benzene Derivatives. *J. Am. Chem. Soc.* **2000**, *122* (39), 9500–9510. https://doi.org/10.1021/ja994497s.

(43) Martin, R. L. Natural Transition Orbitals. *J. Chem. Phys.* **2003**, *118* (11), 4775–4777. https://doi.org/10.1063/1.1558471.

(44) Marín, M.; Telo, J. P.; Collado, D.; Nájera, F.; Pérez-Inestrosa, E.; Pischel, U.; Marín, Á. M.; Telo, J. P.; Collado, D.; Nájera, F.; Pérez-Inestrosa, E.; Pischel, U. Bis(Dioxaborine) Dyes with Variable π-Bridges: Towards Two-Photon Absorbing Fluorophores with Very High Brightness. *Chem. - A Eur. J.* **2018**, *24* (12), 2929–2935. https://doi.org/10.1002/chem.201704544.

(45) Sutherland, R. L.; Mclean, D. G.; Kirkpatrick, S. *Handbook of Nonlinear Optics* , 2nd ed.; 2003.

(46) Negres, R. A.; Hales, J. M.; Kobyakov, A.; Hagan, D. J.; Van Stryland, E. W. Experiment and Analysis of Two-Photon Absorption Spectroscopy Using a White-Light Continuum Probe. *IEEE J. Quantum Electron.* **2002**, *38* (9), 1205–1216. https://doi.org/10.1109/JQE.2002.802448.

(47) Negres, R. A.; Hales, J. M.; Kobyakov, A.; Hagan, D. J.; Van Stryland, E. W. Two-Photon Spectroscopy and Analysis with a White-Light Continuum Probe. *Opt. Lett.* **2002**, *27* (4), 270. https://doi.org/10.1364/ol.27.000270.

(48) Ajami, A.; Husinsky, W.; Ovsianikov, A.; Liska, R. Dispersive White Light Continuum Single

Z-Scan for Rapid Determination of Degenerate Two-Photon Absorption Spectra. *Appl. Phys. B Lasers Opt.* **2018**, *124* (7), 142. https://doi.org/10.1007/s00340-018-7011-0.

(49) Sperber, P.; Penzkofer, A. S0-Sn Two-Photon Absorption Dynamics of Rhodamine Dyes. *Opt. Quantum Electron.* **1986**, *18* (5), 381–401. https://doi.org/10.1007/BF02032565.

(50) Tutt, L. W.; Boggess, T. F. *A Review of Optical Limiting Mechanisms and Devices Using Organics, Fullerenes, Semiconductors and Other Materials*; Pergamon, 1993; Vol. 17, pp 299–338. https://doi.org/10.1016/0079-6727(93)90004-S.

(51) Sheik-Bahae, M.; Said, A. A.; Wei, T. H.; Hagan, D. J.; Van Stryland, E. W. Sensitive Measurement of Optical Nonlinearities Using a Single Beam. *IEEE J. Quantum Electron.* **1990**, *26* (4), 760–769. https://doi.org/10.1109/3.53394.

(52) Chapple, P. B.; Staromlynska, J.; Hermann, J. A.; Mckay, T. J.; Mcduff, R. G. Single-Beam Z-Scan: Measurement Techniques and Analysis. *J. Nonlinear Opt. Phys. Mater.* **1997**, *6* (3), 251–293. https://doi.org/10.1142/S0218863597000204.

(53) Kamada, K.; Matsunaga, K.; Yoshino, A.; Ohta, K. Two-Photon-Absorption-Induced Accumulated Thermal Effect on Femtosecond Z-Scan Experiments Studied with Time-Resolved Thermal-Lens Spectrometry and Its Simulation. *J. Opt. Soc. Am. B* **2003**, *20* (3), 529. https://doi.org/10.1364/josab.20.000529.

(54) Chung, S. J.; Kim, K. S.; Lin, T. C.; He, G. S.; Swiatkiewicz, J.; Prasad, P. N. Cooperative Enhancement of Two-Photon Absorption in Multi-Branched Structures. *J. Phys. Chem. B* **1999**, *103* (49), 10741–10745. https://doi.org/10.1021/jp992846z.

(55) Twarowski, A. J.; Kliger, D. S. Multiphoton Absorption Spectra Using Thermal Blooming. I. Theory. *Chem. Phys.* **1977**, *20* (2), 253–258. https://doi.org/10.1016/0301-0104(77)85029-5.

(56) Bass, M.; Van Stryland, E. W.; Stewart, A. F. Laser Calorimetric Measurement of Two-Photon Absorption. *Appl. Phys. Lett.* **1979**, *34* (2), 142–144. https://doi.org/10.1063/1.90706.

(57) Kliger, D. S. Thermal Lensing: A New Spectroscopic Tool. *Acc. Chem. Res.* **1980**, *13* (5), 129–134. https://doi.org/10.1021/ar50149a001.

(58) Fang, H. L.; Gustafson, T. L.; Swofford, R. L. Two-Photon Absorption Photothermal Spectroscopy Using a Synchronously Pumped Picosecond Dye Laser. Thermal Lensing Spectra of Naphthalene and Diphenylbutadiene. *J. Chem. Phys.* **1983**, *78* (4), 1663–1669. https://doi.org/10.1063/1.444964.

(59) Rice, J. K.; Anderson, R. W. Two-Photon, Thermal Lensing Spectroscopy of Monosubstituted Benzenes in the 1B2u(1Lb) ← 1A1g(1A) and 1B1u(1La) ← 1A1g(1A) Transition Regions. *J. Phys. Chem.* **1986**, *90* (26), 6793–6800. https://doi.org/10.1021/j100284a016.

(60) Tam, A. C.; Patel, C. K. N. Two-Photon Absorption Spectra and Cross-Section Measurements in Liquids. *Nature* **1979**, *280* (5720), 304–306. https://doi.org/10.1038/280304a0.

(61) Van Stryland, E.; Woodall, M. Photoacoustic Measurement of Nonlinear Absorption in Solids. In *Laser Induced Damage In Optical Materials: 1980*; ASTM International, 2009; pp 50–57. https://doi.org/10.1520/stp36996s.

(62) Wilder, J. A.; Findley, G. L. Construction of a Two-Photon Photoacoustic Spectrometer. *Rev. Sci. Instrum.* **1987**, *58* (6), 968–974. https://doi.org/10.1063/1.1139584.

(63) Xu, C.; Webb, W. W. Measurement of Two-Photon Excitation Cross Sections of Molecular

Fluorophores with Data from 690 to 1050 Nm. *J. Opt. Soc. Am. B* **1996**, *13* (3), 481. https://doi.org/10.1364/josab.13.000481.

(64) Drobizhev, M.; Stepanenko, Y.; Dzenis, Y.; Karotki, A.; Rebane, A.; Taylor, P. N.; Anderson, H. L. Extremely Strong Near-IR Two-Photon Absorption in Conjugated Porphyrin Dimers: Quantitative Description with Three-Essential-States Model. *J. Phys. Chem. B* **2005**, *109* (15), 7223–7236. https://doi.org/10.1021/jp044261x.

(65) Makarov, N. S.; Drobizhev, M.; Rebane, A. Two-Photon Absorption Standards in the 550-1600 Nm Excitation Wavelength Range. *Opt. Express* **2008**, *16* (6), 4029. https://doi.org/10.1364/oe.16.004029.

(66) de Reguardati, S.; Pahapill, J.; Mikhailov, A.; Stepanenko, Y.; Rebane, A. High-Accuracy Reference Standards for Two-Photon Absorption in the 680–1050 Nm Wavelength Range. *Opt. Express* **2016**, *24* (8), 9053. https://doi.org/10.1364/oe.24.009053.

(67) Brouwer, A. M. Standards for Photoluminescence Quantum Yield Measurements in Solution (IUPAC Technical Report). *Pure Appl. Chem.* **2011**, *83* (12), 2213–2228. https://doi.org/10.1351/PAC-REP-10-09-31.

(68) Terenziani, F.; Katan, C.; Badaeva, E.; Tretiak, S.; Blanchard-Desce, M. Enhanced Two-Photon Absorption of Organic Chromophores: Theoretical and Experimental Assessments. *Adv. Mater.* **2008**, *20* (24), 4641–4678. https://doi.org/10.1002/adma.200800402.

(69) Esherick, P.; Zinsli, P.; El-Sayed, M. A. The Low Energy Two-Photon Spectrum of Pyrazine Using the Phosphorescence Photoexcitation Method. *Chem. Phys.* **1975**, *10* (2–3), 415–432. https://doi.org/10.1016/0301-0104(75)87053-4.

(70) Singer, L.; Baram, Z.; Ron, A.; Kimel, S. The Two-Photon Phosphorescence Excitation Spectrum of Triphenylene. *Chem. Phys. Lett.* **1977**, *47* (2), 372–376. https://doi.org/10.1016/0009-2614(77)80040-7.

(71) Frederiksen, P. K.; Jørgensen, M.; Ogilby, P. R. Two-Photon Photosensitized Production of Singlet Oxygen. *J. Am. Chem. Soc.* **2001**, *123* (6), 1215–1221. https://doi.org/10.1021/ja003468a.

(72) Denk, W.; Strickler, J. H.; Webb, W. W. Two-Photon Laser Scanning Fluorescence Microscopy. *Science (80-.).* **1990**, *248* (4951), 73–76. https://doi.org/10.1126/science.2321027.

(73) Peticolas, W. L.; Goldsborough, J. P.; Rieckhoff, K. E. Double Photon Excitation in Organic Crystals. *Phys. Rev. Lett.* **1963**, *10* (2), 43–45. https://doi.org/10.1103/PhysRevLett.10.43.

(74) Ehrlich, J. E.; Wu, X. L.; Lee, I.-Y. S.; Hu, Z.-Y.; Röckel, H.; Marder, S. R.; Perry, J. W. Two-Photon Absorption and Broadband Optical Limiting with Bis-Donor Stilbenes. *Opt. Lett.* **1997**, *22* (24), 1843. https://doi.org/10.1364/ol.22.001843.

(75) Reinhardt, B. A.; Brott, L. L.; Clarson, S. J.; Dillard, A. G.; Bhatt, J. C.; Kannan, R.; Yuan, L.; He, G. S.; Prasad, P. N. Highly Active Two-Photon Dyes: Design, Synthesis, and Characterization toward Application. *Chem. Mater.* **1998**, *10* (7), 1863–1874. https://doi.org/10.1021/cm980036e.

(76) Rumi, M.; Barlow, S.; Wang, J.; Perry, J. W.; Marder, S. R. Two-Photon Absorbing Materials and Two-Photon-Induced Chemistry. *Adv. Polym. Sci.* **2008**, *213* (1), 1–95. https://doi.org/10.1007/12_2008_133.

(77) Kim, H. M.; Cho, B. R. Two-Photon Materials with Large Two-Photon Cross Sections. Structure-Property Relationship. *Chem. Commun.* **2009**, No. 2, 153–164.

https://doi.org/10.1039/b813280a.

(78) Pawlicki, M. M.; Collins, H. A.; Denning, R. G.; Anderson, H. L. Two-Photon Absorption and the Design of Two-Photon Dyes. *Angew. Chem. Int. Ed. Engl.* **2009**, *48* (18), 3244–3266. https://doi.org/10.1002/anie.200805257.

(79) Barzoukas, M.; Blanchard-Desce, M. Molecular Engineering of Push-Pull Dipolar and Quadrupolar Molecules for Two-Photon Absorption: A Multivalence-Bond States Approach. *J. Chem. Phys.* **2000**, *113* (10), 3951–3959. https://doi.org/10.1063/1.1288367.

(80) Jagatap, B. N.; Meath, W. J. Contributions of Permanent Dipole Moments to Molecular Multiphoton Excitation Cross Sections. *J. Opt. Soc. Am. B* **2002**, *19* (11), 2673. https://doi.org/10.1364/josab.19.002673.

(81) Marder, S. R.; Torruellas, W. E.; Blanchard-Desce, M.; Ricci, V.; Stegeman, G. I.; Gilmour, S.; Brédas, J. L.; Li, J.; Bublitz, G. U.; Boxer, S. G. Large Molecular Third-Order Optical Nonlinearities in Polarized Carotenoids. *Science (80-.).* **1997**, *276* (5316), 1233–1236. https://doi.org/10.1126/science.276.5316.1233.

(82) Norman, P.; Luo, Y.; Ågren, H. Structure-to-Property Relations for Two-Photon Absorption of Hydrocarbon Oligomers. *Chem. Phys. Lett.* **1998**, *296* (1–2), 8–18. https://doi.org/10.1016/S0009-2614(98)01008-2.

(83) Norman, P.; Luo, Y.; Ågren, H. Two-Photon Absorption in Five-Membered Heteroaromatic Oligomers. *Opt. Commun.* **1999**, *168* (1), 297–303. https://doi.org/10.1016/S0030-4018(99)00250-3.

(84) Porres, L.; Charlot, M.; Entwistle, C. D.; Beeby, A.; Marder, T. B.; Blanchard-Desce, M. Novel Boron Quadrupolar NLO-Phores: Optimization of TPA/Transparency Trade-off via Molecular Engineering. In *Nonlinear Optical Transmission and Multiphoton Processes in Organics III*; Yeates, A. T., Ed.; SPIE, 2005; Vol. 5934, p 59340F. https://doi.org/10.1117/12.618425.

(85) Nguyen, K. A.; Rogers, J. E.; Slagle, J. E.; Day, P. N.; Kannan, R.; Tan, L. S.; Fleitz, P. A.; Pachter, R. Effects of Conjugation in Length and Dimension on Spectroscopic Properties of Fluorene-Based Chromophores from Experiment and Theory. *J. Phys. Chem. A* **2006**, *110* (49), 13172–13182. https://doi.org/10.1021/jp0642645.

(86) Ramakrishna, G.; Goodson, T. Excited-State Deactivation of Branched Two-Photon Absorbing Chromophores: A Femtosecond Transient Absorption Investigation. *J. Phys. Chem. A* **2007**, *111* (6), 993–1000. https://doi.org/10.1021/jp064004n.

(87) Domínguez, Z.; Pais, V. F.; Collado, D.; Vázquez-Domínguez, P.; Albendín, F. N.; Pérez-Inestrosa, E.; Ros, A.; Pischel, U. π-Extended Four-Coordinate Organoboron N,C-Chelates as Two-Photon Absorbing Chromophores. *J. Org. Chem.* **2019**, *84* (21), 13384–13393. https://doi.org/10.1021/acs.joc.9b01542.

(88) Pond, S. J. K. K.; Rumi, M.; Levin, M. D.; Parker, T. C.; Beljonne, D.; Day, M. W.; Brédas, J. L.; Marder, S. R.; Perry, J. W.; Br??das, J. L.; Marder, S. R.; Perry, J. W. One- and Two-Photon Spectroscopy of Donor-Acceptor-Donor Distyrylbenzene Derivatives: Effect of Cyano Substitution and Distortion from Planarity. *J. Phys. Chem. A* **2002**, *106* (47), 11470–11480. https://doi.org/10.1021/jp0267104.

(89) Beverina, L.; Fu, J.; Leclercq, A.; Zojer, E.; Pacher, P.; Barlow, S.; Van Stryland, E. W.; Hagan, D. J.; Brédas, J. L.; Marder, S. R. Two-Photon Absorption at Telecommunications Wavelengths in a Dipolar Chromophore with a Pyrrole Auxiliary Donor and Thiazole Auxiliary Acceptor. *J. Am. Chem. Soc.* **2005**, *127* (20), 7282–7283. https://doi.org/10.1021/ja050688l.

(90) Chung, S. J.; Zheng, S.; Odani, T.; Beverina, L.; Fu, J.; Padilha, L. A.; Biesso, A.; Hales, J. M.; Zhan, X.; Schmidt, K.; Ye, A.; Zojer, E.; Barlow, S.; Hagan, D. J.; Van Stryland, E. W.; Yi, Y.; Shuai, Z.; Pagani, G. A.; Brédas, J. L.; Perry, J. W.; Marder, S. R. Extended Squaraine Dyes with Large Two-Photon Absorption Cross-Sections. *J. Am. Chem. Soc.* **2006**, *128* (45), 14444–14445. https://doi.org/10.1021/ja065556m.

(91) Kannan, R.; He, G. S.; Lin, T. C.; Prasad, P. N.; Vaia, R. A.; Tan, L. S. Toward Highly Active Two-Photon Absorbing Liquids. Synthesis and Characterization of 1,3,5-Triazine-Based Octupolar Molecules. *Chem. Mater.* **2004**, *16* (1), 185–194. https://doi.org/10.1021/cm034358g.

(92) Ventelon, L.; Charier, S.; Moreaux, L.; Mertz, J.; Blanchard-Desce, M. Nanoscale Push-Push Dihydrophenanthrene Derivatives as Novel Fluorophores for Two-Photon-Excited Fluorescence. *Angew. Chemie Int. Ed.* **2001**, *40* (11), 2098–2101. https://doi.org/10.1002/1521-3773(20010601)40:11<2098::AID-ANIE2098>3.0.CO;2-0.

(93) Porrès, L.; Mongin, O.; Katan, C.; Charlot, M.; Pons, T.; Mertz, J.; Blanchard-Desce, M. Enhanced Two-Photon Absorption with Novel Octupolar Propeller-Shaped Fluorophores Derived from Triphenylamine. *Org. Lett.* **2004**, *6* (1), 47–50. https://doi.org/10.1021/ol036041s.

(94) Le Droumaguet, C.; Mongin, O.; Werts, M. H. V.; Blanchard-Desce, M. Towards "Smart" Multiphoton Fluorophores: Strongly Solvatochromic Probes for Two-Photon Sensing of Micropolarity. *Chem. Commun.* **2005**, No. 22, 2802–2804. https://doi.org/10.1039/b502585k.

(95) Mongin, O.; Porrès, L.; Charlot, M.; Katan, C.; Blanchard-Desce, M. Synthesis, Fluorescence, and Two-Photon Absorption of a Series of Elongated Rodlike and Banana-Shaped Quadrupolar Fluorophores: A Comprehensive Study of Structure-Property Relationships. *Chem. - A Eur. J.* **2007**, *13* (5), 1481–1498. https://doi.org/10.1002/chem.200600689.

(96) Varnavski, O.; Yan, X.; Mongin, O.; Blanchard-Desce, M.; Goodson, T. Strongly Interacting Organic Conjugated Dendrimers with Enhanced Two-Photon Absorption. *J. Phys. Chem. C* **2007**, *111* (1), 149–162. https://doi.org/10.1021/jp0640068.

(97) Baur, J. W.; Alexander, M. D.; Banach, M.; Denny, L. R.; Reinhardt, B. A.; Vaia, R. A.; Fleitz, P. A.; Kirkpatrick, S. M. Molecular Environment Effects on Two-Photon-Absorbing Heterocyclic Chromophores. *Chem. Mater.* **1999**, *11* (10), 2899–2906. https://doi.org/10.1021/cm990258s.

(98) Woo, H. Y.; Liu, B.; Kohler, B.; Korystov, D.; Mikhailovsky, A.; Bazan, G. C. Solvent Effects on the Two-Photon Absorption of Distyrylbenzene Chromophores. *J. Am. Chem. Soc.* **2005**, *127* (42), 14721–14729. https://doi.org/10.1021/ja052906g.

(99) Luo, J.; Xie, Z.; Xie, Z.; Lam, J. W. Y.; Cheng, L.; Chen, H.; Qiu, C.; Kwok, H. S.; Zhan, X.; Liu, Y.; Zhu, D.; Tang, B. Z. Aggregation-Induced Emission of 1-Methyl-1,2,3,4,5-Pentaphenylsilole. *Chem. Commun.* **2001**, *18* (18), 1740–1741. https://doi.org/10.1039/b105159h.

(100) Qi, J.; Sun, C.; Li, D.; Zhang, H.; Yu, W.; Zebibula, A.; Lam, J. W. Y.; Xi, W.; Zhu, L.; Cai, F.; Wei, P.; Zhu, C.; Kwok, R. T. K.; Streich, L. L.; Prevedel, R.; Qian, J.; Tang, B. Z. Aggregation-Induced Emission Luminogen with near-Infrared-II Excitation and near-Infrared-I Emission for Ultradeep Intravital Two-Photon Microscopy. *ACS Nano* **2018**, *12* (8), 7936–7945. https://doi.org/10.1021/acsnano.8b02452.

(101) Ma, B.; Zhuang, W.; He, H.; Su, X.; Yu, T.; Hu, J.; Yang, L.; Li, G.; Wang, Y. Two-Photon AIE Probe Conjugated Theranostic Nanoparticles for Tumor Bioimaging and PH-Sensitive Drug

Delivery. *Nano Res.* **2019**, *12* (7), 1703–1712. https://doi.org/10.1007/s12274-019-2426-4.

(102) Alam, P.; He, W.; Leung, N. L. C.; Ma, C.; Kwok, R. T. K.; Lam, J. W. Y.; Sung, H. H. Y.; Williams, I. D.; Wong, K. S.; Tang, B. Z. Red AIE-Active Fluorescent Probes with Tunable Organelle-Specific Targeting. *Adv. Funct. Mater.* **2020**, *30* (10), 1909268. https://doi.org/10.1002/adfm.201909268.

(103) Li, Y.; Liu, S.; Ni, H.; Zhang, H.; Zhang, H.; Chuah, C.; Ma, C.; Wong, K. S.; Lam, J. W. Y.; Kwok, R. T. K.; Qian, J.; Lu, X.; Tang, B. Z. ACQ-to-AIE Transformation: Tuning Molecular Packing by Regioisomerization for Two-Photon NIR Bioimaging. *Angew. Chemie* **2020**, *132* (31), 12922–12926. https://doi.org/10.1002/ange.202005785.

(104) Li, Y.; Tang, R.; Liu, X.; Gong, J.; Zhao, Z.; Sheng, Z.; Zhang, J.; Li, X.; Niu, G.; Kwok, R. T. K.; Zheng, W.; Jiang, X.; Tang, B. Z. Bright Aggregation-Induced Emission Nanoparticles for Two-Photon Imaging and Localized Compound Therapy of Cancers. *ACS Nano* **2020**, *14* (12), 16840–16853. https://doi.org/10.1021/acsnano.0c05610.

(105) Xu, Y.; Zhang, H.; Zhang, N.; Xu, R.; Wang, Z.; Zhou, Y.; Shen, Q.; Dang, D.; Meng, L.; Tang, B. Z. An Easily Synthesized AIE Luminogen for Lipid Droplet-Specific Super-Resolution Imaging and Two-Photon Imaging. *Mater. Chem. Front.* **2021**. https://doi.org/10.1039/d0qm00682c.

(106) Woo, H. Y.; Korystov, D.; Mikhailovsky, A.; Nguyen, T. Q.; Bazan, G. C. Two-Photon Absorption in Aqueous Micellar Solutions. *J. Am. Chem. Soc.* **2005**, *127* (40), 13794–13795. https://doi.org/10.1021/ja054911q.

(107) Binev, I. G.; Kuzmanova, R. B.; Kaneti, J.; Juchnovski, I. N. Determination of Constants of Anionic Substituents Based on Nitrile Infrared Frequencies and Intensities. *J. Chem. Soc. Perkin Trans. 2* **1982**, No. 12, 1533–1536. https://doi.org/10.1039/p29820001533.

(108) Isaacs, N. S. *Physical Organic Chemistry*, 2nd ed.; Wiley: New York, 1995. https://doi.org/10.1021/ja01864a069.

(109) Kavarnos, G. J.; Turro, N. J. Photosensitization by Reversible Electron Transfer: Theories, Experimental Evidence, and Examples. *Chem. Rev.* **1986**, *86* (2), 401–449. https://doi.org/10.1021/cr00072a005.

(110) De Silva, A. P.; Moody, T. S.; Wright, G. D. Fluorescent PET (Photoinduced Electron Transfer) Sensors as Potent Analytical Tools. *Analyst*. Royal Society of Chemistry November 16, 2009, pp 2385–2393. https://doi.org/10.1039/b912527m.

(111) Daly, B.; Ling, J.; De Silva, A. P. Current Developments in Fluorescent PET (Photoinduced Electron Transfer) Sensors and Switches. *Chem. Soc. Rev.* **2015**, *44* (13), 4203–4211. https://doi.org/10.1039/c4cs00334a.

(112) Cao, D.-X.; Fang, Q.; Wang, D.; Liu, Z.-Q.; Xue, G.; Xu, G.-B.; Yu, W.-T. Synthesis and Two-Photon-Excited Fluorescence of Benzothiazole-Based Compounds with Variousπ-Electron Donors. *European J. Org. Chem.* **2003**, *2003* (18), 3628–3636. https://doi.org/10.1002/ejoc.200300272.

(113) Belfield, K. D.; Hagan, D. J.; Van Stryland, E. W.; Schafer, K. J.; Negres, R. A. New Two-Photon Absorbing Fluorene Derivatives: Synthesis and Nonlinear Optical Characterization. *Org. Lett.* **1999**, *1* (10), 1575–1578. https://doi.org/10.1021/ol9909177.

(114) De Boni, L.; Rodrigues, J. J.; Dos Santos, D. S.; Silva, C. H. T. P.; Balogh, D. T.; Oliveira, O. N.; Zilio, S. C.; Misoguti, L.; Mendonça, C. R. Two-Photon Absorption in Azoaromatic Compounds. *Chem. Phys. Lett.* **2002**, *361* (3–4), 209–213. https://doi.org/10.1016/S0009-

2614(02)00892-8.

(115) Ventelon, L.; Moreaux, L.; Mertz, J.; Blanchard-Desce, M. Optimization of Quadrupolar Chromophores for Molecular Two-Photon Absorption. In *Synthetic Metals*; Elsevier, 2002; Vol. 127, pp 17–21. https://doi.org/10.1016/S0379-6779(01)00588-4.

(116) Lin, T. C.; He, G. S.; Prasad, P. N.; Tan, L. S. Degenerate Nonlinear Absorption and Optical Power Limiting Properties of Asymmetrically Substituted Stilbenoid Chromophores. *J. Mater. Chem.* **2004**, *14* (6), 982–991. https://doi.org/10.1039/b313185h.

(117) Bhawalkar, J. D.; He, G. S.; Park, C. K.; Zhao, C. F.; Ruland, G.; Prasad, P. N. Efficient, Two-Photon Pumped Green Upconverted Cavity Lasing in a New Dye. *Opt. Commun.* **1996**, *124* (1–2), 33–37. https://doi.org/10.1016/0030-4018(95)00540-4.

(118) Strehmel, B.; Sarker, A. M.; Detert, H. The Influence of σ and π Acceptors on Two-Photon Absorption and Solvatochromism of Dipolar and Quadrupolar Unsaturated Organic Compounds. *ChemPhysChem* **2003**, *4* (3), 249–259. https://doi.org/10.1002/cphc.200390041.

(119) Lee, H. J.; Sohn, J.; Hwang, J.; Park, S. Y.; Choi, H.; Cha, M. Triphenylamine-Cored Bifunctional Organic Molecules for Two-Photon Absorption and Photorefraction. *Chem. Mater.* **2004**, *16* (3), 456–465. https://doi.org/10.1021/cm0343756.

(120) Weber, G.; Farris, F. J. Synthesis and Spectral Properties of a Hydrophobic Fluorescent Probe: 6-Propionyl-2-(Dimethylamino)Naphthalene. *Biochemistry* **1979**, *18* (14), 3075–3078. https://doi.org/10.1021/bi00581a025.

(121) Huang, Z. L.; Lei, H.; Li, N.; Qiu, Z. R.; Wang, H. Z.; Guo, J. D.; Luo, Y.; Zhong, Z. P.; Liu, X. F.; Zhou, Z. H. Novel Heterocycle-Based Organic Molecules with Two-Photon Induced Blue Fluorescent Emission. *J. Mater. Chem.* **2003**, *13* (4), 708–711. https://doi.org/10.1039/b300924f.

(122) Shao, P.; Huang, B.; Chen, L.; Liu, Z.; Qin, J.; Gong, H.; Ding, S.; Wang, Q. Synthesis and Two-Photon Absorption Properties of Novel Heterocycle-Based Organic Molecules. *J. Mater. Chem.* **2005**, *15* (42), 4502–4506. https://doi.org/10.1039/b507958f.

(123) Kim, H. M.; Choo, H.-J. J.; Jung, S.-Y. Y.; Ko, Y.-G. G.; Park, W.-H. H.; Jeon, S.-J. J.; Kim, C. H.; Joo, T.; Cho, B. R. A Two-Photon Fluorescent Probe for Lipid Raft Imaging: C-Laurdan. *ChemBioChem* **2007**, *8* (5), 553–559. https://doi.org/10.1002/cbic.200700003.

(124) Hwan, M. K.; Byeong, H. J.; Hyon, J.-Y. Y.; Myoung, J. A.; Mun, S. S.; Jin, H. H.; Lee, K. J.; Chul, H. K.; Joo, T.; Hong, S.-C. C.; Bong, R. C.; Kim, H. M.; Jeong, B. H.; Hyon, J.-Y. Y.; An, M. J.; Seo, M. S.; Hong, J. H.; Lee, K. J.; Kim, C. H.; Joo, T.; Hong, S.-C. C.; Cho, B. R. Two-Photon Fluorescent Turn-On Probe for Lipid Rafts in Live Cell and Tissue. *J. Am. Chem. Soc.* **2008**, *130* (13), 4246–4247. https://doi.org/10.1021/ja711391f.

(125) Kim, H. M.; Kim, B. R.; Choo, H.-J.; Ko, Y.-G.; Jeon, S.-J.; Kim, C. H.; Joo, T.; Cho, B. R. Two-Photon Fluorescent Probes for Biomembrane Imaging: Effect of Chain Length. *ChemBioChem* **2008**, *9* (17), 2830–2838. https://doi.org/10.1002/cbic.200800353.

(126) Lim, C. S.; Kim, H. J. H. M.; Lee, J. H.; Tian, Y. S.; Kim, C. H.; Kim, H. J. H. M.; Joo, T.; Cho, B. R. A Two-Photon Turn-On Probe for Lipid Rafts with Minimum Internalization. *ChemBioChem* **2011**, *12* (3), 392–395. https://doi.org/10.1002/cbic.201000609.

(127) Kannan, R.; He, G. S.; Yuan, L.; Xu, F.; Prasad, P. N.; Dombroskie, A. G.; Reinhardt, B. A.; Baur, J. W.; Vaia, R. A.; Tan, L. S. Diphenylaminofluorene-Based Two-Photon-Absorbing Chromophores with Various π-Electron Acceptors. *Chem. Mater.* **2001**, *13* (5), 1896–1904.

https://doi.org/10.1021/cm000747o.

(128) He, G. S.; Gvishi, R.; Prasad, P. N.; Reinhardt, B. A. Two-Photon Absorption Based Optical Limiting and Stabilization in Organic Molecule-Doped Solid Materials. *Opt. Commun.* **1995**, *117* (1–2), 133–136. https://doi.org/10.1016/0030-4018(95)00097-R.

(129) Belfield, K. D.; Schafer, K. J.; Mourad, W.; Reinhardt, B. A. Synthesis of New Two-Photon Absorbing Fluorene Derivatives via Cu-Mediated Ullmann Condensations. *J. Org. Chem.* **2000**, *65* (15). https://doi.org/10.1021/JO991950+.

(130) Abbotto, A.; Beverina, L.; Bozio, R.; Facchetti, A.; Ferrante, C.; Pagani, G. A.; Pedron, D.; Signorini, R. Novel Heterocycle-Based Two-Photon Absorbing Dyes. *Org. Lett.* **2002**, *4* (9), 1495–1498. https://doi.org/10.1021/ol025703v.

(131) Kim, O. K.; Lee, K. S.; Woo, H. Y.; Kim, K. S.; He, G. S.; Swiatkiewicz, J.; Prasad, P. N. New Class of Two-Photon-Absorbing Chromophores Based on Dithienothiophene. *Chem. Mater.* **2000**, *12* (2), 284–286. https://doi.org/10.1021/cm990662r.

(132) He, G. S.; Bhawalkar, J. D.; Zhao, C. F.; Prasad, P. N. Optical Limiting Effect in a Two-Photon Absorption Dye Doped Solid Matrix. *Appl. Phys. Lett.* **1995**, *67* (17), 2433. https://doi.org/10.1063/1.114598.

(133) He, G. S.; Yuan, L.; Cui, Y.; Li, M.; Prasad, P. N. Studies of Two-Photon Pumped Frequency-Upconverted Lasing Properties of a New Dye Material. *J. Appl. Phys.* **1997**, *81* (6), 2529–2537. https://doi.org/10.1063/1.364303.

(134) Kawamata, J.; Akiba, M.; Tani, T.; Harada, A.; Inagaki, Y. Two-Photon Absorption Cross-Sections of Fluorene Derivatives with Cationic Substituents. *Chem. Lett.* **2004**, *33* (4), 448–449. https://doi.org/10.1246/cl.2004.448.

(135) Wu, L. Z.; Tang, X. J.; Jiang, M. H.; Tung, C. H. Two-Photon Induced Fluorescence of Novel Dyes. *Chem. Phys. Lett.* **1999**, *315* (5–6), 379–382. https://doi.org/10.1016/S0009-2614(99)01118-5.

(136) Gu, J.; Yulan, W.; Chen, W. Q.; Dong, X. Z.; Duan, X. M.; Kawata, S. Carbazole-Based 1D and 2D Hemicyanines: Synthesis, Two-Photon Absorption Properties and Application for Two-Photon Photopolymerization 3D Lithography. *New J. Chem.* **2007**, *31* (1), 63–68. https://doi.org/10.1039/b609309d.

(137) Liu, F.; Wu, T.; Cao, J.; Cui, S.; Yang, Z.; Qiang, X.; Sun, S.; Song, F.; Fan, J.; Wang, J.; Peng, X. Ratiometric Detection of Viscosity Using a Two-Photon Fluorescent Sensor. *Chem. - A Eur. J.* **2013**, *19* (5), 1548–1553. https://doi.org/10.1002/chem.201202646.

(138) Yesudas, K. Cationic Cyanine Dyes: Impact of Symmetry-Breaking on Optical Absorption and Third-Order Polarizabilities. *Phys. Chem. Chem. Phys.* **2013**, *15* (44), 19465–19477. https://doi.org/10.1039/c3cp51718g.

(139) Guarin, C. A.; Mendoza-Luna, L. G.; Haro-Poniatowski, E.; Hernández-Pozos, J. L. Two-Photon Absorption Spectrum and Characterization of the Upper Electronic States of the Dye IR780. *Spectrochim. Acta - Part A Mol. Biomol. Spectrosc.* **2021**, *249*, 119291. https://doi.org/10.1016/j.saa.2020.119291.

(140) Juvekar, V.; Lim, C. S.; Lee, D. J.; Park, S. J.; Song, G. O.; Kang, H.; Kim, H. M. An Azo Dye for Photodynamic Therapy That Is Activated Selectively by Two-Photon Excitation. *Chem. Sci.* **2021**, *12* (1), 427–434. https://doi.org/10.1039/d0sc05686c.

(141) Porrès, L.; Mongin, O.; Blanchard-Desce, M. Synthesis, Fluorescence and Two-Photon Absorption Properties of Multichromophoric Boron-Dipyrromethene Fluorophores for Two-

Photon-Excited Fluorescence Applications. *Tetrahedron Lett.* **2006**, *47* (12), 1913–1917. https://doi.org/10.1016/j.tetlet.2006.01.087.

(142) Kucherak, O. A.; Didier, P.; Mèly, Y.; Klymchenko, A. S. Fluorene Analogues of Prodan with Superior Fluorescence Brightness and Solvatochromism. *J. Phys. Chem. Lett.* **2010**, *1* (3), 616–620. https://doi.org/10.1021/jz9003685.

(143) Niko, Y.; Didier, P.; Mely, Y.; Konishi, G. I.; Klymchenko, A. S. Bright and Photostable Push-Pull Pyrene Dye Visualizes Lipid Order Variation between Plasma and Intracellular Membranes. *Sci. Rep.* **2016**, *6* (1), 1–9. https://doi.org/10.1038/srep18870.

(144) Ventelon, L.; Moreaux, L.; Mertz, J.; Blanchard-Desce, M. New Quadrupolar Fluorophores with High Two-Photon Excited Fluorescence. *Chem. Commun.* **1999**, No. 20, 2055–2056. https://doi.org/10.1039/a906182g.

(145) Yang, W. J.; Kim, D. Y.; Jeong, M. Y.; Kim, H. M.; Jeon, S. J.; Cho, B. R. 2,6-Bis(Styryl)Anthracene Derivatives with Large Two-Photon Cross-Sections. *Chem. Commun.* **2003**, *3* (20), 2618–2619. https://doi.org/10.1039/b309124d.

(146) Kim, H. M.; Yang, W. J.; Kim, C. H.; Park, W.-H.; Jeon, S.-J.; Cho, B. R. Two-Photon Dyes Containing Heterocyclic Rings with Enhanced Photostability. *Chem. - A Eur. J.* **2005**, *11* (21), 6386–6391. https://doi.org/10.1002/chem.200500341.

(147) Kato, S. I.; Matsumoto, T.; Ishi-I, T.; Thiemann, T.; Shigeiwa, M.; Gorohmaru, H.; Maeda, S.; Yamashita, Y.; Mataka, S. Strongly Red-Fluorescent Novel Donor-π-Bridge-Acceptor-π-Bridge-Donor (D-π-A-π-D) Type 2,1,3-Benzothiadiazoles with Enhanced Two-Photon Absorption Cross-Sections. *Chem. Commun.* **2004**, No. 20, 2342–2343. https://doi.org/10.1039/b410016f.

(148) Kato, S.; Matsumoto, T.; Shigeiwa, M.; Gorohmaru, H.; Maeda, S.; Ishi-i, T.; Mataka, S. Novel 2,1,3-Benzothiadiazole-Based Red-Fluorescent Dyes with Enhanced Two-Photon Absorption Cross-Sections. *Chem. - A Eur. J.* **2006**, *12* (8), 2303–2317. https://doi.org/10.1002/chem.200500921.

(149) Wang, Y.; Huang, J.; Zhou, H.; Ma, G.; Qian, S.; Zhu, X. H. Synthesis, Optical Properties and Ultrafast Dynamics of a 2,1,3-Benzothiadiazole-Based Red Emitter with Intense Fluorescence and Large Two-Photon Absorption Cross-Section. *Dye. Pigment.* **2012**, *92* (1), 573–579. https://doi.org/10.1016/j.dyepig.2011.06.032.

(150) Yao, S.; Kim, B.; Yue, X.; Colon Gomez, M. Y.; Bondar, M. V.; Belfield, K. D. Synthesis of Near-Infrared Fluorescent Two-Photon-Absorbing Fluorenyl Benzothiadiazole and Benzoselenadiazole Derivatives. *ACS Omega* **2016**, *1* (6), 1149–1156. https://doi.org/10.1021/acsomega.6b00289.

(151) Torres-Moya, I.; Benitez-Martin, C.; Donoso, B.; Tardío, C.; Martín, R.; Carrillo, J. R.; Díaz-Ortiz, Á.; Najera, F.; Prieto, P.; Perez-Inestrosa, E. Extended Alkenyl and Alkynyl Benzotriazoles with Enhanced Two-Photon Absorption Properties as a Promising Alternative to Benzothiadiazoles. *Chem. – A Eur. J.* **2019**, *25* (68), 15572–15579. https://doi.org/10.1002/chem.201903493.

(152) David, S.; Chang, H.; Lopes, C.; Brännlund, C.; Le Guennic, B.; Berginc, G.; Van Stryland, E.; Bondar, M. V.; Hagan, D.; Jacquemin, D.; Andraud, C.; Maury, O. Benzothiadiazole-Substituted Aza-BODIPY Dyes: Two-Photon Absorption Enhancement for Improved Optical Limiting Performances in the Short-Wave IR Range. *Chem. – A Eur. J.* **2021**, *27* (10), chem.202004899. https://doi.org/10.1002/chem.202004899.

(153) Yang, W. J.; Kim, C. H.; Jeong, M. Y.; Lee, S. K.; Piao, M. J.; Jeon, S. J.; Cho, B. R. Synthesis

and Two-Photon Absorption Properties of 9-10-Bis(Arylethynyl) Anthracene Derivatives. *Chem. Mater.* **2004**, *16* (14), 2783–2789. https://doi.org/10.1021/cm035032a.

(154) Morley, J. O. Nonlinear Optical Properties of Organic Molecules. XII. Calculations of the Hyperpolarizabilities of Donor-Acceptor Polyynes. *Int. J. Quantum Chem.* **1993**, *46* (1), 19–26. https://doi.org/10.1002/qua.560460103.

(155) Anderson, H. L. Conjugated Porphyrin Ladders. *Inorg. Chem.* **1994**, *33* (5), 972–981. https://doi.org/10.1021/ic00083a022.

(156) Lin, V. S. Y.; DiMagno, S. G.; Therien, M. J. Highly Conjugated, Acetylenyl Bridged Porphyrins: New Models for Light-Harvesting Antenna Systems. *Science (80-.).* **1994**, *264* (5162), 1105–1111. https://doi.org/10.1126/science.8178169.

(157) Terenziani, F.; Le Droumaguet, C.; Katan, C.; Mongin, O.; Blanchard-Desce, M. Effect of Branching on Two-Photon Absorption in Triphenylbenzene Derivatives. *ChemPhysChem* **2007**, *8* (5), 723–734. https://doi.org/10.1002/cphc.200600689.

(158) Zipfel, W. R.; Williams, R. M.; Webb, W. W. Nonlinear Magic: Multiphoton Microscopy in the Biosciences. *Nature Biotechnology*. Nature Publishing Group November 2003, pp 1369–1377. https://doi.org/10.1038/nbt899.

(159) Benninger, R. K. P.; Piston, D. W. Two-Photon Excitation Microscopy for the Study of Living Cells and Tissues. *Curr. Protoc. Cell Biol.* **2013**, *59* (1). https://doi.org/10.1002/0471143030.cb0411s59.

(160) Strickler, J. H.; Webb, W. W. Two-Photon Excitation in Laser Scanning Fluorescence Microscopy. In *CAN-AM Eastern '90*; Antos, R. L., Krisiloff, A. J., Eds.; SPIE, 1991; Vol. 1398, pp 107–118. https://doi.org/10.1117/12.47787.

(161) Wu, E.-S.; Strickler, J. H.; Harrell, W. R.; Webb, W. W. Two-Photon Lithography for Microelectronic Application. In *Optical/Laser Microlithography V*; Cuthbert, J. D., Ed.; SPIE, 1992; Vol. 1674, p 776. https://doi.org/10.1117/12.130367.

(162) Schafer, K. J.; Hales, J. M.; Balu, M.; Belfield, K. D.; Van Stryland, E. W.; Hagan, D. J. Two-Photon Absorption Cross-Sections of Common Photoinitiators. *J. Photochem. Photobiol. A Chem.* **2004**, *162* (2–3), 497–502. https://doi.org/10.1016/S1010-6030(03)00394-0.

(163) Cumpston, B. H.; Ehrlich, J. E.; Erskine, L. L.; Heikal, A. A.; Hu, Z. Y.; Lee, I. Y. S.; Levin, M. D.; Marder, S. R.; McCord, D. J.; Perry, J. W.; Rockel, H.; Rumi, M.; Wu, X. L. New Photopolymers Based on Two-Photon Absorbing Chromophores and Application to Three-Dimensional Microfabrication and Optical Storage. In *Materials Research Society Symposium - Proceedings*; MRS, 1997; Vol. 488, pp 217–225. https://doi.org/10.1557/proc-488-217.

(164) Cumpston, B. H.; Ananthavel, S. P.; Barlow, S.; Dyer, D. L.; Ehrlich, J. E.; Erskine, L. L.; Heikal, A. A.; Kuebler, S. M.; Lee, I. Y. S.; McCord-Maughon, D.; Qin, J.; Röckel, H.; Rumi, M.; Wu, X. L.; Marder, S. R.; Perry, J. W. Two-Photon Polymerization Initiators for Three-Dimensional Optical Data Storage and Microfabrication. *Nature* **1999**, *398* (6722), 51–54. https://doi.org/10.1038/17989.

(165) Kawata, S.; Sun, H. B.; Tanaka, T.; Takada, K. Finer Features for Functional Microdevices. *Nature* **2001**, *412* (6848), 697–698. https://doi.org/10.1038/35089130.

(166) Kuebler, S. M.; Rumi, M.; Watanabe, T.; Braun, K.; Cumpston, B. H.; Heikal, A. A.; Erskine, L. L.; Thayumanavan, S.; Barlow, S.; Marder, S. R.; Perry, J. W. Optimizing Two-Photon Initiators and Exposure Conditions for Three-Dimensional Lithographic Microfabrication. *J.*

Photopolym. Sci. Technol. **2001**, *14* (4), 657–668. https://doi.org/10.2494/photopolymer.14.657.

(167) Maruo, S.; Nakamura, O.; Kawata, S. Three-Dimensional Microfabrication with Two-Photon-Absorbed Photopolymerization. *Opt. Lett.* **1997**, *22* (2), 132. https://doi.org/10.1364/OL.22.000132.

(168) Maruo, S.; Kawata, S. Two-Photon-Absorbed near-Infrared Photopolymerization for Three-Dimensional Microfabrication. *J. Microelectromechanical Syst.* **1998**, *7* (4), 411–415. https://doi.org/10.1109/84.735349.

(169) Joshi, M. P.; Pudavar, H. E.; Swiatkiewicz, J.; Prasad, P. N.; Reianhardt, B. A. Three-Dimensional Optical Circuitry Using Two-Photon-Assisted Polymerization. *Appl. Phys. Lett.* **1999**, *74* (2), 170–172. https://doi.org/10.1063/1.123283.

(170) Belfield, K. D.; Schafer, K. J.; Liu, Y.; Liu, J.; Ren, X.; Stryland, E. Van. Multiphoton-Absorbing Organic Materials for Microfabrication, Emerging Optical Applications and Non-Destructive Three-Dimensional Imaging. *J. Phys. Org. Chem.* **2000**, *13* (12), 837–849. https://doi.org/10.1002/1099-1395(200012)13:12<837::AID-POC315>3.0.CO;2-5.

(171) Lu, Y.; Hasegawa, F.; Goto, T.; Ohkuma, S.; Fukuhara, S.; Kawazu, Y.; Totani, K.; Yamashita, T.; Watanabe, T. Highly Sensitive Two-Photon Chromophores Applied to Three-Dimensional Lithographic Microfabrication: Design, Synthesis and Characterization towards Two-Photon Absorption Cross Section. *J. Mater. Chem.* **2004**, *14* (1), 75–80. https://doi.org/10.1039/b309023j.

(172) Scrimgeour, J. D.Phil. Thesis, University of Oxford, 2005.

(173) Kawata, S.; Kawata, Y. Three-Dimensional Optical Data Storage Using Photochromic Materials. *Chem. Rev.* **2000**, *100* (5), 1777–1788. https://doi.org/10.1021/cr980073p.

(174) Sun, H. B.; Kawata, S. Two-Photon Photopolymerization and 3D Lithographic Microfabrication. *Advances in Polymer Science*. Springer, Berlin, Heidelberg 2004, pp 169–273. https://doi.org/10.1007/b94405.

(175) Zhou, W.; Kuebler, S. M.; Braun, K. L.; Yu, T.; Cammack, J. K.; Ober, C. K.; Perry, J. W.; Marder, S. R. An Efficient Two-Photon-Generated Photoacid Applied to Positive-Tone 3D Microfabrication. *Science (80-.).* **2002**, *296* (5570), 1106–1109. https://doi.org/10.1126/science.296.5570.1106.

(176) Kuebler, S. M.; Braun, K. L.; Zhou, W.; Cammack, J. K.; Yu, T.; Ober, C. K.; Marder, S. R.; Perry, J. W. Design and Application of High Sensitivity Two-Photon Initiators for Three-Dimensional Microfabrication. *J. Photochem. Photobiol. A Chem.* **2003**, *158* (2–3), 163–170. https://doi.org/10.1016/S1010-6030(03)00030-3.

(177) Walker, E.; Rentzepis, P. M. Two-Photon Technology: A New Dimension. *Nat. Photonics* **2008**, *2* (7), 406–408. https://doi.org/10.1038/nphoton.2008.121.

(178) Peticolas, W. L.; Rieckhoff, K. E. Double-Photon Excitation of Organic Molecules in Dilute Solution. *The Journal of Chemical Physics*. American Institute of PhysicsAIP September 29, 1963, pp 1347–1348. https://doi.org/10.1063/1.1734440.

(179) Giordmaine, J. A.; Rentzepis, P. M.; Shapiro, S. L.; Wecht, K. W. Two-Photon Excitation of Fluorescence by Picosecond Light Pulses. *Appl. Phys. Lett.* **1967**, *11* (7), 216–218. https://doi.org/10.1063/1.1755105.

(180) Rentzepis, P. M.; Mitschele, C. J.; Saxman, A. C. Measurement of Ultrashort Laser Pulses by Three-Photon Fluorescence. *Appl. Phys. Lett.* **1970**, *17* (3), 122–125.

https://doi.org/10.1063/1.1653331.

(181) Rapp, W.; Gronau, B. Laser Emission from Two Xanthene Dyes via Double-Photon Excitation. *Chem. Phys. Lett.* **1971**, *8* (6), 529–532. https://doi.org/10.1016/0009-2614(71)80084-2.

(182) Topp, M. R.; Rentzepis, P. M. Picosecond Stimulated Emission in a Fluorescent Solution Following Two-Photon Absorption. *Phys. Rev. A* **1971**, *3* (1), 358–364. https://doi.org/10.1103/PhysRevA.3.358.

(183) Rubinov, A. N.; Richardson, M. C.; Sala, K.; Alcock, A. J. Generation of Single-Picosecond Dye Laser Pulses Using One- and Two-Photon Traveling-Wave Excitation. *Appl. Phys. Lett.* **1975**, *27* (6), 358–360. https://doi.org/10.1063/1.88476.

(184) Prokhorenko, V. I.; Tikhonov, E. A.; Shpak, M. T. Superradiant Dye Solution Laser with Two-Photon Picosecond Optical Pumping. *Sov. J. quantum Electron.* **1981**, *11* (1), 139–140. https://doi.org/10.1070/qe1981v011n01abeh005399.

(185) Qiu, P.; Penzkofer, A. Intense Ultrashort Pulse Generation in a Two-Photon Pumped Generator-Amplifier System. *Appl. Phys. B Photophysics Laser Chem.* **1989**, *48* (2), 115–124. https://doi.org/10.1007/BF00692136.

(186) Zaporozhchenko, V. A.; Kachinskiĭ, A. V; Korol'kov, M. V; Chekhlov, O. V. Some Features of Ultrashort Pulse Generation in a Distributed Feedback Dye Laser with Two-Photon Pumping. *Sov. J. Quantum Electron.* **1989**, *19* (9), 1179–1181. https://doi.org/10.1070/qe1989v019n09abeh009018.

(187) Kwok, A. S.; Gillespie, J. B.; Serpengüzel, A.; Hsieh, W.-F.; Chang, R. K. Two-Photon-Pumped Lasing in Microdroplets. *Opt. Lett.* **1992**, *17* (20), 1435. https://doi.org/10.1364/ol.17.001435.

(188) Mukherjee, A. Two-Photon Pumped Upconverted Lasing in Dye Doped Polymer Waveguides. *Appl. Phys. Lett.* **1993**, *62* (26), 3423–3425. https://doi.org/10.1063/1.109036.

(189) He, G. S.; Lin, T.-C.; Chung, S.-J.; Zheng, Q.; Lu, C.; Cui, Y.; Prasad, P. N. Two-, Three-, and Four-Photon-Pumped Stimulated Cavityless Lasing Properties of Ten Stilbazolium-Dyes Solutions. *J. Opt. Soc. Am. B* **2005**, *22* (10), 2219. https://doi.org/10.1364/josab.22.002219.

(190) Fan, H.-H.; Wang, H.-Z.; Tian, Y.-P. Four-Photon Process Induced Upconversion Lasing. *Chinese Phys. Lett.* **2005**, *22* (5), 1152–1154.

(191) Tang, X. J.; Wu, L. Z.; Zhang, L. P.; Tung, C. H. Two-Photon-Pumped Frequency-Upconverted Yellow Lasing in a Novel Dye Solution. *Chem. Phys. Lett.* **2002**, *356* (5–6), 573–576. https://doi.org/10.1016/S0009-2614(02)00416-5.

(192) Tang, X. J.; Wu, L. Z.; Zhang, L. P.; Tung, C. H. Two-Photon-Pumped Frequency-Upconverted Lasing and Optical Power Limiting Properties of Vinylbenzothiazole-Containing Compounds in Solution. *Phys. Chem. Chem. Phys.* **2002**, *4* (23), 5744–5747. https://doi.org/10.1039/b206259c.

(193) He, G. S.; Tan, L.-S.; Zheng, Q.; Prasad, P. N. Multiphoton Absorbing Materials: Molecular Designs, Characterizations, and Applications. *Chem. Rev.* **2008**, *108* (4), 1245–1330. https://doi.org/10.1021/cr050054x.

(194) Spangler, C. W. Recent Development in the Design of Organic Materials for Optical Power Limiting. *Journal of Materials Chemistry*. The Royal Society of Chemistry January 1, 1999, pp 2013–2020. https://doi.org/10.1039/a902802a.

(195) He, G. S.; Liu, S. H. *Physics of Nonlinear Optics*; WORLD SCIENTIFIC, 1999. https://doi.org/10.1142/3648.

(196) Lemercier, G.; Mulatier, J. C.; Martineau, C.; Anémian, R.; Andraud, C.; Wang, I.; Stéphan, O.; Amari, N.; Baldeck, P. Two-Photon Absorption: From Optical Power Limiting to 3D Microfabrication. *Comptes Rendus Chim.* **2005**, *8* (8 SPEC. ISS.), 1308–1316. https://doi.org/10.1016/j.crci.2004.11.038.

(197) Anderson, R. R.; Parrish, J. A. The Optics of Human Skin. *J. Invest. Dermatol.* **1981**, *77*, 13–19. https://doi.org/10.1111/1523-1747.ep12479191.

(198) Smith, A. M.; Mancini, M. C.; Nie, S. Bioimaging: Second Window for in Vivo Imaging. *Nature Nanotechnology*. Nature Publishing Group 2009, pp 710–711. https://doi.org/10.1038/nnano.2009.326.

(199) Sordillo, L. A.; Pu, Y.; Pratavieira, S.; Budansky, Y.; Alfano, R. R. Deep Optical Imaging of Tissue Using the Second and Third Near-Infrared Spectral Windows. *J. Biomed. Opt.* **2014**, *19* (5), 056004. https://doi.org/10.1117/1.jbo.19.5.056004.

(200) Prodi, L.; Rampazzo, E.; Rastrelli, F.; Speghini, A.; Zaccheroni, N. Imaging Agents Based on Lanthanide Doped Nanoparticles. *Chemical Society Reviews*. Royal Society of Chemistry July 21, 2015, pp 4922–4952. https://doi.org/10.1039/c4cs00394b.

(201) Guo, H.; Aleyasin, H.; Chen, J.; Qin, L.; Ratan, R. R.; Xie, S.; Cho, S.; Gong, W.; Chen, Y. Recent Advances in Two-Photon Imaging: Technology Developments and Biomedical. *Chinese Opt. Lett. Vol. 11, Issue 1, pp. 011703-* **2013**, *11* (1), 011703-.

(202) Guo, H.; Aleyasin, H.; Howard, S. S.; Dickinson, B. C.; Lin, V. S.; Haskew-Layton, R. E.; Xu, C.; Chen, Y.; Ratan, R. R. Two-Photon Fluorescence Imaging of Intracellular Hydrogen Peroxide with Chemoselective Fluorescent Probes. *J. Biomed. Opt.* **2013**, *18* (10), 106002. https://doi.org/10.1117/1.JBO.18.10.106002.

(203) Alim, I.; Haskew-Layton, R. E.; Aleyasin, H.; Guo, H.; Ratan, R. R. Spatial, Temporal, and Quantitative Manipulation of Intracellular Hydrogen Peroxide in Cultured Cells. In *Methods in Enzymology*; Academic Press Inc., 2014; Vol. 547, pp 251–273. https://doi.org/10.1016/B978-0-12-801415-8.00014-X.

(204) Carter, M.; Shieh, J. Chapter 5 - Microscopy. In *Guide to Research Techniques in Neuroscience*; Elsevier, 2015; pp 117–144. https://doi.org/10.1016/B978-0-12-800511-8.00005-8.

(205) Pawley, J. B. *Handbook of Biological Confocal Microscopy: Third Edition*; Springer US, 2006. https://doi.org/10.1007/978-0-387-45524-2.

(206) Graf, B. W.; Boppart, S. A. Imaging and Analysis of Three-Dimensional Cell Culture Models. *Methods Mol. Biol.* **2010**, *591*, 211–227. https://doi.org/10.1007/978-1-60761-404-3_13.

(207) Hemmer, E.; Venkatachalam, N.; Hyodo, H.; Hattori, A.; Ebina, Y.; Kishimoto, H.; Soga, K. Upconverting and NIR Emitting Rare Earth Based Nanostructures for NIR-Bioimaging. *Nanoscale*. The Royal Society of Chemistry December 7, 2013, pp 11339–11361. https://doi.org/10.1039/c3nr02286b.

(208) Xu, C.; Zipfel, W.; Shear, J. B.; Williams, R. M.; Webb, W. W. Multiphoton Fluorescence Excitation: New Spectral Windows for Biological Nonlinear Microscopy. *Proc. Natl. Acad. Sci. U. S. A.* **1996**, *93* (20), 10763–10768. https://doi.org/10.1073/pnas.93.20.10763.

(209) Lim, C. S.; Cho, B. R. Two-Photon Probes for Biomedical Imaging. *Tetrahedron* **2015**, *71* (43), 8219–8249. https://doi.org/10.1016/j.tet.2015.06.083.

(210) Danylchuk, D. I.; Jouard, P.-H.; Klymchenko, A. S. Targeted Solvatochromic Fluorescent Probes for Imaging Lipid Order in Organelles under Oxidative and Mechanical Stress. *J. Am.*

Chem. Soc. **2021**, *143* (2), 912–924. https://doi.org/10.1021/jacs.0c10972.

(211) Yang, Z.; He, Y.; Lee, J. H.; Park, N.; Suh, M.; Chae, W. S.; Cao, J.; Peng, X.; Jung, H.; Kang, C.; Kim, J. S. A Self-Calibrating Bipartite Viscosity Sensor for Mitochondria. *J. Am. Chem. Soc.* **2013**, *135* (24), 9181–9185. https://doi.org/10.1021/ja403851p.

(212) Zhu, H.; Fan, J.; Du, J.; Peng, X. Fluorescent Probes for Sensing and Imaging within Specific Cellular Organelles. *Acc. Chem. Res.* **2016**, *49* (10), 2115–2126. https://doi.org/10.1021/acs.accounts.6b00292.

(213) Zielonka, J.; Joseph, J.; Sikora, A.; Hardy, M.; Ouari, O.; Vasquez-Vivar, J.; Cheng, G.; Lopez, M.; Kalyanaraman, B. Mitochondria-Targeted Triphenylphosphonium-Based Compounds: Syntheses, Mechanisms of Action, and Therapeutic and Diagnostic Applications. *Chemical Reviews*. American Chemical Society August 9, 2017, pp 10043–10120. https://doi.org/10.1021/acs.chemrev.7b00042.

(214) Wagner, N.; Stephan, M.; Höglinger, D.; Nadler, A. A Click Cage: Organelle-Specific Uncaging of Lipid Messengers. *Angew. Chemie Int. Ed.* **2018**, *57* (40), 13339–13343. https://doi.org/10.1002/anie.201807497.

(215) Goujon, A.; Colom, A.; Straková, K.; Mercier, V.; Mahecic, D.; Manley, S.; Sakai, N.; Roux, A.; Matile, S. Mechanosensitive Fluorescent Probes to Image Membrane Tension in Mitochondria, Endoplasmic Reticulum, and Lysosomes. *J. Am. Chem. Soc.* **2019**, *141* (8), 3380–3384. https://doi.org/10.1021/jacs.8b13189.

(216) Li, L. L.; Li, K.; Li, M. Y.; Shi, L.; Liu, Y. H.; Zhang, H.; Pan, S. L.; Wang, N.; Zhou, Q.; Yu, X. Q. BODIPY-Based Two-Photon Fluorescent Probe for Real-Time Monitoring of Lysosomal Viscosity with Fluorescence Lifetime Imaging Microscopy. *Anal. Chem.* **2018**, *90* (9), 5873–5878. https://doi.org/10.1021/acs.analchem.8b00590.

(217) Kong, X.; Yin, J.; Li, M.; Zhu, L.; Dong, B.; Ma, Y.; Lin, W. Simultaneously Imaging of SO2 in Lysosomes and Mitochondria Based on a Dual Organelle-Targeted Fluorescent Probe. *Sensors Actuators, B Chem.* **2019**, *292*, 80–87. https://doi.org/10.1016/j.snb.2019.04.094.

(218) Zhang, H.; Fan, J.; Dong, H.; Zhang, S.; Xu, W.; Wang, J.; Gao, P.; Peng, X. Fluorene-Derived Two-Photon Fluorescent Probes for Specific and Simultaneous Bioimaging of Endoplasmic Reticulum and Lysosomes: Group-Effect and Localization. *J. Mater. Chem. B* **2013**, *1* (40), 5450–5455. https://doi.org/10.1039/c3tb20646g.

(219) Ghosh, S.; Nandi, S.; Ghosh, C.; Bhattacharyya, K. Fluorescence Dynamics in the Endoplasmic Reticulum of a Live Cell: Time-Resolved Confocal Microscopy. *ChemPhysChem* **2016**, *17* (18), 2818–2823. https://doi.org/10.1002/cphc.201600425.

(220) Collot, M.; Fam, T. K.; Ashokkumar, P.; Faklaris, O.; Galli, T.; Danglot, L.; Klymchenko, A. S. Ultrabright and Fluorogenic Probes for Multicolor Imaging and Tracking of Lipid Droplets in Cells and Tissues. *J. Am. Chem. Soc.* **2018**, *140* (16), 5401–5411. https://doi.org/10.1021/jacs.7b12817.

(221) Collot, M.; Kreder, R.; Tatarets, A. L.; Patsenker, L. D.; Mely, Y.; Klymchenko, A. S. Bright Fluorogenic Squaraines with Tuned Cell Entry for Selective Imaging of Plasma Membrane vs. Endoplasmic Reticulum. *Chem. Commun.* **2015**, *51* (96), 17136–17139. https://doi.org/10.1039/c5cc06094j.

(222) Hirayama, T.; Inden, M.; Tsuboi, H.; Niwa, M.; Uchida, Y.; Naka, Y.; Hozumi, I.; Nagasawa, H. A Golgi-Targeting Fluorescent Probe for Labile Fe(Ii) to Reveal an Abnormal Cellular Iron Distribution Induced by Dysfunction of VPS35. *Chem. Sci.* **2019**, *10* (5), 1514–1521. https://doi.org/10.1039/c8sc04386h.

(223) Yu, W.; So, P. T. C.; French, T.; Gratton, E. Fluorescence Generalized Polarization of Cell Membranes: A Two-Photon Scanning Microscopy Approach. *Biophys. J.* **1996**, *70* (2 I), 626–636. https://doi.org/10.1016/S0006-3495(96)79646-7.

(224) Gaus, K.; Gratton, E.; Kable, E. P. W.; Jones, A. S.; Gelissen, I.; Kritharides, L.; Jessup, W. Visualizing Lipid Structure and Raft Domains in Living Cells with Two-Photon Microscopy. *Proc. Natl. Acad. Sci. U. S. A.* **2003**, *100* (26), 15554–15559. https://doi.org/10.1073/pnas.2534386100.

(225) Hwan, M. K.; Byeong, H. J.; Hyon, J. Y.; Myoung, J. A.; Mun, S. S.; Jin, H. H.; Lee, K. J.; Chul, H. K.; Joo, T.; Hong, S. C.; Bong, R. C. Two-Photon Fluorescent Turn-on Probe for Lipid Rafts in Live Cell and Tissue. *J. Am. Chem. Soc.* **2008**, *130* (13), 4246–4247. https://doi.org/10.1021/ja711391f.

(226) Chang, C. J.; Jaworski, J.; Nolan, E. M.; Sheng, M.; Lippard, S. J. A Tautomeric Zinc Sensor for Ratiometric Fluorescence Imaging: Application to Nitric Oxide-Induced Release of Intracellular Zinc. *Proc. Natl. Acad. Sci. U. S. A.* **2004**, *101* (5), 1129–1134. https://doi.org/10.1073/pnas.0308079100.

(227) Kim, H. M.; Kim, B. R.; Hong, J. H.; Park, J. S.; Lee, K. J.; Cho, B. R. A Two-Photon Fluorescent Probe for Calcium Waves in Living Tissue. *Angew. Chemie - Int. Ed.* **2007**, *46* (39), 7445–7448. https://doi.org/10.1002/anie.200701720.

(228) Baek, N. Y.; Heo, C. H.; Lim, C. S.; Masanta, G.; Cho, B. R.; Kim, H. M. A Highly Sensitive Two-Photon Fluorescent Probe for Mitochondrial Zinc Ions in Living Tissue. *Chem. Commun.* **2012**, *48* (38), 4546–4548. https://doi.org/10.1039/c2cc31077e.

(229) Kim, H. M.; Yang, P. R.; Seo, M. S.; Yi, J. S.; Hong, J. H.; Jeon, S. J.; Ko, Y. G.; Lee, K. J.; Cho, B. R. Magnesium Ion Selective Two-Photon Fluorescent Probe Based on a Benzo[h]Chromene Derivative for in Vivo Imaging. *J. Org. Chem.* **2007**, *72* (6), 2088–2096. https://doi.org/10.1021/jo062341m.

(230) Kim, H. M.; Jung, C.; Kim, B. R.; Jung, S. Y.; Hong, J. H.; Ko, Y. G.; Lee, K. J.; Cho, B. R. Environment-Sensitive Two-Photon Probe for Intracellular Free Magnesium Ions in Live Tissue. *Angew. Chemie - Int. Ed.* **2007**, *46* (19), 3460–3463. https://doi.org/10.1002/anie.200700169.

(231) Kim, H. M.; Kim, B. R.; An, M. J.; Hong, J. H.; Lee, K. J.; Cho, B. R. Two-Photon Fluorescent Probes for Long-Term Imaging of Calcium Waves in Live Tissue. *Chem. - A Eur. J.* **2008**, *14* (7), 2075–2083. https://doi.org/10.1002/chem.200701453.

(232) Nolan, E. M.; Lippard, S. J. Small-Molecule Fluorescent Sensors for Investigating Zinc Metalloneurochemistry. *Acc. Chem. Res.* **2009**, *42* (1), 193–203. https://doi.org/10.1021/ar8001409.

(233) Kim, H. J.; Han, J. H.; Kim, M. K.; Lim, C. S.; Kim, H. M.; Cho, B. R. Dual-Color Imaging of Sodium/Calcium Ion Activities with Two-Photon Fluorescent Probes. *Angew. Chemie Int. Ed.* **2010**, *49* (38), 6786–6789. https://doi.org/10.1002/anie.201002907.

(234) Kim, M. K.; Lim, C. S.; Hong, J. T.; Han, J. H.; Jang, H.; Kim, H. M.; Cho, B. R. Sodium-Ion-Selective Two-Photon Fluorescent Probe for In Vivo Imaging. *Angew. Chemie Int. Ed.* **2010**, *49* (2), 364–367. https://doi.org/10.1002/anie.200904835.

(235) Masanta, G.; Lim, C. S.; Kim, H. J.; Han, J. H.; Kim, H. M.; Cho, B. R. A Mitochondrial-Targeted Two-Photon Probe for Zinc Ion. *J. Am. Chem. Soc.* **2011**, *133* (15), 5698–5700. https://doi.org/10.1021/ja200444t.

(236) Dong, X.; Han, J. H.; Heo, C. H.; Kim, H. M.; Liu, Z.; Cho, B. R. Dual-Color Imaging of Magnesium/Calcium Ion Activities with Two-Photon Fluorescent Probes. *Anal. Chem.* **2012**, *84* (19), 8110–8113. https://doi.org/10.1021/ac302210v.

(237) Tian, Y. S.; Lee, H. Y.; Lim, C. S.; Park, J.; Kim, H. M.; Shin, Y. N.; Kim, E. S.; Jeon, H. J.; Park, S. B.; Cho, B. R. A Two-Photon Tracer for Glucose Uptake. *Angew. Chemie Int. Ed.* **2009**, *48* (43), 8027–8031. https://doi.org/10.1002/anie.200901175.

(238) Lim, C. S.; Chung, C.; Kim, H. M.; An, M. J.; Tian, Y. S.; Chun, H. J.; Cho, B. R. A Two-Photon Turn-on Probe for Glucose Uptake. *Chem. Commun.* **2012**, *48* (15), 2122–2124. https://doi.org/10.1039/c2cc16792a.

(239) Lee, J. H.; Lim, C. S.; Tian, Y. S.; Han, J. H.; Cho, B. R. A Two-Photon Fluorescent Probe for Thiols in Live Cells and Tissues. *J. Am. Chem. Soc.* **2010**, *132* (4), 1216–1217. https://doi.org/10.1021/ja9090676.

(240) Lim, C. S.; Masanta, G.; Kim, H. J.; Han, J. H.; Kim, H. M.; Cho, B. R. Ratiometric Detection of Mitochondrial Thiols with a Two-Photon Fluorescent Probe. *J. Am. Chem. Soc.* **2011**, *133* (29), 11132–11135. https://doi.org/10.1021/ja205081s.

(241) Bae, S. K.; Heo, C. H.; Choi, D. J.; Sen, D.; Joe, E. H.; Cho, B. R.; Kim, H. M. A Ratiometric Two-Photon Fluorescent Probe Reveals Reduction in Mitochondrial H2S Production in Parkinson's Disease Gene Knockout Astrocytes. *J. Am. Chem. Soc.* **2013**, *135* (26), 9915–9923. https://doi.org/10.1021/ja404004v.

(242) Lim, C. S.; Das, S. K.; Yang, S. Y.; Kim, E. S.; Chun, H. J.; Cho, B. R. Quantitative Estimation of the Total Sulfide Concentration in Live Tissues by Two-Photon Microscopy. *Anal. Chem.* **2013**, *85* (19), 9288–9295. https://doi.org/10.1021/ac402042k.

(243) Furuta, T.; Wang, S. S. H.; Dantzker, J. L.; Dore, T. M.; Bybee, W. J.; Callaway, E. M.; Denk, W.; Tsien, R. Y. Brominated 7-Hydroxycoumarin-4-Ylmethyls: Photolabile Protecting Groups with Biologically Useful Cross-Sections for Two Photon Photolysis. *Proc. Natl. Acad. Sci. U. S. A.* **1999**, *96* (4), 1193–1200. https://doi.org/10.1073/pnas.96.4.1193.

(244) Fedoryak, O. D.; Dore, T. M. Brominated Hydroxyquinoline as a Photolabile Protecting Group with Sensitivity to Multiphoton Excitation. *Org. Lett.* **2002**, *4* (20), 3419–3422. https://doi.org/10.1021/ol026524g.

(245) Kiskin, N. I.; Chillingworth, R.; McCray, J. A.; Piston, D.; Ogden, D. The Efficiency of Two-Photon Photolysis of a "Caged" Fluorophore, o-1-(2-Nitrophenyl)Ethylpyranine, in Relation to Photodamage of Synaptic Terminals. *Eur. Biophys. J.* **2002**, *30* (8), 588–604. https://doi.org/10.1007/s00249-001-0187-x.

(246) Petit, M.; Tran, C.; Roger, T.; Gallavardin, T.; Dhimane, H.; Palma-Cerda, F.; Blanchard-Desce, M.; Acher, F. C.; Ogden, D.; Dalko, P. I. Substitution Effect on the One- and Two-Photon Sensitivity of DMAQ "Caging" Groups. *Org. Lett.* **2012**, *14* (24), 6366–6369. https://doi.org/10.1021/ol3031704.

(247) Tran, C.; Gallavardin, T.; Petit, M.; Slimi, R.; Dhimane, H.; Blanchard-Desce, M.; Acher, F. C.; Ogden, D.; Dalko, P. I. Two-Photon "Caging" Groups: Effect of Position Isomery on the Photorelease Properties of Aminoquinoline-Derived Photolabile Protecting Groups. *Org. Lett.* **2015**, *17* (3), 402–405. https://doi.org/10.1021/ol5035035.

(248) Matsuzaki, M.; Ellis-Davies, G. C. R.; Nemoto, T.; Miyashita, Y.; Iino, M.; Kasai, H. Dendritic Spine Geometry Is Critical for AMPA Receptor Expression in Hippocampal CA1 Pyramidal Neurons. *Nat. Neurosci.* **2001**, *4* (11), 1086–1092. https://doi.org/10.1038/nn736.

(249) Suzuki, A. Z.; Watanabe, T.; Kawamoto, M.; Nishiyama, K.; Yamashita, H.; Ishii, M.; Iwamura, M.; Furuta, T. Coumarin-4-Ylmethoxycarbonyls as Phototriggers for Alcohols and Phenols. *Org. Lett.* **2003**, *5* (25), 4867–4870. https://doi.org/10.1021/ol0359362.

(250) Lin, W.; Lawrence, D. S. A Strategy for the Construction of Caged Diols Using a Photolabile Protecting Group. *J. Org. Chem.* **2002**, *67* (8), 2723–2726. https://doi.org/10.1021/jo0163851.

(251) Zhu, Y.; Pavlos, C. M.; Toscano, J. P.; Dore, T. M. 8-Bromo-7-Hydroxyquinoline as a Photoremovable Protecting Group for Physiological Use: Mechanism and Scope. *J. Am. Chem. Soc.* **2006**, *128* (13), 4267–4276. https://doi.org/10.1021/ja0555320.

(252) Lu, M.; Fedoryak, O. D.; Moister, B. R.; Dore, T. M. Bhc-Diol as a Photolabile Protecting Group for Aldehydes and Ketones. *Org. Lett.* **2003**, *5* (12), 2119–2122. https://doi.org/10.1021/ol034536b.

(253) Hishikawa, K.; Nakagawa, H.; Furuta, T.; Fukuhara, K.; Tsumoto, H.; Suzuki, T.; Miyata, N. Photoinduced Nitric Oxide Release from a Hindered Nitrobenzene Derivative by Two-Photon Excitation. *J. Am. Chem. Soc.* **2009**, *131* (22), 7488–7489. https://doi.org/10.1021/ja8093668.

(254) Furuta, T.; Watanabe, T.; Tanabe, S.; Sakyo, J.; Matsuba, C. Phototriggers for Nucleobases with Improved Photochemical Properties. *Org. Lett.* **2007**, *9* (23), 4717–4720. https://doi.org/10.1021/ol702106t.

(255) Furuta, T.; Manabe, K.; Teraoka, A.; Murakoshi, K.; Ohtsubo, A.; Suzuki, A. Design, Synthesis, and Photochemistry of Modular Caging Groups for Photoreleasable Nucleotides. *Org. Lett.* **2012**, *14* (24), 6182–6185. https://doi.org/10.1021/ol3029093.

(256) Ando, H.; Furuta, T.; Tsien, R. Y.; Okamoto, H. Photo-Mediated Gene Activation Using Caged RNA/DNA in Zebrafish Embryos. *Nat. Genet.* **2001**, *28* (4), 317–325. https://doi.org/10.1038/ng583.

(257) Brown, S. B.; Brown, E. A.; Walker, I. The Present and Future Role of Photodynamic Therapy in Cancer Treatment. *Lancet Oncology*. Lancet Oncol August 1, 2004, pp 497–508. https://doi.org/10.1016/S1470-2045(04)01529-3.

(258) Bhawalkar, J. D.; Kumar, N. D.; Zhao, C. F.; Prasad, P. N. Two-Photon Photodynamic Therapy. *J. Clin. Laser Med. Surg.* **1997**, *15* (5), 201–204. https://doi.org/10.1089/clm.1997.15.201.

(259) Arnbjerg, J.; Johnsen, M.; Frederiksen, P. K.; Braslavsky, S. E.; Ogilby, P. R. Two-Photon Photosensitized Production of Singlet Oxygen: Optical and Optoacoustic Characterization of Absolute Two-Photon Absorption Cross Sections for Standard Sensitizers in Different Solvents. *J. Phys. Chem. A* **2006**, *110* (23), 7375–7385. https://doi.org/10.1021/jp0609986.

(260) Nielsen, C. B.; Johnsen, M.; Arnbjerg, J.; Pittelkow, M.; Mcllroy, S. P.; Ogilby, P. R.; Jørgensen, M. Synthesis and Characterization of Water-Soluble Phenylene-Vinylene-Based Singlet Oxygen Sensitizers for Two-Photon Excitation. *J. Org. Chem.* **2005**, *70* (18), 7065–7079. https://doi.org/10.1021/jo050507y.

(261) Belfield, K. D.; Corredor, C. C.; Morales, A. R.; Dessources, M. A.; Hernandez, F. E. Synthesis and Characterization of New Fluorene-Based Singlet Oxygen Sensitizers. *J. Fluoresc.* **2006**, *16* (1), 105–110. https://doi.org/10.1007/s10895-005-0008-1.

(262) Andrasik, S. J.; Belfield, K. D.; Bondar, M. V.; Hernandez, F. E.; Morales, A. R.; Przhonska, O. V.; Yao, S. One- and Two-Photon Singlet Oxygen Generation with New Fluorene-Based

Photosensitizers. *ChemPhysChem* **2007**, *8* (3), 399–404. https://doi.org/10.1002/cphc.200600568.

(263) Morone, M.; Beverina, L.; Abbotto, A.; Silvestri, F.; Collini, E.; Ferrante, C.; Bozio, R.; Pagani, G. A. Enhancement of Two-Photon Absorption Cross-Section and Singlet-Oxygen Generation in Porphyrins upon β-Functionalization with Donor-Acceptor Substituents. *Org. Lett.* **2006**, *8* (13), 2719–2722. https://doi.org/10.1021/ol060742i.

(264) Ogawa, K.; Hasegawa, H.; Inaba, Y.; Kobuke, Y.; Inouye, H.; Kanemitsu, Y.; Kohno, E.; Hirano, T.; Ogura, S. I.; Okura, I. Water-Soluble Bis(Imidazolylporphyrin) Self-Assemblies with Large Two-Photon Absorption Cross Sections as Potential Agents for Photodynamic Therapy. *J. Med. Chem.* **2006**, *49* (7), 2276–2283. https://doi.org/10.1021/jm051072+.

(265) Dy, J. T.; Ogawa, K.; Satake, A.; Ishizumi, A.; Kobuke, Y. Water-Soluble Self-Assembled Butadiyne-Bridged Bisporphyrin: A Potential Two-Photon-Absorbing Photosensitizer for Photodynamic Therapy. *Chem. - A Eur. J.* **2007**, *13* (12), 3491–3500. https://doi.org/10.1002/chem.200601205.

(266) Arnbjerg, J.; Jiménez-Banzo, A.; Paterson, M. J.; Nonell, S.; Borrell, J. I.; Christiansen, O.; Ogilby, P. R. Two-Photon Absorption in Tetraphenylporphycenes: Are Porphycenes Better Candidates than Porphyrins for Providing Optimal Optical Properties for Two-Photon Photodynamic Therapy? *J. Am. Chem. Soc.* **2007**, *129* (16), 5188–5199. https://doi.org/10.1021/ja0688777.

(267) Ogawa, K.; Kobuke, Y. Two-Photon Photodynamic Therapy by Water-Soluble Self-Assembled Conjugated Porphyrins. *BioMed Research International*. Hindawi Limited 2013, p 11. https://doi.org/10.1155/2013/125658.

(268) Gerschman, R.; Gilbert, D. L.; Nye, S. W.; Dwyer, P.; Fenn, W. O. Oxygen Poisoning and X-Irradiation: A Mechanism in Common. *Science (80-.).* **1954**, *119* (3097), 623–626. https://doi.org/10.1126/science.119.3097.623.

(269) Gerschman, R.; Gilbert, D. L.; Nye, S. W.; Fenn, W. O. Influence of X-Irradiation on Oxygen Poisoning in Mice. *Proc. Soc. Exp. Biol. Med.* **1954**, *86* (1), 27–29. https://doi.org/10.3181/00379727-86-21002.

(270) Apel, K.; Hirt, H. Reactive Oxygen Species: Metabolism, Oxidative Stress, and Signal Transduction. *Annual Review of Plant Biology*. Annu Rev Plant Biol 2004, pp 373–399. https://doi.org/10.1146/annurev.arplant.55.031903.141701.

(271) Kagan, V. E.; Quinn, P. J. Toward Oxidative Lipidomics of Cell Signaling. *Antioxid. Redox Signal.* **2004**, *6* (2), 199–202. https://doi.org/10.1089/152308604322899260.

(272) West, J. D.; Marnett, L. J. Endogenous Reactive Intermediates as Modulators of Cell Signaling and Cell Death. *Chemical Research in Toxicology*. Chem Res Toxicol February 2006, pp 173–194. https://doi.org/10.1021/tx050321u.

(273) Rhee, S. G. H2O2, a Necessary Evil for Cell Signaling. *Science*. American Association for the Advancement of Science June 30, 2006, pp 1882–1883. https://doi.org/10.1126/science.1130481.

(274) Lesser, M. P. Oxidative Stress in Marine Environments: Biochemistry and Physiological Ecology. *Annual Review of Physiology*. Annu Rev Physiol 2006, pp 253–278. https://doi.org/10.1146/annurev.physiol.68.040104.110001.

(275) Winterbourn, C. C. Reconciling the Chemistry and Biology of Reactive Oxygen Species. *Nature Chemical Biology*. Nature Publishing Group March 23, 2008, pp 278–286.

https://doi.org/10.1038/nchembio.85.

(276) Martínez-Reyes, I.; Cuezva, J. M. The H+-ATP Synthase: A Gate to ROS-Mediated Cell Death or Cell Survival. *Biochimica et Biophysica Acta - Bioenergetics*. Elsevier July 1, 2014, pp 1099–1112. https://doi.org/10.1016/j.bbabio.2014.03.010.

(277) Avery, S. V. Molecular Targets of Oxidative Stress. *Biochemical Journal*. Portland Press March 1, 2011, pp 201–210. https://doi.org/10.1042/BJ20101695.

(278) Scialò, F.; Fernández-Ayala, D. J.; Sanz, A. Role of Mitochondrial Reverse Electron Transport in ROS Signaling: Potential Roles in Health and Disease. *Front. Physiol.* **2017**, *8* (JUN), 428. https://doi.org/10.3389/fphys.2017.00428.

(279) Sack, M. N.; Fyhrquist, F. Y.; Saijonmaa, O. J.; Fuster, V.; Kovacic, J. C. Basic Biology of Oxidative Stress and the Cardiovascular System: Part 1 of a 3-Part Series. *Journal of the American College of Cardiology*. Elsevier USA July 11, 2017, pp 196–211. https://doi.org/10.1016/j.jacc.2017.05.034.

(280) Hassan, S. Z.; Gheita, T. A.; Kenawy, S. A.; Fahim, A. T.; El-Sorougy, I. M.; Abdou, M. S. Oxidative Stress in Systemic Lupus Erythematosus and Rheumatoid Arthritis Patients: Relationship to Disease Manifestations and Activity. *Int. J. Rheum. Dis.* **2011**, *14* (4), 325–331. https://doi.org/10.1111/j.1756-185X.2011.01630.x.

(281) Kim, H.; Yang, J.; Kim, M. J.; Choi, S.; Chung, J.-R.; Kim, J.-M.; Yoo, Y. H.; Chung, J.; Koh, H. Tumor Necrosis Factor Receptor-Associated Protein 1 (TRAP1) Mutation and TRAP1 Inhibitor Gamitrinib-Triphenylphosphonium (G-TPP) Induce a Forkhead Box O (FOXO)-Dependent Cell Protective Signal from Mitochondria. *J. Biol. Chem.* **2016**, *291* (4), 1841–1853. https://doi.org/10.1074/jbc.M115.656934.

(282) Moloney, J. N.; Cotter, T. G. ROS Signalling in the Biology of Cancer. *Seminars in Cell and Developmental Biology*. Elsevier Ltd August 1, 2018, pp 50–64. https://doi.org/10.1016/j.semcdb.2017.05.023.

(283) Aviello, G.; Knaus, U. ROS in Gastrointestinal Inflammation: Rescue Or Sabotage? *Br. J. Pharmacol.* **2017**, *174* (12), 1704–1718. https://doi.org/10.1111/bph.13428.

(284) Ahmadinejad, F.; Geir Møller, S.; Hashemzadeh-Chaleshtori, M.; Bidkhori, G.; Jami, M.-S. Molecular Mechanisms behind Free Radical Scavengers Function against Oxidative Stress. *Antioxidants* **2017**, *6* (3), 51. https://doi.org/10.3390/antiox6030051.

(285) Valko, M.; Izakovic, M.; Mazur, M.; Rhodes, C. J.; Telser, J. Role of Oxygen Radicals in DNA Damage and Cancer Incidence. *Mol. Cell. Biochem.* **2004**, *266* (1–2), 37–56. https://doi.org/10.1023/B:MCBI.0000049134.69131.89.

(286) Rodriguez-Muñiz, G. M.; Gomis, J.; Arques, A.; Amat, A. M.; Marin, M. L.; Miranda, M. A. Hydroxyl Radical as an Unlikely Key Intermediate in the Photodegradation of Emerging Pollutants. *Photochem. Photobiol.* **2014**, *90* (6), 1467–1469. https://doi.org/10.1111/php.12325.

(287) Halliwell, B.; Gutteridge, J. M. C. *Free Radicals in Biology and Medicine*; Oxford University Press, 2015. https://doi.org/10.1093/acprof:oso/9780198717478.001.0001.

(288) Lambeth, J. D. NOX Enzymes and the Biology of Reactive Oxygen. *Nature Reviews Immunology*. Nature Publishing Group 2004, pp 181–189. https://doi.org/10.1038/nri1312.

(289) Nathan, C.; Cunningham-Bussel, A. Beyond Oxidative Stress: An Immunologist's Guide to Reactive Oxygen Species. *Nature Reviews Immunology*. Nat Rev Immunol May 2013, pp 349–361. https://doi.org/10.1038/nri3423.

(290) Boveris, A.; Chance, B. The Mitochondrial Generation of Hydrogen Peroxide. General Properties and Effect of Hyperbaric Oxygen. *Biochem. J.* **1973**, *134* (3), 707–716. https://doi.org/10.1042/bj1340707.

(291) Turrens, J. F. Superoxide Production by the Mitochondrial Respiratory Chain. *Biosci. Rep.* **1997**, *17* (1), 3–8. https://doi.org/10.1023/A:1027374931887.

(292) Turrens, J. F. Mitochondrial Formation of Reactive Oxygen Species. *J. Physiol.* **2003**, *552* (2), 335–344. https://doi.org/10.1113/jphysiol.2003.049478.

(293) Finkel, T. Signal Transduction by Reactive Oxygen Species. *J. Cell Biol.* **2011**, *194* (1), 7–15. https://doi.org/10.1083/jcb.201102095.

(294) Halliwell, B.; Gutteridge, J. M. C. Biologically Relevant Metal Ion-Dependent Hydroxyl Radical Generation An Update. *FEBS Lett.* **1992**, *307* (1), 108–112. https://doi.org/10.1016/0014-5793(92)80911-Y.

(295) Walling, C. Intermediates in the Reactions of Fenton Type Reagents. *Acc. Chem. Res.* **1998**, *31* (4), 155–157. https://doi.org/10.1021/ar9700567.

(296) Imlay, J. A. Cellular Defenses against Superoxide and Hydrogen Peroxide. *Annu. Rev. Biochem.* **2008**, *77* (1), 755–776. https://doi.org/10.1146/annurev.biochem.77.061606.161055.

(297) Gowrishankar, S.; Ferguson, S. M. Lysosomes Relax in the Cellular Suburbs. *J. Cell Biol.* **2016**, *212* (6), 617–619. https://doi.org/10.1083/jcb.201602082.

(298) Nohl, H.; Gille, L. Lysosomal ROS Formation. *Redox Rep.* **2005**, *10* (4), 199–205. https://doi.org/10.1179/135100005X70170.

(299) Boya, P.; Kroemer, G. Lysosomal Membrane Permeabilization in Cell Death. *Oncogene*. Nature Publishing Group October 27, 2008, pp 6434–6451. https://doi.org/10.1038/onc.2008.310.

(300) Kallunki, T.; Olsen, O. D.; Jäättelä, M. Cancer-Associated Lysosomal Changes: Friends or Foes? *Oncogene*. Nature Publishing Group April 18, 2013, pp 1995–2004. https://doi.org/10.1038/onc.2012.292.

(301) Cadet, J. Oxidative Damage to DNA: Formation, Measurement and Biochemical Features. *Mutat. Res. Mol. Mech. Mutagen.* **2003**, *531* (1–2), 5–23. https://doi.org/10.1016/j.mrfmmm.2003.09.001.

(302) Leichert, L. I.; Gehrke, F.; Gudiseva, H. V.; Blackwell, T.; Ilbert, M.; Walker, A. K.; Strahler, J. R.; Andrews, P. C.; Jakob, U. Quantifying Changes in the Thiol Redox Proteome upon Oxidative Stress in Vivo. *Proc. Natl. Acad. Sci. U. S. A.* **2008**, *105* (24), 8197–8202. https://doi.org/10.1073/pnas.0707723105.

(303) Yin, H.; Xu, L.; Porter, N. A. Free Radical Lipid Peroxidation: Mechanisms and Analysis. *Chemical Reviews*. Chem Rev October 12, 2011, pp 5944–5972. https://doi.org/10.1021/cr200084z.

(304) Umezawa, N.; Tanaka, K.; Urano, Y.; Kikuchi, K.; Higuchi, T.; Nagano, T. Novel Fluorescent Probes for Singlet Oxygen. *Angew. Chemie - Int. Ed.* **1999**, *38* (19), 2899–2901. https://doi.org/10.1002/(SICI)1521-3773(19991004)38:19<2899::AID-ANIE2899>3.0.CO;2-M.

(305) Gabe, Y.; Urano, Y.; Kikuchi, K.; Kojima, H.; Nagano, T. Highly Sensitive Fluorescence Probes for Nitric Oxide Based on Boron Dipyrromethene Chromophore - Rational Design of

Potentially Useful Bioimaging Fluorescence Probe. *J. Am. Chem. Soc.* **2004**, *126* (10), 3357–3367. https://doi.org/10.1021/ja037944j.

(306) Gomes, A.; Fernandes, E.; Lima, J. L. F. C. Fluorescence Probes Used for Detection of Reactive Oxygen Species. *J. Biochem. Biophys. Methods* **2005**, *65* (2–3), 45–80. https://doi.org/10.1016/j.jbbm.2005.10.003.

(307) Dickinson, B. C.; Huynh, C.; Chang, C. J. A Palette of Fluorescent Probes with Varying Emission Colors for Imaging Hydrogen Peroxide Signaling in Living Cells. *J. Am. Chem. Soc.* **2010**, *132* (16), 5906–5915. https://doi.org/10.1021/ja1014103.

(308) Ahn, H. Y.; Fairfull-Smith, K. E.; Morrow, B. J.; Lussini, V.; Kim, B.; Bondar, M. V.; Bottle, S. E.; Belfield, K. D. Two-Photon Fluorescence Microscopy Imaging of Cellular Oxidative Stress Using Profluorescent Nitroxides. *J. Am. Chem. Soc.* **2012**, *134* (10), 4721–4730. https://doi.org/10.1021/ja210315x.

(309) Chan, M. S.; Xu, D.; Guo, L.; Tam, D. Y.; Liu, L. S.; Chen, Y.; Wong, M. S.; Lo, P. K. Cyanine Fluorophores for Cellular Protection against ROS in Stimulated Macrophages and Two-Photon ROS Detection. *Org. Biomol. Chem.* **2015**, *13* (26), 7307–7312. https://doi.org/10.1039/c5ob00643k.

(310) Wu, L.; Sedgwick, A. C.; Sun, X.; Bull, S. D.; He, X. P.; James, T. D. Reaction-Based Fluorescent Probes for the Detection and Imaging of Reactive Oxygen, Nitrogen, and Sulfur Species. *Acc. Chem. Res.* **2019**, *52* (9), 2582–2597. https://doi.org/10.1021/acs.accounts.9b00302.

(311) Tsakanova, G.; Arakelova, E.; Ayvazyan, V.; Ayvazyan, A.; Tatikyan, S.; Grigoryan, R.; Sargsyan, N.; Arakelyan, A. Two-Photon Imaging of Oxidative Stress in Living Erythrocytes as a Measure for Human Aging. *Biomed. Opt. Express* **2020**, *11* (7), 3444. https://doi.org/10.1364/boe.393898.

(312) Li, L.; Wang, X.; Sun, C.; Xu, T.; Yang, Z.; Zhang, Z.; Feng, Y.; Fang, M.; Chen, M.; Wang, X.; Meng, X. Design of a Two-Photon Fluorescent Probe for Ratiometric Imaging of Endogenous Hypochlorite in Mitochondria. *Dye. Pigment.* **2020**, *181*, 108548. https://doi.org/10.1016/j.dyepig.2020.108548.

(313) Song, W.; Dong, B.; Lu, Y.; Li, Z.; Zhang, W.; Lin, W. Two-Photon Fluorescent Sensors for Visual Detection of Abnormal Superoxide Anion in Diabetes Mice. *Sensors Actuators, B Chem.* **2021**, *332*, 129537. https://doi.org/10.1016/j.snb.2021.129537.

(314) Masanta, G.; Heo, C. H.; Lim, C. S.; Bae, S. K.; Cho, B. R.; Kim, H. M. A Mitochondria-Localized Two-Photon Fluorescent Probe for Ratiometric Imaging of Hydrogen Peroxide in Live Tissue. *Chem. Commun.* **2012**, *48* (29), 3518–3520. https://doi.org/10.1039/c2cc00034b.

(315) Seo, E. W.; Han, J. H.; Heo, C. H.; Shin, J. H.; Kim, H. M.; Cho, B. R. A Small-Molecule Two-Photon Probe for Nitric Oxide in Living Tissues. *Chem. - A Eur. J.* **2012**, *18* (39), 12388–12394. https://doi.org/10.1002/chem.201201197.

(316) Ilina, K.; Henary, M. Cyanine Dyes Containing Quinoline Moieties: History, Synthesis, Optical Properties, and Applications. *Chem. – A Eur. J.* **2021**, *27* (13), 4230–4248. https://doi.org/10.1002/chem.202003697.

(317) Kundu, K.; Knight, S. F. F.; Willett, N.; Lee, S.; Taylor, W. R. R.; Murthy, N. Hydrocyanines: A Class of Fluorescent Sensors That Can Image Reactive Oxygen Species in Cell Culture, Tissue, and In Vivo. *Angew. Chemie Int. Ed.* **2009**, *48* (2), 299–303. https://doi.org/10.1002/anie.200804851.

(318) Pais, V. F. V. F.; Alcaide, M. M. M.; Lopez-Rodriguez, R.; Collado, D.; Najera, F.; Perez-Inestrosa, E.; Alvarez, E.; Lassaletta, J. M. J. M.; Fernandez, R.; Ros, A.; Pischel, U.; Lõpez-Rodríguez, R.; Collado, D.; Nájera, F.; Pérez-Inestrosa, E.; Álvarez, E.; Lassaletta, J. M. J. M.; Fernández, R.; Ros, A.; Pischel, U. Strongly Emissive and Photostable Four-Coordinate Organoboron N,C Chelates and Their Use in Fluorescence Microscopy. *Chem. - A Eur. J.* **2015**, *21* (43), 15369–15376. https://doi.org/10.1002/chem.201501626.

(319) Pais, V. F.; Ramírez-López, P.; Romero-Arenas, A.; Collado, D.; Pérez-inestrosa, E.; Fernández, R.; Lassaletta, J. M.; Ros, A.; Nájera, F.; Pérez-inestrosa, E.; Fernández, R.; Lassaletta, J. M.; Ros, A.; Pischel, U. Red-Emitting Tetracoordinate Organoboron Chelates: Synthesis, Photophysical Properties, and Fluorescence Microscopy. *J. Org. Chem.* **2016**, *81* (20), 9605–9611. https://doi.org/10.1021/acs.joc.6b01569.

(320) Marín, M.; Telo, J. P.; Collado, D.; Nájera, F.; Pérez-Inestrosa, E.; Pischel, U. Bis(Dioxaborine) Dyes with Variable π-Bridges: Towards Two-Photon Absorbing Fluorophores with Very High Brightness. *Chem. - A Eur. J.* **2018**, *24* (12), 2929–2935. https://doi.org/10.1002/chem.201704544.

(321) James, M. J.; O'Brien, P.; Taylor, R. J. K.; Unsworth, W. P. Synthesis of Spirocyclic Indolenines. *Chem. - A Eur. J.* **2015**, 2856–2881. https://doi.org/10.1002/chem.201503835.

(322) Liu, T.; Liu, X.; Spring, D. R.; Qian, X.; Cui, J.; Xu, Z. Quantitatively Mapping Cellular Viscosity with Detailed Organelle Information via a Designed PET Fluorescent Probe. *Sci. Rep.* **2014**, *4*, 1–7. https://doi.org/10.1038/srep05418.

(323) Stockert, J. C.; Horobin, R. W.; Colombo, L. L.; Blázquez-Castro, A. Tetrazolium Salts and Formazan Products in Cell Biology: Viability Assessment, Fluorescence Imaging, and Labeling Perspectives. *Acta Histochemica*. Elsevier GmbH April 1, 2018, pp 159–167. https://doi.org/10.1016/j.acthis.2018.02.005.

(324) Cadet, J.; Douki, T.; Ravanat, J. L. Oxidatively Generated Damage to Cellular DNA by UVB and UVA Radiation. *Photochemistry and Photobiology*. Blackwell Publishing Inc. January 1, 2015, pp 140–155. https://doi.org/10.1111/php.12368.

(325) Kumar, T. R.; Muralidhara. Induction of Oxidative Stress by Organic Hydroperoxides in Testis and Epididymal Sperm of Rats in Vivo. *J. Androl.* **2007**, *28* (1), 77–85. https://doi.org/10.2164/jandrol.106.000265.

(326) Benitez-Martin, C.; Guadix, J. A.; Pearson, J. R.; Najera, F.; Perez-Pomares, J. M.; Perez-Inestrosa, E. A Turn-on Two-Photon Fluorescent Probe for Detecting Lysosomal Hydroxyl Radicals in Living Cells. *Sensors Actuators, B Chem.* **2019**, *284*, 744–750. https://doi.org/10.1016/j.snb.2018.12.163.

(327) Flinck, M.; Kramer, S. H.; Pedersen, S. F. Roles of PH in Control of Cell Proliferation. *Acta Physiol.* **2018**, *223* (3), e13068. https://doi.org/10.1111/apha.13068.

(328) Lagadic-Gossmann, D.; Huc, L.; Lecureur, V. Alterations of Intracellular PH Homeostasis in Apoptosis: Origins and Roles. *Cell Death Differ.* **2004**, *11* (9), 953–961. https://doi.org/10.1038/sj.cdd.4401466.

(329) Barott, K. L.; Barron, M. E.; Tresguerres, M. Identification of a Molecular PH Sensor in Coral. *Proc. R. Soc. B Biol. Sci.* **2017**, *284* (1866), 20171769. https://doi.org/10.1098/rspb.2017.1769.

(330) Nogueira, L.; Shiah, A. A.; Gandra, P. G.; Hogan, M. C. Ca 2+ -Pumping Impairment during Repetitive Fatiguing Contractions in Single Myofibers: Role of Cross-Bridge Cycling. *Am. J. Physiol. Integr. Comp. Physiol.* **2013**, *305* (2), R118–R125.

https://doi.org/10.1152/ajpregu.00178.2013.

(331) Delpiano, L.; Thomas, J. J.; Yates, A. R.; Rice, S. J.; Gray, M. A.; Saint-Criq, V. Esomeprazole Increases Airway Surface Liquid PH in Primary Cystic Fibrosis Epithelial Cells. *Front. Pharmacol.* **2018**, *9*, 1462. https://doi.org/10.3389/fphar.2018.01462.

(332) Casey, J. R.; Grinstein, S.; Orlowski, J. Sensors and Regulators of Intracellular PH. *Nat. Rev. Mol. Cell Biol.* **2010**, *11* (1), 50–61. https://doi.org/10.1038/nrm2820.

(333) Fang, B.; Wang, D.; Huang, M.; Yu, G.; Li, H. Hypothesis on the Relationship Between the Change in Intracellular PH and Incidence of Sporadic Alzheimer's Disease or Vascular Dementia. *Int. J. Neurosci.* **2010**, *120* (9), 591–595. https://doi.org/10.3109/00207454.2010.505353.

(334) Chen, J. H.; Xu, W.; Sheppard, D. N. Altering Intracellular PH Reveals the Kinetic Basis of Intraburst Gating in the CFTR Cl− Channel. *J. Physiol.* **2017**, *595* (4), 1059–1076. https://doi.org/10.1113/JP273205.

(335) Swietach, P.; Wigfield, S.; Cobden, P.; Supuran, C. T.; Harris, A. L.; Vaughan-Jones, R. D. Tumor-Associated Carbonic Anhydrase 9 Spatially Coordinates Intracellular PH in Three-Dimensional Multicellular Growths. *J. Biol. Chem.* **2008**, *283* (29), 20473–20483. https://doi.org/10.1074/jbc.M801330200.

(336) Fukuda, T.; Ewan, L.; Bauer, M.; Mattaliano, R. J.; Zaal, K.; Ralston, E.; Plotz, P. H.; Raben, N. Dysfunction of Endocytic and Autophagic Pathways in a Lysosomal Storage Disease. *Ann. Neurol.* **2006**, *59* (4), 700–708. https://doi.org/10.1002/ana.20807.

(337) Taylor, J. S.; Deutsch, C. Fluorinated Alpha-Methylamino Acids as 19F NMR Indicators of Intracellular PH. *Biophys. J.* **1983**, *43* (3), 261–267. https://doi.org/10.1016/S0006-3495(83)84349-5.

(338) Caner, T.; Abdulnour-Nakhoul, S.; Brown, K.; Islam, M. T.; Hamm, L. L.; Nakhoul, N. L. Mechanisms of Ammonia and Ammonium Transport by Rhesus-Associated Glycoproteins. *Am. J. Physiol. Physiol.* **2015**, *309* (11), C747–C758. https://doi.org/10.1152/ajpcell.00085.2015.

(339) Han, J.; Burgess, K. Fluorescent Indicators for Intracellular PH. *Chem. Rev.* **2010**, *110* (5), 2709–2728. https://doi.org/10.1021/cr900249z.

(340) Li, X.; Gao, X.; Shi, W.; Ma, H. Design Strategies for Water-Soluble Small Molecular Chromogenic and Fluorogenic Probes. *Chem. Rev.* **2014**, *114* (1), 590–659. https://doi.org/10.1021/cr300508p.

(341) Hou, J.-T.; Ren, W. X.; Li, K.; Seo, J.; Sharma, A.; Yu, X.-Q.; Kim, J. S.; Kikuchi, K.; DeBerardinis, R. J.; Gao, J.; Tang, B. Z.; Tang, B. Z. Fluorescent Bioimaging of PH: From Design to Applications. *Chem. Soc. Rev.* **2017**, *46* (8), 2076–2090. https://doi.org/10.1039/C6CS00719H.

(342) Ning, P.; Hou, L.; Feng, Y.; Xu, G.; Bai, Y.; Yu, H.; Meng, X. Real-Time Visualization of Autophagy by Monitoring the Fluctuation of Lysosomal PH with a Ratiometric Two-Photon Fluorescent Probe. *Chem. Commun.* **2019**, *55* (12), 1782–1785. https://doi.org/10.1039/C8CC09517E.

(343) Jiang, A.; Chen, G.; Xu, J.; Liu, Y.; Zhao, G.; Liu, Z.; Chen, T.; Li, Y.; James, T. D. Ratiometric Two-Photon Fluorescent Probe for: In Situ Imaging of Carboxylesterase (CE)-Mediated Mitochondrial Acidification during Medication. *Chem. Commun.* **2019**, *55* (76), 11358–11361. https://doi.org/10.1039/c9cc05759e.

(344) Zhang, T.; Xu, D.; Poon, C. Y.; Wang, X.; Bolze, F.; Li, H. W.; Wong, M. S. Tuning the PKa of Two-Photon Bis-Chromophoric Probes for Ratiometric Fluorescence Imaging of Acidic PH in Lysosomes. *Talanta* **2019**, *202*, 34–41. https://doi.org/10.1016/j.talanta.2019.04.042.

(345) Lu, X.; Zhang, G.; Li, D.; Tian, X.; Ma, W.; Li, S.; Zhang, Q.; Zhou, H.; Wu, J.; Tian, Y. Thiophene Aromatic Amine Derivatives with Two-Photon Activities as Probes for the Detection of Picric Acid and PH. *Dye. Pigment.* **2019**, *170*, 107641. https://doi.org/10.1016/j.dyepig.2019.107641.

(346) Wang, F.; Liu, D.; Shen, Y.; Liu, J.; Li, D.; Tian, X.; Zhang, Q.; Wu, J.; Li, S.; Tian, Y. A Two-Photon Mitochondria-Targeted Fluorescent Probe for the Detection of PH Fluctuation in Tumor and Living Cells. *Dye. Pigment.* **2019**, *166*, 92–97. https://doi.org/10.1016/j.dyepig.2019.03.033.

(347) Jiang, X.; Liu, Z.; Yang, Y.; Li, H.; Qi, X.; Ren, W. X.; Deng, M.; Lü, M.; Wu, J.; Liang, S. A Mitochondria-Targeted Two-Photon Fluorescent Probe for Sensing and Imaging PH Changes in Living Cells. *Spectrochim. Acta - Part A Mol. Biomol. Spectrosc.* **2020**, *224*, 117435. https://doi.org/10.1016/j.saa.2019.117435.

(348) Kim, H. M.; Cho, B. R. Small-Molecule Two-Photon Probes for Bioimaging Applications. *Chem. Rev.* **2015**, *115* (11), 5014–5055. https://doi.org/10.1021/cr5004425.

(349) Chen, S.; Zhao, M.; Su, J.; Zhang, Q.; Tian, X.; Li, S.; Zhou, H.; Wu, J.; Tian, Y. Two Novel Two-Photon Excited Fluorescent PH Probes Based on the A-π-D-π-A System for Intracellular PH Mapping. *Dye. Pigment.* **2017**, *136*, 807–816. https://doi.org/10.1016/j.dyepig.2016.09.020.

(350) Dong, B.; Song, X.; Kong, X.; Wang, C.; Zhang, N.; Lin, W. A Tumor-Targeting and Lysosome-Specific Two-Photon Fluorescent Probe for Imaging PH Changes in Living Cells. *J. Mater. Chem. B* **2017**, *5* (5), 988–995. https://doi.org/10.1039/c6tb02957d.

(351) Luo, W.; Jiang, H.; Tang, X.; Liu, W. A Reversible Ratiometric Two-Photon Lysosome-Targeted Probe for Real-Time Monitoring of PH Changes in Living Cells. *J. Mater. Chem. B* **2017**, *5* (24), 4768–4773. https://doi.org/10.1039/c7tb00838d.

(352) Xu, D.; Li, Y.; Poon, C. Y.; Chan, H. N.; Li, H. W.; Wong, M. S. A Zero Cross-Talk Ratiometric Two-Photon Probe for Imaging of Acid PH in Living Cells and Tissues and Early Detection of Tumor in Mouse Model. *Anal. Chem.* **2018**, *90* (15), 8800–8806. https://doi.org/10.1021/acs.analchem.8b00520.

(353) Ma, J.; Li, W.; Li, J.; Shi, R.; Yin, G.; Wang, R. A Small Molecular PH-Dependent Fluorescent Probe for Cancer Cell Imaging in Living Cell. *Talanta* **2018**, *182*, 464–469. https://doi.org/10.1016/J.TALANTA.2018.01.088.

(354) Han, Z.; Tan, J.; Wei, T.; Zhang, Y.; Xiao, H.; Xu, L.; He, B. Two Novel Two-Photon Fluorescent Probes for Low PH Values and Cell Imaging Based on Spirobifluorene Motif. *Sensors Actuators, B Chem.* **2018**, *255*, 2290–2297. https://doi.org/10.1016/j.snb.2017.09.053.

(355) Dou, Y.; Kenry, K.; Liu, J.; Zhang, F.; Cai, C.; Zhu, Q. 2-Styrylquinoline-Based Two-Photon AIEgens for Dual Monitoring of PH and Viscosity in Living Cells. *J. Mater. Chem. B* **2019**, *7* (48), 7771–7775. https://doi.org/10.1039/C9TB02036E.

(356) Rosenberg, L. S.; Simons, J.; Schulmans, S. G. Determination of PKa Values of N-Heterocyclic Bases by Fluorescence Spectrophotometry. *Talanta* **1979**, *26* (9), 867–871. https://doi.org/10.1016/0039-9140(79)80267-2.

(357) Berezin, M. Y.; Kao, J.; Achilefu, S. PH-Dependent Optical Properties of Synthetic

Fluorescent Imidazoles. *Chem. - A Eur. J.* **2009**, *15* (14), 3560–3566. https://doi.org/10.1002/chem.200801784.

(358) Yanai, T.; Tew, D. P.; Handy, N. C. A New Hybrid Exchange-Correlation Functional Using the Coulomb-Attenuating Method (CAM-B3LYP). *Chem. Phys. Lett.* **2004**, *393* (1–3), 51–57. https://doi.org/10.1016/j.cplett.2004.06.011.

(359) Tomasi, J.; Mennucci, B.; Cammi, R. Quantum Mechanical Continuum Solvation Models. *Chem. Rev.* **2005**, *105* (8), 2999–3094. https://doi.org/10.1021/cr9904009.

(360) Belletête, M.; Brisse, F.; Durocher, G.; Gravel, D.; Héroux, A.; Popowycz, A. Electronic and Molecular Structure of 2-Phenyl-3,3-Dimethyl-3H-Indole Molecular Fluorescence Probe and the Molecular Structure of Its Dimer. *J. Mol. Struct.* **1993**, *297*, 63–80. https://doi.org/10.1016/0022-2860(93)80160-W.

(361) Ohkuma, S.; Moriyama, Y.; Takano, T. Identification and Characterization of a Proton Pump on Lysosomes by Fluorescein-Isothiocyanate-Dextran Fluorescence. *Proc. Natl. Acad. Sci. U. S. A.* **1982**, *79* (9), 2758–2762. https://doi.org/10.1073/pnas.79.9.2758.

(362) Richardson, D. S.; Gregor, C.; Winter, F. R.; Urban, N. T.; Sahl, S. J.; Willig, K. I.; Hell, S. W. SRpHi Ratiometric PH Biosensors for Super-Resolution Microscopy. *Nat. Commun.* **2017**, *8* (1), 577. https://doi.org/10.1038/s41467-017-00606-4.

(363) Benitez-Martin, C.; Guadix, J. A.; Pearson, J. R.; Najera, F.; Perez-Pomares, J. M.; Perez-Inestrosa, E. Indolenine-Based Derivatives as Customizable Two-Photon Fluorescent Probes for PH Bioimaging in Living Cells. *ACS Sensors* **2020**, *5* (4), 1068–1074. https://doi.org/10.1021/acssensors.9b02590.

(364) Schrader, M.; Godinho, L. F.; Costello, J. L.; Islinger, M. The Different Facets of Organelle Interplay-An Overview of Organelle Interactions. *Front. Cell Dev. Biol.* **2015**, *3*, 56. https://doi.org/10.3389/fcell.2015.00056.

(365) Murley, A.; Nunnari, J. The Emerging Network of Mitochondria-Organelle Contacts. *Mol. Cell* **2016**, *61* (5), 648–653. https://doi.org/10.1016/j.molcel.2016.01.031.

(366) Burté, F.; Carelli, V.; Chinnery, P. F.; Yu-Wai-Man, P. Disturbed Mitochondrial Dynamics and Neurodegenerative Disorders. *Nat. Rev. Neurol.* **2015**, *11* (1), 11–24. https://doi.org/10.1038/nrneurol.2014.228.

(367) Mc Donald, J. M.; Krainc, D. Lysosomal Proteins as a Therapeutic Target in Neurodegeneration. *Annu. Rev. Med.* **2017**, *68*, 445–458. https://doi.org/10.1146/annurev-med-050715-104432.

(368) Plotegher, N.; Duchen, M. R. Mitochondrial Dysfunction and Neurodegeneration in Lysosomal Storage Disorders. *Trends Mol. Med.* **2017**, *23* (2), 116–134. https://doi.org/10.1016/j.molmed.2016.12.003.

(369) Wong, Y. C.; Kim, S.; Peng, W.; Krainc, D. Regulation and Function of Mitochondria–Lysosome Membrane Contact Sites in Cellular Homeostasis. *Trends Cell Biol.* **2019**, *29* (6), 500–513. https://doi.org/10.1016/j.tcb.2019.02.004.

(370) Bode, W.; Huber, R. Structural Basis of the Endoproteinase-Protein Inhibitor Interaction. *Biochim. Biophys. Acta - Protein Struct. Mol. Enzymol.* **2000**, *1477* (1–2), 241–252. https://doi.org/10.1016/S0167-4838(99)00276-9.

(371) Turk, V.; Turk, B.; Turk, D. Lysosomal Cysteine Proteases: Facts and Opportunities. *EMBO J.* **2001**, *20* (17), 4629–4633. https://doi.org/10.1093/emboj/20.17.4629.

(372) Zorova, L. D.; Popkov, V. A.; Plotnikov, E. Y.; Silachev, D. N.; Pevzner, I. B.; Jankauskas, S. S.; Babenko, V. A.; Zorov, S. D.; Balakireva, A. V.; Juhaszova, M.; Sollott, S. J.; Zorov, D. B. Mitochondrial Membrane Potential. *Anal. Biochem.* **2018**, *552*, 50–59. https://doi.org/10.1016/j.ab.2017.07.009.

(373) Mazat, J. P.; Devin, A.; Ransac, S. Modelling Mitochondrial ROS Production by the Respiratory Chain. *Cell. Mol. Life Sci.* **2020**, *77* (3), 455–465. https://doi.org/10.1007/s00018-019-03381-1.

(374) Coppotelli, G.; Ross, J. M. Mitochondria in Ageing and Diseases: The Super Trouper of the Cell. *Int. J. Mol. Sci.* **2016**, *17* (5), 711. https://doi.org/10.3390/ijms17050711.

(375) Luo, Y.; Ma, J.; Lu, W. The Significance of Mitochondrial Dysfunction in Cancer. *Int. J. Mol. Sci.* **2020**, *21* (16), 1–24. https://doi.org/10.3390/ijms21165598.

(376) Gao, J.; Wang, L.; Liu, J.; Xie, F.; Su, B.; Wang, X. Abnormalities of Mitochondrial Dynamics in Neurodegenerative Diseases. *Antioxidants* **2017**, *6* (2), 25. https://doi.org/10.3390/antiox6020025.

(377) Levine, B.; Klionsky, D. J. Development by Self-Digestion: Molecular Mechanisms and Biological Functions of Autophagy. *Dev. Cell* **2004**, *6* (4), 463–477. https://doi.org/10.1016/S1534-5807(04)00099-1.

(378) Mizushima, N.; Yoshimori, T.; Levine, B. Methods in Mammalian Autophagy Research. *Cell* **2010**, *140* (3), 313–326. https://doi.org/10.1016/j.cell.2010.01.028.

(379) Kanki, T.; Furukawa, K.; Yamashita, S. ichi. Mitophagy in Yeast: Molecular Mechanisms and Physiological Role. *Biochim. Biophys. Acta - Mol. Cell Res.* **2015**, *1853* (10), 2756–2765. https://doi.org/10.1016/j.bbamcr.2015.01.005.

(380) Stotland, A.; Gottlieb, R. A. Mitochondrial Quality Control: Easy Come, Easy Go. *Biochim. Biophys. Acta - Mol. Cell Res.* **2015**, *1853* (10), 2802–2811. https://doi.org/10.1016/j.bbamcr.2014.12.041.

(381) Han, Y.; Li, M.; Qiu, F.; Zhang, M.; Zhang, Y. H. Cell-Permeable Organic Fluorescent Probes for Live-Cell Long-Term Super-Resolution Imaging Reveal Lysosome-Mitochondrion Interactions. *Nat. Commun.* **2017**, *8*, 1–9. https://doi.org/10.1038/s41467-017-01503-6.

(382) Zheng, X.; Zhu, W.; Ni, F.; Ai, H.; Gong, S.; Zhou, X.; Sessler, J. L.; Yang, C. Simultaneous Dual-Colour Tracking Lipid Droplets and Lysosomes Dynamics Using a Fluorescent Probe. *Chem. Sci.* **2019**, *10* (8), 2342–2348. https://doi.org/10.1039/C8SC04462G.

(383) Chen, W.; Han, J.; She, J.; Wang, F.; Zhu, L.; Yu, R. Q.; Jiang, J. H. Simultaneous Imaging of Lysosomal and Mitochondrial Viscosity during Mitophagy Using Molecular Rotors with Dual-Color Emission. *Chem. Commun.* **2020**, *56*, 7797–7800. https://doi.org/10.1039/d0cc00868k.

(384) Lee, M. H.; Han, J. H.; Lee, J. H.; Park, N.; Kumar, R.; Kang, C.; Kim, J. S. Two-Color Probe to Monitor a Wide Range of PH Values in Cells. *Angew. Chemie Int. Ed.* **2013**, *52* (24), 6206–6209. https://doi.org/10.1002/anie.201301894.

(385) Liu, Y.; Zhou, J.; Wang, L.; Hu, X.; Liu, X.; Liu, M.; Cao, Z.; Shangguan, D.; Tan, W. A Cyanine Dye to Probe Mitophagy: Simultaneous Detection of Mitochondria and Autolysosomes in Live Cells. *J. Am. Chem. Soc.* **2016**, *138* (38), 12368–12374. https://doi.org/10.1021/jacs.6b04048.

(386) Hou, L.; Ning, P.; Feng, Y.; Ding, Y.; Bai, L.; Li, L.; Yu, H.; Meng, X. Two-Photon Fluorescent Probe for Monitoring Autophagy via Fluorescence Lifetime Imaging. *Anal. Chem.* **2018**, *90*

(12), 7122–7126. https://doi.org/10.1021/acs.analchem.8b01631.

(387) Jiménez-Sánchez, A.; Lei, E. K.; Kelley, S. O. A Multifunctional Chemical Probe for the Measurement of Local Micropolarity and Microviscosity in Mitochondria. *Angew. Chemie Int. Ed.* **2018**, *57* (29), 8891–8895. https://doi.org/10.1002/anie.201802796.

(388) Liu, Y.; Teng, L.; Chen, L.; Ma, H.; Liu, H. W.; Zhang, X. B. Engineering of a Near-Infrared Fluorescent Probe for Real-Time Simultaneous Visualization of Intracellular Hypoxia and Induced Mitophagy. *Chem. Sci.* **2018**, *9* (24), 5347–5353. https://doi.org/10.1039/c8sc01684d.

(389) Zou, Z.; Yan, Q.; Ai, S.; Qi, P.; Yang, H.; Zhang, Y.; Qing, Z.; Zhang, L.; Feng, F.; Yang, R. Real-Time Visualizing Mitophagy-Specific Viscosity Dynamic by Mitochondria-Anchored Molecular Rotor. *Anal. Chem.* **2019**, *91* (13), 8574–8581. https://doi.org/10.1021/acs.analchem.9b01861.

(390) Li, X.; Hu, Y.; Li, X.; Ma, H. Mitochondria-Immobilized Near-Infrared Ratiometric Fluorescent PH Probe to Evaluate Cellular Mitophagy. *Anal. Chem.* **2019**, *91* (17), 11409–11416. https://doi.org/10.1021/acs.analchem.9b02782.

(391) Rao, Q.; Yang, M.; Liu, G.; Wang, J.; Bu, Y.; Zhang, J.; Zhu, X.; Chen, G.; Zhu, W.; Zhou, H. Real-Time Monitoring Apoptosis and Autophagy among Multiple Organelles by Adjusting the Slight Structure. *Sensors Actuators, B Chem.* **2020**, *302*, 127169. https://doi.org/10.1016/j.snb.2019.127169.

(392) Kim, H. M.; Cho, B. R. Small-Molecule Two-Photon Probes for Bioimaging Applications. *Chem. Rev.* **2015**, *115* (11), 5014–5055. https://doi.org/10.1021/cr5004425.

(393) Perelman, A.; Wachtel, C.; Cohen, M.; Haupt, S.; Shapiro, H.; Tzur, A. JC-1: Alternative Excitation Wavelengths Facilitate Mitochondrial Membrane Potential Cytometry. *Cell Death Dis.* **2012**, *3* (11), 430. https://doi.org/10.1038/cddis.2012.171.

(394) Terenziani, F.; Katan, C.; Badaeva, E.; Tretiak, S.; Blanchard-Desce, M. Enhanced Two-Photon Absorption of Organic Chromophores: Theoretical and Experimental Assessments. *Adv. Mater.* **2008**, *20* (24), 4641–4678. https://doi.org/10.1002/adma.200800402.

(395) Skloot, R. Henrietta's Dance https://pages.jh.edu/jhumag/0400web/01.html (accessed Jun 2, 2021).

(396) R&D Systems. Flow Cytometry Protocol for Analysis of Cell Viability using Propidium Iodide: R&D Systems https://www.rndsystems.com/resources/protocols/flow-cytometry-protocol-analysis-cell-viability-using-propidium-iodide (accessed Jun 2, 2021).

(397) Chao, X.; Qi, Y.; Zhang, Y. Highly Photostable Fluorescent Tracker with PH-Insensitivity for Long-Term Imaging of Lysosomal Dynamics in Live Cells. *ACS Sensors* **2021**, *6*, 786–796. https://doi.org/10.1021/acssensors.0c01588.

(398) Niu, L. Q.; Huang, J.; Yan, Z. J.; Men, Y. H.; Luo, Y.; Zhou, X. M.; Wang, J. M.; Wang, J. H. Fluorescence Detection of Intracellular PH Changes in the Mitochondria-Associated Process of Mitophagy Using a Hemicyanine-Based Fluorescent Probe. *Spectrochim. Acta - Part A Mol. Biomol. Spectrosc.* **2019**, *207*, 123–131. https://doi.org/10.1016/j.saa.2018.09.015.

(399) Fan, L.; Ge, J.; Zan, Q.; Wang, X.; Wang, S.; Zhang, Y.; Dong, W.; Shuang, S.; Dong, C. Real-Time Tracking the Mitochondrial Membrane Potential by a Mitochondria-Lysosomes Migration Fluorescent Probe with NIR-Emissive AIE Characteristics. *Sensors Actuators, B Chem.* **2021**, *327*, 128929. https://doi.org/10.1016/j.snb.2020.128929.

(400) Casey, J. R.; Grinstein, S.; Orlowski, J. Sensors and Regulators of Intracellular PH. *Nat. Rev.*

Mol. Cell Biol. **2010**, *11* (1), 50–61. https://doi.org/10.1038/nrm2820.

(401) Reers, M.; Smith, T. W.; Chen, L. B. J-Aggregate Formation of a Carbocyanine as a Quantitative Fluorescent Indicator of Membrane Potential. *Biochemistry* **1991**, *30* (18), 4480–4486. https://doi.org/10.1021/bi00232a015.

(402) Perelman, A.; Wachtel, C.; Cohen, M.; Haupt, S.; Shapiro, H.; Tzur, A. JC-1: Alternative Excitation Wavelengths Facilitate Mitochondrial Membrane Potential Cytometry. *Cell Death Dis.* **2012**, *3* (11), 430. https://doi.org/10.1038/cddis.2012.171.

(403) Irie, M.; Fukaminato, T.; Matsuda, K.; Kobatake, S. Photochromism of Diarylethene Molecules and Crystals: Memories, Switches, and Actuators. *Chem. Rev.* **2014**, *114* (24), 12174–12277. https://doi.org/10.1021/cr500249p.

(404) Brown, G. H. *Photochromism*; Wiley: New York, 1971.

(405) Finch, C. A. *Photochemistry and Polymeric Systems*; Kelly, J. M., McArdle, C. B., de Maunder, M. J., Eds.; RSC, 1994; Vol. 35. https://doi.org/10.1002/pi.1994.210350212.

(406) Irie, M.; Mohri, M. Thermally Irreversible Photochromic Systems. Reversible Photocyclization of Diarylethene Derivatives. *J. Org. Chem.* **1988**, *53* (4), 803–808. https://doi.org/10.1021/jo00239a022.

(407) Nakamura, S.; Irie, M. Thermally Irreversible Photochromic Systems. A Theoretical Study. *J. Org. Chem.* **1988**, *53* (26), 6136–6138. https://doi.org/10.1021/jo00261a035.

(408) Bälter, M.; Li, S.; Nilsson, J. R.; Andréasson, J.; Pischel, U. An All-Photonic Molecule-Based Parity Generator/Checker for Error Detection in Data Transmission. *J. Am. Chem. Soc.* **2013**, *135* (28), 10230–10233. https://doi.org/10.1021/ja403828z.

(409) Valeur, B.; Berberan-Santos, M. N. *Molecular Fluorescence: Principles and Applications*, 2nd editio.; GmbH, W.-V. V., Ed.; 2001.

(410) Preus, S. a|e - UV-Vis-IR Spectral Software http://www.fluortools.com/ (accessed Jun 8, 2021).

(411) Heller, H. G.; Langan, J. R. Photochromic Heterocyclic Fulgides. Part 3.(1) The Use of (E)-a-(2.5- Dimethyl-3-f Urylethylidene) (Isopropylidene)Succinic Anhydride as a Simple Convenient Chemical Actinometer. **1981**, 341–343.

(412) Glaze, A. P.; Heller, H. G.; Whittall, J. Photochromic Heterocyclic Fulgides. Part 7. (E)-Adamantylidene-[1-(2,5- Dimethyl-3-Furyl)Ethylidene]Succinic Anhydride and Derivatives: Model Photochromic Compounds for Optical Recording Media. *J. Chem. Soc. Perkin Trans. 2* **1992**, No. 4, 591–594. https://doi.org/10.1039/p29920000591.

(413) Boule, P.; Pilichowski, J. F. Comments about the Use of AberchromeTM 540 in Chemical Actinometry. *J. Photochem. Photobiol. A Chem.* **1993**, *71* (1), 51–53. https://doi.org/10.1016/1010-6030(93)87008-B.

(414) Benitez-Martin, C.; Li, S.; Dominguez-Alfaro, A.; Najera, F.; Pérez-Inestrosa, E.; Pischel, U.; Andréasson, J. Toward Two-Photon Absorbing Dyes with Unusually Potentiated Nonlinear Fluorescence Response. *J. Am. Chem. Soc.* **2020**, *142* (35), 14854–14858. https://doi.org/10.1021/JACS.0C07377.

(415) Rumi, M.; Perry, J. W. Two-Photon Absorption: An Overview of Measurements and Principles. *Adv. Opt. Photonics* **2010**, *2* (4), 451. https://doi.org/10.1364/aop.2.000451.

(416) Frisch, M. J.; Trucks, G. W.; Schlegel, H. B.; Scuseria, G. E.; Robb, M. A.; Cheeseman, J. R.; Scalmani, G.; Barone, V.; Petersson, G. A.; Nakatsuji, H.; Li, X.; Caricato, M.; Marenich, A. V;

Bloino, J.; Janesko, B. G.; Gomperts, R.; Mennucci, B.; Hratchian, H. P.; Ortiz, J. V; Izmaylov, A. F.; Sonnenberg, J. L.; Williams-Young, D.; Ding, F.; Lipparini, F.; Egidi, F.; Goings, J.; Peng, B.; Petrone, A.; Henderson, T.; Ranasinghe, D.; Zakrzewski, V. G.; Gao, J.; Rega, N.; Zheng, G.; Liang, W.; Hada, M.; Ehara, M.; Toyota, K.; Fukuda, R.; Hasegawa, J.; Ishida, M.; Nakajima, T.; Honda, Y.; Kitao, O.; Nakai, H.; Vreven, T.; Throssell, K.; Montgomery Jr., J. A.; Peralta, J. E.; Ogliaro, F.; Bearpark, M. J.; Heyd, J. J.; Brothers, E. N.; Kudin, K. N.; Staroverov, V. N.; Keith, T. A.; Kobayashi, R.; Normand, J.; Raghavachari, K.; Rendell, A. P.; Burant, J. C.; Iyengar, S. S.; Tomasi, J.; Cossi, M.; Millam, J. M.; Klene, M.; Adamo, C.; Cammi, R.; Ochterski, J. W.; Martin, R. L.; Morokuma, K.; Farkas, O.; Foresman, J. B.; Fox, D. J. Gaussian16 Revision A.03. 2016.

(417) Yanai, T.; Tew, D. P.; Handy, N. C. A New Hybrid Exchange-Correlation Functional Using the Coulomb-Attenuating Method (CAM-B3LYP). *Chem. Phys. Lett.* **2004**, *393* (1–3), 51–57. https://doi.org/10.1016/j.cplett.2004.06.011.

(418) Tomasi, J.; Mennucci, B.; Cammi, R. Quantum Mechanical Continuum Solvation Models. *Chem. Rev.* **2005**, *105* (8), 2999–3094. https://doi.org/10.1021/cr9904009.

(419) Sumanont, Y.; Murakami, Y.; Tohda, M.; Vajragupta, O.; Matsumoto, K.; Watanabe, H. *Evaluation of the Nitric Oxide Radical Scavenging Activity of Manganese Complexes of Curcumin and Its Derivative*; 2004; Vol. 27.

(420) Qiu, L.-Q.; Lai, W. S.; Stumpo, D. J.; Blackshear, P. J. Mouse Embryonic Fibroblast Cell Culture and Stimulation. *Bio-protocol* **2016**, *6* (13). https://doi.org/10.21769/BioProtoc.1859.

(421) Schindelin, J.; Arganda-Carreras, I.; Frise, E.; Kaynig, V.; Longair, M.; Pietzsch, T.; Preibisch, S.; Rueden, C.; Saalfeld, S.; Schmid, B.; Tinevez, J. Y.; White, D. J.; Hartenstein, V.; Eliceiri, K.; Tomancak, P.; Cardona, A. Fiji: An Open-Source Platform for Biological-Image Analysis. *Nature Methods*. Nature Publishing Group July 2012, pp 676–682. https://doi.org/10.1038/nmeth.2019.

(422) Rueden, C. T.; Schindelin, J.; Hiner, M. C.; DeZonia, B. E.; Walter, A. E.; Arena, E. T.; Eliceiri, K. W. ImageJ2: ImageJ for the next Generation of Scientific Image Data. *BMC Bioinformatics* **2017**, *18* (1), 529. https://doi.org/10.1186/s12859-017-1934-z.

Appendix I

NMR spectra

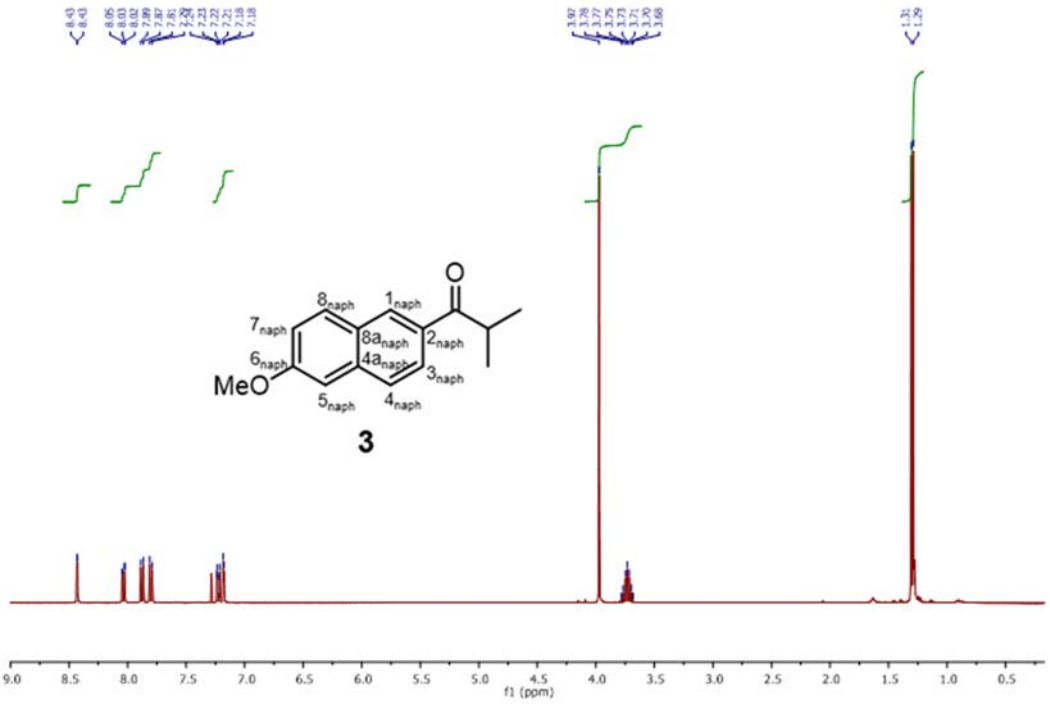

^{1}H-NMR (400 MHz) spectrum of compound **3** in $CDCl_3$

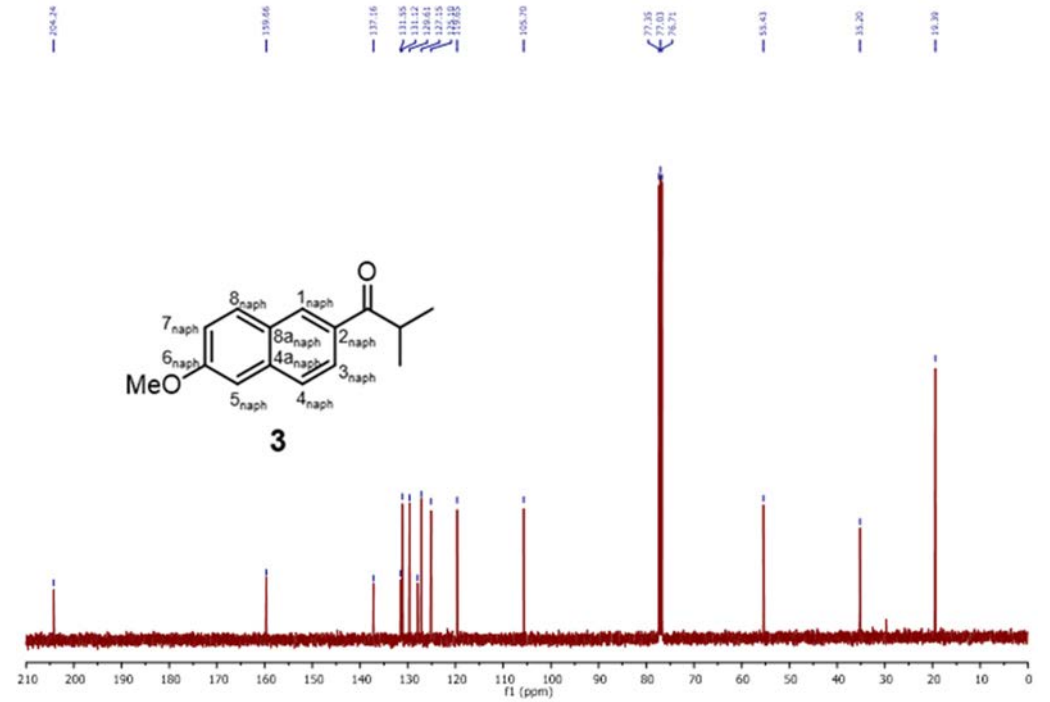

^{13}C-NMR (101 MHz) spectrum of compound **3** in $CDCl_3$

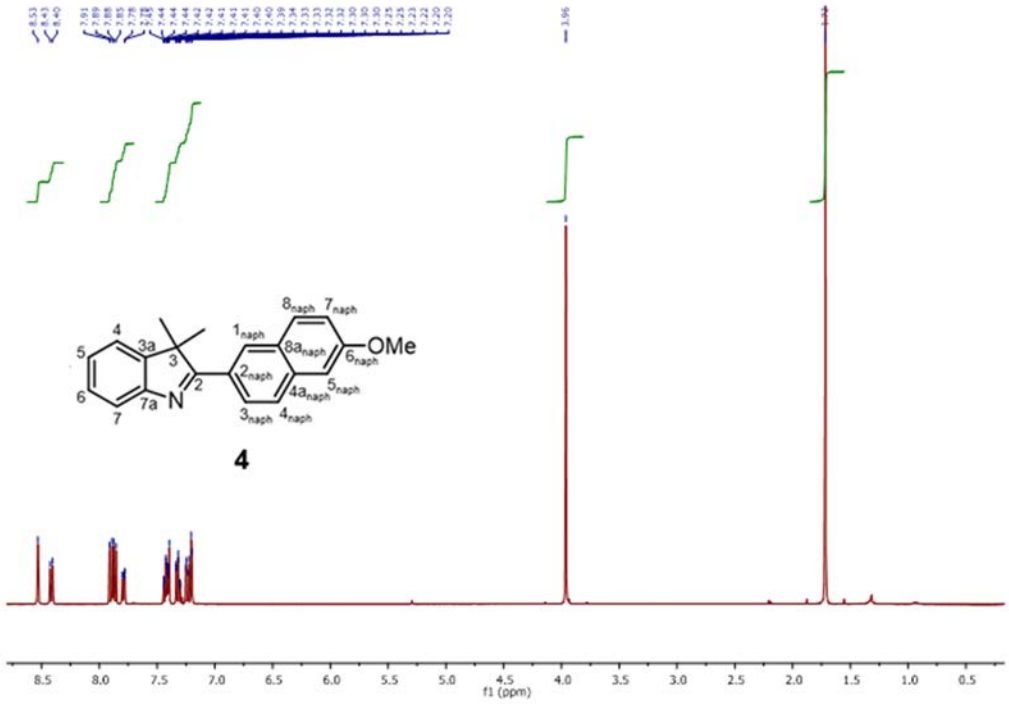

^{1}H-NMR (400 MHz) spectrum of compound **4** in $CDCl_3$.

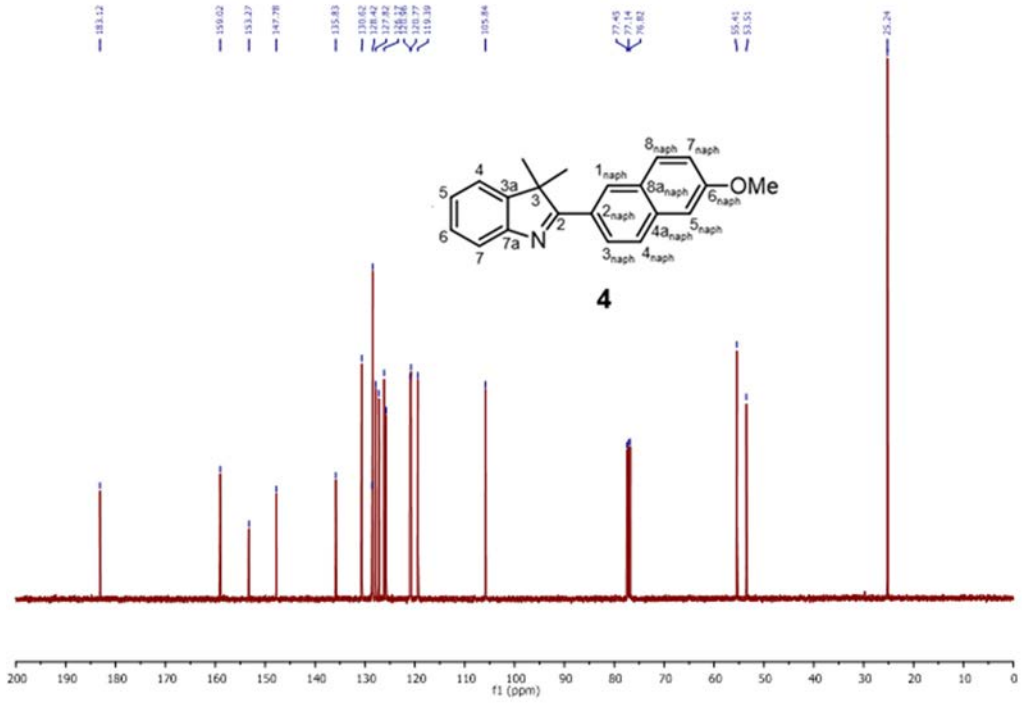

^{13}C-NMR (101 MHz) spectrum of compound **4** in $CDCl_3$

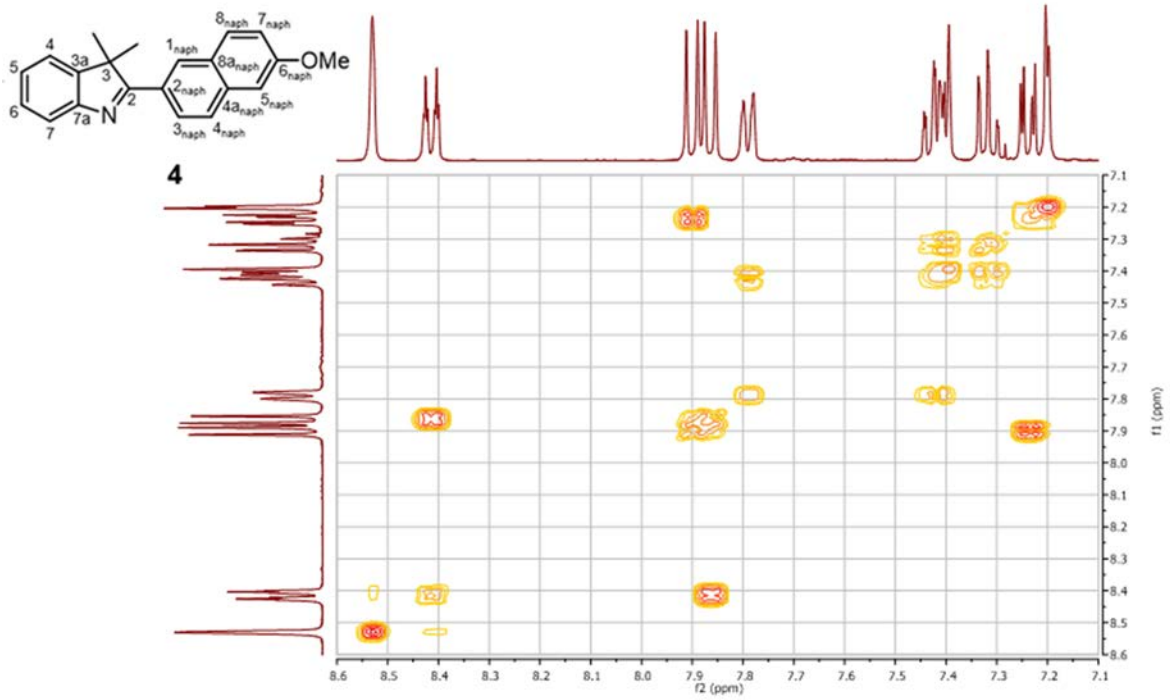

^{1}H-^{1}H COSY (400 MHz) spectrum of compound **4** in $CDCl_3$ (aromatic region)

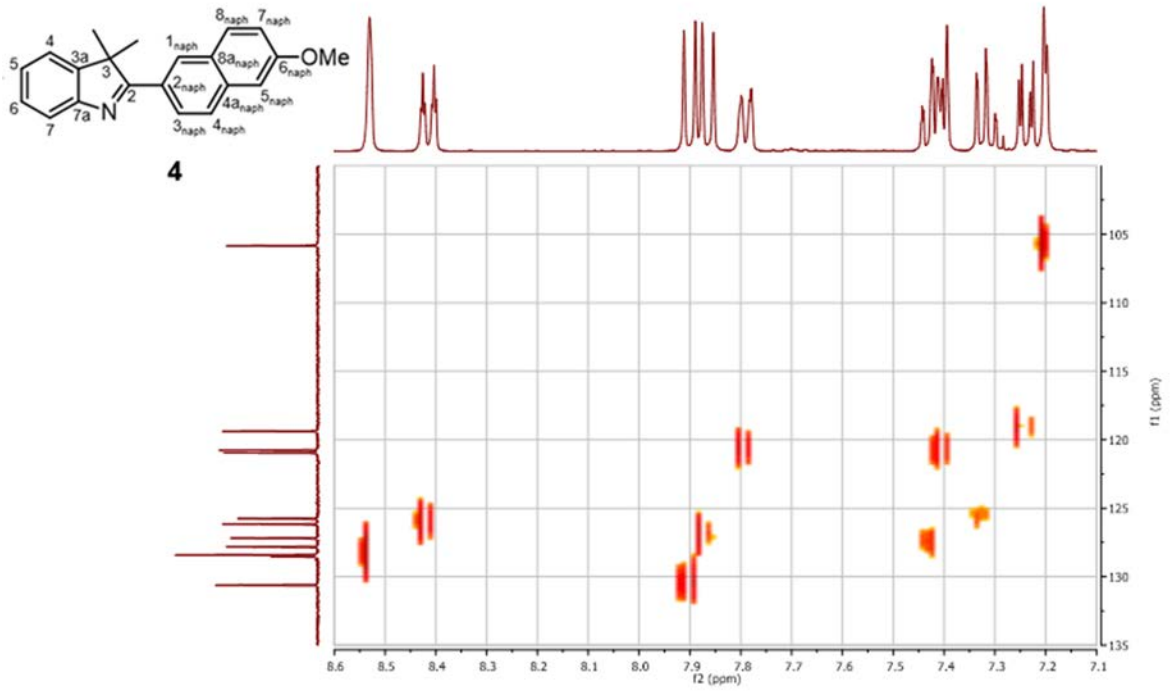

^{1}H-^{13}C HSQC spectrum of compound **4** in $CDCl_3$ (aromatic region)

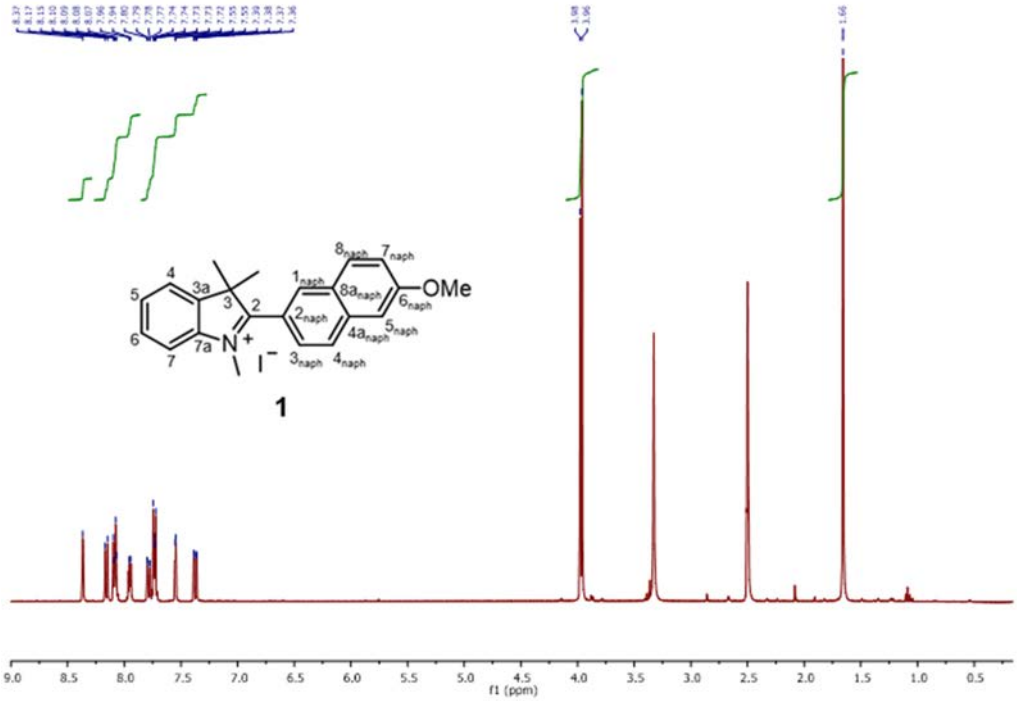

^{1}H-NMR (400 MHz) spectrum of compound **1** in DMSO-d_6

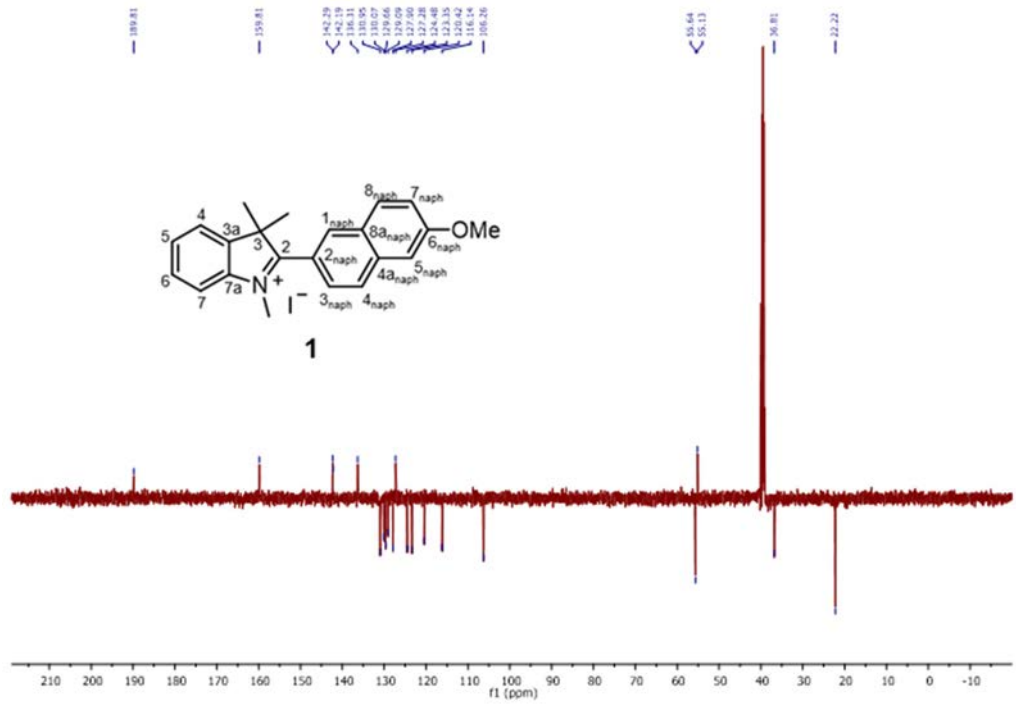

^{13}C-NMR SEFT (101 MHz) spectrum of compound **1** in DMSO-d_6

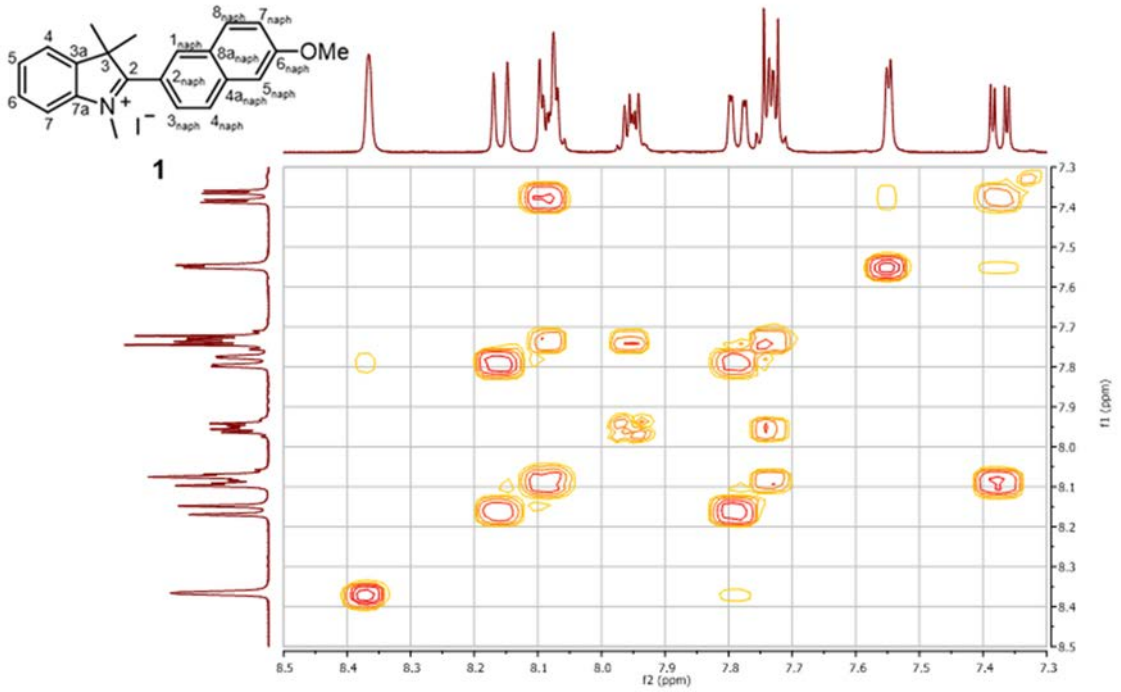

^{1}H-^{1}H COSY (400 MHz) spectrum of compound **1** in DMSO-d_6 (aromatic region)

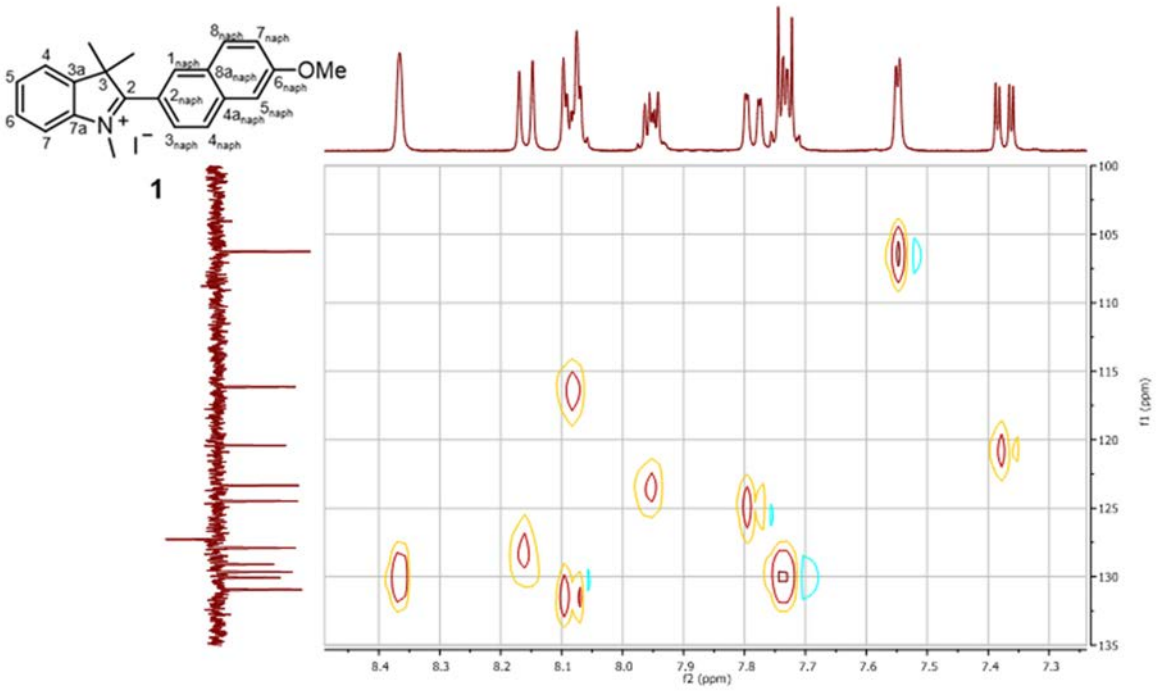

^{1}H-^{13}C HSQC spectrum of compound **1** in DMSO-d_6 (aromatic region)

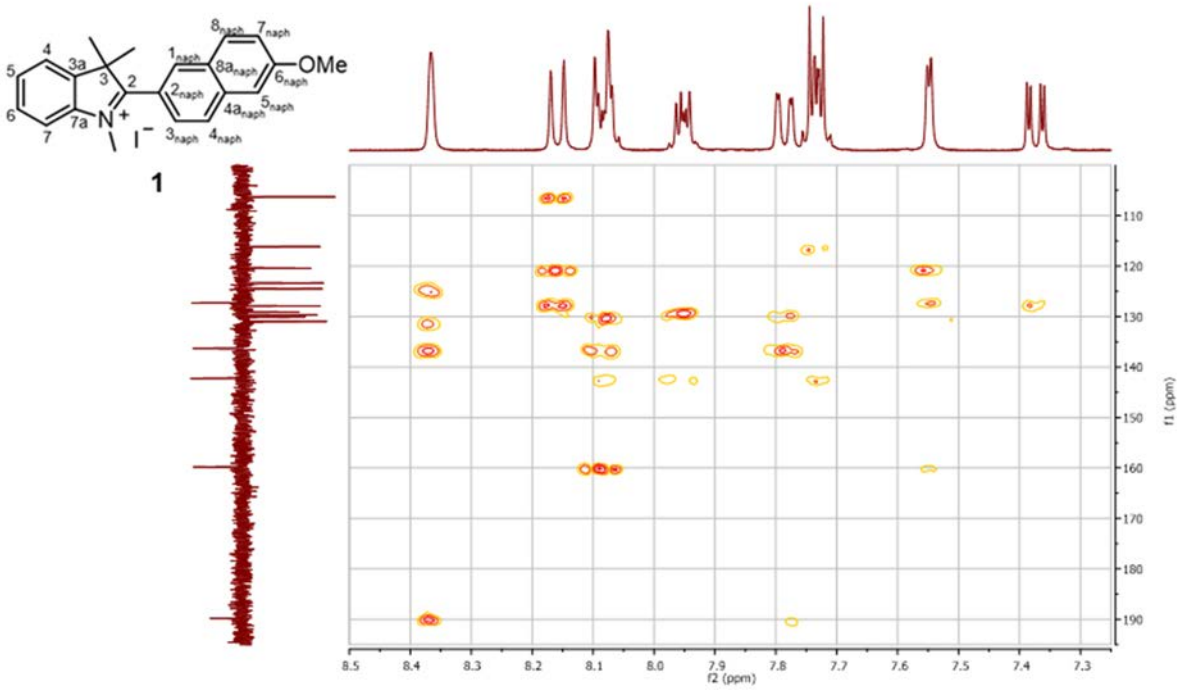

^{1}H-^{13}C HMBC spectrum of compound **1** in DMSO-d_6 (aromatic region)

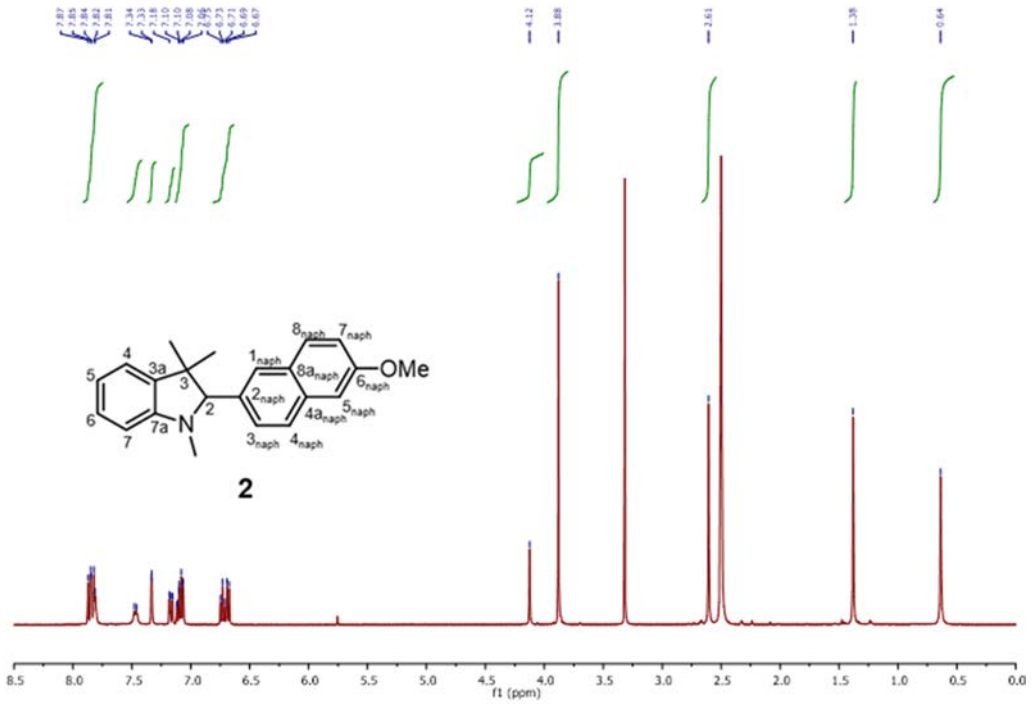

^{1}H-NMR (400 MHz) spectrum of compound **2** in DMSO-d_6

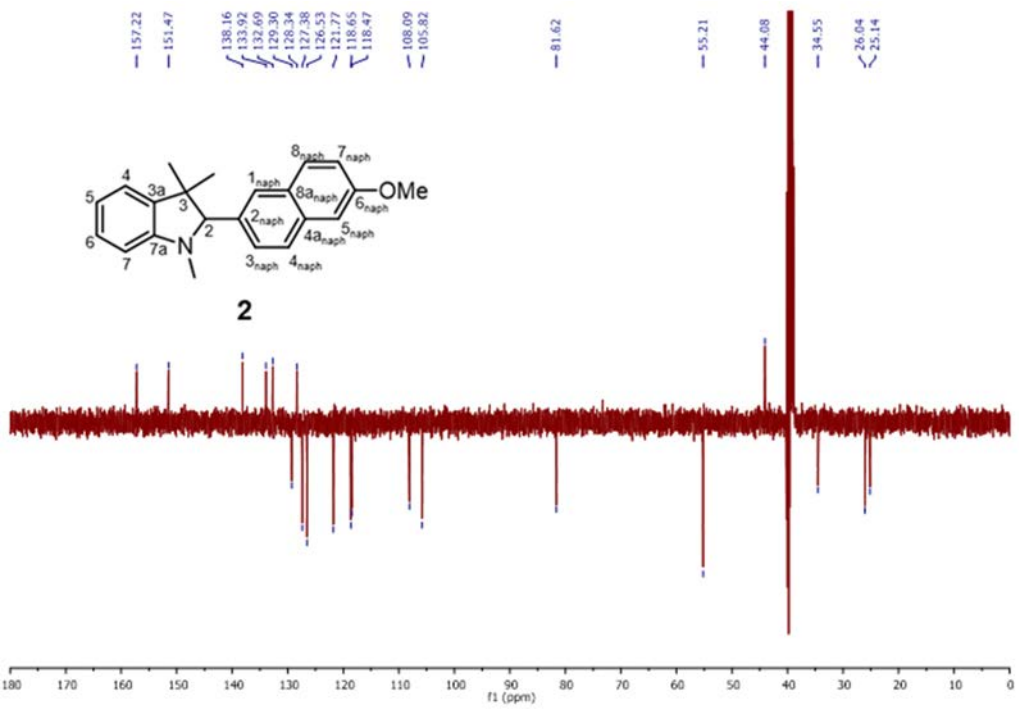

^{13}C-NMR SEFT (101 MHz) spectrum of compound **2** in DMSO-d_6

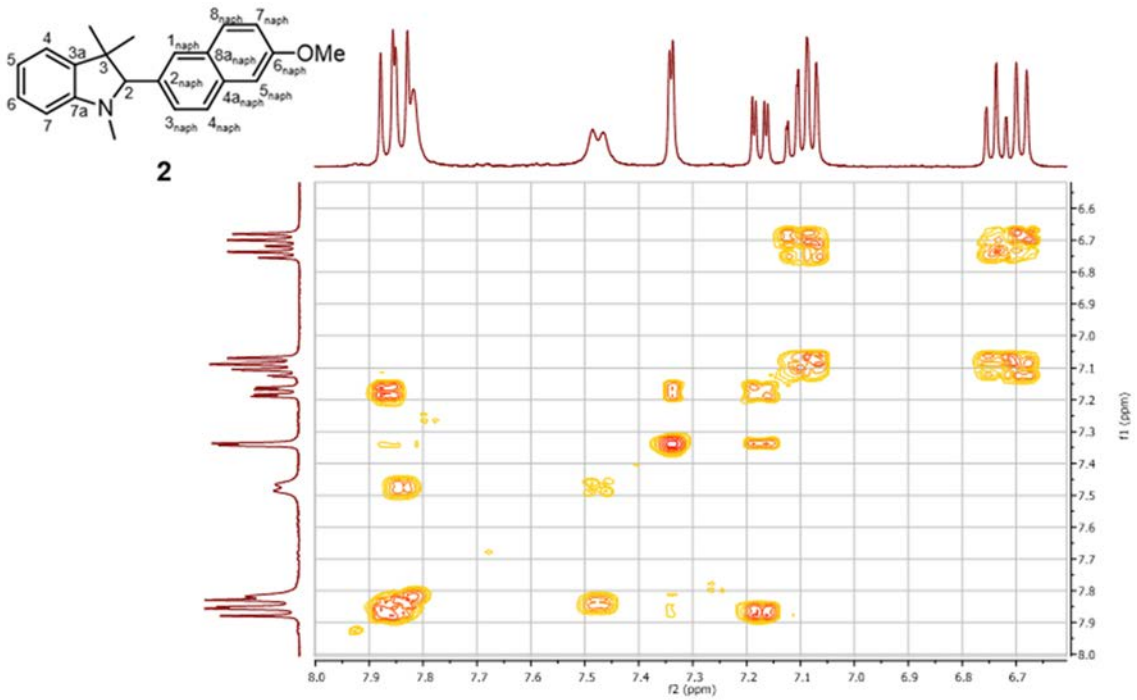

^{1}H-^{1}H COSY (400 MHz) spectrum of compound **2** in DMSO-d_6 (aromatic region)

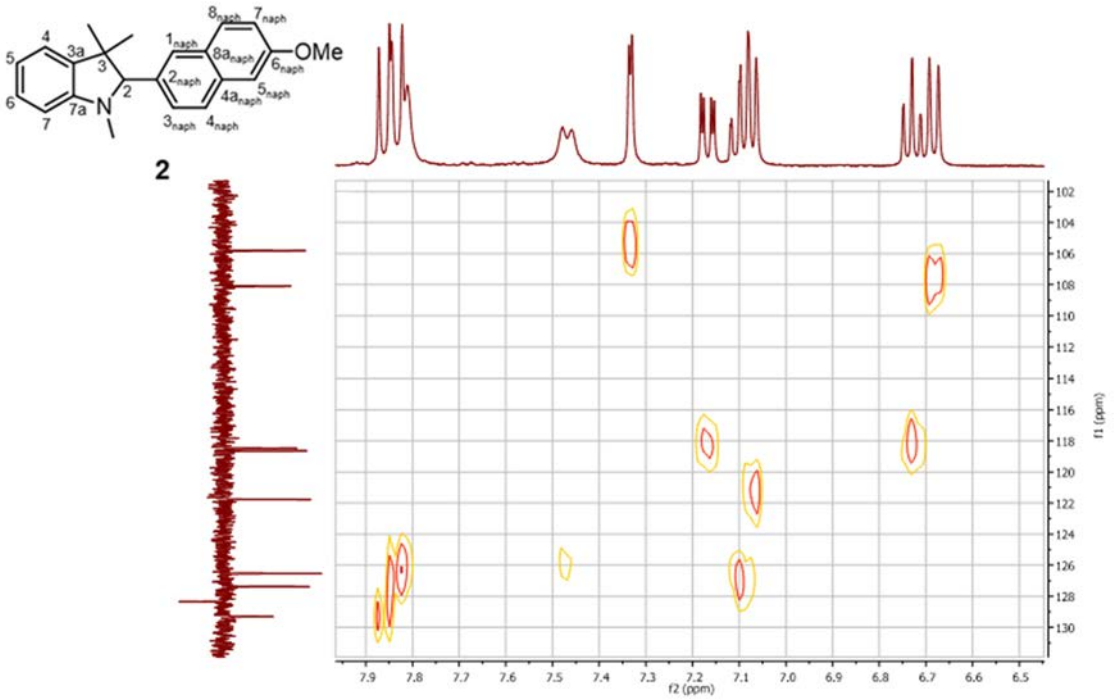

^{1}H-^{13}C HSQC spectrum of compound **2** in DMSO-d_6 (aromatic region)

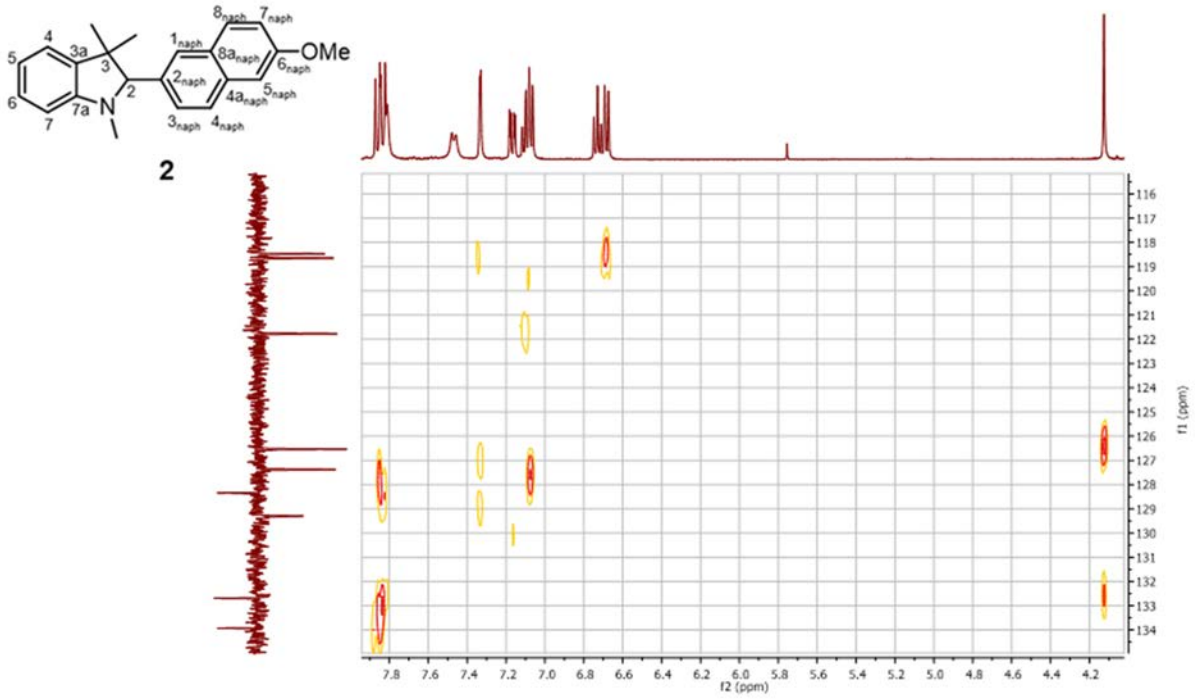

^{1}H-^{13}C HMBC spectrum of compound **2** in DMSO-d_6 (aromatic region)

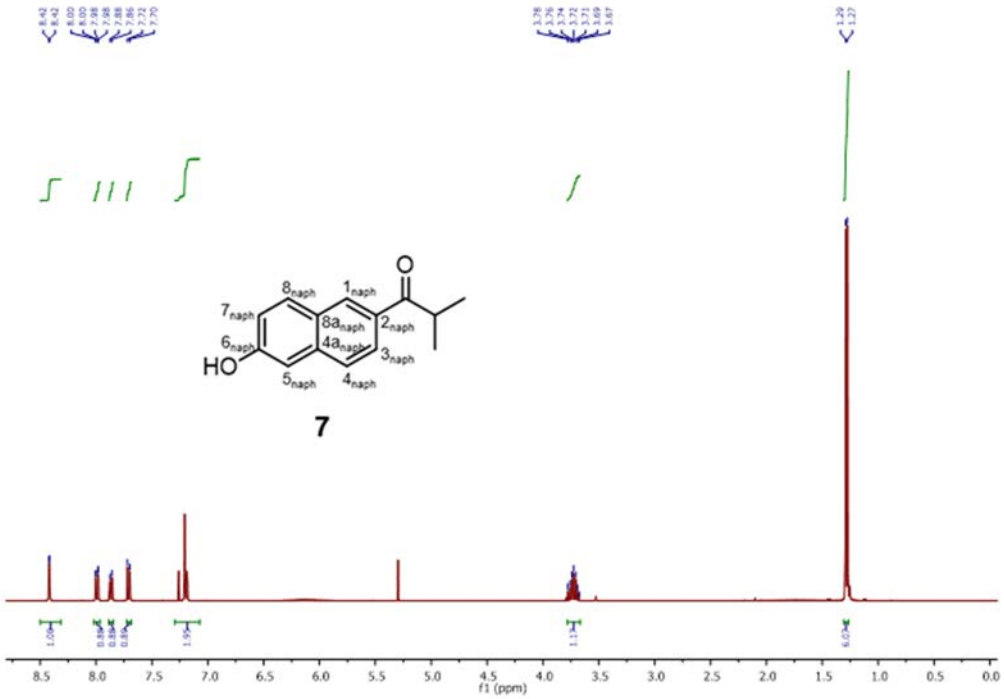

^{1}H-NMR (400 MHz) spectrum of compound **7** in $CDCl_3$.

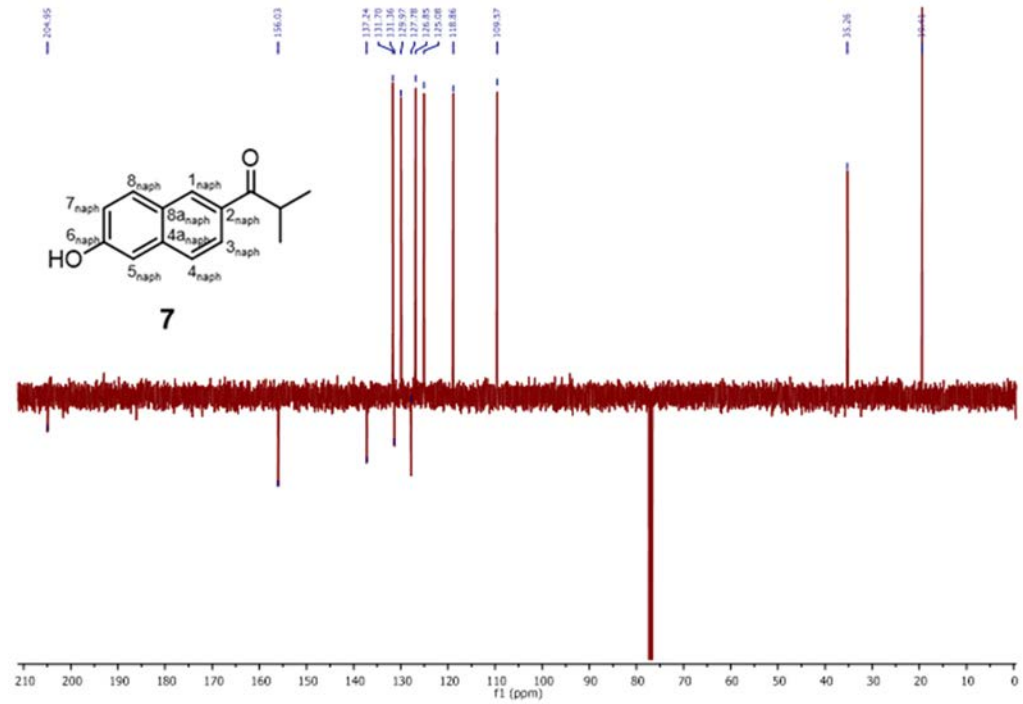

^{13}C-NMR SEFT (101 MHz) spectrum of compound **7** in $CDCl_3$

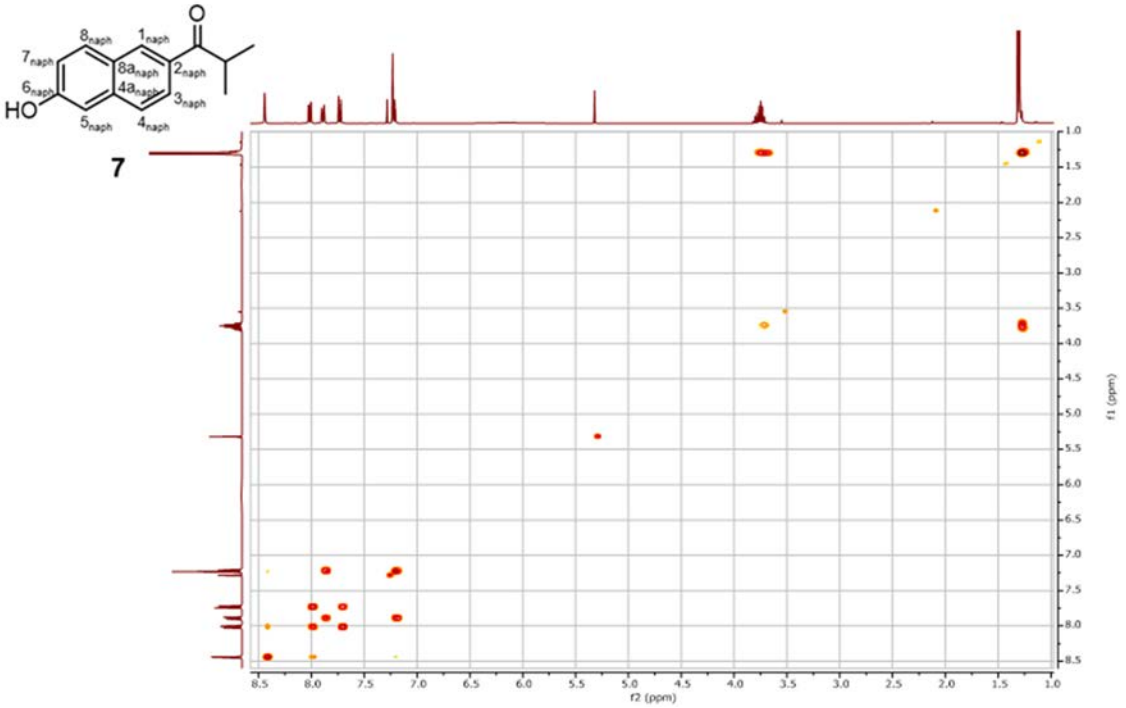

^{1}H-^{1}H COSY (400 MHz) spectrum of compound **7** in $CDCl_3$

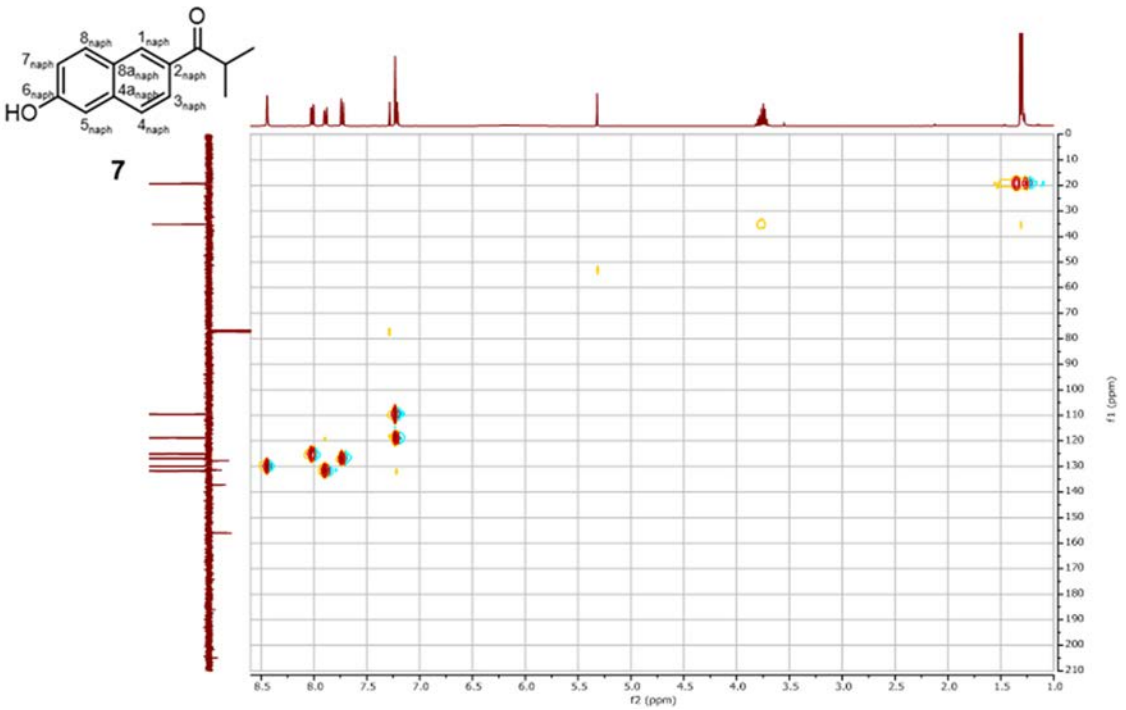

^{1}H-^{13}C HSQC spectrum of compound **7** in $CDCl_3$

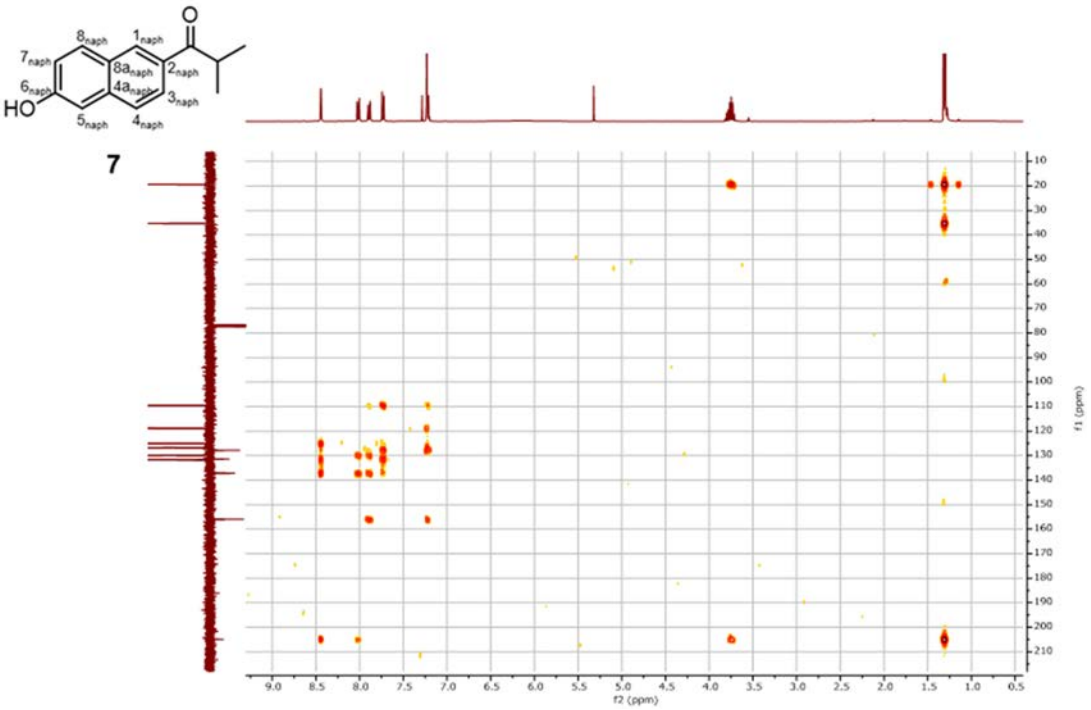

^{1}H-^{13}C HMBC spectrum of compound **7** in $CDCl_3$

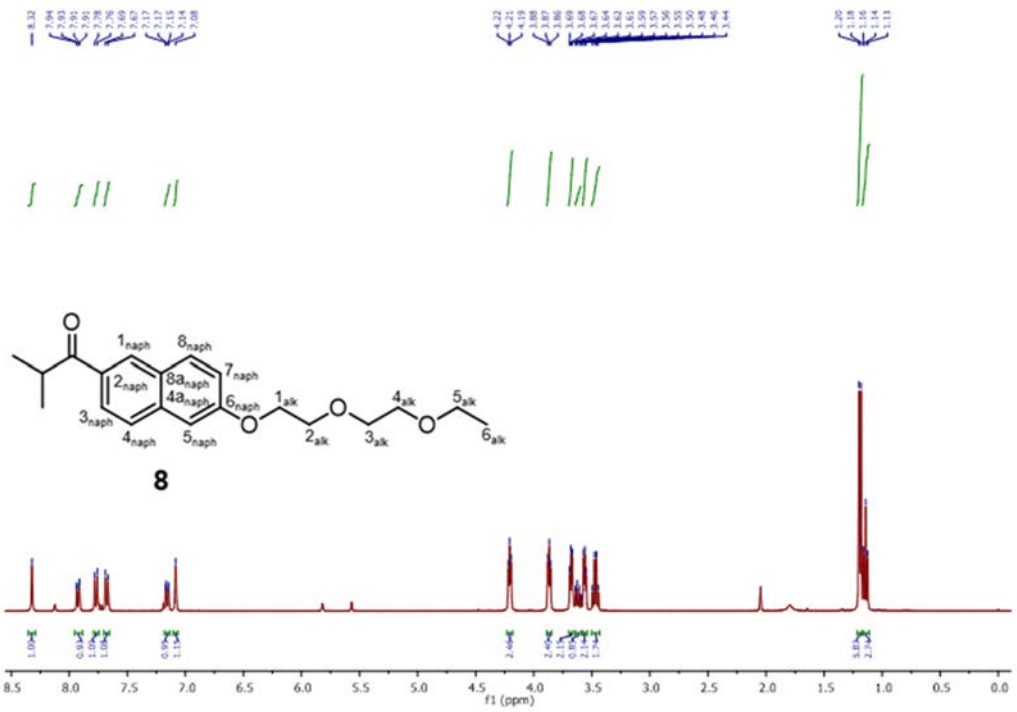

^{1}H-NMR (400 MHz) spectrum of compound **8** in $CDCl_3$.

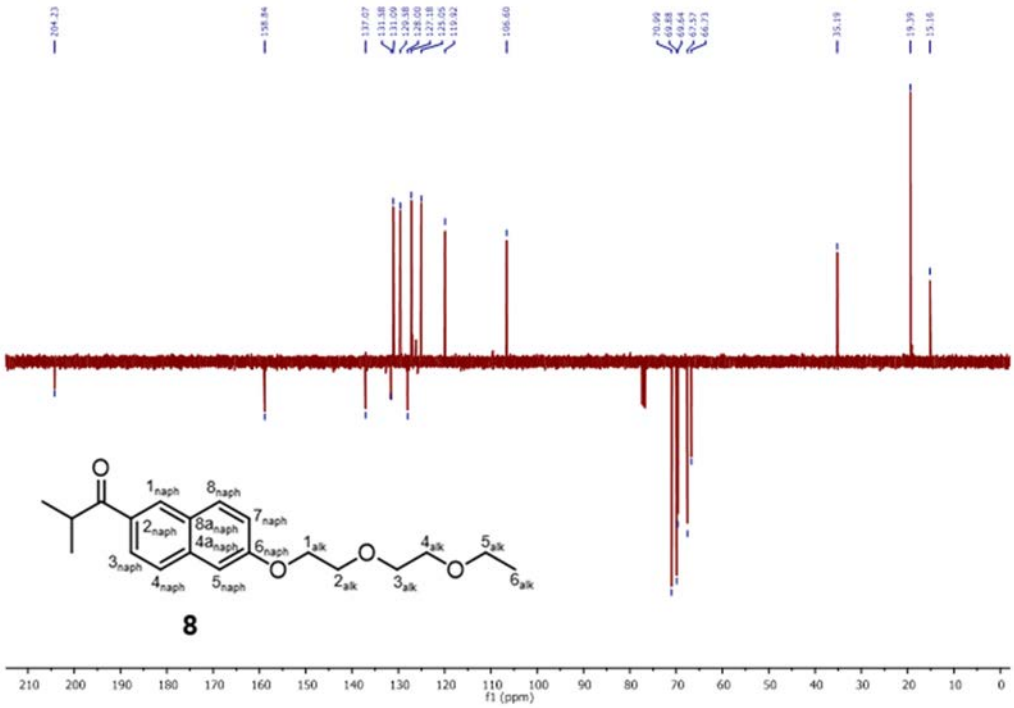

^{13}C-NMR SEFT (101 MHz) spectrum of compound **8** in $CDCl_3$

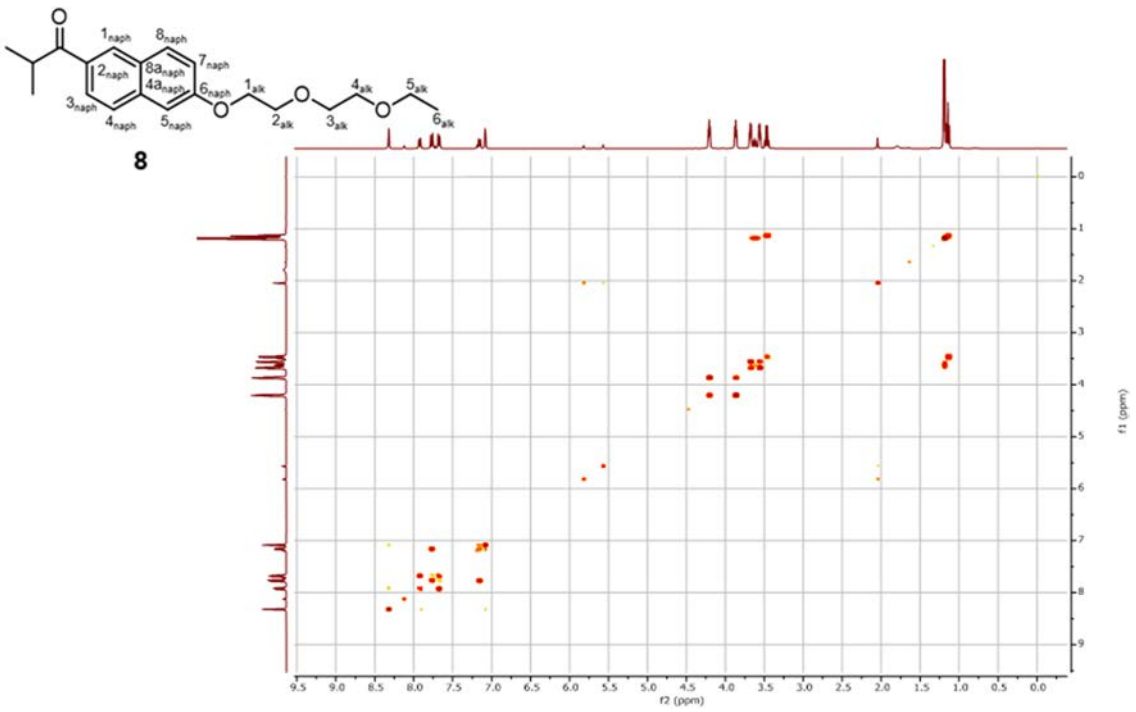

^{1}H-^{1}H COSY (400 MHz) spectrum of compound **8** in $CDCl_3$

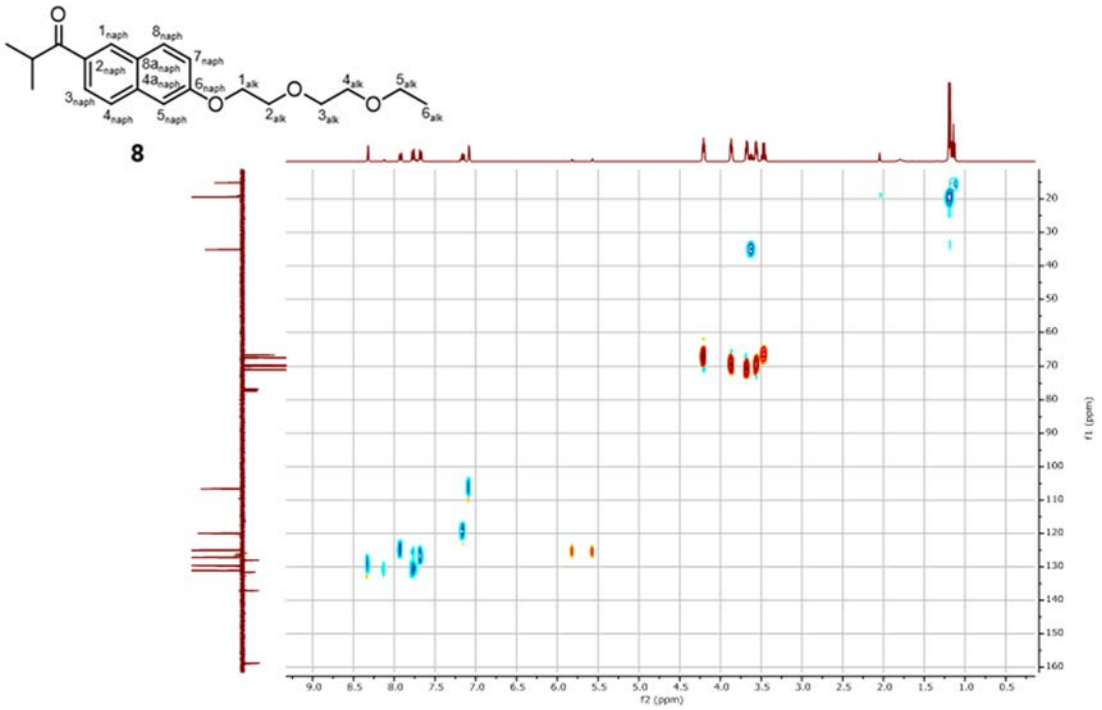

^{1}H-^{13}C HSQC spectrum of compound **8** in $CDCl_3$

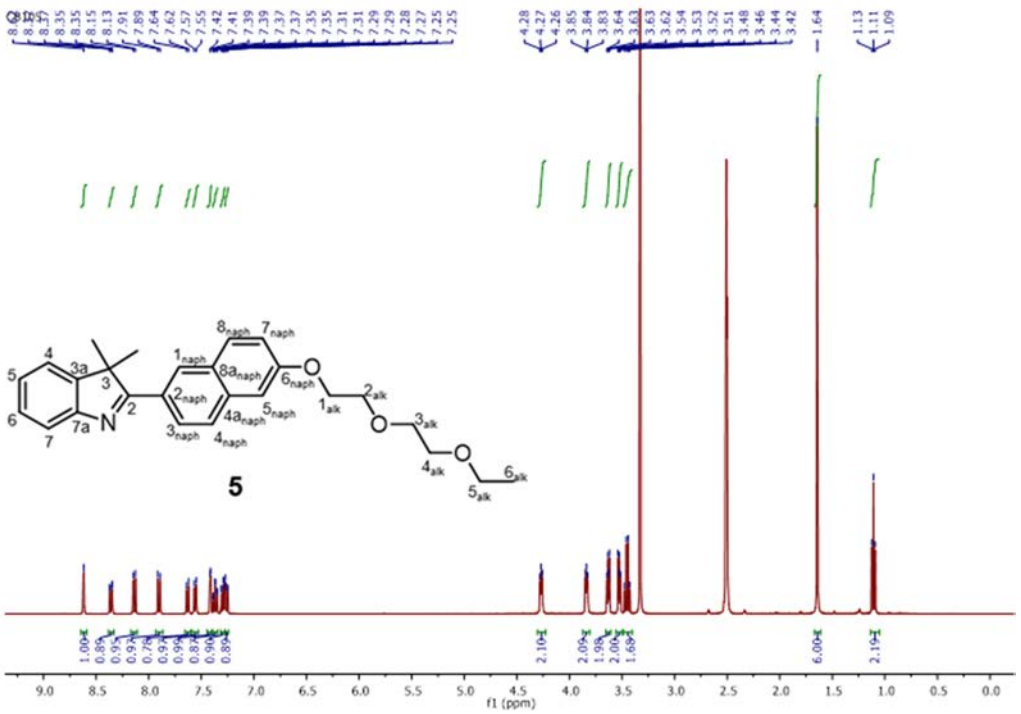

^{1}H-NMR (400 MHz) spectrum of compound **5** in DMSO-d_6

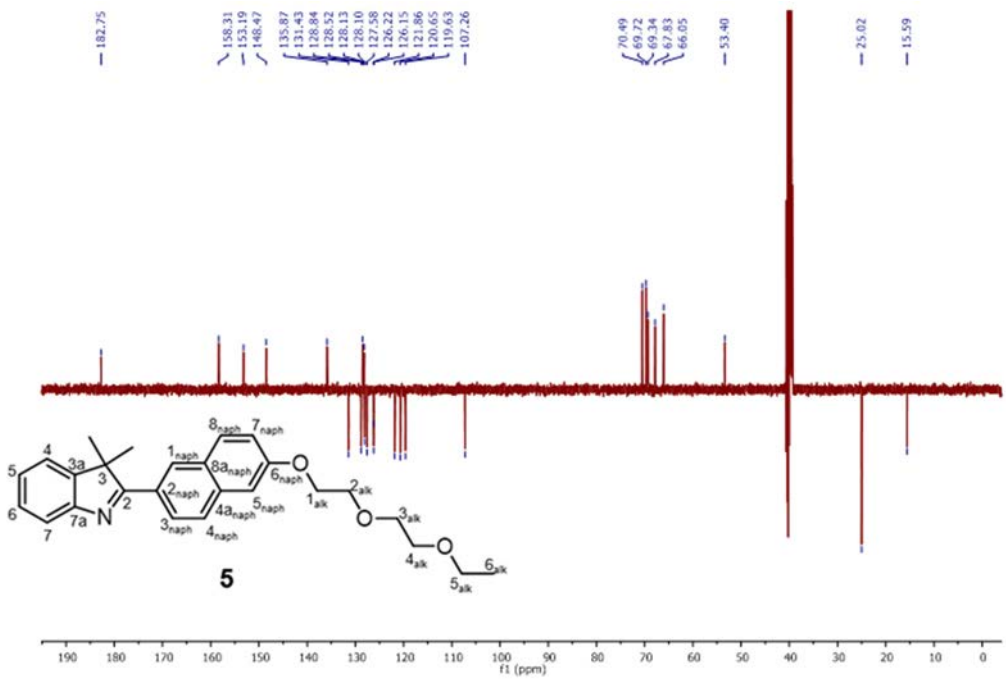

^{13}C-NMR SEFT (101 MHz) spectrum of compound **5** in DMSO-d_6

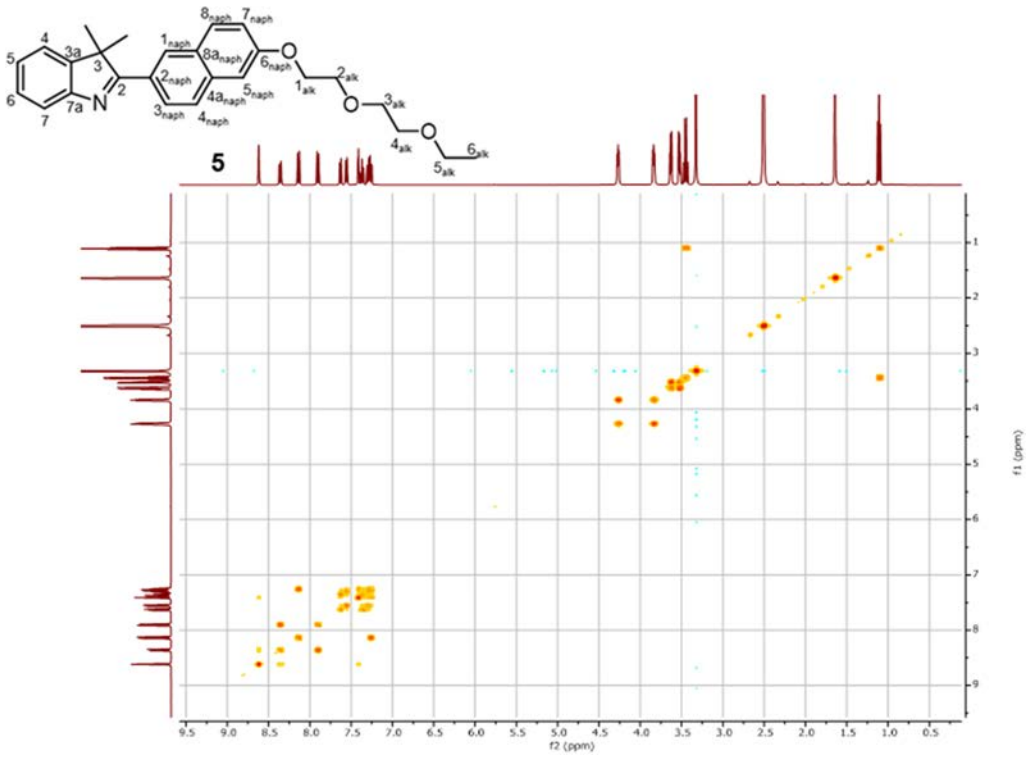

^{1}H-^{1}H COSY (400 MHz) spectrum of compound **5** in DMSO-d_6

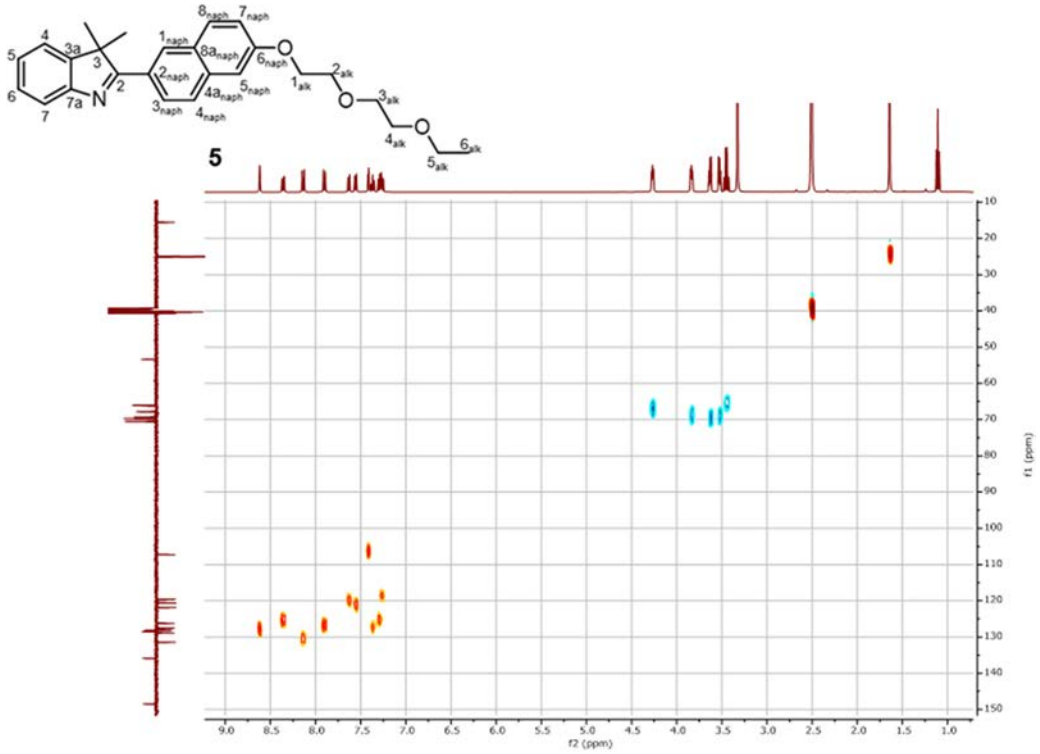

^{1}H-^{13}C HSQC spectrum of compound **5** in DMSO-d_6

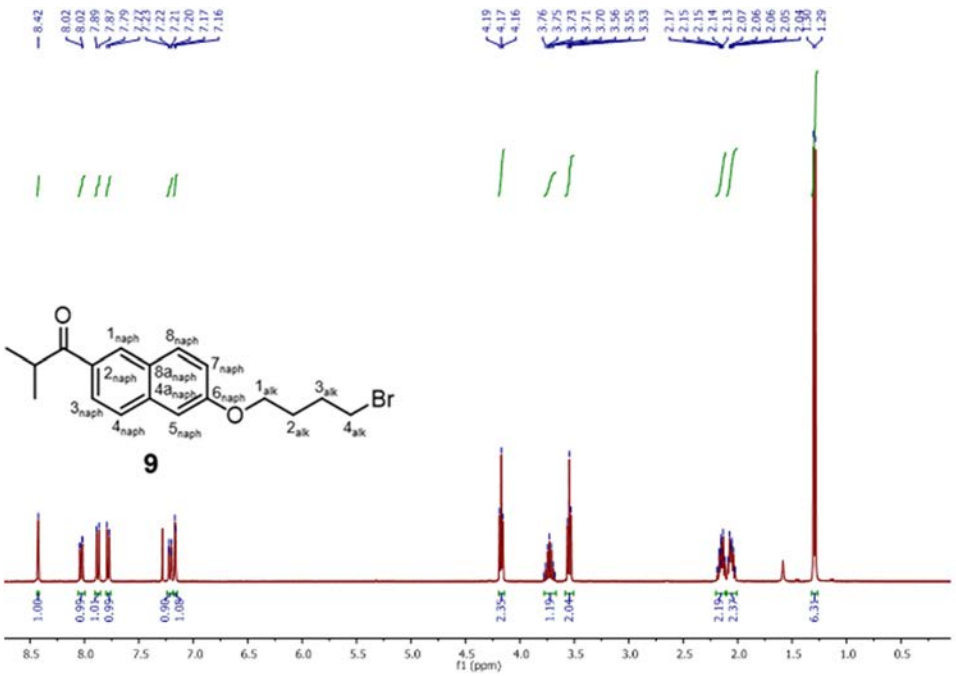

^{1}H-NMR (400 MHz) spectrum of compound **9** in $CDCl_3$.

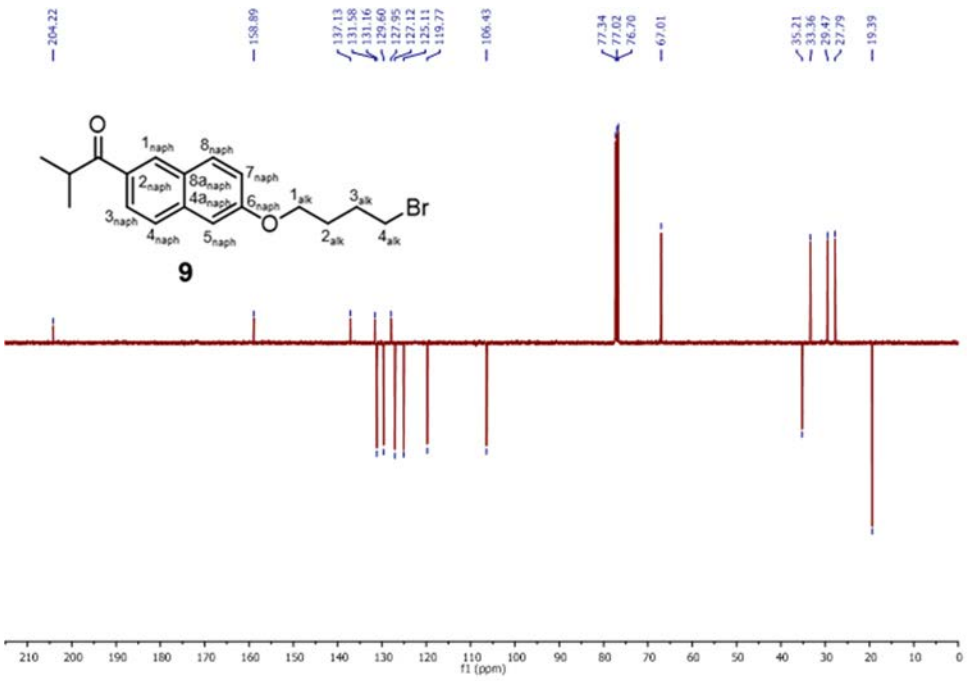

^{13}C-NMR SEFT (101 MHz) spectrum of compound **9** in $CDCl_3$

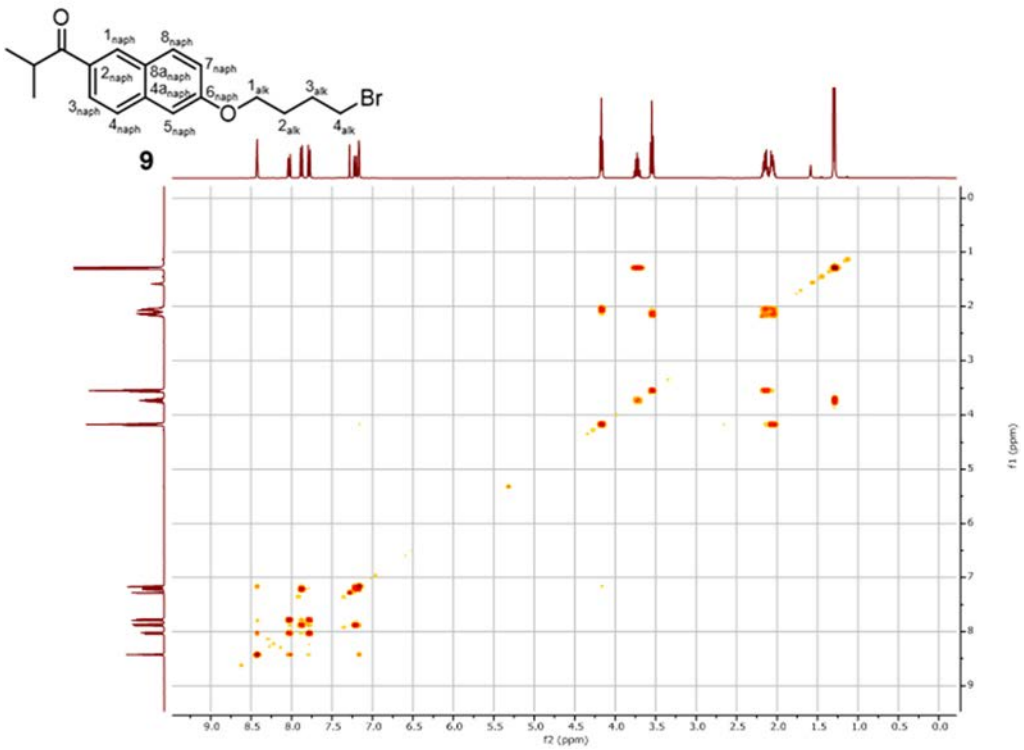

^{1}H-^{1}H COSY (400 MHz) spectrum of compound **9** in $CDCl_3$

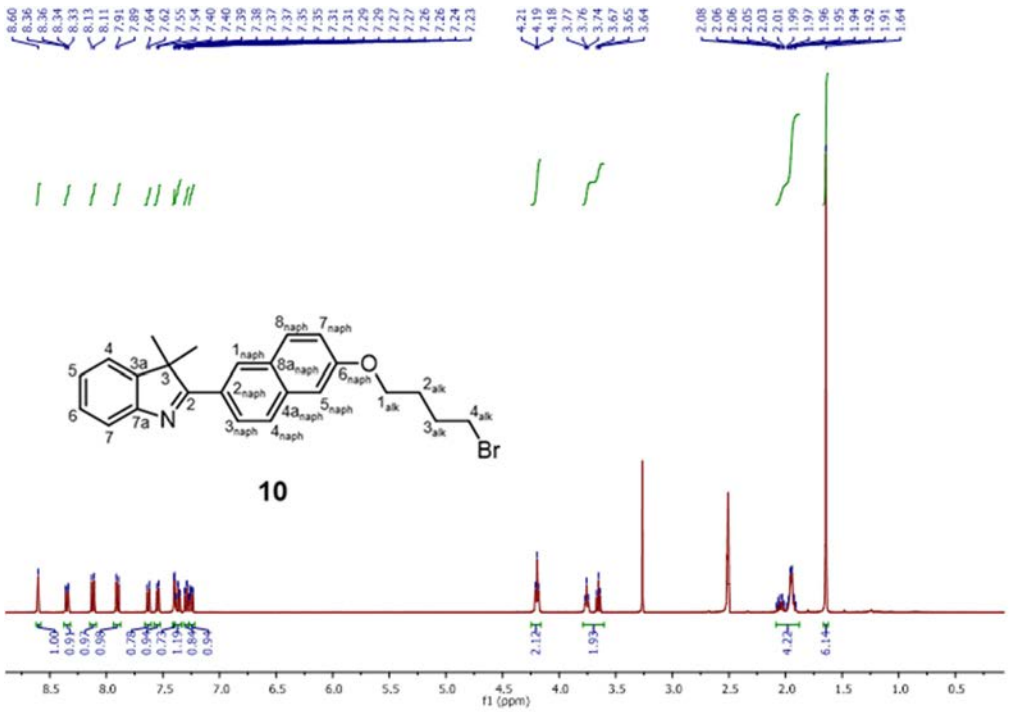

^{1}H-NMR (400 MHz) spectrum of compound **10** in DMSO-d_6

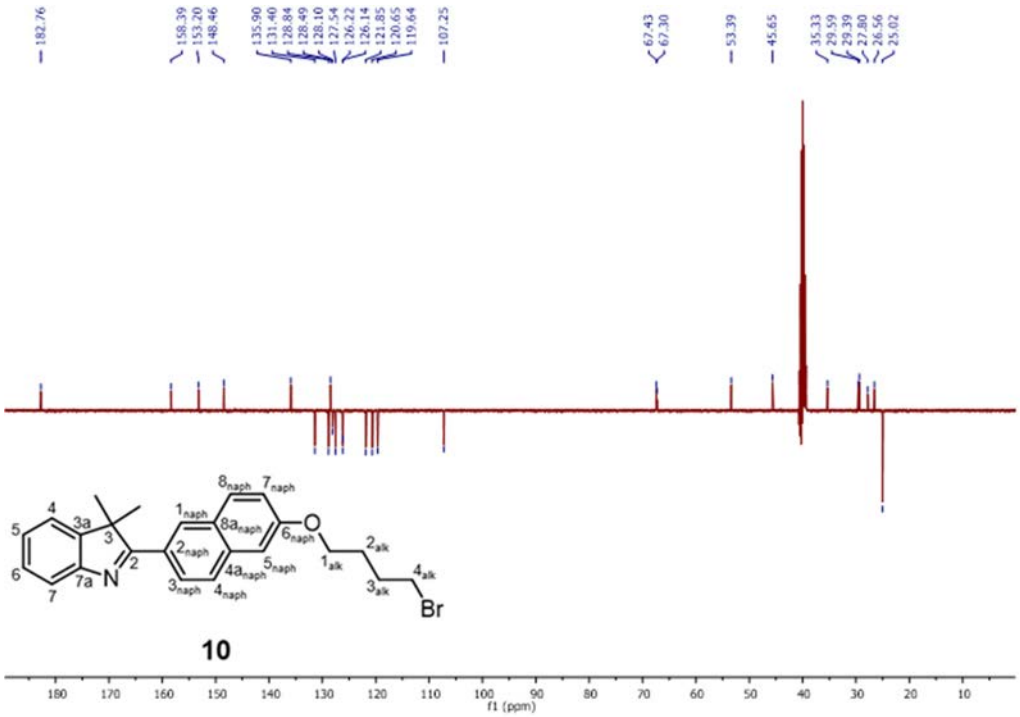

^{13}C-NMR SEFT (101 MHz) spectrum of compound **10** in DMSO-d_6

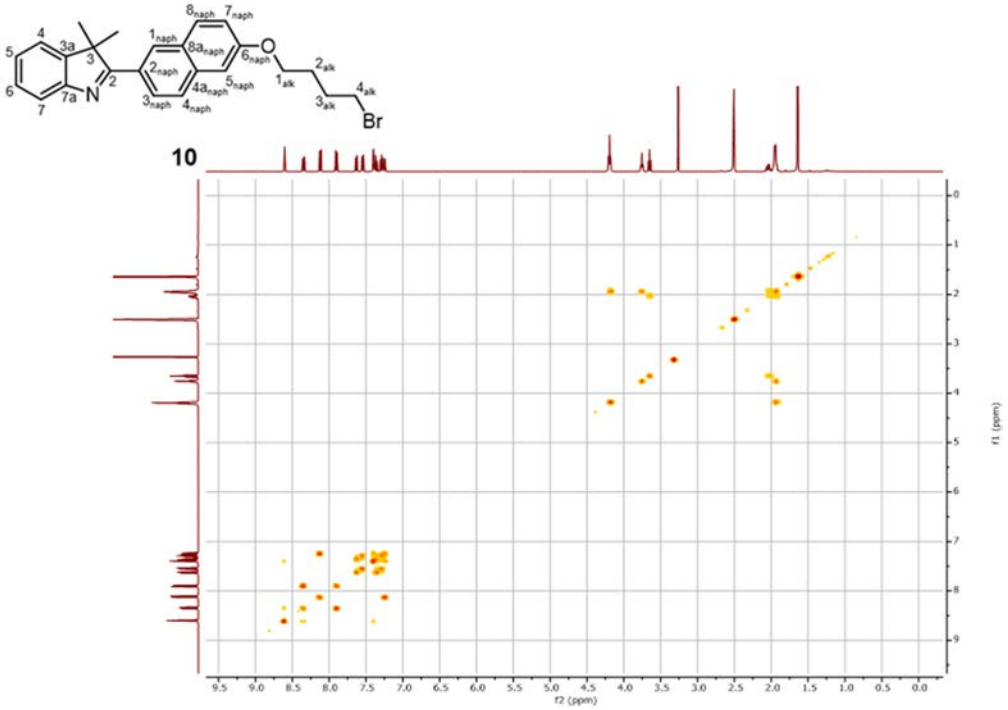

^{1}H-^{1}H COSY (400 MHz) spectrum of compound **10** in DMSO-d_6

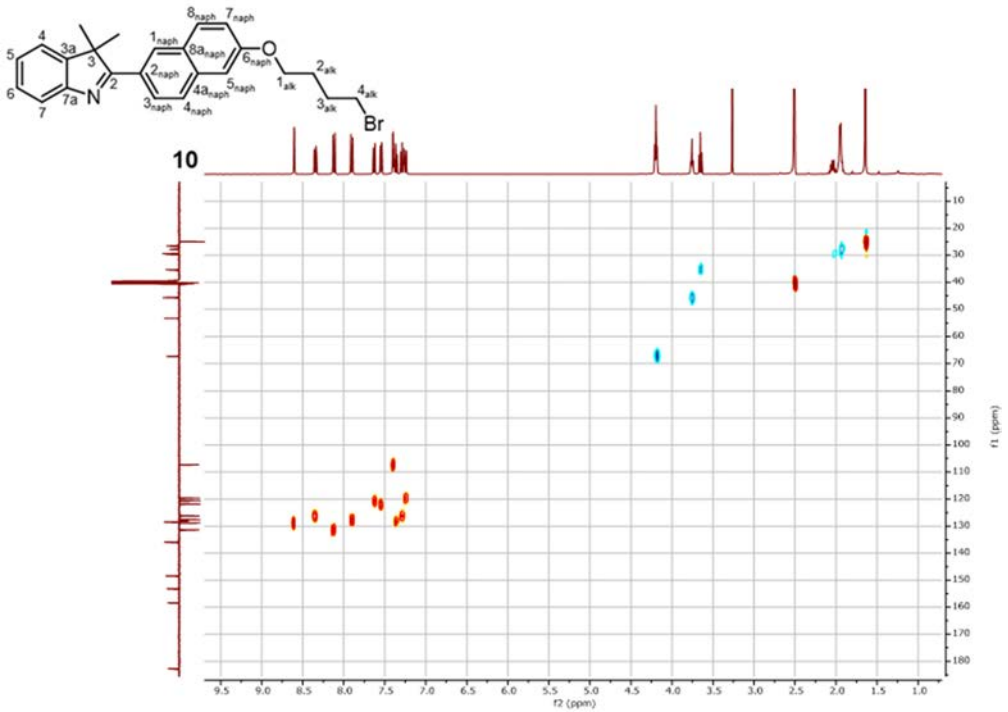

^{1}H-^{13}C HSQC spectrum of compound **10** in DMSO-d_6

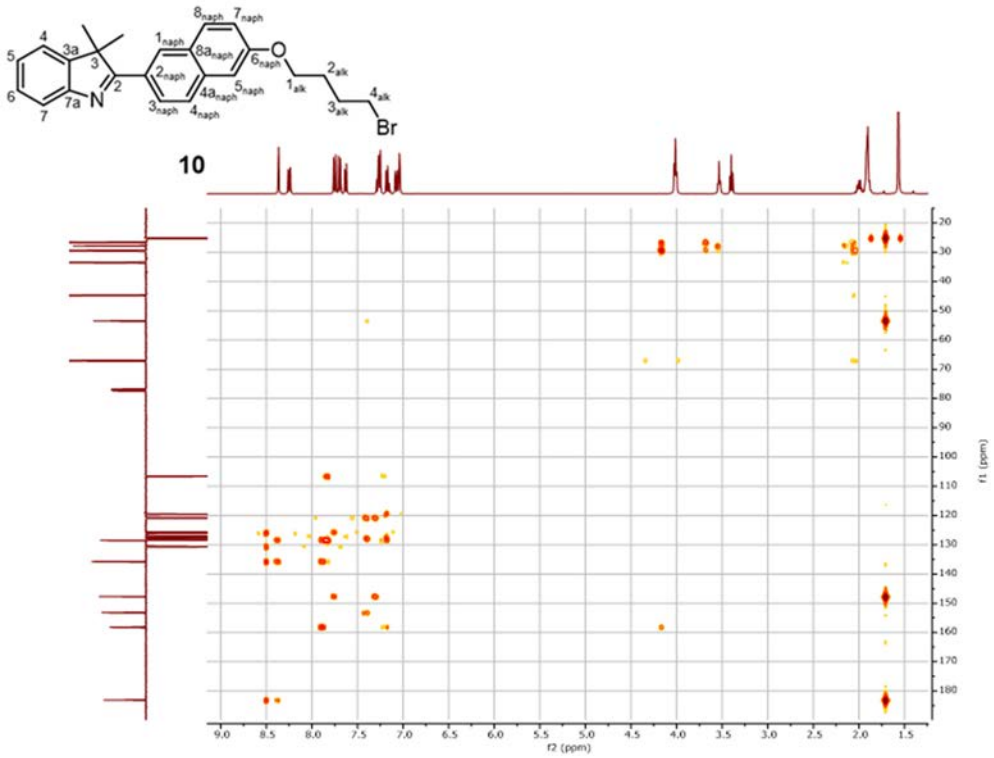

^{1}H-^{13}C HMBC spectrum of compound **10** in DMSO-d_6

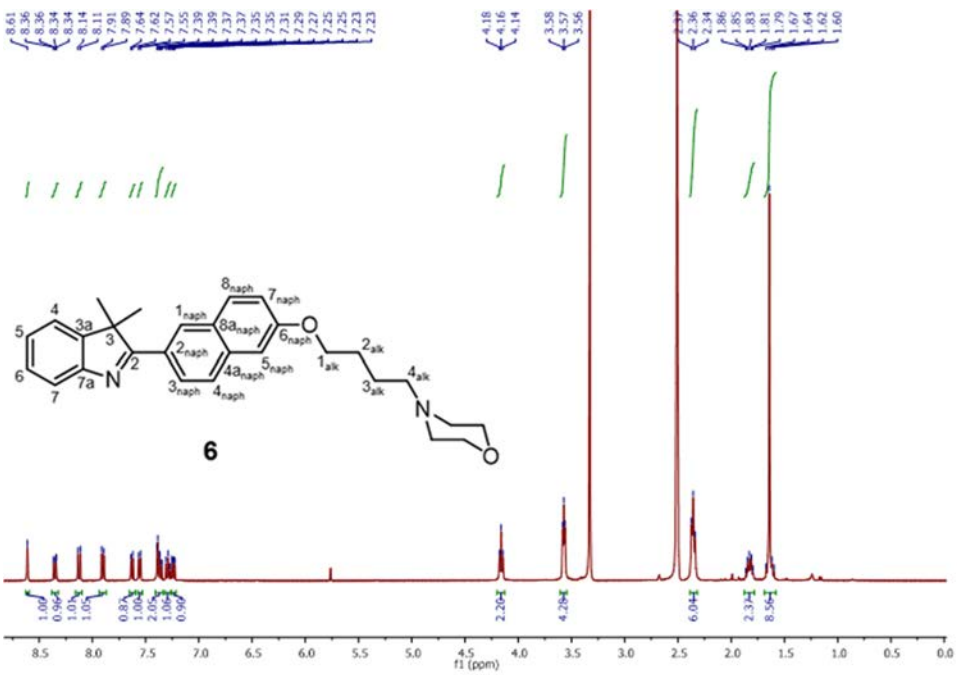

^{1}H-NMR (400 MHz) spectrum of compound **6** in DMSO-d_6

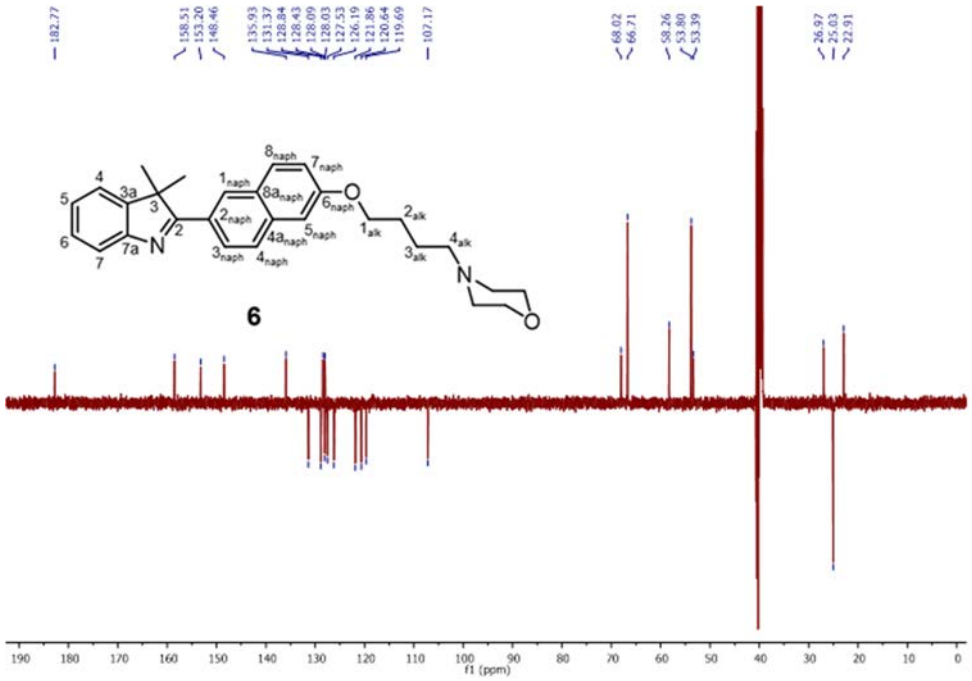

^{13}C-NMR SEFT (101 MHz) spectrum of compound **6** in DMSO-d_6

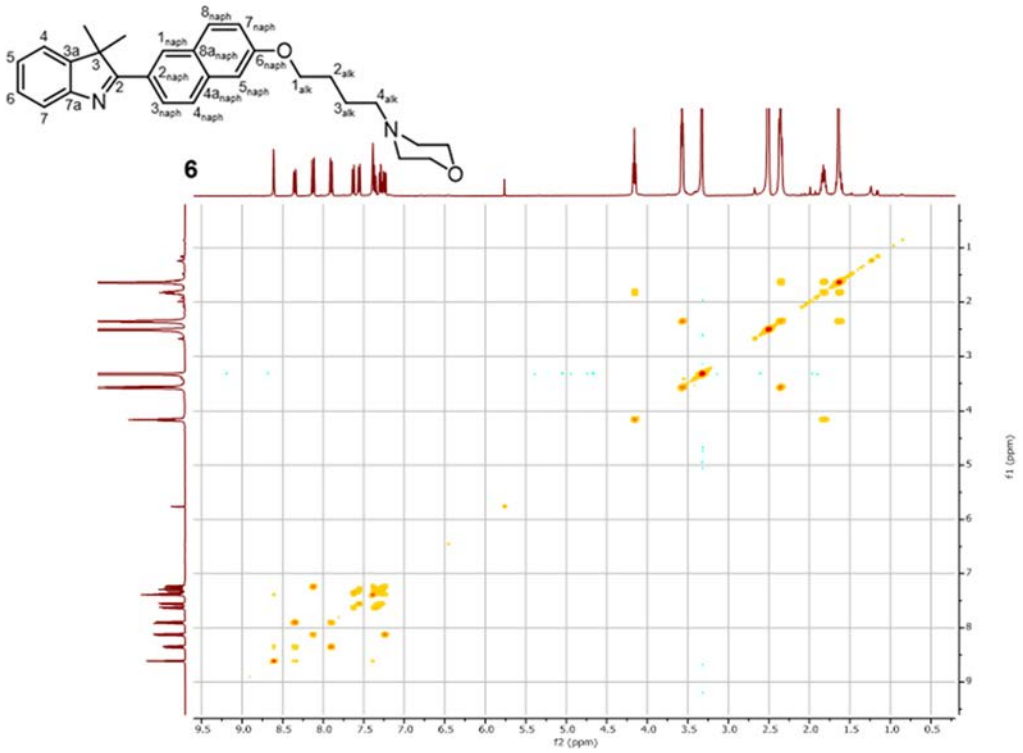

^{1}H-^{1}H COSY (400 MHz) spectrum of compound **6** in DMSO-d_6

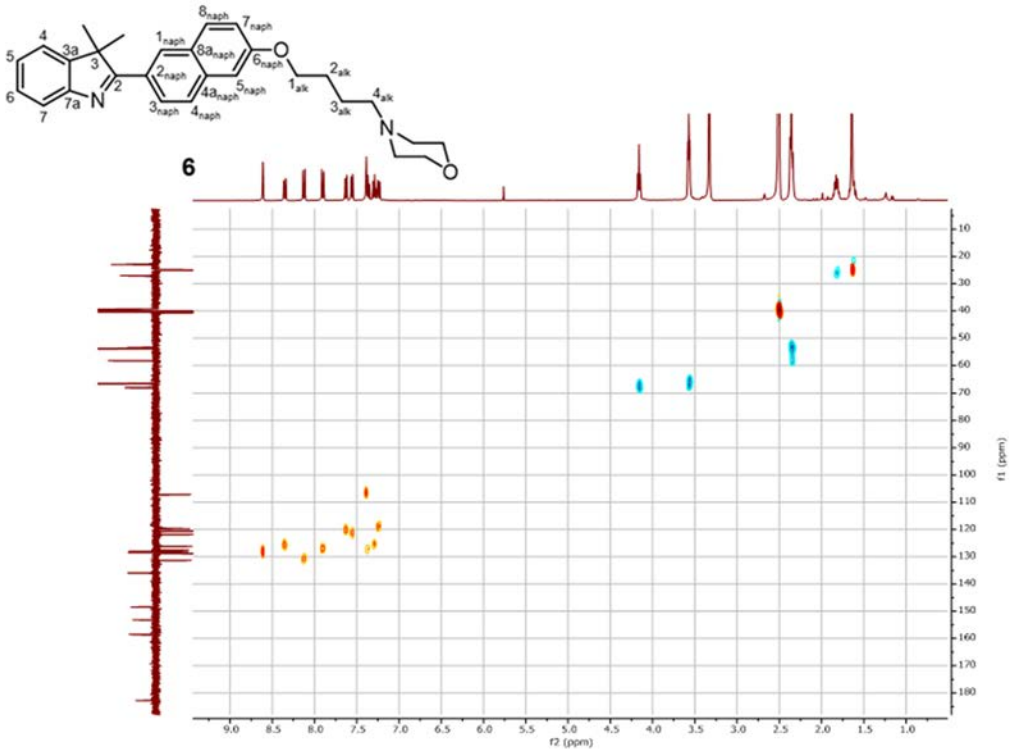

^{1}H-^{13}C HSQC spectrum of compound **6** in DMSO-d_6

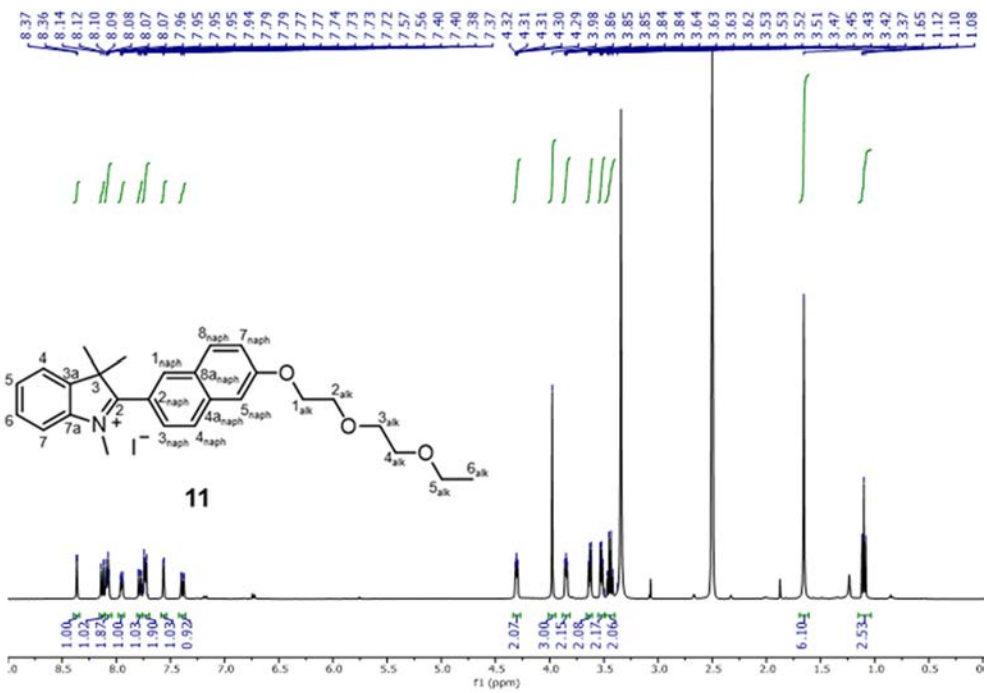

^{1}H-NMR (400 MHz) spectrum of compound **11** in DMSO-d_6

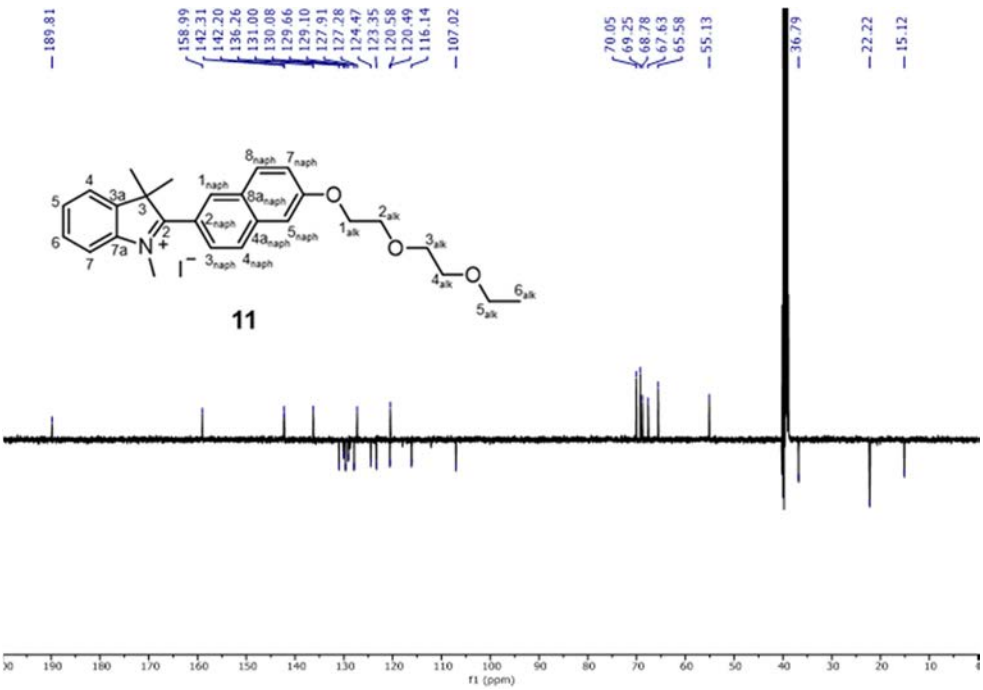

^{13}C-NMR SEFT (101 MHz) spectrum of compound **11** in DMSO-d_6

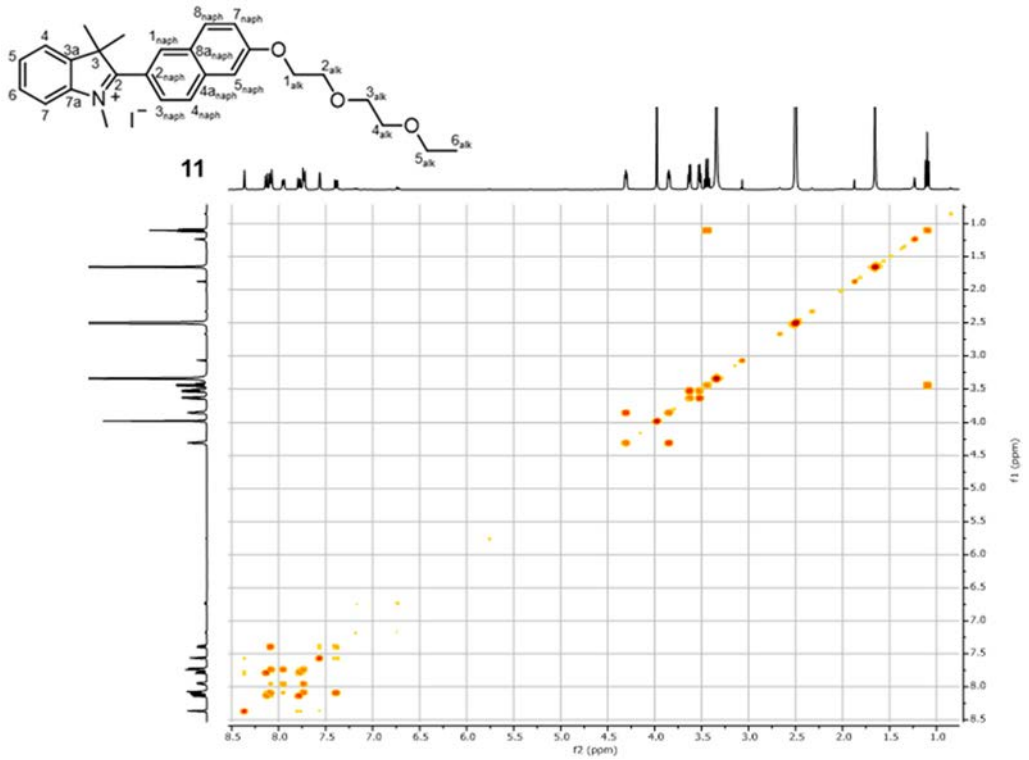

^{1}H-^{1}H COSY (400 MHz) spectrum of compound **11** in DMSO-d_6

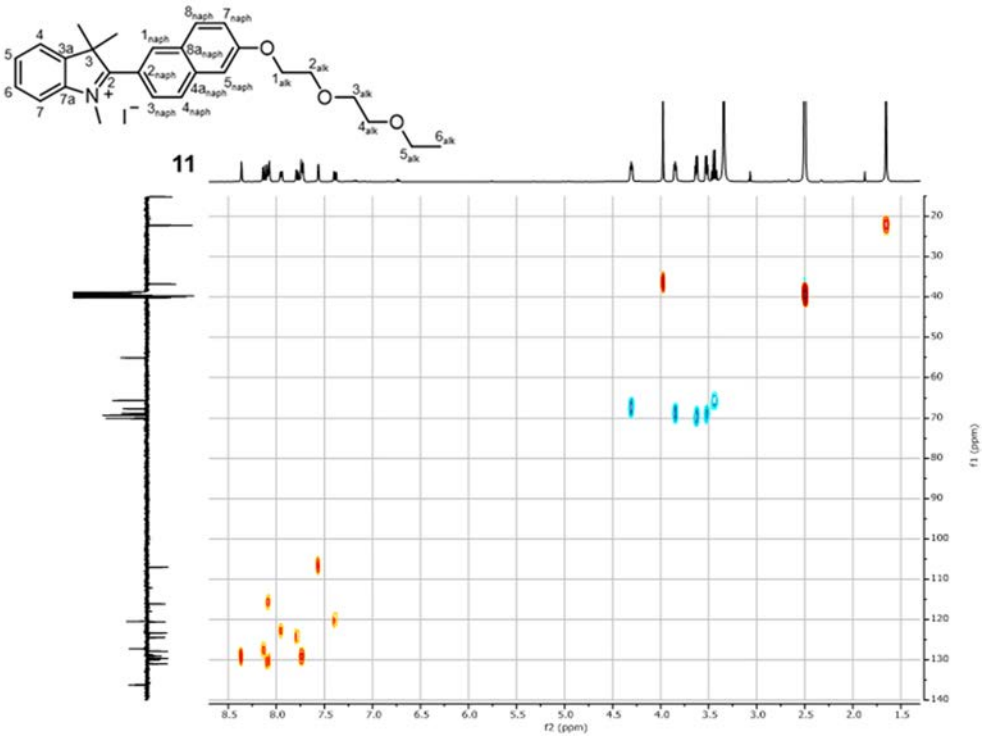

^{1}H-^{13}C HSQC spectrum of compound **11** in DMSO-d_6

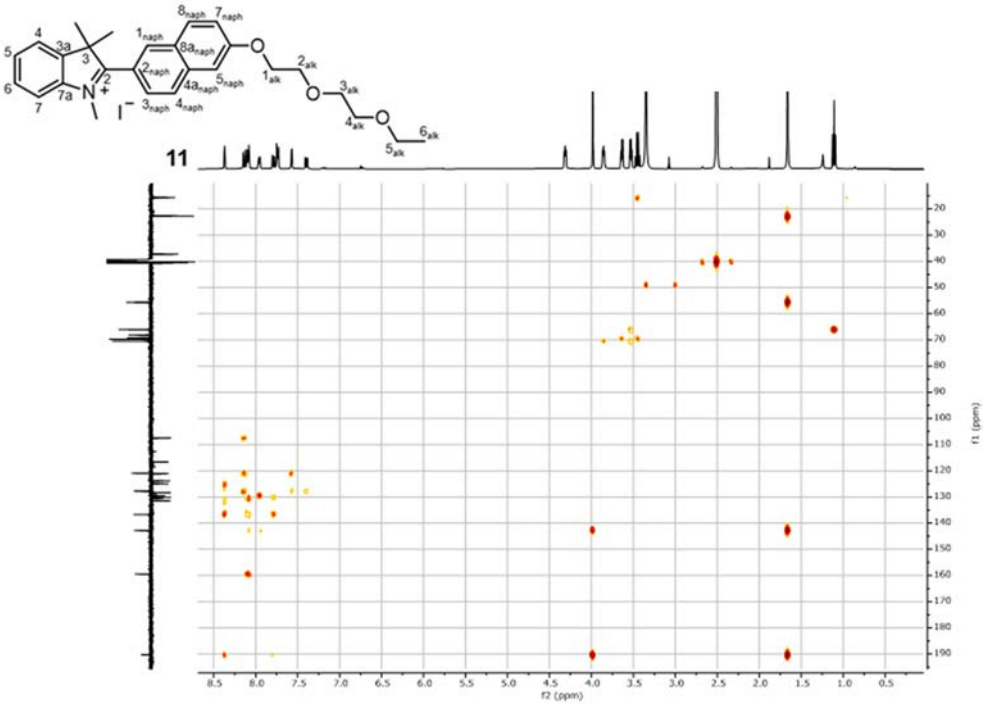

^{1}H-^{13}C HMBC spectrum of compound **11** in DMSO-d_6

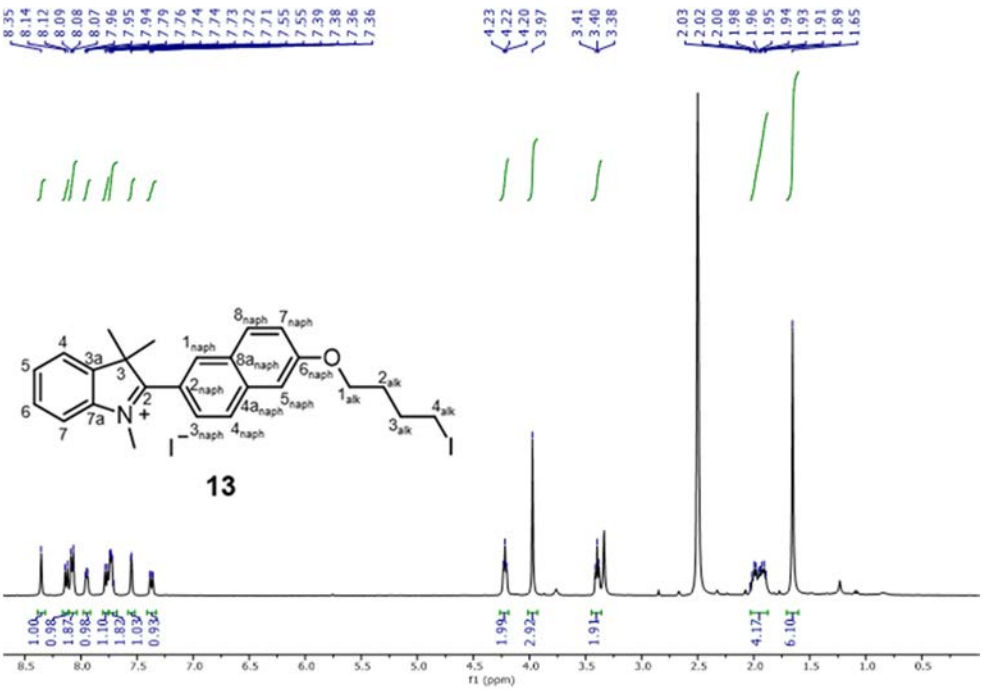

^{1}H-NMR (400 MHz) spectrum of compound **13** in DMSO-d_6

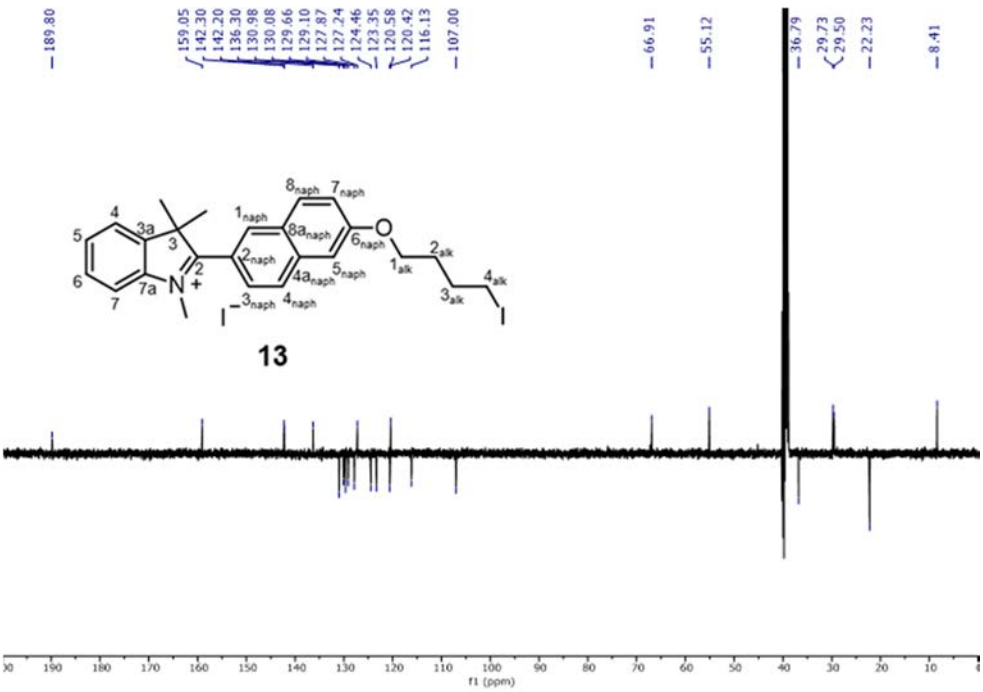

^{13}C-NMR SEFT (101 MHz) spectrum of compound **13** in DMSO-d_6

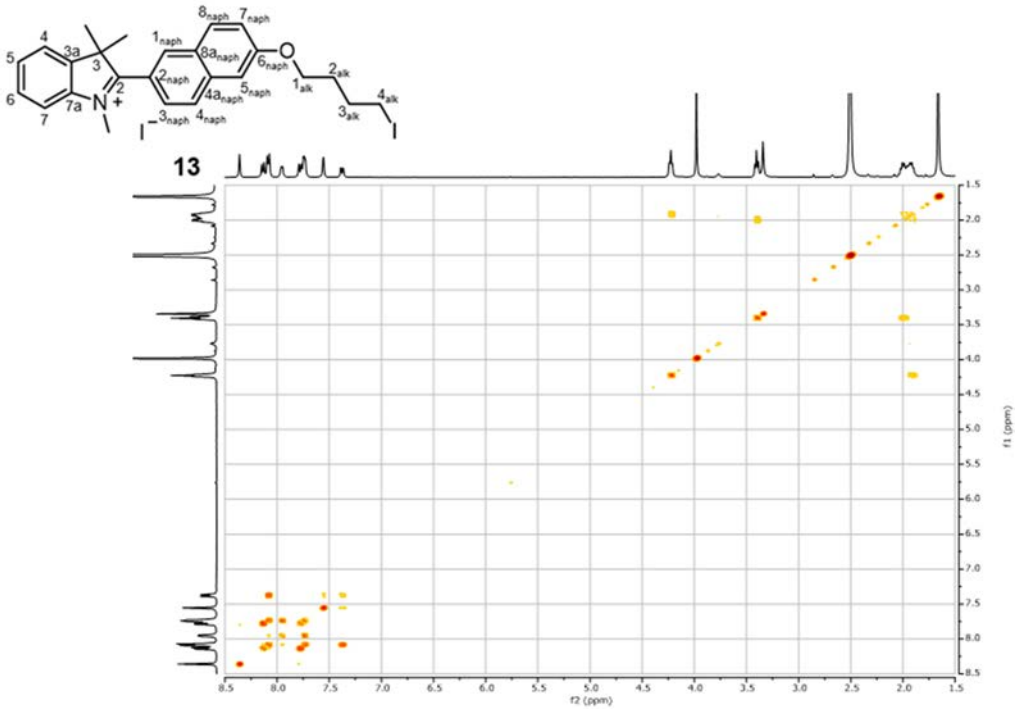

^{1}H-^{1}H COSY (400 MHz) spectrum of compound **13** in DMSO-d_6

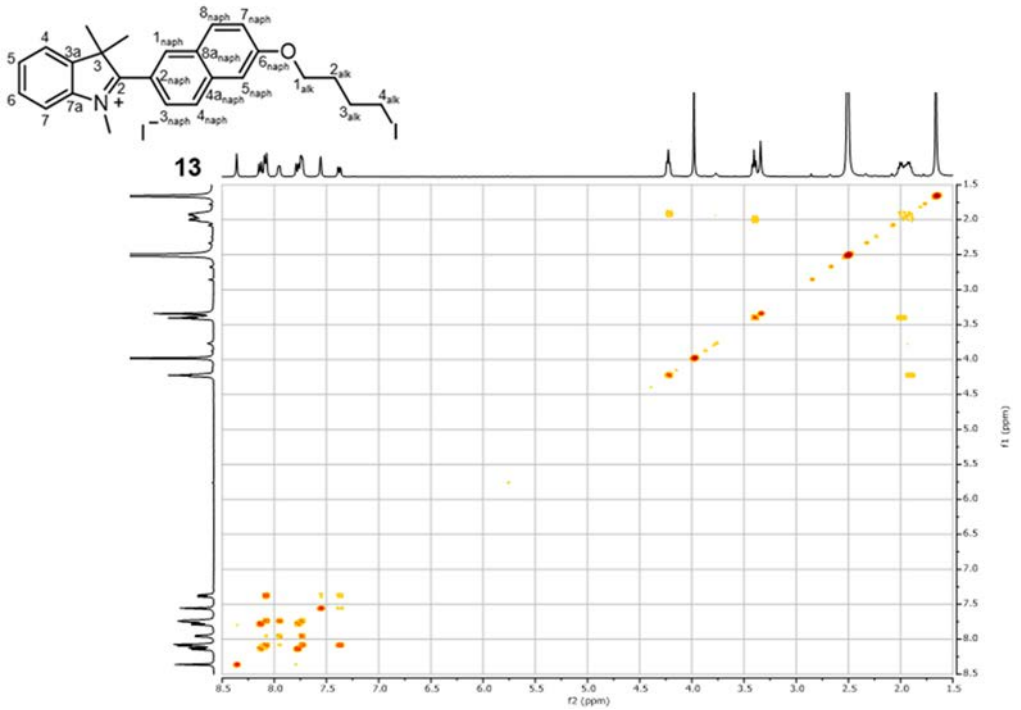

^{1}H-^{13}C HSQC spectrum of compound **13** in DMSO-d_6

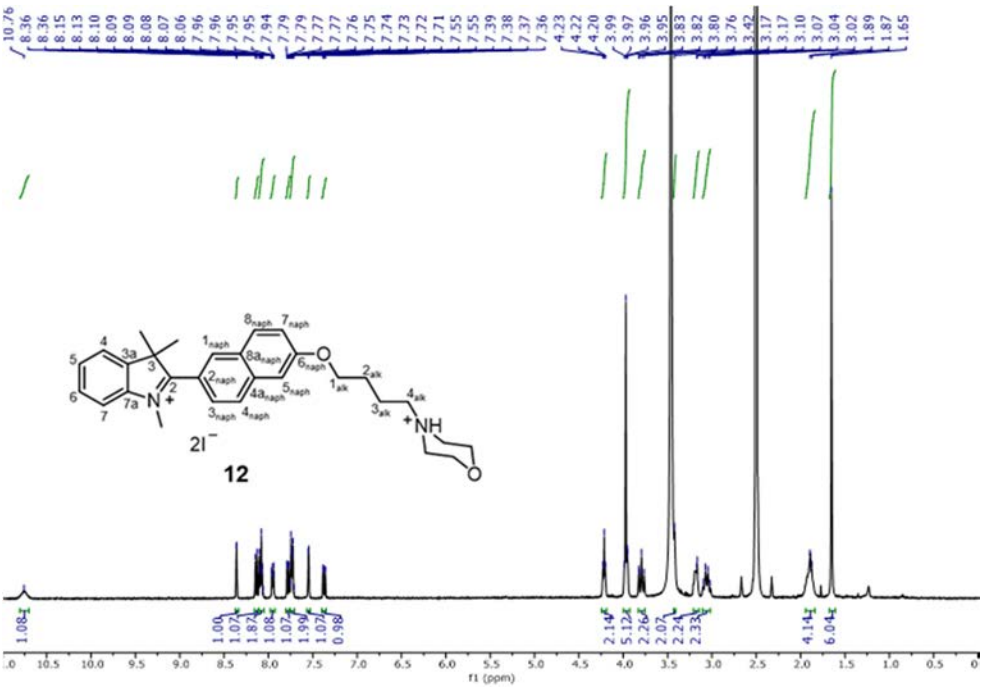

^{1}H-NMR (400 MHz) spectrum of compound **12** in DMSO-d_6

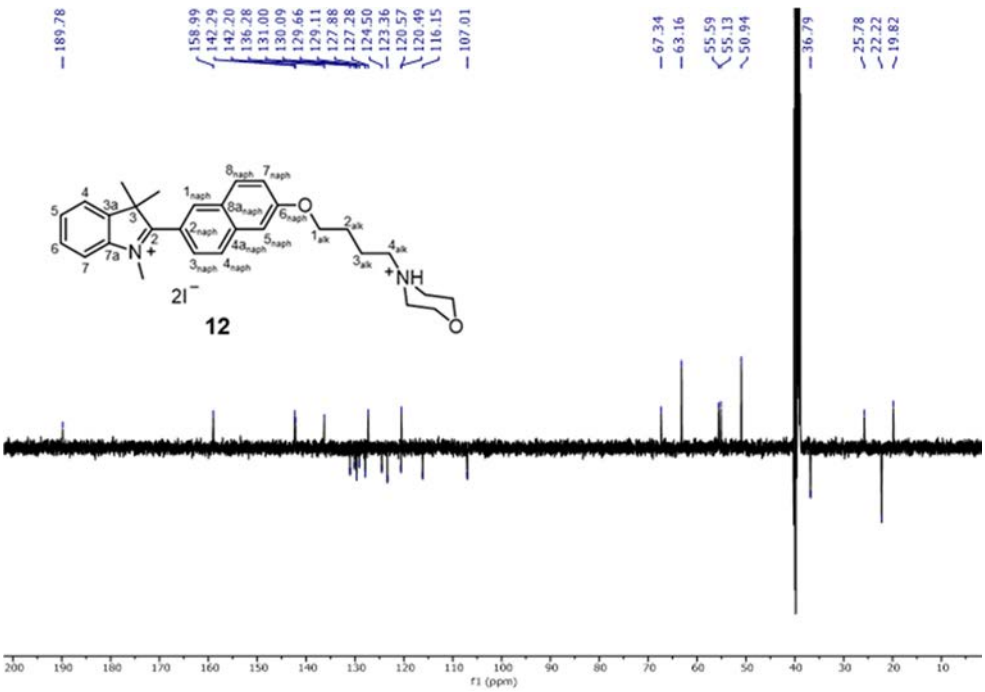

^{13}C-NMR SEFT (101 MHz) spectrum of compound **12** in DMSO-d_6

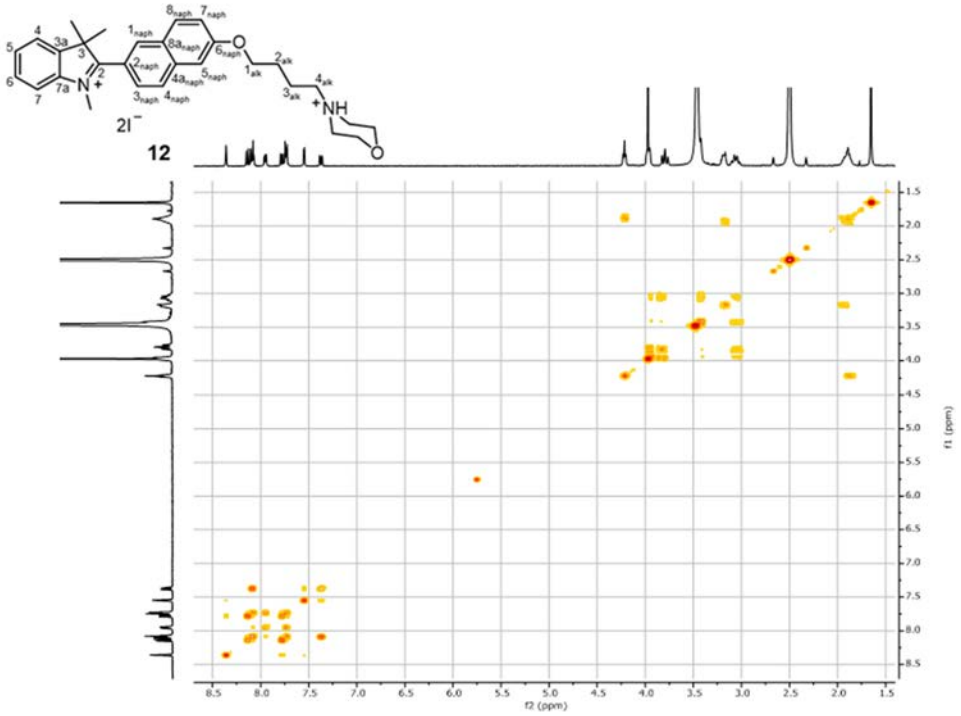

^{1}H-^{1}H COSY (400 MHz) spectrum of compound **12** in DMSO-d_6

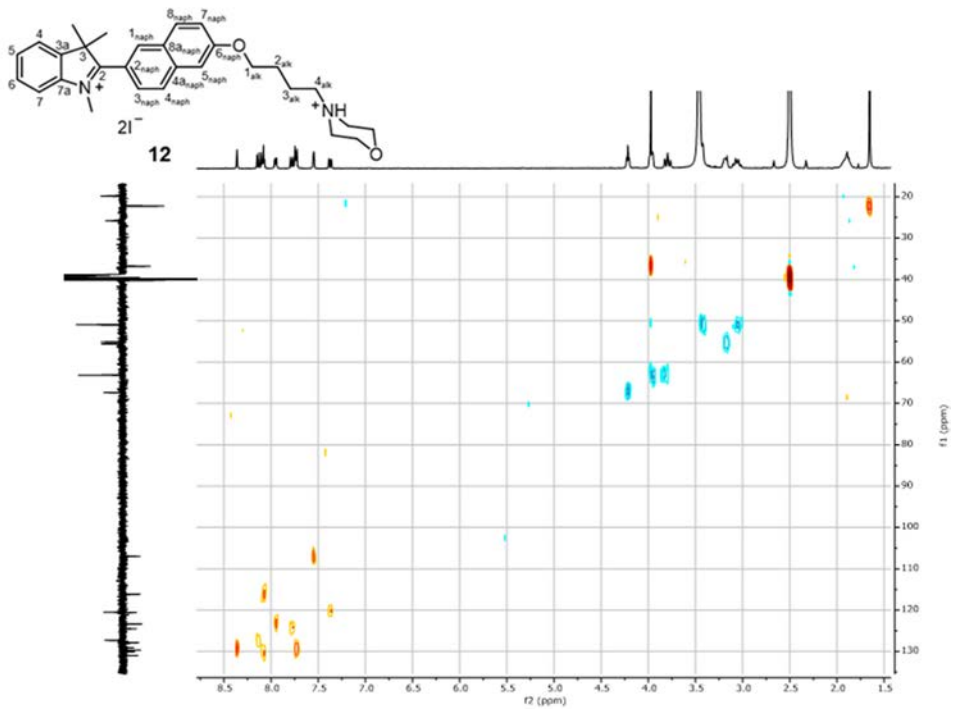

^{1}H-^{13}C HSQC spectrum of compound **12** in DMSO-d_6

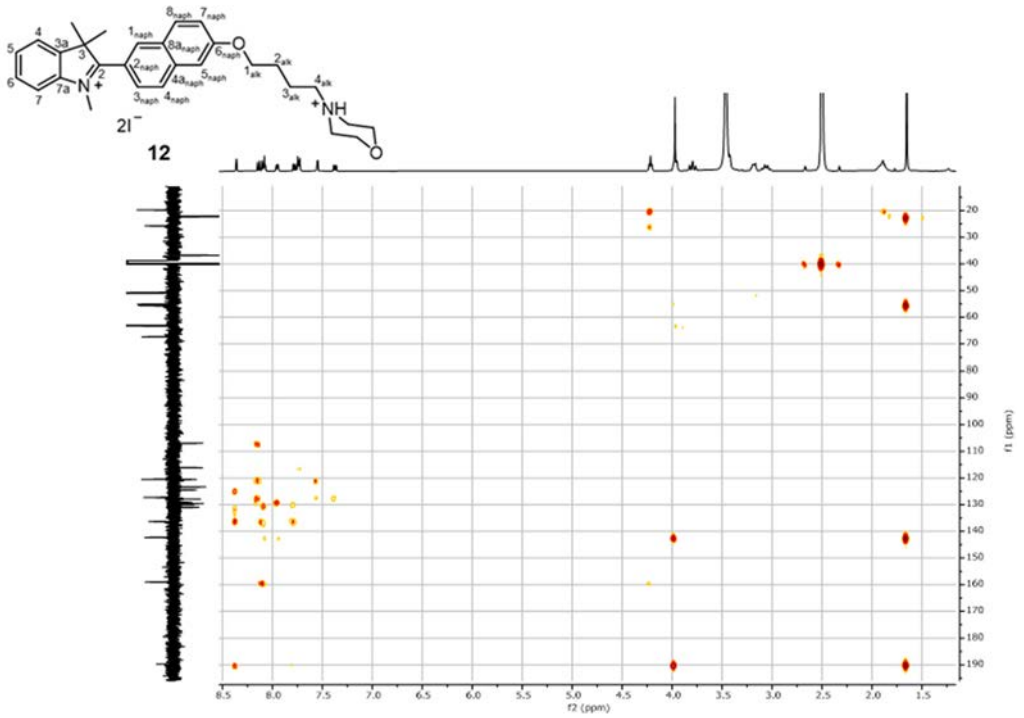

^{1}H-^{13}C HMBC spectrum of compound **12** in DMSO-d_6

INFORME DE VALORACIÓN DE TESIS
THESIS EXAMINER'S REPORT

Título de la tesis / Thesis title: Synthesis and characterization of new chromophores with two-photon absorption properties and study of their application in bioimaging

Doctorando / PhD candidate: Carlos Benítez Martín

Informe redactado por / Examiner's name: Prof. Dr. Dario Bassani

RESUMEN VALORACIÓN / ASSESSMENT SUMMARY

	Excelente Excellent	Buena Good	Suficiente Fair	Deficiente Poor
Originalidad / Originality	X			
Metodología / Methodology	X			
Relevancia de los resultados/ Relevance of results	X			
Discusión y Conclusiones Discussion and conclusions	X			
Bibliografía / References		X		
Presentación / Presentation		X		
Publicaciones / Publications	X			

RECOMENDACIÓN / RECOMMENDATION

[X] Acceptar /**Accept**
[_] Cambios Menores / **Minor Corrections**
[_] Cambios Mayores / **Major Corrections**
[_] Rechazar / **Revise and Resubmit**

Explicación de las recomendaciones. La calificación otorgada dependerá del tipo de comentarios realizados por el evaluador y del tiempo que considera el experto que el doctorando necesita para llevar a cabo los cambios sugeridos: menos de 1 mes para **cambios menores**, menos de 3 meses para **cambios mayores**. En el caso en que el evaluador considere que el doctorando necesita más de 3 meses para incorporar los cambios sugeridos, la evaluación debe ser negativa (**Rechazar**). Una recomendación de **aceptar** indica que el revisor considera que la tesis presentada no necesita cambios.
Explanation of Recommendations. The examiner should recommend **Accept** if no changes are required to the manuscript. Other recommendations suggest that changes are required, and they depend on the kind of changes and the estimated time required to implement them. Minor corrections must be completed within one month, and major modifications may require up to three months to implement. If the examiner considers that the suggested changes are substantial enough to require more than 3 months, the recommendation shall be **Revise and re-submit**.

Por favor, indique en la siguiente página una justificación de la valoración otorgada siguiendo el esquema propuesto, e incluya una lista detallada con los cambios que se sugiere incorporar en la tesis.

Please use the following pages to justify your recommendation and to list your suggested changes.

Edificio Pabellón de Gobierno. Campus El Ejido. 29071
Tel.: 952 13 10 28 / 952 13 14 61 / 952 13 71 10
E-mail: doctorado@uma.es

INFORME JUSTIFICATIVO DE LA VALORACION OTORGADA / DETAILED Report:

Use tantas páginas como necesite / use as many pages as needed

1. PUNTOS FUERTES DE LA TESIS / STRENGTHS

The manuscript proposed by Mr. Carlos Benítez Martín describes the design, synthesis, and photophysical investigation of a series of indolenine and indolinium derivatives possessing large two-photon absorption cross sections. Their non-linear optical properties are explored in detail under different operational environments to elaborate functional cellular probes for different markers. A particularly strong point of the thesis is the completion, by the candidate, of numerous in vivo cellular studies to demonstrate the applicability of the techniques for real-world sub-cellular imaging applications. This highly interdisciplinary aspect is a tremendous achievement that demonstrates that the candidate was able to take full advantage of the interdisciplinarity offered by the host laboratory. Another strong point of the work is the rational design of two-photon absorbing molecules. This is a difficult task in that it involves complex experimental procedures for measuring the active cross-section, compounded by the fact that few design paradigms are known in the literature. Mr. Benítez starts with some basic requirements such as the presence of non-centrosymmetrical push-pull chromophores present in indolenines to design off-on probes for mapping reactive oxygen species in cells. In contrast to other sensors in which the presence of reactive oxygen species leads to the extinction of the luminescence, the design of off-on sensors represents a great achievement due to the much higher sensitivity and selectivity of the sensor. Reactive oxygen species are indicative of oxidative stress in cells and it is evident that the sensors obtained by Mr. Benítez set a new standard in terms of selectivity and sensitivity. These are further combined with the inherent advantages of two-photon excitation such as deeper tissue penetration and higher resolution. Cell-viability studies were also undertaken to determine tolerance thresholds in living organisms, thus allowing real-time imaging of oxidative stress in living cells. During the exploration of the photophysical properties of the naphthyl-indole chromophores, Mr. Benítez noticed that some derivatives possessed pH-sensing capabilities. This was exploited to yield a family of pH sensitive probes with very low cytotoxicity (below 0,01 mM) with applications in sub-cellular (eg cytoplasmic) imaging. A particularly noteworthy achievement of Mr. Benítez is the design and synthesis of organelle-specific labelling probes active in two-photon imaging. Such probes are essential tools in elucidating and understanding interactions between sub-cellular organisms that are essential for life, including cell-trafficking processes. Understandably, these cannot be followed using conventional staining methods that are cytotoxic. Rather than designing several probes each specific for one single organelle, Mr. Benítez instead prepared probes whose photophysical properties varied substantially depending on which organelle they are internalized. This elegant solution allows usage of a single chromophore (therefore simplifying instrumental constraints to a single excitation wavelength) to follow different intracellular species as nicely demonstrated by the numerous colocalization imaging studies he performed on HeLa cells. In yet another interesting development, Mr. Benítez proposes the combination of two-photon excitation with an intramolecular switchable quenching process to achieve four-photon excitation. This novel concept is explained in detail and corroborated by the design and photophysical investigation of a complex dyad incorporating a dithienylethene switch and fluorene donor. This system displays quasi-quartic response on the incident light intensity, which could lead to significant improvements in localization resolutions. Finally, the thesis is written in a concise yet informative style that assists the reader with ample introductions that are distributed amongst the individual

chapters. The language combines both chapters in English and in Spanish, demonstrating the excellent international skills of the candidate. In key places, such as the summary of the work, the objectives, and the conclusion, the sections are duplicated in both languages to ensure legibility in an international context.

2. PUNTOS DÉBILES / WEAKNESSES

The thesis represents a significant advance in the design of two-photon active probes for in-vivo cellular imaging using non-linear optical properties. There are no particular weaknesses that need to be addressed and the manuscript can be submitted in its present form. One may nonetheless note that the full comprehension of the research is contingent on the understanding of both Spanish and English.

Use tantas páginas como necesite / use as many pages as needed

3. CAMBIOS SUGERIDOS / SUGGESTED CHANGES (1/2)

3.1 Cambios obligatorios / Mandatory changes

No mandatory changes are requested

Use tantas páginas como necesite / use as many pages as needed

3. CAMBIOS SUGERIDOS / SUGGESTED CHANGES (2/2)

3.2 Otros cambios propuestos / Optional changes and suggestions for improvement

If space permits, the objectives and conclusions (chapters 2 and 7, respectively) could be expanded in a more literal style.

Fecha / Date (dd/mm/yy): Sept. 10th, 2021

Firmado / Signature:

.....

INFORME DE VALORACIÓN DE TESIS
THESIS EXAMINER'S REPORT

Título de la tesis / Thesis title: Synthesis and characterization of new chromophores with two-photon absorption properties and study of their application in bioimaging

Doctorando / PhD candidate: Carlos Benítez Martín

Informe redactado por / Examiner's name: Prof. Dr. Cristian A. Strassert

RESUMEN VALORACIÓN / ASSESSMENT SUMMARY

	Excelente Excellent	Buena Good	Suficiente Fair	Deficiente Poor
Originalidad / Originality	X			
Metodología / Methodology	X			
Relevancia de los resultados/ Relevance of results	X			
Discusión y Conclusiones Discussion and conclusions	X			
Bibliografía / References	X			
Presentación / Presentation	X			
Publicaciones / Publications	X			

RECOMENDACIÓN / RECOMMENDATION

[X] Acceptar /**Accept**
[_] Cambios Menores / **Minor Corrections**
[_] Cambios Mayores / **Major Corrections**
[_] Rechazar / **Revise and Resubmit**

Explicación de las recomendaciones. La calificación otorgada dependerá del tipo de comentarios realizados por el evaluador y del tiempo que considera el experto que el doctorando necesita para llevar a cabo los cambios sugeridos: menos de 1 mes para **cambios menores**, menos de 3 meses para **cambios mayores**. En el caso en que el evaluador considere que el doctorando necesita más de 3 meses para incorporar los cambios sugeridos, la evaluación debe ser negativa (**Rechazar**). Una recomendación de **aceptar** indica que el revisor considera que la tesis presentada no necesita cambios.
Explanation of Recommendations. The examiner should recommend **Accept** if no changes are required to the manuscript. Other recommendations suggest that changes are required, and they depend on the kind of changes and the estimated time required to implement them. Minor corrections must be completed within one month, and major modifications may require up to three months to implement. If the examiner considers that the suggested changes are substantial enough to require more than 3 months, the recommendation shall be **Revise and re-submit**.

Por favor, indique en la siguiente página una justificación de la valoración otorgada siguiendo el esquema propuesto, e incluya una lista detallada con los cambios que se sugiere incorporar en la tesis.

Please use the following pages to justify your recommendation and to list your suggested changes.

Edificio Pabellón de Gobierno. Campus El Ejido. 29071
Tel.: 952 13 10 28 / 952 13 14 61 / 952 13 71 10
E-mail: doctorado@uma.es

INFORME JUSTIFICATIVO DE LA VALORACION OTORGADA / DETAILED Report:

Use tantas páginas como necesite / use as many pages as needed

1. PUNTOS FUERTES DE LA TESIS / STRENGTHS

The doctoral thesis is correctly written, and the results are presented in a coherent and systematic manner.

I very much enjoyed the quality of the graphical work as well as the in-depth photophysical characterization of the products paired with the assessment of their applicability in bioimaging – these are beautifully elegant results.

The conclusions are adequately supported by experimental evidence and put in context of previously published work. Most of the experimental results and their discussion have been published in international peer-reviewed journals, meaning that they have been evaluated by external referees according to the highest scientific standards at international level. The high impact factor of the publications demonstrates the scientific and technical relevance of the work.

The guidance and supervision of the experienced doctoral mentors further guarantee that the content of this work can be defended by the candidate aiming the doctoral degree.

2. PUNTOS DÉBILES / WEAKNESSES

I have no negative comments.

Edificio Pabellón de Gobierno. Campus El Ejido. 29071
Tel.: 952 13 10 28 / 952 13 14 61 / 952 13 71 10
E-mail: doctorado@uma.es

Edificio Pabellón de Gobierno. Campus El Ejido. 29071
Tel.: 952 13 10 28 / 952 13 14 61 / 952 13 71 10
E-mail: doctorado@uma.es

Use tantas páginas como necesite / use as many pages as needed

3. CAMBIOS SUGERIDOS / SUGGESTED CHANGES (1/2)

3.1 Cambios obligatorios / Mandatory changes

I have no changes to suggest.

Edificio Pabellón de Gobierno. Campus El Ejido. 29071
Tel.: 952 13 10 28 / 952 13 14 61 / 952 13 71 10
E-mail: doctorado@uma.es

Use tantas páginas como necesite / use as many pages as needed

3. CAMBIOS SUGERIDOS / SUGGESTED CHANGES (2/2)

3.2 Otros cambios propuestos / Optional changes and suggestions for improvement

No further comments.

Fecha / Date (dd/mm/yy): 16.09.2021

Firmado / Signature:

Univ.-Prof. Dr. Cristian A. Strassert

Response to reviewers

Comments to Dr. Cristian Strassert

I would like to thank Dr. Strassert for his report. I appreciate his very positive comments about the thesis.

Comments to Dr. Dario Bassani

First, I would like to thank Dr. Bassani for his thorough report on the thesis, and the kind and positive comments.

Concerning to the suggestions of Dr. Bassani, I find the objectives and conclusions more straightforward in the current style. I think that their schematic description improves the readability and the understanding of the concepts that they summarize. Although I consider that no changes are needed, I appreciate his suggestion.